AUTOMATED 3D MICROASSEMBLY WITH PRECISION ADJUSTED HYBRID SUPERVISORY CONTROLLER

by

ADITYA N. DAS

Presented to the Faculty of the Graduate School of
The University of Texas at Arlington in Partial Fulfillment
of the Requirements
for the Degree of

DOCTOR OF PHILOSOPHY

THE UNIVERSITY OF TEXAS AT ARLINGTON

December 2009

Everything that can be, will be somewhere, sometime...

ACKNOWLEDGEMENTS

I would like to thank my supervising professor Dr. Dan Popa for constantly motivating and encouraging me, and also for his invaluable advice during the course of my doctoral studies.

I would also like to extend my thanks to Dr. Frank Lewis, Dr. Kamesh Subbarao and Dr. Jeongsik Sin for their guidence in my research and invaluable suggestions.

Lastly, I would like to thank Dr. Harry Stephanou for providing the support and oppertunity for me to carry out necessary experimentations at the Texas Micro Factory in Automation and Robotics Research Institute (ARRI).

Finally, I would like to express my deep gratitude to my parents.

November 12, 2009

ABSTRACT

AUTOMATED 3D MICROASSEMBLY WITH PRECISION ADJUSTED HYBRID SUPERVISORY CONTROLLER

ADITYA N. DAS, Ph.D.

The University of Texas at Arlington, 2009

Supervising Professor: Dan O. Popa

Unlike semiconductor integrated circuits (ICs), newer microsystems combine sensors, actuators, mechanical structures, electronics, and optics on a single substrate. In such a diversified system, heterogeneous manipulation of the components becomes unavoidable. In an effort to find a solution to reduced yields and speeds in manufacturing at the micro-scale, research initiated in 1990s has sought to understand top-down aspects of micromanipulation, sensor-based precision control of robots, self alignment effects using compliant micro structure designs, and so on. From these research, automated microassembly emerges as an enabling technology for micro manufacturing that offers well-known pathways to building heterogeneous microsystems with a higher degree of robustness and more complex designs than monolithic fabrication. The success of assembly in micro domain, however, is directly related to the level of precision design and automation. Control and planning are two defining factors for the microassembly yield and its cycle time. Assembly at the microscale harbors many difficult challenges due to scaling of physics, stringent tolerance budget, high precision requirements, limited work volumes, and so on.

These difficulties warrant new control and planning algorithms, different than their macro-scale counterparts.

In this research, a hybrid controller for automated MEMS assembly has been formalized using precision metrics such as resolution, repeatability and accuracy (RRA). A *"high yield assembly condition (HYAC)"* has been proposed as a quantitative metric to assess success or failure of microassembly. Using this quantitative tool, the precision-adjusted hybrid controller switches between open, closed, and calibrated operation in the microassembly cell. Additionally, this research modifies traditional robot motion planning algorithms by introducing discontinuous sensor field measurements and proposes a planning algorithm referred to as *"precise path search"*. Unlike conventional "star" path-planners in macro scale, this algorithm prioritizes the attained precision over distance, and hence will select more precise assembly plans than the faster ones. The instantaneous as well as cumulative intricacy in a multipart microassembly scenario is identified by flagging the subtasks with binary *"complexity indices (CI)"* and updating them throughout the assembly process. The proposed hybrid controller dynamically adapts to the assembly process based on these complexity indices for the subtasks.

The proposed framework has been demonstrated for multiple microassembly scenarios including assembly of a MEMS optical spectrum analyzer called *"Microspectrometer"* and a micro robot called *"ARRIpede"*. Both systems pose several challenges in manufacturing such as workspace identification, motion planning for robot end-effectors, optical and mechanical alignment of components, heterogeneous micro part integration, and so on. Simulation and experimental results for the assemblies of these microsystems are presented to indicate that the proposed hybrid controller lead to high yields at faster cycle times than conventional precision control methods. The concepts described in this dissertation have been applied and embodied into robotic

assembly cells, assembly simulators and concurrent microengineering tools, such as a reconfigurable microassembly system called "μ^3", programming of an extensive automation software application called "*Neptune 3.0*", programming of a virtual reality simulation software application called "*Microsim 1.0*", design, construction and packaging of miniature electronic backpack modules for untethered microsystems.

TABLE OF CONTENTS

ACKNOWLEDGEMENTS iv

ABSTRACT v

LIST OF FIGURES xiii

LIST OF TABLES xviii

Chapter Page

1. INTRODUCTION 1

1.1 Motivation 1

1.1.1 Potential areas of application for microsystems 3

1.1.2 Characteristics of microsystems 5

1.1.3 Silicon MEMS and non-silicon MEMS 6

1.1.4 Insufficiency of conventional microfabrication processes 7

1.1.5 Heterogeneous MEMS assembly: A solution for miniaturization 8

1.1.6 Classification in MEMS assembly 8

1.1.7 Automated microassembly - An industry perspective 9

1.1.8 Challenges in automated microassembly 10

1.1.9 Concurrency in MEMS manufacturing through microassembly 12

1.2 Deterministic serial top-down approach to automated MEMS assembly with the use of hybrid control 13

1.3 Contributions 15

1.4 Thesis organization 18

2. BACKGROUND 21

2.1 MEMS and microassembly 21

2.2 Study of physics in microdomain for micro manipulation 23
2.3 MEMS control 24
2.4 Controls for assembly in micro domain 25
2.5 Microassembly systems 28
2.6 Modular MEMS assembly 29
2.7 Planning for microassembly 30
2.7.1 An overview on conventional path planning techniques 31
2.8 Concurrent engineering 32
2.9 Multiscale multi-robot assembly/packaging systems at ARRI 33
2.9.1 M^3: Macro-meso-micro scale assembly system 33
2.9.2 μ^3: Meso-micro-nano scale assembly system 35
2.9.3 N^3: Wafer level assembly with Nano scale positioners 38
3. ASSEMBLY PLANNING IN MICRO DOMAIN 42
3.1 Precision metrics: Resolution, Repeatability and Accuracy 42
3.1.1 Classical representation 42
3.1.2 Redefining the metrics for microassembly 44
3.2 Assemblability criterion 49
3.2.1 Categorization of microassembly task uncertainties 50
3.2.2 High Yield Assembly Condition (HYAC) 52
3.3 Planning motion path for microassembly 53
3.3.1 Requirements of path planning 54
3.3.2 Precision issues with path tracking in microscale 56
3.4 Uncertainties in robot kinematics and their effect on precision 57
3.4.1 Robot forward kinematics 58
3.4.2 Uncertainties in robot parameters 60
3.5 Searching for a precise path in microassembly 69

3.5.1 Precise path search algorithm (PPSA) 70
3.5.2 Example of a simple planning scenario 72
3.6 Kinematics evaluation and planning with a typical PPR microassembly robotic manipulator 73
3.6.1 Forward kinematics and spatial Jacobian for the PPR robot 74
3.6.2 Numerical analysis with static and dynamic errors 76
3.7 Discussion on experimental setups for minimizing uncertainty in robot tracking 81
4. PRECISION ADJUSTED HYBRID CONTROLLER 84
4.1 $2\frac{1}{2}D$ microassembly and compliant micro mechanism 85
4.2 Complexity Index (CI) in microassembly workcell 87
4.3 Hybrid controller for microassembly 89
4.3.1 Design of the hybrid controller 90
4.4 Automation steps in microassembly workcell 92
4.4.1 Offline estimation of motion path and task complexity 92
4.4.2 Verification of microassembly process in virtual 3D 101
4.4.3 Calibration of workcell 103
4.4.4 Online execution of hybrid controller and event handling . . . 105
4.5 Experimentation in a microassembly workcell 106
4.5.1 Scenario description 106
4.5.2 Optimization of servoing based on precision requirement and time consumption 109
4.5.3 Optimization of microassembly based on yield, time and cost 113
5. MICROSPECTROMETER: A CASE STUDY FOR MANUFACTURING OF A COMPLEX MOEMS 116
5.1 Related research on MOEMS 117

5.2 Releated work on miniaturization of spectrometer 117
5.3 Design and working principle of ARRI's microspectrometer 118
5.3.1 Working principle 118
5.3.2 Design 121
5.4 Tolerance analysis 122
5.5 Evaluation of precision budget 128
5.5.1 Fabrication uncertainty (σ_1^2) 129
5.5.2 Vision system uncertainty (σ_s^2) 130
5.5.3 Fixturing uncertainty (σ_2^2) 132
5.5.4 Robot uncertainty (σ_3^2) 133
5.6 Assembly of microspectrometer 134
5.6.1 Description of assembly operations and process flow 134
5.6.2 Microspectrometer assembly tasklist and hybrid controller implementation 140
5.6.3 Manufacturability metrics analysis 142
5.7 Optical coupling analysis 142
5.7.1 Steps involving coarse alignment 142
5.7.2 Steps involving fine alignment 149
5.8 Spectrum results 152
6. CONCURRENT MICROMANUFACTURING FOR MICROSYSTEMS . . 155
6.1 Need of concurrent engineering in MEMS development 155
6.2 Characteristics and requirements for concurrent micromanufacturing 156
6.2.1 Areas for concurrency in micromanufacturing via microassembly 158
6.3 Discussion on the range of choices for different parameters 159
6.3.1 Family of actuators and sensors 159

6.3.2 Materials for microsystems 161
6.3.3 Trade-offs among design, fabrication and assembly 161
6.3.4 Packaging of MEMS 162
6.3.5 Compliant vs. non-compliant mechanism for microassembly 164
6.4 Centralized database and query-based evaluator for micromanufacturing process analysis 165
6.5 Example: automated microassembly of ARRIpede microrobot 167
6.5.1 Microrobot description 167
6.5.2 Setting the requirements 167
6.5.3 Finding the solutions 168
6.5.4 Assembly scheme, packaging with electronic backpack 169
6.6 A few other examples: Compliant, noncompliant and heterogeneous microsystems 172
7. CONCLUSION 176
7.1 Conclusion 176
7.2 Future work 179
Appendix
A. HARDWARE CONFIGURATION - μ^3 MICROASSEMBLY SYSTEM . . 180
B. SOFTWARE APPLICATION - NEPTUNE 3.0 194
C. SIMULATION IN VIRTUAL REALITY - MICROSIM 2.0 213
D. MINIATURE ELECTRONIC BACKPACK FOR MICROSYSTEMS . . . 216
E. DERIVATION OF EFFECT OF UNCERTAINTIES 228
REFERENCES 231
BIOGRAPHICAL STATEMENT 243

LIST OF FIGURES

Figure		Page
1.1	Market analysis for microsystems (source: nexus III)	4
2.1	M^3 multiscale assembly system at ARRI's Micro Factory	34
2.2	Diagram and picture of a MOEMS device, including Kovar package, MEMS die, fiber-optics and wire-bonds	35
2.3	μ^3 microassembly system at ARRI's Micro Factory	36
2.4	Examples of micro assemblies using μ^3, including 50μm thick SOI thermal MEMS with out of plane passive and actuated grippers, as well as active zero-force sockets	38
2.5	A row of standing passive Zyvex jammers obtained by calibration and assembly scripting	39
2.6	ARRI's Microspectrometer built on a 1cm x 1cm silicon die	40
2.7	Miniature micro souvenir showing the model of a set of buildings and Texas flag	40
2.8	Miniature micro souvenir showing the model of a roman temple	41
2.9	Miniature micro souvenirs showing the model of Eiffel Tower	41
3.1	Classical representations for precision	43
3.2	Control and planning structure for microassembly	54
3.3	Uncertainty in robot precision	61
3.4	Effect of static uncertainty on robot precision	62
3.5	Precise path planning example	72
3.6	Base robot (M_3) of the μ^3 microassembly system	73
3.7	3D rendering of the (M_3) robot of the μ^3 microassembly system	74
3.8	A PPR robot equivalent to the M_3 robot of μ^3 system	75

3.9 A PPR robot with dynamic motion-uncertainties 77
3.10 A PPR robot with static and dynamic errors 78
3.11 Redundant robot configuration based on precision evaluation 81
3.12 Stage position metrology device from Zygo Metrology Solutions 82
3.13 Calibration using single sensor 83
4.1 2D assembly 86
4.2 $2\frac{1}{2}D$ assembly 86
4.3 3D assembly 87
4.4 Output feedback controller state-space block diagram 90
4.5 Hybrid supervisory controller state-space block diagram 91
4.6 Raw data collected from stationary sensor over stationary feature . . 93
4.7 Histogram and probability density function 94
4.8 Gaussian approximation of sensor precision 94
4.9 Uncertainty in robot positioning 95
4.10 Raw data from accuracy test experiment for a PPR robot 96
4.11 Data distribution (with Gaussian fit) for accuracy test experiment for the PPR robot 96
4.12 Raw data from repeatability test experiment for the PPR robot . . . 97
4.13 Data distribution (with Gaussian fit) for repeatability test experiment for the PPR robot 97
4.14 Design tolerance given to a MEMS part for assembly 98
4.15 Fixturing uncertainty in MEMS parts 99
4.16 Misalignment is MEMS part (inner polygon)inside holder(outer polygon) after detethering 99
4.17 Data distribution (with Gaussian fit) for detethering 100
4.18 Data distribution (with Gaussian fit) for die placement 100
4.19 Microassembly in virtual reality 101

4.20 Simulation results from repeated microassembly in virtual 3D 102

4.21 Rotated coordinate frames attached to M_1 and M_3 manipulators and calibration of M_1 end-effector using a 3- point teaching method 104

4.22 Discrete transit point based online event handling 106

4.23 Process flow for automated microassembly with precision adjusted hybrid controller 107

4.24 A typical assembly scenario for complex microassembly 108

4.25 Time consumption in different method of servoing with variation in required accuracy 110

4.26 Error propagation during servoing for different cases 111

4.27 Time consumed in servoing for different cases (without including calibration time) 112

4.28 Time consumed in servoing and calibration for different cases (including calibration time) 113

4.29 Time taken during hybrid loop, closed loop and open loop control . . 114

4.30 Accuracy achieved during hybrid loop, closed loop and open loop control 115

5.1 Working principle of microspectrometer 119

5.2 3D rendering of the microspectrometer with the components locations 122

5.3 Layout of the thermal actuator for scanning mirror mechanism 123

5.4 Layout of the MEMS die for microspectrometer 124

5.5 Micro-components used in FTIR microoptical bench with dimensions 125

5.6 Misalignment in fiber coupling with ball lens 126

5.7 Effect of mirror tilt angle in microspectrometer 127

5.8 Effect of misalignment in beam splitter 128

5.9 Frabrication error distribution in DRIE process 129

5.10 Measurement data for repeated readings from vision system 130

5.11 Probability density function calculation for sensor precision 131

5.12 Uncertainty distribution in sensor precision 132

5.13 Fixturing uncertainty distribution 133

5.14 Micro jammer and micro needle 135

5.15 Assembly of MEMS parts by micro jammer 136

5.16 Assembly of ball lens with vacuum nozzle 137

5.17 Epoxy bond strength test experiment 138

5.18 Completely assembled of microspectrometer 139

5.19 Comparative analysis of precision adjusted hybrid controller with pure open loop and pure closed loop control (results from 10 experimental microassembly attempts in each case are shown) 143

5.20 Power transmission with and without collimation 144

5.21 Test of fiber offset 145

5.22 Experimental setup and implementation of machine vision edge detection technique for tilt correction 146

5.23 Machine vision edge detection for mirror tilt measurement and adjustment 147

5.24 Coarse alignment of the fiber 147

5.25 Diameter of the spot on the mirror vs. the corresponding fiber distance from the ball lens surface 148

5.26 Image consisting of two laser spots projected onto a microscope CCD camera with a 5x zoom lens. Fine rotations of the beamsplitter cause the distance d between the spots to converge to zero 149

5.27 Decrease in laser spot separation in μm using spot Jacobian servoing 151

5.28 Joint angle increments in mrad during servoing 152

5.29 (a) Spectrogram data (intensity vs. samples), (b) Actuation profile of the MEMS mirror (voltage vs. displacement) and (c) Spectrum of calculated laser source (635nm) from our MEMS FTIR spectrometer 154

6.1 Concurrent micromanufacturing framework 156
6.2 Compliant microassembly vs noncompliant microassembly 165
6.3 Compliant and noncompliant microparts 166
6.4 Centralized database structure for concurrent micromanufacturing . . 167
6.5 Query-based evaluator for concurrent micromanufacturing 168
6.6 Arripede microrobot device die 170
6.7 Arripede microrobot device die 172
6.8 Arripede gait signal as observed by a CRO (for four channels) 173
6.9 Arripede microrobot packaged with electronics backpack 174
6.10 Construction of a multilayer MEMS structure 175

LIST OF TABLES

Table		Page
4.1	Comparison among different control schemes	85
4.2	Control schemes based on complexity index	89
5.1	Robot system precision test σ_3^2	134
5.2	Cost function comparison for 1200 simulated microspectrometer assemblies in virtual 3D	142
6.1	Typical characteristics for different MEMS actuators	160
6.2	Typical characteristics for different MEMS sensors	160

CHAPTER 1

INTRODUCTION

1.1 Motivation

As the world enters the new millennium, miniaturization technology is capturing attention of the populous. In recent times, numerous scientific research and developments dwell on shrinking existing devices, as well as on building new products with reduced spatial dimensions. Lesser energy requirement, easier portability, and lower cost are only a few of the many motivating factors driving the research. It all started when the first transistor was built at Bell Laboratories on December 16, 1947. Invented during mid twentieth century, semiconductor technology revolutionized miniaturization of sophisticated electronic systems by exceptionally reducing the size of passive and active components. An example could be the recent developments in high density CMOS memory chip manufacturing with average half-pitch, which defines the smallest feature size in a repeated array to be as low as 45 nanometers.

Amidst all the significant progresses, however, mechanical sensing and actuation devices that require component level mobility in some form or other, remained untouched by miniaturization until MEMS (*Micro-Electro-Mechanical-Systems*) technology came into picture during late twentieth century. MEMS technology enabled the construction of microscale objects on a monolithic substrate through either additive or subtractive chemical micro-machining processes available to date. Using suitable designs and following proper fabrication steps smaller mechanical structures with limited mobility were made and integrated on a chip along with the electronics to be used as sensors.

At first, parts made using such monolithic fabrication methods were generally thin and weak, having very low resistance to deformation under external stresses as well as over aging. This restricted the designs of the earlier MEMS products, such as pressure sensors and accelerometers to be primarily *in-plane*. In late 1990s, with availability of high precision robotic manipulators and stronger MEMS parts made using high aspect ratio manufacturing processes such as DRIE (*Deep Reactive Ion Etching*) [1] and LIGA (*LIthographie, Galvanoformung, Abformung*) [2], it became possible to release the micro parts off the substrate and manipulate them in 3D space without damaging them. This gave birth to *3D MEMS assembly* as an alternative way for micro-manufacturing. The newer microsystems made using 3D MEMS assembly promise higher strength, robustness, and design simplicity. Unlike micro-manipulation studies of 90's, which focused on understanding physics in small scales and using it for achieving mobility of micro-sized objects, hardly controllable and observable however, 3D microassembly incorporates a structured framework for handling micro components. This methodical approach has brought about a change in the way the micro domain used to be perceived in past and opened up whole new avenues for industrialization of MEMS.

Out-of-plane manipulation of micro-sized parts using high precision robots offers flexibility to integrate different materials, have comparatively simpler design and smaller real-estate, and use reconfigurable modular structures. However, automated microassembly also requires addressing control and planning related challenges. Higher volume production of miniaturized devices requires the successful operation at required throughput and yield across multiple scales of tolerance, part dimension and workspace limitations. Typically, sequential microassembly requires a high precision micromanipulator and motion control, either by off-line programming with calibration or by on-line sensory feedback control. The later can be accomplished via

a microscope or a force sensor integrated with the gripper, or both. However, the price paid in assembly speed is considerable, resulting in low assembly throughputs. On the other hand, faster open loop control does not necessarily ensure high assembly yields, especially in case of complex and sequential processes. This suggests the need for hybrid control structures and real-time adaptive planning schemes in order to maximize the advantages and minimize the drawbacks. Once the challenges are overcome, automated 3D microassembly can offer a viable and cost effective way for microsystem manufacturing.

1.1.1 Potential areas of application for microsystems

The extensive scope and easy availability of silicon machining technology, which had been the cornerstone for the success in semiconductor industry, has given birth to the a new breed of miniaturized systems called Micro-Electro-Mechanical-Systems (MEMS) in the early 80s. The very first application of MEMS was in automobile industry as accelerometers which are indeed the simplest form of devices possible, consisting of little more than a cantilever beam with a proof mass (also known as seismic mass) and some type of deflection sensing circuitry. Over the years, however, the spectrum has grown into a full-fledged industry having applications extending over a wide range of products. NEXUS III report [3] on market analysis for microsystems and MEMS details opportunities for 26 MEMS/MST products. Chief among these are read/write heads with 50 percent share and micro-displays, which will overtake inkjet heads in 2009, as Texas Instruments forges ahead with the DLP chip for front projectors and rear projection TVs. Fast growing markets for microphones, RF MEMS, and tire pressure monitors are examined next to established pressure and motion sensors, which are increasingly driven by consumer applications. Emerging markets include wafer probes, micro-motors, micro-spectrometers, micro-pumps and

micro-reaction products. Also there are products that will begin to impact markets at the end of the decade, namely micro fuel cells, MEMS memories and e-fuses, chip coolers and liquid lenses for autofocus/zoom in camera phones.

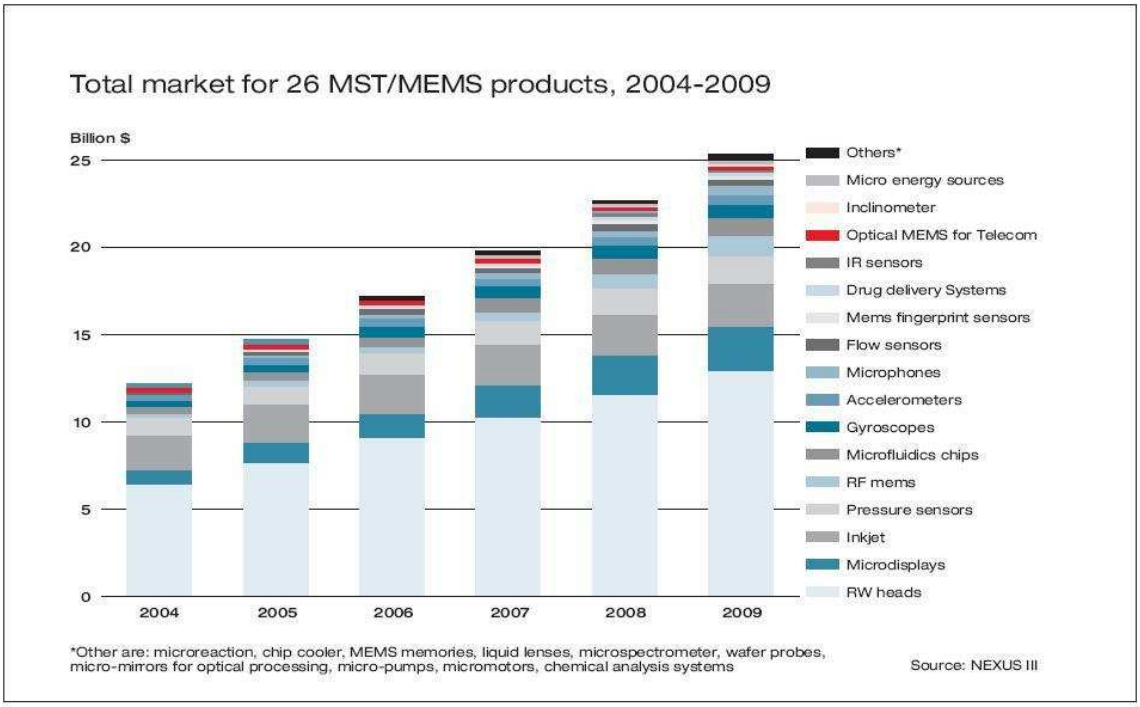

Figure 1.1. Market analysis for microsystems (source: nexus III).

From the figure it reflects that over the next five years, this market is predicted to grow at a rate of 16 percent per year from 12 billion dollars in 2004 to 25 billion dollars in 2009. Additionally, other associative MEMS systems that can be used in popular consumer products such as cell phones, iPods, Wii etc., helping further miniaturization, open up a new manufacturing paradigm for MEMS. All these suggest that microsystems sensors and actuators are consolidating their position in established markets and finding new applications, leveraging a combination of low

manufacturing costs, compact size, low weight and power consumption, as well as increased intelligence and multi-functionality.

1.1.2 Characteristics of microsystems

There are three characteristic features of MEMS technologies that promise its true potential: *miniaturization*, *multiplicity*, and *microelectronics*. Miniaturization enables the production of compact, quick-response devices. Multiplicity refers to the batch fabrication inherent in semiconductor processing, which allows hundreds of components to be easily and concurrently fabricated. Microelectronics provides the intelligence to MEMS and allows the merger of sensors, actuators, and logic to build closed-loop components and systems. The two prevalent technologies that enable drastic miniaturization of industrial products are *microsystems technology (MST)* and *nanotechnology (NT)*. The MST, which started mainly as a "Top-down" approach in miniaturization, evolves from the invention of transistors, as mentioned previously. Nanotechnology (NT) started as a "Bottom-up" approach in miniaturization expanding into "Top-down" types with the availability of sophisticated nano-manipulation systems such as Atomic Force Microscope (AFM) and nano-probes [4]. Despite the fact that both MST and NT are viable enabling technologies for miniaturization of industrial products, they are built on fundamentally different theories and principles. Due to the inheritance from thoroughly-researched and well-established IC fabrication methodologies MST has proven its advantages in commercialization which is obvious from the market study. Bottom-up approach to miniaturization, although still in its infancy, is also getting recognition and can have promising potential in near future.

1.1.3 Silicon MEMS and non-silicon MEMS

Developments of microsystems have been studied with many different types of materials and with wide variety of physical effects. However, considering the domination of silicon based integrated systems it would rather be fair to categorize the microsystems into two types: *silicon based* and *non-silicon based*.

Measured by mass, silicon makes up 25.7 percent of the Earth's crust and is the second most abundant element in the Earth's crust, after oxygen. Silicon is usually found in the form of silicon dioxide (also known as silica), and silicate. Elemental silicon is the principal component of most semiconductor devices, most importantly integrated circuits (IC). Silicon is widely used in IC systems because it remains a semiconductor at higher temperatures and because its native oxide is easily grown in a furnace and forms a better semiconductor or dielectric interface than any other material. Silicon also offers good mechanical strength and flexibility for machining releasable part and strong joints. With these characteristics, silicon became the first choice for MEMS which also got significant support from the well established IC fabrication industry and chemical micromachining processes.

In recent times, a new form of microsystems known as BioMEMS [5] has emerged as an interesting area of study. Areas of research and applications in BioMEMS range from diagnostics, such as DNA and protein micro-arrays, to novel materials for Bio-MEMS, micro-fluidics, tissue engineering, surface modification, implantable BioMEMS, systems for drug delivery and many more. Microfabrication of silicon-based structures is usually achieved by repeating sequences of photolithography, etching by strong chemicals, and deposition steps in order to produce the desired configuration of features which are not well proven for bio-compatibility. Hence people have looked into non-silicon based microsystems as well as other forms of microfabrication steps. Materials such as polymers, metals, glass, ceramic etc are being explored

as viable non-silicon based microsystems and bio-compatible fabrication steps are being researched.

Although there have been many research for non-silicon based microsystems, silicon still remains the primary platform for MEMS technology. However, if non-silicon based microsystems are to be developed then microassembly might prove to be an important and viable solution providing flexibility to integrate multiple heterogeneous components.

1.1.4 Insufficiency of conventional microfabrication processes

The successful miniaturization and multiplicity of traditional electronics systems would not have been possible without IC fabrication technology. Therefore, IC fabrication technology, or micro-fabrication, has so far been the primary enabling technology for the development of MEMS. This IC fabrication technology which is essentially silicon surface micromachining such as lithography, etching etc. has its limitations as *monolithic* integration of electronics and micromechanics inevitably compromises both subsystems. In case of monolithic fabrication the surface micromachined components having erected structures generally have limited "out-of-plane" stiffness and require complex locking mechanisms to prevent flexing of micro parts. The thin parts have very low strength and robustness to defend themselves against un-modeled disturbances, mishandling and aging. The interlocking mechanism takes up large foot-print and requires time consuming expensive fabrication steps. The fabrication steps are monolithic and thus heterogeneous integration of components is not an option.

1.1.5 Heterogeneous MEMS assembly: A solution for miniaturization

In contrast to monolithic surface micromachining, *microassembly* can promise to extend MEMS beyond the confines of silicon micromachining. Microassembly refers to the manipulation and joining of parts of microscale dimensions in a structured environment by robotic manipulators with high precision. In assembly the locking mechanism can be kept fairly simple and thus the die area can be utilized efficiently. The parts are simple in design and easier to fabricate. The assembled parts and the assemblies can have much higher strength and robustness in comparison to their monolithic counterparts, thus providing significant resistance to deformation under the influence of unwanted disturbance and aging.

1.1.6 Classification in MEMS assembly

Miniaturization assembly can have two types of approaches: top-down and bottom-up. These micro-scale assembly methods can be classified based on throughput (serial or parallel), deliberate intervention (deterministic or stochastic), type of end-effectors (contact, non-contact) or level of human intervention (manual, teleoperated or automated) etc.

The past decade has seen considerable progress made in the field of top-down precision assembly. It has been widely accepted for some time that assembly at small scales requires not only very high precision, but also new architectures to deal with large number of parts and control of interactions from one size scale to another. In addition, manufacturing of miniaturized devices requires the successful operation at required throughput and yield across multiple scales of tolerance, part dimension and workspace limitations.

On the opposite side of the spectrum, bottom-up self-assembly methods have been proposed to address challenges related to manipulation of large numbers of

parts. In such cases, the complexity of the assembly is addressed by the design of the parts, coupled by the presence of a physical field (magnetic, electric, thermal, fluidic, vibration) agitating all components to encourage preferential formation of interconnects.

In addition to serial microassembly, there are other non-conventional ways of microassembly which are worth considering such as parallel/exponential assembly, modular assembly or self assembly. The first two can be considered forms of deterministic microassembly where the yield is affected by the precision in tool/part alignment. On the other hand, self assembly can be considered as a stochastic process which is generally random in nature and dependent on the physical process parameters. Self-assembly concept is considered to be the ultimate futuristic solution to mass production of nano-scale products. Examples of self assembly include nano products have been fabricated using modified micro-fabrication techniques such as chemical vapor deposition and epitaxial molecular growth. These techniques, though proven feasible, lack in consistency and desirable rates in production and also are not very cost-effective yet.

Deliberate top-down assembly methods can assemble very complex structures, however the yield, and throughput of the assembly system is limited, while its costs are high. Stochastic bottom-up assembly methods, on the other hand, can assemble very large numbers of parts, are less expensive, but the complexity of achievable assemblies is limited. Clearly, a compromise between the two methods is needed.

1.1.7 Automated microassembly - An industry perspective

Although microassembly has the potential to offer a viable way of building todays complex microsystems consisting of multiple heterogeneous components with high accuracy, yield and performance reliability, the bright picture of market growth,

however, represents only a small fraction of the maximum potential benefits of the microassembly. The principal reason for this gap is due to the lack of reliable, cost-effective packaging and automated assembly technologies for micro and nanoscale products [6]. On an average, it is in a range of 30-90 percent of the overall cost of the product. Cost-effective MEMS packaging is the key factor that attributes to the success of microsystem products in marketplace. The principal cause for the high cost of assembly of micro-scaled products is lack of automation in microassembly. Most of microassembly practices require human operators to pick and place minute parts manually, using high powered microscopes and micro-tweezers.

Manual assembly is prohibitively expensive, tiresome and time consuming. Above all, the operators stress and eye strain associated with assembling such minute parts make it impossible to meet the extremely stringent requirements in precision and thus achieve the necessary quality and reliability of the finished products. Although the assembly and packaging of integrated circuits and the associated electronic systems have reached a stage of maturity of being close to full automation and the same applies to a few established micro-scaled devices including inkjet printer heads and read-write heads for information storage systems and the inertia sensors for automotive airbag deployment systems, automated microassembly technology for the other estimated nine billion microsystem devices remains to be developed.

Therefore it becomes imperative that automated microassembly should be formalized and made available for rapid prototyping of a wide range of microsystems.

1.1.8 Challenges in automated microassembly

The basic requirement of an automated microassembly is that it must be able to transport parts and components of micro-scale and be able to manipulate them so that precise spatial relation with micro-scale tolerances can be established for die alignment

and parts insertion, and for certain packaging processes such as die bonding, device sealing, etc. The associated challenges with automated microassembly are many; such as theory of design, scaling of physics, process modeling, intelligent control, sensing, verification etc. These critical factors have been explored in past by various research groups to improve the automation in microassembly.

Micromanipulation has long been an active area of study where numerous researches have been conducted to understand the scaling of physics in micro domain. As the size of component shrink, the mass to surface ratio gets smaller and smaller. This make the gravitational force smaller and smaller and concurrently surface forces grow dominant. This phenomena of scaling of conventional laws of physics give rise to effects such as stiction, capillary effect etc. which pose challenges to microassembly as parts tend to stick to the end effector making it hard to release.

Sensing is important in any form of assembly as it provide real time information about the status of the process. In micro scale, sensor integration is hard to achieve due to very small work volume and possible risk of affecting the precision. Sensing in microscale has been mainly of two types: contact and non-contact. Vision based sensors such as microscopes are examples of non-contact sensors used for microassembly. These are generally bulky and thus cannot be used in large number. Also the frequency of sensing is slow in case of vision based sensors. The other types of sensors used are contact sensors such as force sensors. Force sensors can be built small enough to be integrated with microassembly but in case of contact sensors additional mechanical components are needed to be attached either to the manipulator or the MEMS device, which affects the precision of the tool.

Planning and control are the integral parts of assembly. In microassembly the tolerances allowed for joints and parts are very stringent. In a limited assembly workspace in micro-scale and with manipulator and end-effectors much larger in size

than the manipulated parts, subsequent assemblies get harder and harder due to increasing level of obtrusion posed by previous assemblies. Therefore a highly precise control system is needed for microassembly tasks. However, such control systems are generally slower due to feedback process time and complex computation.

Unlike assembly in macro scale, deterministic automation at the micro scale is necessarily more holistic. This means that the design and control of the assembly cell, robots, parts and end-effectors occurs concurrently, and that the performance of such architecture needs to be evaluated not only in terms of adjusted precision metrics but also in terms of yield, cost and throughput.

To be employed in a realistic industry application scenario in a cost effective and reconfigurable robust automated microassembly scheme is a must. However these parameters such as yield, speed and cost are normally mutually exclusive which means trying to achieve one compromises the others.

1.1.9 Concurrency in MEMS manufacturing through microassembly

In addition to the challenges mentioned in the previous subsection, there also exist several other issues which require deliberation while transforming a microsystem prototype into a product. Manufacturable products, which can be commercialized in a profitable manner, only sustain the rigors of consumer market over longer period of time. Yield, throughput and cost are three major factors that decide the manufacturability of a product and optimization among these conflicting parameters often becomes imperative in a production cycle.

Earlier MEMS products, developed using surface micro machining processes inherited from well-established semiconductor fabrication technologies, enjoyed the ease in manufacturing without much trouble. However, today's wide range of microsystems are much more complex in nature with some level of heterogeneity involved in

structural design and thus can only be constructed through microassembly. In such cases, due to the involvement of highly unrelated processes, such as chemical fabrications, mechanical assemblies and so on, it becomes very difficult to keep track of the cost functions for production cycle. Therefore, without implementing concurrent engineering among processes it's hard to make the newer microsystems manufacturable.

Design, fabrication, assembly, packaging and testing are the main manufacturing steps for a microsystem. Conventionally, these steps are followed serially. In order to incorporate concurrency among them it is necessary to build a process analyzing framework which can handle the logistics in micromanufacturing by quantitatively deciding the effect of any specific process parameters on the following processes. Additionally, reliable prediction of cost functions for a set of process parameters can allow better selectivity and also can result in minimum iterations in a development cycle, thus keeping the cost low.

1.2 Deterministic serial top-down approach to automated MEMS assembly with the use of hybrid control

As discussed in previous subsections, a realistic microassembly scheme demands for higher yield, lower assembly time and lower cost. Among all the types of approach to microassembly, serial assembly is most precise and thus can ensure very high yield. Top down serial assembly methodology is a well known concept and can be easily reconfigured for multiple types of assemblies with less effort. Serial assembly, however, is a slow process as it deals with one assembly at a time. When coupled with very stringent tolerance requirements, the amount of time consumed in serial assembly can further deteriorate due to the inclusion of closed loop feedback control. An open-loop approach to serial microassembly has advantages over closed-loop control as it uses only driving modules of the robot to move the micropart without any sensing.

However, open-loop driving is sensitive to parameter uncertainties and thus can result in a low yield and performance reliability. Therefore, it becomes a trade-off in choosing the type of control depending upon the microassembly process or even a mixture of two in an optimized fashion.

If observed closely, it becomes apparent that in microscale the tolerance budgets generally vary from task to task. Some tasks such as part pickup, part detethering etc require less precision and can be automated with open loop control. On the other hand, some tasks such as part placement, component alignment etc require comparatively higher degree of precision and have to be done in closed loop with some type of active feedback systems such as force or vision. The open loop control is faster than closed loop control but less accurate than it. The closed loop control, on the other hand, is much slower depending upon the number and type of sensor feedback and their processing time. The slowness of the closed loop process inhibits the microassembly from achieving the goal of mass production where as the inaccuracy of the open loop process inhibits the microassembly from achieving the yield and performance reliability. Therefore the need for a hybrid control arises that adjust the precision by switching between these two based on the task. The task based precision adjustment hybrid control can offer higher yield as well as performance in less time.

From the above discussion we can see that, if properly used, serial top-down approach to microassembly can offer very high yield; almost 99%. The assembly process, however, will be comparatively slower. In order to resolve this issue a hybrid control structure can be used which can reduce the process time while keeping the yield high. Hybrid control structures are, however, only effective if the hybridization is planned properly. A comprehensive understanding of the precision in the workcell and tolerance budgets in assemblies is required for implementing hybrid control. Evaluating precision in micro domain can become difficult due to localization and

measurement uncertainties of sensors used. Conventional definitions, designed for macroscale robotics, often do not help in accurately measuring the precision metrics such as resolution, repeatability and accuracy in microscale. Thus the ways these precision metrics are perceived require revisiting in order to help in planning and control in micro domain.

A precision adjusted hybrid controller in conjunction with a precise assembly planning algorithm can provide solution to realistic mass production of complex heterogeneous microsystems with high yield through serial top-down microassembly.

To summarize in a broader prospect; specific, quantitative design rules, coupled with MEMS technology can offer a realistic pathway to realize complex assemblies of micro-sized components with guaranteed yield and throughput.

1.3 Contributions

This thesis makes the following contributions to the research in micro-scale assembly in order to improve the existing schemes and offer novel solutions to the problem.

- An inequality called *"High Yield Assembly Condition (HYAC)"* has been formulated to quantify the uncertainties in a microassembly scenario. The HYAC is based on individual precision of involved objects such as microparts, assembly types, robotic manipulators and end effectors. The HYAC serves as a deterministic guideline to estimate the yield in a microassembly process.
- Precision metrics such as *"resolution, repeatability and accuracy (RRA)"* are redefined from their classical definition to provide a robust way of quantifying precision in micro domain. We include sensor precision and robot motion path as variables to define the RRA metrics. These definitions are used as guidelines in determining the planning and control schemes for a specific microassembly

scenario as well as reconfiguring the system all together for different microsystems.

- A binary term called *"complexity index"* has been introduced in order to categorize different microassembly subtasks based on the ease of execution. Tasks which have higher tolerance or require minimal sensor feedback, are termed as *"Easy to assemble"* tasks and the complexity index is flagged by a *'0'*. On the other hand, *"Hard to assemble"* tasks, requiring much more precision in alignment, having less tolerance, or needing frequent use of sensor feedback, are said to have complexity index of *'1'*. These indices are also dynamically updated throughout the assembly process, thus helping the control to intelligently adapt to the task in hand.
- A novel *"task-based, precision-adjusted hybrid controller"* has been proposed for automated 3D microassembly. Using an event driven process weighting scheme a specific assembly step is flagged as complex or non-complex through the *"complexity indices"*. Then this information is used by the hybrid supervisory controller to time-multiplex the control structure in between open loop control, calibration based feed-forward control and visual servoing based closed loop during assembly execution steps.
- We formulate a *"Precise path search algorithm (PPSA)"* for motion planning in microassembly. The robot kinematic is presented as a product of exponentials including the static uncertainties from links as well as dynamic uncertainties form joint motion. The algorithm takes into consideration of the individual precision in linkage along robot degrees of freedom and searches for a precise non-colliding feasible motion path in the microassembly configuration space. Unlike conventional *"shortest path search algorithms"*, the *"precise path search*

algorithms" gives priority to minimizing the error in robot tracking in a restricted sensing workspace.

- A comprehensive case study for the proposed planning algorithm and hybrid control structure has been conducted through automated 3D microassembly and packaging of a complex heterogeneous micro opto electro mechanical system (MOEMS) called *"Fourier transform microspectrometer"*. The working principle of the microspectrometer is based on scanning mirror type Michelson interferometry. With design, fabrication, assembly, packaging and detail mechanical and optical characterization this complete microsystem has been prototyped to operate for spectrum analysis applications in a wide range of visible and near infra-red (NIR). Potential applications include portable gas-detector, color/quality control unit in fabric industry or winery etc.
- Aspects of concurrent micromanufacturing via automated microassembly has been studied and implemented through a modular centralized database structure to reliably predict the feasibility of a microsystem development process under specific manufacturability cost functions such as yield, throughput and cost. A software application has been developed in order to process system specific information queried from the database and provide possible solutions for micromanufacturing bounded by certain user-defined cost functions.
- Automated 3D microassembly of other compliant and non-compliant complex microsystems has been studied and implemented; including a micro robot called *"ARRIpede"*. Miniature *"on-chip electronics"* have been proto-typed for power supply and logic control of untethered self sustainable microsystems. Several other 3D micro structures are built using compliant/non-compliant heterogeneous micro components.

Other technical contributions made during this research include system level configuration of a reconfigurable microassembly system called "μ^3", programming of an extensive automation software application called *"Neptune 3.0"*, programming of a virtual reality simulation software application called *"Microsim 1.0"*, design, construction and packaging of miniature electronic backpack modules for untethered microsystems.

1.4 Thesis organization

Chapter 2 highlights on the background of microassembly. This section surveys recent research in microassembly, beginning with directed methods, i.e. "pick-and-place". Micromachining techniques can furnish both manipulators and assembly pallets for organizing microparts. In order to pick up and release microparts, however, the scaling of physical forces must be carefully considered. Conventionally microfabricated elements can sometimes be designed with the ability to either assemble by self-actuation upon release or by means of electrical actuation. The major research thrust, however, has targeted parallel processes that enable large numbers of parts to be assembled simultaneously with micron-scale precision. These processes are categorized as either deterministic or stochastic, depending on whether the microparts are initially organized. Impressive results have been achieved in the past few years using both approaches. Deterministic parallel assembly has similarities to the rapidly evolving chip-scale packaging technologies, but concerns microstructure-on-substrate placement rather than chip-on-board assembly. Stochastic or self-assembly processes are also being applied successfully. In section 2 some of the contemporary research work has been discussed. Chapter 2 also introduces multiple multiscale assembly/packaging systems configured at ARRI's Texasmicrofactory.

In chapter 3, a criterion for assemblability defined as *"High Yield Assembly Condition (HYAC)"* has been introduced. Considering from a microassembly point of view, the precision metrics i.e. *"resolution, repeatability and accuracy (RRA)"* are re-defined and evaluation schemes are proposed to experimentally determine them. These RRA metrics are used as variables in identifying the kinematics of the manipulation system. Based on this system identification a novel *"precise path search algorithm (PPSA)"* has been proposed in order to minimize the expected uncertainty during an assembly task and to satisfy HYAC. Planning with unlimited sensing ability as well as restricted sensing is considered and corresponding effects on manufacturing cost functions have been discussed in this section.

Chapter 4 presents a precision adjusted hybrid controller for microassembly. Using a novel task intricacy allocation method the assembly subtasks are flagged by binary *"Complexity Indices (CI)"* based on whether they are *"easy to execute"* or *"hard to execute"*. These indices are updated real-time which dynamically switches the control structure as per requirement. In this section, formulation of the controller, real-time deployment and performance analysis are discussed.

To verify the usefulness of the theoretical findings, alignment and automated assembly/packaging of a microspectrometer has been studied and demonstrated in chapter 5. The microspectrometer is a complex micro-opto-electro-mechanical system (MOEMS) consisting of several heterogeneous components. Sub-millimeter sized MEMS parts were fabricated out of silicon-on-insulator (SOI) wafer using DRIE process and assembled on a 1cm x 1cm silicon die by a microassembly system called μ^3 at ARRI's Texas Micro Factory. The assembled microspectrometer is capable of recovering the wavelength of light in a wide range of visible and near infra red spectrum with 5nm resolution. Detailed analysis on automated assembly, testing and spectrum results are presented in this section.

Chapter 6 includes discussion on concurrent micromanufacturing. Through several compliant and non-compliant MEMS design based microsystems, it has been discussion how concurrency can be achieved among widely diverse micromanufacturing processes and how it can be implemented effectively to ensure high yield, throughput and low cost. Integration of heterogeneous components using a range of end effectors has been presented in this chapter in order to demonstrate the reconfigurability of the framework and scope of microassembly, in general.

Finally chapter 7 concludes the thesis with future work. In this section conclusions regarding the theoretical finding were drawn and enforced with the aid of detailed comparative performance analysis. A three point comparison based on yield, speed and cost demonstrates the usefulness of the proposed hybrid supervisory controller and the motion planning scheme. In addition to current findings, future direction to research and potential areas of interest have been recognized and mentioned in this section.

Summary of tools such as hardware setups, software modules, virtual reality simulation applications and electronics subsystems including of circuit designs and microcontroller coding can be found in appendices A, B, C and D respectively.

CHAPTER 2

BACKGROUND

2.1 MEMS and microassembly

Over the past decade microsystems technology has undergone significant improvements targeting a wide range of applications. Once limited in few sensory parts for automobiles such as accelerometers, pressure sensors and inertial sensors, Micro Electro Mechanical Systems (MEMS) in recent time have a wide range of applications spanning among disk drive read/write heads, displays, inkjet printers, radio frequency components, gyroscopes, finger print readers, drug delivery systems and many more with a projected market of multi billion dollars in the coming years.

MEMS technology inherits it from integrated circuits (IC) that was established and widely popularized during later half of the last century. Almost all of recent times microsystem products are thus evidently built using surface micromachining techniques similar to those used in IC industry. Parts made using such monolithic fabrication methods are generally thin and weak having very low resistance to deformation and flexing under the influence of external disturbances as well as aging. Building complex structures using surface micromachining involves high cost, joints consumes large footprint and composition of heterogeneous component is almost impossible.

Past research in assembly in micro domain can broadly be divided into two categories: *micromanipulation* and *microassembly*. In the early days, large portion of microassembly related research was dedicated to understanding the scaling of physical phenomena such as gravity, capillary forces, friction, electromagnetism, elasticity,

electrostatics etc in micro scale. Contemporary research also saw a few instances of manipulation of micro objects such as micro spheres etc using different physical effects in an *unstructured* manner. As the understanding about scaling of physics in micro domain became more and more clear and with the advent of high precision robotics manipulators, microassembly has arisen as the focus point of research where people started handling micro parts much more efficiently in a structured environment. Deterministic serial and parallel assembly in microscale becomes feasible with the availability of stronger micro parts with high aspect ratio fabricated using deep reaction ion etching (DRIE) process. During the same period, different compliant snap fastening designs were explored to make assembly in micro domain more tolerable and easier to overcome stiction effects between parts.

In spite of much progress, microassembly has not able to become a realistic alternative to surface micromachining techniques to mass-produce microsystems. The reasons for the insufficiency can be broadly accredited to the lack of generality and absence of automation. Control and robotics in micro scale is highly stringent in tolerance and constrained in manipulation. Limited workspace, high precision requirements, large variation in comparative geometry of micro parts, well optimized control system for rapid construction of microsystems with high yield, accurate motion planning and reconfigurable automation are some of the major focus areas in 3D microassembly. Efficient solutions to these aspects can ensure the feasibility and usefulness of microassembly in sculpturing many current microsystems as well as exploring numerous uncharted areas of implementation in near future.

2.2 Study of physics in microdomain for micro manipulation

In early work on study of micro domain forces and phenomena in micromanipulation Arai et al. studied attractive forces and handling strategies in micromanipulation [7], also Fearing surveyed the stick effects for micro parts handling [8].

In analysis of micro operations based on analytical micro force models Saito et al. analyzed pick and place operation of micro spheres based on micro forces [9], Sitti and Hashimoto modeled some cases in manipulation of nano particles using AFM tips [10], Zhou and Nelson theoretically and experimentally studied adhesion forces between a sphere and a plane under different material and environment conditions [11].

Research in computational micro force models include works where Feddema et al. built a computational model of Van der Waals forces and electrostatic forces for interactions between a micro sphere and a micro cube [12]; based on the model, they addressed the effects of micro domain forces to the assembly planning [13].

Research on simulation of different modes in micromanipulation, includes works where Rollot et al. studied various modes in micromanipulation by combining analytical micro force models and Newton-Euler dynamics [14]. The simulation was done very thoroughly except that it did not take into the consideration the contact, and thus it cannot simulate the whole manipulation process.

Dynamic model for micro operations research include works where Zhou et al. have built a computational model for micro operations that combines micro domain forces with a dynamic model of multi-body contact [15]. This model was the first step to simulate the interactions in handling micro parts. Based on the model, virtual reality manipulation environment can be developed.

In micro domain, detachment of micro objects from each other is as difficult as attachment process due to surface effects. Thus properties of microscale objects in

contact are important factors for microassembly. Several models have been proposed for such analysis of contact force [16]. Clevy et al. have proposed a device which enables the study of pull-off forces according to the preload force and the contact angle [17].

2.3 MEMS control

A microsystem can encompass a number or sensors and/or actuators within a very small space (usually in the order of 10^{-6}meters) for a wide variety of applications. Initial methodologies for development of microsystems were heavily dominated by the semiconductor integrated circuits (IC) fabrication technology which is essentially a monolithic surface micromachining process [18]. The surface micromachining techniques can be classified into two types according to the manufacturing process; additive or subtractive. In both cases, however, the MEMS parts are manufactured in bulk from a single large wafer (primarily silicon). As there were very few requirements for the MEMS parts to be handled individually or moved off the surface to join with each other, early control applications in MEMS were mainly of operational control type such as input shaping and monitoring of the sensors or controlling the actuators or signal/data processing. Operational control systems for MEMS devices can be of two types; closed loop [19] or open loop [20]. Control schemes for a wide variety MEMS sensors and actuators have been explored in past. In case of sensors, applications of feedback control systems design to optical MEMS switching devices have already been considered [21, 22]. Instances of variable structure control where the dynamics of a nonlinear system is altered via application of a high-frequency switching control has been modeled and shown through a sliding mode control in [23]. In [24] a combined feed-forward and feedback control system has been discussed for the probe tip positioning. An adaptive force-balancing control scheme with actua-

tor limits for a MEMS Z-axis gyroscope has been proposed in [25] in order to identify major fabrication imperfections so that they are properly compensated. Extensive research has also been undertaken in past for the modeling and control of the two widely used MEMS actuator types; electrostatic and thermal. In [26] implementation and simulation of a closed-loop stroke-length PID control of a lateral comb actuator is presented. In [27] a transient FEA was used to obtain a dynamic response for the hot arm and the cold arm actuator and a chevron actuator. Procedure to reduce the order of the complex MEMS device model was described in [28].

2.4 Controls for assembly in micro domain

Although monolithic fabrication methods for production of MEMS devices were sufficient enough in early days of MEMS technology which has a very limited range of applications such as accelerometers in automotives and a few optical switches, it is no longer proving to be adequate for MEMS applications in recent time. With a very large spectrum of potential application fields spanning among read/write heads, micro-displays, printer heads, pressure sensors, micro-fluidics chips, gyroscopes, fingerprint sensors, IR sensors, drug delivery systems, inclinometers, micro energy sources, microphones, micro memories, micro-pumps, chemical analysis systems and many more; todays microsystems have become much more complex and conglomeratic in nature. Under this scenario, microassembly can be put into work with much higher efficiency than the surface micromachining processes and can become a viable option to build robust complex microsystems. A large part of recent research in MEMS are thus diverting into microassembly and aspects of controls in microrobotics. With growing popularity of microassembly and application spectrum of Micro-Electro-Mechanical System (MEMS), necessity for robust and complex control systems also has increased to control and operate the wide range of microsystems.

Understanding about assembly is no new concept as mankind has long been utilizing it since the dawn of the age. The advancement of human race from the Dark Age to the present era is highly indebted to the industrial revolution over the past centuries which have been boosted by many scientific discoveries over the time about the Nature and inventions to manipulate it. Industrial control and automation has undergone several refinements over the past years to bring itself to a robust standardized format. Extending this well-established theory into microscale for MEMS assembly is, however, not that straightforward. There are several issues but the main reason is the change in Governing Dynamics. The laws of physics change when switch has been made from macroscale to microscale. The surface forces such as capillary effect, surface tension, stiction etc. become more dominant than the volumetric forces such as gravity. For example, a simple pick-and-place operation gets complicated as the MEMS parts are harder to pick up due to the stiction between the part and the substrate; also parts are harder to place due to the stiction between the part and the end-effector. Another crucial factor in any realistic application of MEMS is rapid prototyping or mass production which may not be that essential in macroscale. Therefore control systems of macroscale assembly cannot be implemented very usefully in microscale and hence efficient control systems must be developed for microassembly addressing the pertaining factors.

Similar to macroscale, microscale assembly can also be categorized into two types; top-down and bottom-up. The bottom-up approach deals with self assembly and generally stochastic in nature where as the top-down approach involves deterministic serial or parallel assembly and stochastic parallel assembly. In case of bottom-up approach or the stochastic self assembly, in contrast to the macroscopic concepts of manipulators and path planning, a molecular system may be analyzed as an ensemble of particles evolving toward a state of minimal potential energy. Crystal growth

[29], antibody-antigen recognition, and most other chemical and biological behaviors [30, 31] are mediated by thermal motion and inter-particle forces. Thermodynamic analysis shows the potential for massively parallel operation, forming assemblies of 106 or more elements in seconds [32]. A self assembly of gold prisms is discussed in [33] using guiding routes. In spite of the strong enthusiasm expressed by scientists and engineers and their high expectations on the potential benefits of bottom-up microassembly, and the colossal amount of monies that have invested in the Research and Development by governments and private sectors in the past decade, the current state remains at the stage of technological development with rudimentary products reported in the public domain. Top-down approach, on the other hand, has resulted in many commercial successes in recent times. The two primary ways of sensing in MEMS assembly that has been implemented in past are vision and force. Visually guided microassembly using optical microscopes and active vision techniques [34] has been incorporated in past to improve the assembly. Force sensors have also been used to measure the parts mating force and consequently improving the assembly by drawing an indirect interpretation of the misalignment [35]. Other developments in closed loop microassembly include vision based force sensing [36], capacitance sensing, combined vision and force sensing [37] etc. In some cases fuzzy logic and neural network has been used to assist the vision based microassembly [38]. The throughput of serial microassembly is limited by the number of micromanipulators in the array and their bandwidth. Given that microfabrication processes can yield millions of devices, it is intriguing to consider whether large ensembles of microparts can be assembled simultaneously. Such deterministic parallel microassembly refers to direct, wafer-to-wafer transfer of microstructures. The initial demonstration of wafer-to-wafer transfer involved vacuum micro-packaging [39]. Wafer-scale transfer of HexSil microactuators was demonstrated in [40].

2.5 Microassembly systems

With the advent of microassembly as a viable solution for construction of microsystems, many parallel researches were initiated to develop microassembly systems. These systems are based many different principles. For instance Wang et Al. discussed a fuzzy PD controller based microassembly system [41]. Kim et Al. proposed a precision robot system with modular actuators and MEMS micro gripper for micro system assembly [42]. Yang and Nelson demonstrated wafer-level 3D microassembly system for MEMS fabrication [43]. Schmitt et Al. presented image based controlling of microassembly systems [44]. Flexure hinge mechanism based precision robot manipulator were developed for high precision assembly tasks [45]. Interesting result have been demonstrated for vibration based microassembly system [46]. Kim et Al. have proposed flexible microassembly system based hybrid manipulation scheme [47]. A good overview of environmental influences on microassembly processes as well as the construction of a controlled climate system can be found in [48]. A visually guided six degree of freedom based microassembly system has been demonstrated by Institute of Robotics and Intelligent Systems (IRIS) [49]. Nelson et al. have demonstrated sensor based microassembly [50] which used vision based feedback control for automated microassembly. Fatikow et Al. have demonstrated mobile piezoelectric micro-robot based microassembly system [51] and also presented control architecture in microscale [52]. In other example for control system design for micromanipulation, work from Clevy et al. [53] is noteworthy in which the use of a piezo gripper to actively grasp and manipulate microparts has been shown.

Although directed microassembly methods using vision or force sensing feedback has been tested with substantial success in past, it also has some prevailing issues associated with the scheme. Obtaining accurate sensor data is difficult. In case of contact sensors such as force measurement, sensors cannot be easily placed on tiny

precision instruments without making them bulky or compromising their functionality. Image processing is still slow, costly, difficult to program, and susceptible to reflection and other noise. Moreover, the view may be obstructed by tools that are orders of magnitude larger than the parts being handled. Even when reliable images are obtained, one major challenge is how to coordinate and calibrate gross actuator motion with sensor data. On the other hand open loop control systems for MEMS assembly can solve simpler pick and place tasks of same type but not complex steps involving different path length or different part type without incurring significant amount of misalignment error. Such open loop systems, although effectively faster, are not free from limitations arising from adhesive forces between gripper and object can be significant when compared to gravitational forces. These adhesive forces arise primarily from surface tension, Van der Waals, and electrostatic attractions and can be a fundamental limitation to part handling. Mardanov, Seyfried and Fatikow discussed an automated microassembly station [54].

2.6 Modular MEMS assembly

Modular MEMS is another popular field of research in recent times. Considering the high cost and time associated with micro fabrication processes, one can see that it is a good idea to use modular designs instead of rigid dedicated structures for building microsystem. Advantages of modular design include easy compatibility, ease to repair and cost reduction through process standardization. A recent example of a very well designed modular fastener allowing 3D compliant assembly with SOI MEMS parts is the *Zyvex* connector [55]. In this work it has been demonstrated that using a robust passive end-effector and compliant MEMS part designs, fabricated in a 50 micron thick single crystal silicon (SCS) deep reactive ion etched (DRIE) process, pick and place assembly of MEMS components can be accomplished reliably though directed

assembly. In [56] modular MEMS components are used to build an optical switching network. In [57] a modular BioMEMS platform for tissue engineering is presented which combines silicon, glass and polymers as building blocks.

2.7 Planning for microassembly

Unlike macro scale manufacturing, microassembly does not cherish the luxury of having *off-the-shelf* components such as standard nuts and bolts. Neither there exist any *ready-to-use* robotic manipulation system to carry out microassembly steps. Different microsystems consist of different types of microparts which are generally batch produced through expensive and time consuming fabrication methods. In addition to these component level issues, if we also consider system level issues, we can observe that assembly in micro domain is essentially a *device-specific* process i.e. tolerance in alignment is dictated by the functionality of the device. Therefore, as one would find, the most efficient way to address a micro manufacturing process will be to follow a holistic approach. This means that the design and control of the assembly cell, robots, parts and end-effectors occurs concurrently, and that the performance of such architecture needs to be evaluated not only in terms of adjusted precision metrics but also in terms of yield, cost and throughput.

Another important factor in micro manufacturing is the ability to accommodate complexity. As assembly of complex microsystems requires high controllability, in our research, we have selected deterministic serial top-down approach due to its high accuracy. In an automated serial process the task list must be carefully configured to optimize the cost functions: *"yield, throughput and cost"*.

Path planning is one of the two building blocks for automated microassembly. Traditionally, path planning algorithms search for a collision free shortest route from

the source to the goal. These algorithms are effective only if the robot tracking along the path is flawless.

2.7.1 An overview on conventional path planning techniques

There has been a wealth of research on path planning in an environment that contains a set of obstacles. Especially the concept of "visibility" [58] and "space decomposition" [59] play fundamental roles in path planning in two dimensions. When dealing with dynamic domains, an issue arises regarding how to represent time information when the environment changes. A powerful concept is space-time in which an additional dimension represents time. Idea of a configuration space has been used for motion planning among stationary obstacles. Intuitively, the configuration space is obtained by shrinking the robot to a point, while growing the obstacle by the size of the robot. The problem of finding a path of minimal total length in two and three dimensions has attracted much attention. The visibility graph has been an important combinatorial structure in planning shortest path among stationary polygonal obstacles in the plane, as well as acquiring information about the environment while exploring it in two dimensions. In relevant approaches for planning there are many adopted ways. Geometrical methods include pre-calculation of the configuration space, working directly with the workspace, skeleton graph [60], Voronoi diagrams [61], visibility graphs. There are methods based on classical mechanics, cell decomposition methods including quadtrees/octrees [62]. Approximations e.g. convex hull [63] also have been used. Another popular method is the potential field approach [64]. Other approaches include heuristic methods for special situations, learning methods e.g. neural nets [65] and genetic algorithms [66], stochastic methods e.g. fuzzy logic [67] and so on.

Among the search algorithms [68] the main categories are uninformed search, list search, tree search, graph search, informed search, adversarial search, constraint

satisfaction search, genetic algorithm etc. Linear search, interpolation search, binary search, range search are some of the examples of list search methods. In tree search the types include breadth-first search, depth-first search, iterative-deepening search, depth-limited search, bidirectional search, uniform-cost search. The popularly used Dijkstra's algorithm [69] is an example of graph search. Other graph search algoritms include Kruskal's algorithm [70], nearest neighbor algorithm [71], Prim's algorithm [72]. The widely used A^* [73], B^* [74], D^* [75] and best first search algorithms are types of informed search. Adversarial search includes minimax algorithm, search tree pruning, alpha-beta pruning. Constraint Satisfaction search includes combinatorial search, Backtracking. Finally genetic Algorithm is among the recent developments of search algorithms.

Visibility graph, cell decomposition and potential field method are the three widely used ways for path planning problems.

2.8 Concurrent engineering

The idea for concurrent engineering was first introduced in 1983, when Don Reinertsen (while a consultant at McKinsey & Co.) proposed in Electronic Business magazine the idea to quantify the value of development speed for new products *("6 months delay can be worth 33% of life cycle profits").* A few years later, the Institute of Defense (IDA), a Department of Defense (DoD) sponsored organization which administers two federally funded research and development centers, proposed in June 1988 the first definition of concurrent engineering (CE) as follows:

"CE is a systematic approach to the integrated concurrent design of products and their related processes, including manufacture and support. This approach is intended to cause the developers, from the outset, to consider all elements of the

product life cycle from conception through disposal, including quality, cost, schedule and user requirements" [76].

Hoffman [77] pointed out that CE must include human variables, technical variables and business requirements. The CE approach has been discussed through some linked concepts in [78]. In [79] design for manufacturability has been discussed from a fabrication view point. Further proposition on design and packaging aiming for manufacturability has been mentioned in [80]. Test structures for variability has been discussed in [81]. However, currently there are no standards for design for manufacturability from a microassembly prospect.

2.9 Multiscale multi-robot assembly/packaging systems at ARRI

2.9.1 M^3: Macro-meso-micro scale assembly system

M^3 (short for Macro-Meso-Micro platform) shown in Figure 2.1 operates across scales and precision levels from the macro to the micro scales, and its design follows a specific set of rules that ensures desired accuracy and assembly yield [82]. The M^3 packaging system was engineered to allow for quick reconfiguration of the assembly cell, to address both process and precision manipulation challenges, and to target low-volume, high-value MEMS packaging.

There are four robots that cooperate within the M^3 platform. A large linear (XY) range for three of these manipulators is based on a linear motor implemented as a large platen surface (approximately 48 inch x 36 inch) with pucks riding on a 15 μm air bearing. Such positioning systems have been used in the past and are based on the original Automatix platform that is currently commercially available as Robotworld by Motoman. An advantage of this configuration is the ability to add more robots in the workspace.

In order to assemble the MOEMS (Micro Opto Electro Mechanical System) several end-effectors are used such as a capillary micro nozzle, a pneumatic gripper, a fiber gripper, a custom mounting bracket etc that are picked up from a tool tray via a pneumatic tool changer by the robot manipulator. The overall accuracy of the robots is determined by many factors, including mechanical design (kinematics and stiffness of the robotic chain), feedback sensors (e.g. their type and resolution), and joint actuators (e.g. their accuracy and associated controller).

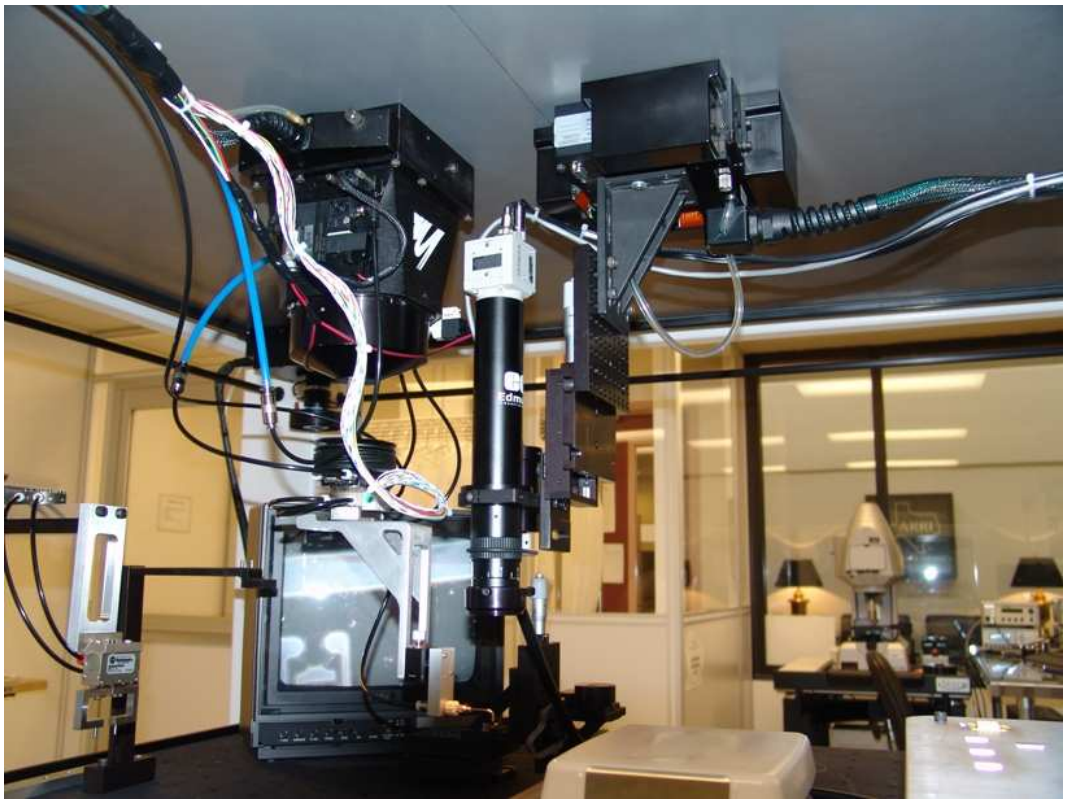

Figure 2.1. M^3 multiscale assembly system at ARRI's Micro Factory.

One type of MOEMS that we can manufacture with M^3 is shown in Figure 2.2, and consists of both micro and meso-scale parts such as Kovar carrier package and lid, optical fibers fed through the carrier, a silicon MEMS die with DRIE trenches aligned

to the optical fiber, a glass cap die, wire-bonds, miniature solder preforms, and a lid for device sealing. The nominal dimensions of these parts are as follows: a base of 2.54cm x 2.54cm Kovar package, 60cm long optical fibers with 126μm diameter Au-coated tips, 50μm thick 12mmx12mm SnAu preforms for attaching the MEMS die to the package, 12mm x 12mm footprint of the SOI MEMS die, a 750μm x 750μm glass cap chip, and 1mm diameter, 4.5mm height Indium preforms for fiber to package attachment.

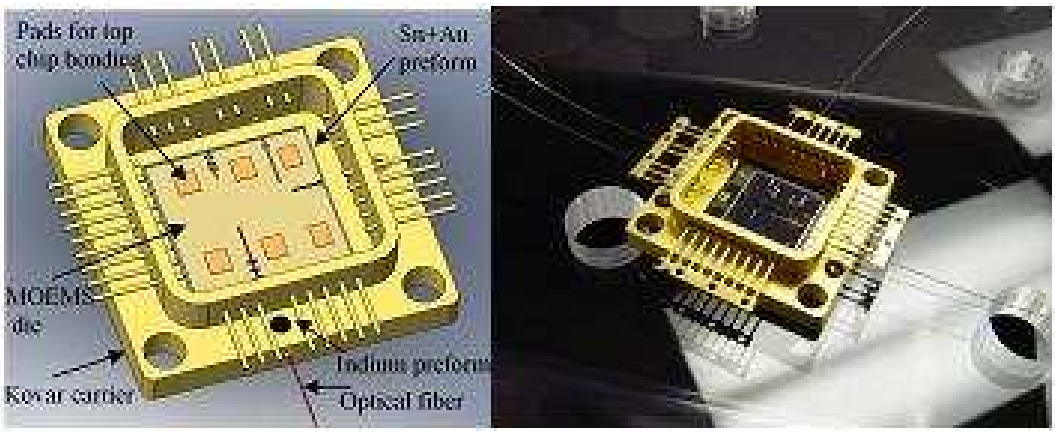

Figure 2.2. Diagram and picture of a MOEMS device, including Kovar package, MEMS die, fiber-optics and wire-bonds.

Rigorous computational approach has been used to evaluate the tolerance budget of a given assembly task, the positioning accuracy of the manipulators, tool and fixture resources, and quantitative measures to assign manipulator tasks.

2.9.2 μ^3: Meso-micro-nano scale assembly system

The meso-nano 3-D microassembly station called μ^3, shown in Figure 2.3, is part of a family of multiscale robotic systems being developed in our lab, including the M^3 assembly system (macro-micro). As a result, they share some of the multiscale

design principles and controls. The μ^3 is equipped with additional microgrippers and stereo microscope vision. This platform is capable of motion resolutions of 3nm and is small enough to be used inside of a scanning electron microscope (SEM) for nanomanipulation. The μ^3 kinematic configuration is unique to the assembly of typical $2\frac{1}{2}$D microparts fabricated on a wafer [83].

Figure 2.3. μ^3 microassembly system at ARRI's Micro Factory.

The μ^3 platform is a table-top 3D assembly station configured using 19 DOF discrete stages arranged into 3 robotic manipulators with 3 nm resolution. μ^3 is used to achieve both serial and deterministic parallel micro/nano scale assembly outside and inside the SEM. μ^3 consists of three manipulators (M_1, M_2, M_3) sharing a common $25cm^3$ workspace. M_1 and M_1 are two robotic manipulator arms with 7 degrees

of freedom each. They consist of XYZ coarse and fine linear stages, including the PI (Physik Instruments) Nanocube for nanoscale fine motion. A rotation stage provides a terminating roll DOF (θ) axis which is key for 3D assemblies of $2\frac{1}{2}$D MEMS components. Mounted at the end of the manipulator chains are kinematic mounting pairs that provide for end-effector reconfigurability. The central manipulator M_3 is a high precision 5 DOF robot consisting of a XYθ mechanism placed on a 2 axis tilt stage. This robot carries custom designed fixtures for microparts (the dies/substrate) and a custom designed hotplate for process ability such as interconnect solder reflow.

The system manages 3D stereo vision for part location, manipulator calibration, kinematics, trajectory planning, assembly and packaging sequence execution and 1D machine vision for visual servoing during calibration. These features will be discussed in the following sections.

Figures 2.4 and 2.5 show images of repeated MEMS assemblies obtained using this method. Some of the SEM photographs contain active sockets and active out of plane actuators (such as a vertically assembled gripper). The active components are actuated through wire-bonds and reflown solder connectors that increase the mechanical stiffness of the snap-fastener. These basic building blocks are being utilized to construct 3+ DOF MEMS robots that are entirely located on substrate.

In addition to these homogeneous MEMS part assemblies, the μ^3 is also capable of doing heterogeneous assembly. To manipulate different types of parts made out of silicon, glass, plastic or metal etc of different shape and size, the μ^3 system uses vacuum needles, active piezo and electrostatic grippers in addition to the passive jammer that is used for compliant assembly. Figure 2.6 shows an example of such an complex heterogeneous microassembly in the form of a microspectrometer consisting of multiple silicon and glass components of various size and shape. Details about the

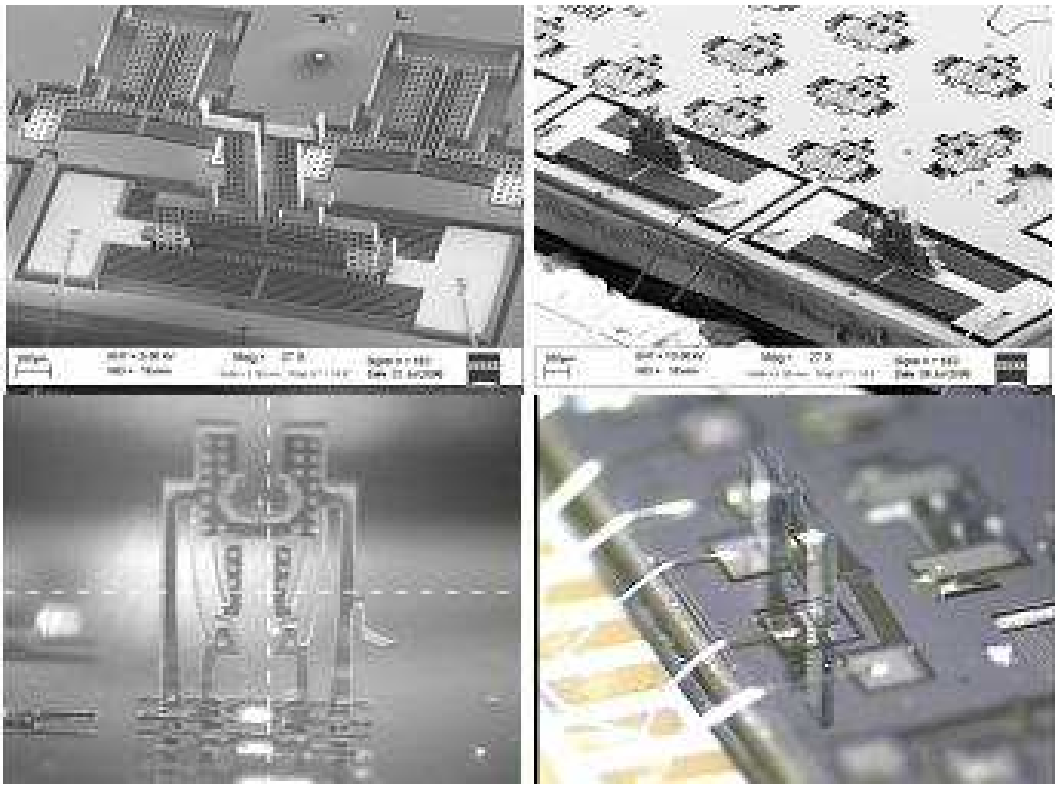

Figure 2.4. Examples of micro assemblies using μ^3, including 50μm thick SOI thermal MEMS with out of plane passive and actuated grippers, as well as active zero-force sockets.

design, assembly and characterization of the microspectrometer will be discussed in chapter 5.

Figures 2.7, 2.8 and 2.9 shows miniature 3D models of structures built in microscale on a 1cm x 1cm silicon die.

To increase the stiffness of the joints in the structure, an epoxy glue has been used which can be cured by ultra-violet light.

2.9.3 N^3: Wafer level assembly with Nano scale positioners

Taking the idea of modular multiscale assembly to one scale further down, the N^3 has been envisaged as a wafer level assembly system. Comprising of die-scale

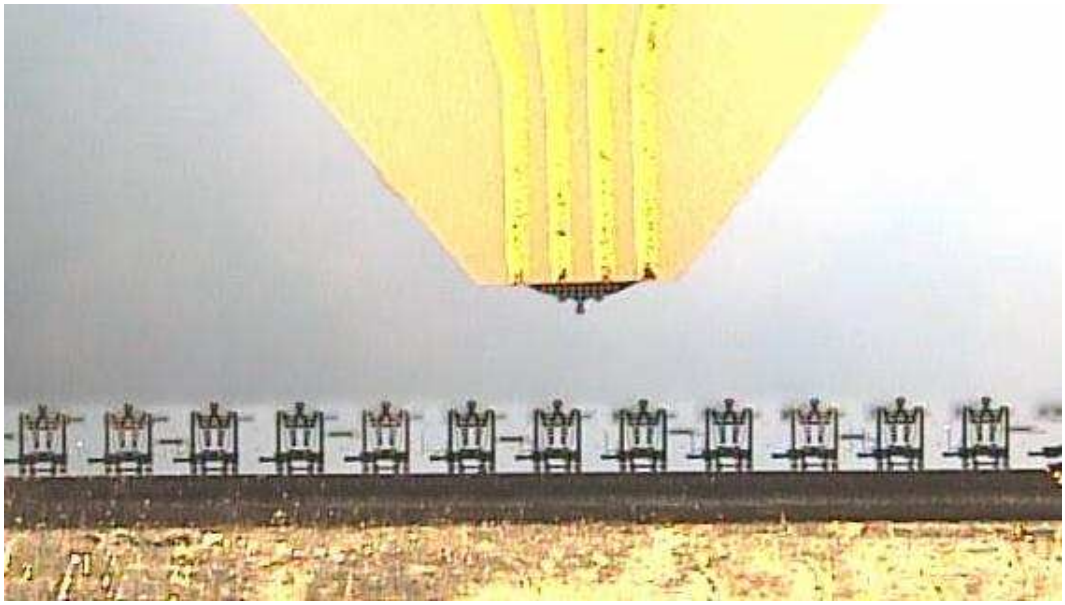

Figure 2.5. A row of standing passive Zyvex jammers obtained by calibration and assembly scripting.

micro robots and micro sensors, the N^3 will be fully capable to accomplish handling and assembly of micron and sub-micron sized parts with nano meter order precision. The N^3, when completed, will be one of its kind self-sufficient micro-nano assembly system converting the concept of microfactory into reality. Integrated with miniature power modules and logic electronics, this assembly system can be used to build future microsystems on a parallel assembly process.

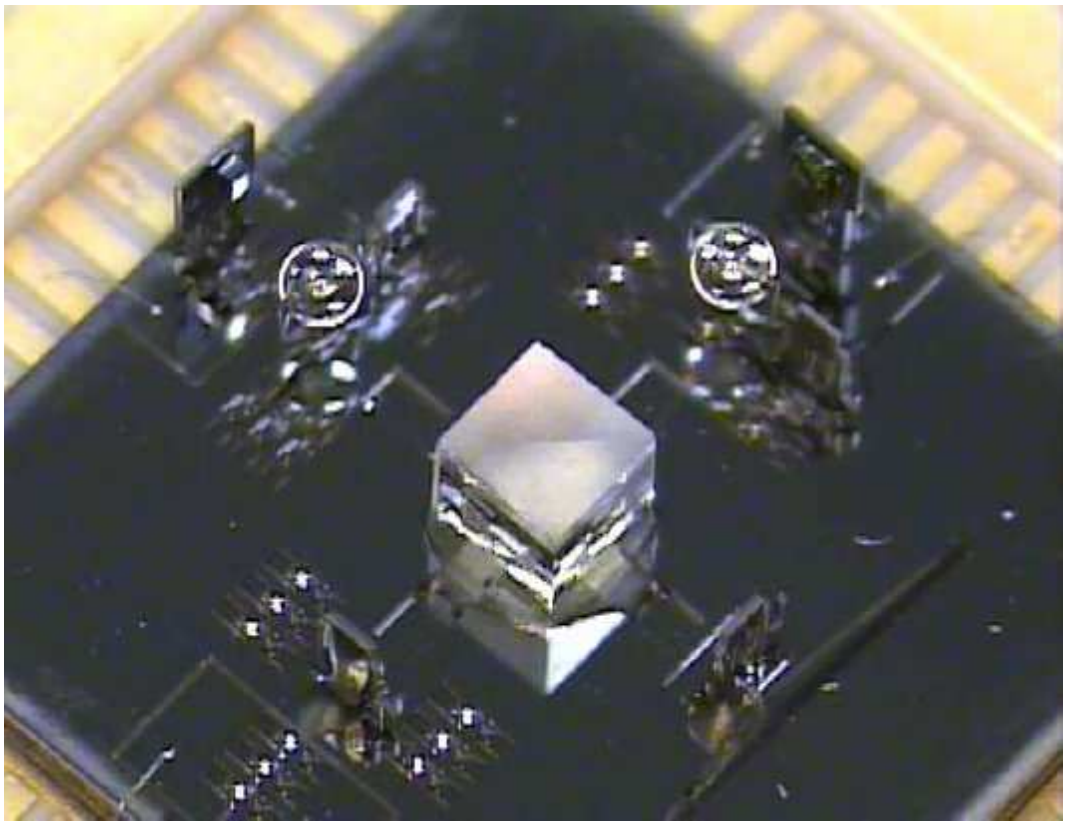

Figure 2.6. ARRI's Microspectrometer built on a 1cm x 1cm silicon die.

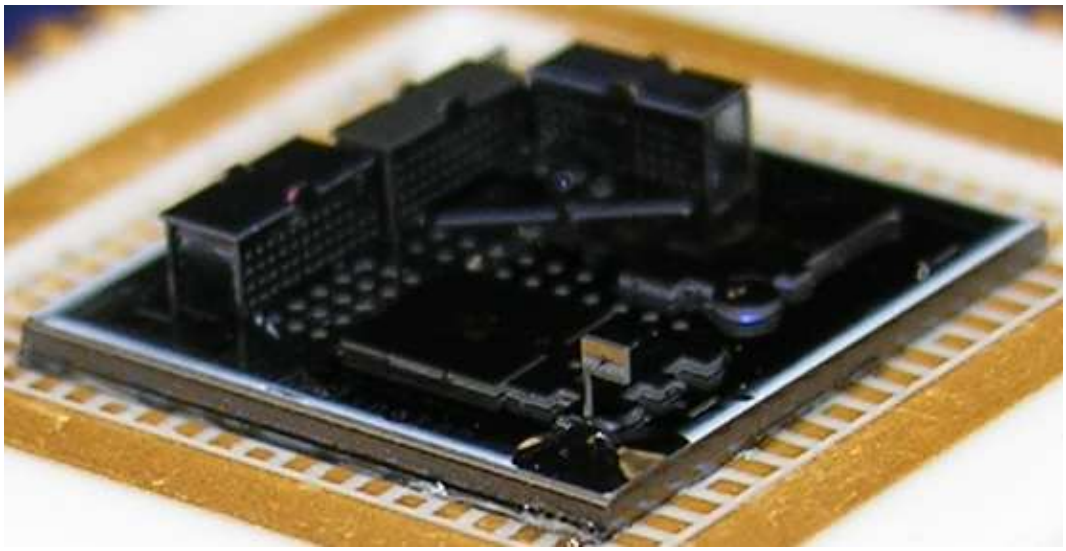

Figure 2.7. Miniature micro souvenir showing the model of a set of buildings and Texas flag.

Figure 2.8. Miniature micro souvenir showing the model of a roman temple.

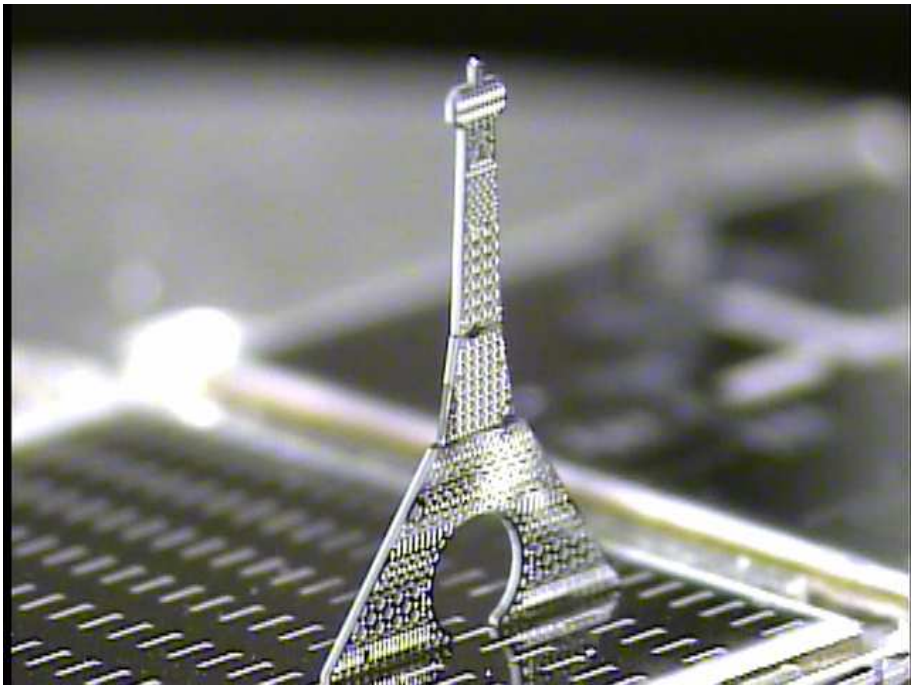

Figure 2.9. Miniature micro souvenirs showing the model of Eiffel Tower.

CHAPTER 3

ASSEMBLY PLANNING IN MICRO DOMAIN

Planning a complex microassembly operation comprising of multiple heterogeneous parts is often difficult due to very high precision requirements. In macro scale, precision of the sensor system is generally very high in comparison to the tolerance budgets, thus measurement uncertainty in calibration and feedback control can be ignored. However, at the micro scale the tolerance budgets are very stringent, often in the range of sensor precision, and sensing accuracy plays a vital role in determining the yield and throughput of planning and control scheme.

Therefore, in this chapter, we begin by redefining the classical exegesis for precision metrics from a micro assembly point of view. Then we formulate a quantitative tool for higher yield in microassembly from statistical stand point. Based on this tool, and by studying the kinematic linkage precision of robotic manipulators, we propose an assembly planning method to ensure high yields and fast speeds.

3.1 Precision metrics: Resolution, Repeatability and Accuracy

3.1.1 Classical representation

The precision of a robot can be classified into the three categories: accuracy, repeatability and resolution.

Motion accuracy of the robot system is the degree of closeness of a directed position to its actual (true) value. Repeatability, on the other hand, is the degree to which further movements show the same or similar results. Statistically, accuracy and repeatability can be represented as in the figure 3.1 [84]. By taking a span interval

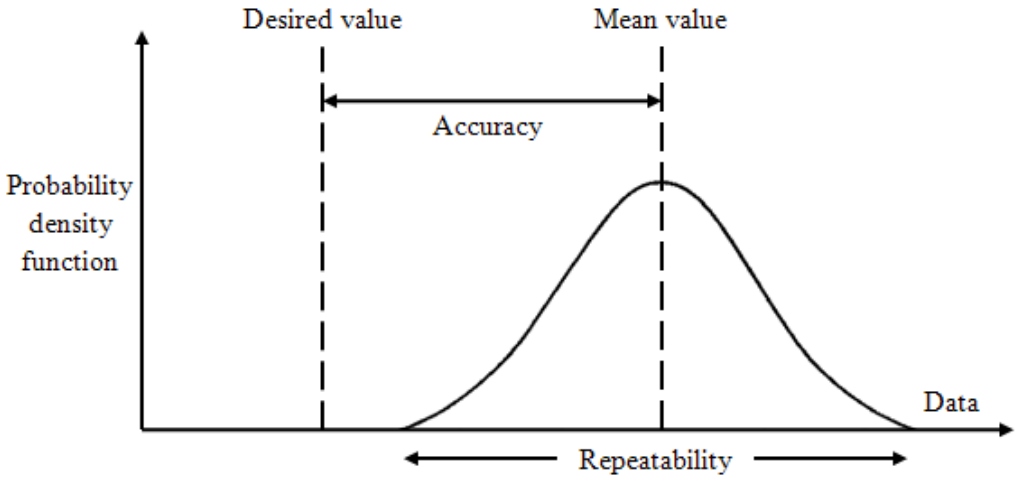

Figure 3.1. Classical representations for precision.

of three standard deviations, it can be ensured that 99.7% of the measured values will lie within. The results of calculations or a measurement can be accurate but not repeatable, repeatable but not accurate, neither, or both.

Definition

A measurement system or computational method is called *valid* if it is both accurate and repeatable.

If the robot is not valid under normal conditions then a precision improvement technique can be used to enhance the accuracy and repeatability. Visual servoing is one such technique which uses feedback information extracted from a vision sensor to control the motion of a robot. Visual Servoing (VS) [85] techniques are broadly classified into the following types: (i) Image Based (IBVS), (ii) Position Based (PBVS) and (iii) Hybrid Approach. IBVS is also referred to as a feature based technique. This is because the VS algorithm uses features extracted from the image to directly provide a command to the robot. Typically, all the information extracted, from the image features, and used in control happens in 2D. In most cases it is in the image

space (image coordinates). A point to be noted is that the robot may still move in 3D. PBVS is sometimes referred to as Pose Based VS, and is a model based technique. The pose of the object of interest is estimated with respect to the camera and then a command is issued to the robot controller. In this case, the image features are extracted as well. But the feature information is used to estimate 3D information (pose of the object in Cartesian space). Hence servoing occurs in 3D. Hybrid approaches use some combination of the 2D and 3D servoing. There have been a few different approaches to hybrid servoing such as; 2-1/2-D Servoing, Motion Partition Based, Partitioned DOF Based etc.

The third and final precision metric, resolution, is often used in conjunction with visual servoing to determine the servo gain by specifying the minimum incremental motion possible by the robot. Efficient visual servoing is possible only for a high resolution robot. For low resolution robots visual servoing may lead to instability due to overshoot.

3.1.2 Redefining the metrics for microassembly

In the above discussion on precision metrics and visual servoing, its assumed that the sensor systems used to measure these parameters have no measurement error. This critical assumption may not hold true as the size of assembly work-cell shrinks significantly as in case of microassembly. For example: a machine vision system with $1\mu m$ accuracy can be a great tool for assembly tasks with 1mm tolerance but it will prove insufficient for assembly tasks with few micron tolerances. One way to improve accuracy of vision based sensors is to increase the magnification. However, as the magnification increase it also reduces the field of view. Thus, a large area cannot be actively monitored with a stationary sensor, and if a mobile sensor is used, then the localization uncertainty further degrades the sensing accuracy. Integration of large

number of sensors is also not feasible due to their bulkiness and the limitations of smaller work space.

Considering these issues, in this section we will define the precision metrics i.e. resolution, repeatability and accuracy to include the sensor precision as well as process setup.

Assumptions:

We will use Gaussian distributions to represent uncertainties in a microassembly work-cell, which are experimentally evaluated. In general, positioning uncertainties of robot end-effectors are tied to the *manipulability ellipsoid* [86]. This suggests that the uncertainties are multivariate Gaussian distributions. However, there are other sources of errors such as vibration, ambient uncertainties etc., hence the uncertainties in robot positioning may not always be Gaussian. However, if the distributions are not Gaussian, we can reasonably approximate them with a sum of Gaussian distributions [87]. In this work, we also assume that the Gaussian distributions from multiple sources of uncertainties are independent, i.e. for example, the uncertainty from fabrication is not dependent on uncertainty from fixturing, or detethering parts. Likewise, the uncertainty from robot positioning is independent of these two uncertainties as well. Therefore for independent Gaussian distributions we can simply add their variances and the *"central limit theorem"* holds true [88].

3.1.2.1 Sensor precision

The sensor precision is defined as the repeatability in sensor measurements. To determine this, the sensor is placed over a stationary target and readings are taken after fixed interval of time. The distribution of differences in these readings constitute a dataset which, when statistically analyzed, can give a quantitative measure for the repeatability of the systems. If the sensor is moved onto the target for each

reading from any arbitrary location in the workspace, then the total uncertainty is a combination of the uncertainty in localization and uncertainty in measurement. The localization uncertainty further depends on the robotic stages, the sensor is mounted on. Mathematically, under Gaussian, independent assumptions:

$$\sigma_s^2 = \sigma_s^2(localization) + \sigma_s^2(measurement). \tag{3.1}$$

If the sensor is fixed then the localization uncertainty is zero, and thus the sensor precision depends only on measurement uncertainty.

In a microassembly workcell the space is too limited to incorporate a large number of external sensors. Furthermore, sensors with high precision often have low field of operation. Considering these limitations, we propose the following schemes for determining the precision metrics experimentally.

3.1.2.2 Accuracy of robot manipulation system

To measure the accuracy of a robot we use the following procedure.

1. A feature is selected on the robot end-effector to be tracked by a sensor field.
2. The robot is moved to place the feature in a stationary and zero referenced sensor field. The sensor measurement is taken and termed as reference reading.
3. Next the robot is moved to certain position q_j (joint coordinates) in 3D by moving through a distance D_{qj} using one or more joints.
4. After reaching q_j the current position is set as pseudo origin, i.e. $q_j \rightarrow q_{j0}$.
5. The positional uncertainty at this origin has been computed using the joint encoder readings, and is denoted as $\sigma_{q_{j0}}^2$.

6. After setting the pseudo origin the robot is moved from the pseudo origin to reference point q_{ref} in order to place the feature under the sensor field. The error in actual reading and reference reading is noted.
7. Steps 3 through step 6 are repeated multiple times, and thus a sample set is obtained for error distribution between actual reading and reference reading. An accuracy distribution is approximated using the following equation:

$$\sigma_{acc}^2 = \lim_{n\to\infty}\left(\frac{1}{n}\left(\sum_{j=1}^{n}(q_j - q_{ref}) + \sigma_{q_{j0}}^2\right)\right) + \sigma_s^2,$$

where $\sigma_{q_{j0}}^2$ is a function of the displacement P_j. Hence we can rewrite the above equation as:

$$\sigma_{acc}^2 = \lim_{n\to\infty}\left(\frac{1}{n}\left(\sum_{j=1}^{n}(q_j - q_{ref}) + \sigma_{q_{j0}}^2(P_j)\right)\right) + \sigma_s^2. \tag{3.2}$$

3.1.2.3 Repeatability of robot manipulation system

To measure the repeatability of the robot we use the following procedure.

1. A feature is selected on the robot end-effector to be tracked by a sensor field.
2. The robot is moved between two predefined but arbitrary points one of which is measured through a sensor field.
3. Step 2 is repeated multiple times and thus a sample set is obtained for error distribution between the actual reading and the reference reading. A repeatability distribution is approximated using the following equation:

$$\sigma_{rep}^2 = \lim_{n\to\infty}\left(\frac{1}{n}\left(\sum_{j=1}^{n}(q_j(P_j) - q_{ref})\right)^2\right) + \sigma_s^2, \tag{3.3}$$

where P_j is the path travelled by the j^{th} link.

3.1.2.4 Resolution of robot manipulation system

To measure the resolution of the system we use the following procedure.

1. A feature is selected on the robot end-effecter to be tracked a sensor field.
2. The robot is moved within the sensor field to multiple displacement values gradually decreasing in geometric progression with common ratio of $\frac{1}{2}$.
3. At the iteration where the sensor reading is same as the previous reading, the measurement is stopped and the resolution of the manipulator system is calculated using the following equation.

$$\sigma_{res}^2 = min\left(\lim_{(q_j - q_{j-1})\to 0} \left| q_j\left(P_j\right) - q_{j-1}\left(P_j\right) + \sigma_s^2 \right|\right). \tag{3.4}$$

The resolution of the system is used to determine the gain factor during servoing. Note that the resolution in consideration here is not just the resolution of the robot; rather it is the resolution of the sensor system in conjunction with the manipulator. Thus higher this resolution is the smoother the servoing will be.

3.1.2.5 Servoing of robot manipulation system

Servoing with the parts refers to adjusting the position of a feature on the part based on feedback from the sensor used to measure that feature. In a precision assembly cell, servoing (regulation) of the feature vector to zero can be accomplished using an approximate sensor based Jacobian function $J_R : R^M \rightarrow R^{6\times M}$ (M is the robot operation space) by setting joint increments for robot R as:

$$\Delta q = -\lambda J_R^{-1}\left(q_0\right) K_{SPi}, \tag{3.5}$$

where K_{SPi} is the 6D pose of feature i on part P as measured by sensor S, $\lambda > 0$ is a positive small constant, and q_0 is a constant joint vector "close" enough

to the actual joint vector. Note that this servoing algorithm works, "locally" around q_0, as is the case with small joint variations during microassembly. The Jacobian can be estimated numerically, or by differentiation of the forward kinematics map K obtained after calibration.

3.2 Assemblability criterion

Assume that a microassembly process A, carried out to assemble a specific microsystem. A, can be divided into individual subtasks A_1, A_2,..., A_n, where n is the number of continuous operations involving a single robot, a single part or a single tool:

$$A = \sum_{i=1}^{n} A_i. \tag{3.6}$$

Success of the designated assembly process can be represented as:

$$S(A) = \bigcap_{i=1}^{n} S(A_i). \tag{3.7}$$

where S is the success factor of the assembly/bonding process (a Boolean value). From equation 3.7 it can be inferred that the manufacturing success requires all subtasks to succeed.

In a sequential microassembly process the order of subtasks can be configured in many ways. We are interested in finding a set of ways in which the success of entire assembly is guaranteed i.e.

$$\underset{k=1\rightarrow n!}{max} \left(\sum_{i=1}^{n} S(A_i(O_k)) \right) = n, \tag{3.8}$$

where O_k is the order of subtasks in the sequence, $k = 1...n$. If at least one solution for O_k is not found to satisfy the condition in equation 3.8, then the assembly

will fail, and thus a change of design will be necessary, including new values for tolerances and substrate layout.

3.2.1 Categorization of microassembly task uncertainties

We treat subtasks A_i as a combination of two types of positioning operations at the microscale: *controllable* and *uncontrollable*. Controllable operations A_i^m refer to spatial manipulation of components using robots. This type of manipulation will be considered to be actively controllable within certain tolerance bounds with Gaussian statistics.

On the other hand, uncontrollable operations A_i^b refer to change in component position based on the material properties and interaction forces at the microscale. Friction based interference fitting, pneumatic grasping, surface tension, capillary stiction, adhesive bonding, etc., are some of the examples of uncontrollable operations. They depend on surface properties of the microparts and can act both in favor and against the assembly. We assume such operations to be uncontrollable in the sense that the assembly system will not actively correct their errors. However the effects can be predicted through appropriate models.

Success of subtask A_i requires that the sum of the errors e from A_i^m and A_i^b must be less than the design tolerance for the assembly. If we consider $\sigma^2_{process}$ to be the process tolerance then, for successful assembly of the subtask A_i, we must ensure that:

$$\sigma^2_{process} > e\left(A_i^m\right) + e\left(A_i^b\right). \tag{3.9}$$

The uncertainty should also include fabrication process variances, such as patterning, photolithography, DRIE, etc, that alter the tolerance of the microparts. If

we assume this error distribution to be $\sigma^2_{fabrication}$, then the overall assembly tolerance can be represented as follows:

$$\sigma_1^2 = \mu_{layout} + \sigma^2_{fabrication}. \tag{3.10}$$

In equation 3.10 the square term defines the assembly tolerance as a Gaussian distribution. μ_{layout} is the tolerance given during design.

The error due to uncontrolled operations $e\left(A_i^b\right)$ can be represented as a sum of error distributions from individual behaviors as observed from models, such as finite element analysis.

$$\begin{aligned} e\left(A_i^b\right) &= \sigma^2_{frictionfitting} + \sigma^2_{thermalchange} + ... + \sigma^2_{bondingshrinkage} + ... + \sigma^2_{materialproperty} \\ &= \sigma_4^2. \end{aligned} \tag{3.11}$$

Let's now consider the controllable operations A_i^m. Assembly motion can be executed using different types of control schemes, such as:

1. Open loop control, using die layout and direct robot commands without any calibration.
2. Feed-forward control, using die layout and calibration of the pick-up robot.
3. Feedback or closed loop control, using active sensing based servoing and calibration.

For case (1) and case (2) it is necessary that the components in the assembly layout must match their positions in the design layout. However, in reality, the layouts do not exactly match for reasons such as tether design for fixturing the parts, fabrication uncertainties, environmental disturbances etc. Such uncertainty, assumed to be Gaussian in part position, is denoted as variance σ^2_{part}. In addition, the end-effector manufacturing imperfections will also have an uncertainty $\sigma^2_{end-effector}$. Alternatively,

in case (3), where the parts and the end-effector are located using one or more sensors, the positioning accuracy will be dependent on the sensor precision. The total part-end-effector position error distribution can be represented as follows:

$$\sigma_2^2 = \begin{cases} \sigma_{part}^2 + \sigma_{end\ effector}^2 & open\ loop \\ \sigma_{sensor\ position}^2 + \sigma_{sensor\ measurement}^2 & closed\ loop \end{cases} \tag{3.12}$$

Next, we introduce the robot uncertainty σ_3^2, or the variance of the positional error distribution of the end-effector. Thus equation 3.9 can be rewritten using equations 3.10-3.12 as:

$$\sigma_1^2 > \sigma_2^2 + \sigma_3^2 + \sigma_4^2. \tag{3.13}$$

The inequality in equation 3.13 is termed as the *"High Yield Assembly Condition (HYAC)"*.

3.2.2 High Yield Assembly Condition (HYAC)

Lemma

The "High Yield Assembly Condition (HYAC)", as described by the equation 3.13, states that:

"Under Gaussian uncertainty assumptions, a 99% (3σ) assembly yield can be guaranteed if the combined uncertainty of locating and positioning of microparts and end-effector is smaller than the assembly tolerance.".

The HYAC is therefore a quantitative way to predict the individual success factor *'S'* of assembly. Therefore, in equation 3.8 $S = 1$ if HYAC is true, and $S = 0$ if HYAC is false for a specific assembly subtask. Furthermore, note that in the inequality for HYAC:

1. σ_1^2 is *"measurable"* but not *"correctable"*.

2. σ_2^2 is *"measurable"* and *"correctable"* in some cases, but this requires additional processes and resources.
3. σ_3^2 is both *"measurable"* and *"correctable"*; assuming the robot precision can be improved.

The goal is to satisfy the HYAC and consequently make $S = 1$. In next chapter a controller will be presented which will make sure that σ_3^2 is minimized, depending on the complexity of the assembly task.

Combining the factors of σ_4^2 as given in 3.11, it can be treated as *"scaling uncertainty"* based on their origin or *"grasping uncertainty"* based on their affecting area. Whichever way it is interpreted though, σ_4^2 is a highly unpredictable parameter. It depends on several factors such as micropart dimensions, environmental variation, micro gripper design, surface forces, Van der Waal forces, electrostatic effects and so on. σ_4^2 can be minimized by proper component design. The remaining error due to σ_4^2 uncertainty, assuming that it is small, can be rectified by either mechanical correction techniques or by active servoing through additional degrees of freedom.

A framework is shown in figure 3.2 depicting how the *'HYAC'* can be incorporated in a microassembly scenario.

As seen from the figure 3.2 *'HYAC'* serves as a supervisor in both offline and online phase of microassembly. In the offline pre-assembly stage it helps in predicting precision in manipulator motion path; thus selecting a precise path. In online execution stage the *'HYAC'* is used to determines the control structure in real-time.

3.3 Planning motion path for microassembly

In a manipulator workspace $\Re^6$ there exists infinite number of possible solutions to finding a *non-colliding path* from any arbitrary point P_1 to another arbitrary point

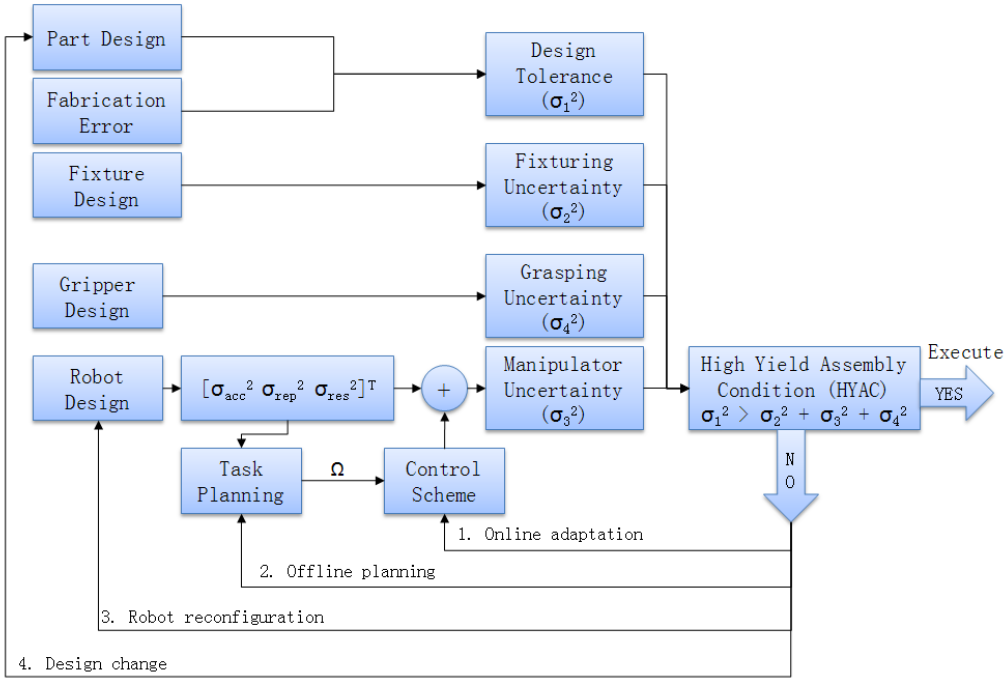

Figure 3.2. Control and planning structure for microassembly.

P_2. Among these, there also exists a set of solutions which result in least travelling distance between the two points. These are called *"Shortest Path"* and the algorithms which specifically search for such solutions are known as *"Shortest Path Search Algorithms"*. There are numerous shortest path search algorithm (as discussed in previous chapter) which are motivated by the goal to achieve minimum travel time in tracking.

3.3.1 Requirements of path planning

In a microassembly scenario, planning is essentially finding a solution to robot kinematics problem which deals with aspects of redundancy, collision avoidance and singularity avoidance.

Kinematically redundant robots have more degrees of freedom than necessary to perform a given task. Hence, in addition to following desired Cartesian trajectories, redundant robot can also satisfy task constraints, singularity and obstacle avoidance,

and dexterity maximization. The redundancy of a robotic system depends not only on the arm itself but also on the task to be carried out. In a microassembly scenario, redundancy in robotic manipulators has both advantages and disadvantages. Redundancy helps in positioning the end-effector in a tightly constrained work volume. Also it helps in executing the process faster by allowing individual oppositely directed motions along single degree of freedom. However, redundancy also negatively affects the precision. In micro domain, where the tolerances are highly stringent, the uncertainty in robot end-effector, due to inertia of individual stages and mechanical complexity of the hardware, significantly affects the precision.

Obstacle problems in microassembly are also slightly different than macro scale. In macro scale, obstacles can be broadly classified into two types: static and dynamic. Static obstacles appear in the *configuration space* from the beginning and continue to exist at its fixed location until the end. Whereas dynamic obstacles appear and disappear at a particular location at any specific time within the configuration space. Now, if a microassembly configuration is considered, assemblies themselves act as obstacles. As microassemblies are generally carried out in a very structured environment the existing static obstacles can be mapped in to workspace precisely. Each new assembly adds up to the obstacles. As the assembly locations are pre-defined and the size and shape of the microparts are known, these obstacles can also be mapped with accuracy. Thus these type of obstacles cannot be classified as dynamic obstacles but they can be termed as timed obstacles. Thus the obstacle configuration scheme in microassembly can be theorized as *cumulative obstacles*.

Lastly, singularity is defined as a position in the robot workspace where one or more joints no longer represent independent controlling variables. Commonly used to indicate a position where a particular mathematical formulation fails. A robot singularity occurs when robot axes are redundant or when the robot is in certain con-

figurations that require extremely high joint rates to move at some nominal speed in Cartesian space. Singularity can be classified into two types; *physical* and *representational*. Physical singularities have a physical origin, and are found in any mathematical representation used to describe the kinematics. Here the space of wrenches on the end-effector that are taken up passively by the mechanical structure of the robot (i.e., without needing any joint torques to be kept in static equilibrium) increases its dimension. Consequently the end-effector looses one or more degrees of freedom. On the other hand representational singularities exist due to minimal coordinate representation. In microassembly redundancy is helpful as the work volume is small and constrained. But this also helps in increasing the chance of singularities.

3.3.2 Precision issues with path tracking in microscale

In microassembly, tracking is not as easy as in macro scale; primarily due to very high precision requirements and limited feedback sensing for error correction. Although they ensure least travel time, the *"shortest path search algorithms"* do not necessarily guarantee high precision, especially with open loop tracking control, in reaching at the goal. Therefore in systems where precision requirements are absolutely critical, such as in microassembly manipulators, the shortest path search algorithms cannot be used as effectively as they are in macroscale.

Therefore, new paradigms must be established in order to give priority to attainable precision over travel distance. In our research, we will be proposing such an algorithm, defined as *"Precise Path Search Algorithm (PPSA)"*, which analyzes the kinematic configuration of the robotic manipulators, considers different sources of misalignments and their effects on overall positioning, and offers a set of paths from source to goal in which the uncertainty is predicted to be minimum.

3.4 Uncertainties in robot kinematics and their effect on precision

Serial robotic manipulator systems are essentially a continuous chain of links connected to each other through either revolute or prismatic joints. In order to track a complete path, one or more links in this kinematic chain are actuated along their designated axes through specific amounts. So we can write the total path 'P_{TOTAL}' as a combination of path segments '$P_i s$', each corresponding to a link in the robot chain. Thus:

$$P_{TOTAL} = P_1 + P_2 + ... + P_i + ... + P_n = \sum_{i=1}^{n} P_i. \tag{3.14}$$

In actual, each link motion is subjected to some error in positioning due to several reasons such as misalignments, faulty configuration, motional errors and so on. Hence we can rewrite the above equation as follows:

$$P_{actual} = \sum_{i=1}^{n} \left(P_i + \delta P_i\right). \tag{3.15}$$

where δP_i is the error in link positioning. This error can further be categorized into three categories; *static*, *dynamic* and *flex*. The static errors are due to faulty robot kinematic link configuration where as dynamic errors come from motion errors. Notice that the static errors do not vary with travel path where as dynamic ones do. Additionally the flex error arises from the fact that the robots are not completely stiff. Thus they deform by small amount under high velocity motions as well as environmental effects.

$$\delta P_i = \delta P_i^{static} + \delta P_i^{dynamic} + \delta P_i^{flex}. \tag{3.16}$$

We can assume the flex error to be negligibly low for the robots placed in a controlled environment such as clean room and vibration tables. Also for slow moving robots this error is further reduced. Thus we can write, for such cases:

$$\delta P_i = \delta P_i^{static} + \delta P_i^{dynamic}. \tag{3.17}$$

3.4.1 Robot forward kinematics

Mathematically the forward kinematic model of a robotic system can be computed from three factors:

1. the direction axis vector of the robot links: $\vec{\omega}$
2. the axis point for the robot link: $\vec{q}$
3. the motion angles (in case of revolute joints) or displacements (in case of prismatic joints): θ

There are two commonly used methods to compute the forward kinematics of a robotic manipulation system; *"Denavit Hartenburg Convention"* [89] and *"Product of exponentials"* [90]. In this chapter we will use the *"product of exponentials"* method to compute the kinematic uncertainties for robotic manipulators.

In the *"Product of exponentials"* method we write a term called *'twist'* to represent the transformation of a link. The *twist* 'ξ' is calculated using the following formula:

$$\xi_i\,(revolute) = \begin{bmatrix} -\omega_i \times q_i \\ \\ \omega_i \end{bmatrix}, \xi_i\,(prismatic) = \begin{bmatrix} v_i \\ \\ 0 \end{bmatrix}. \tag{3.18}$$

Next the exponential of twist is computed as follows:

$$e^{\hat{\xi}\theta} = \begin{bmatrix} e^{\hat{\omega}\theta} & \left(I - e^{\hat{\omega}\theta}\right)(\omega \times v) + \omega\omega^T v\theta \\ 0 & 1 \end{bmatrix}, \tag{3.19}$$

where

$$e^{\hat{\omega}\theta} = I + \hat{\omega} sin\theta + \hat{\omega}^2 (1 - sin\theta). \tag{3.20}$$

This is called *Rodriguez's formula*.

Expanding above equation we get:

$$e^{\hat{\omega}\theta} = \begin{bmatrix} \omega_1^2 v_\theta + c_\theta & \omega_1\omega_2 v_\theta - \omega_3 s_\theta & \omega_1\omega_3 v_\theta + \omega_2 s_\theta \\ \omega_1\omega_2 v_\theta + \omega_3 s_\theta & \omega_2^2 v_\theta + c_\theta & \omega_2\omega_3 v_\theta - \omega_1 s_\theta \\ \omega_1\omega_3 v_\theta - \omega_2 s_\theta & \omega_2\omega_3 v_\theta + \omega_1 s_\theta & \omega_3^2 v_\theta + c_\theta \end{bmatrix}. \tag{3.21}$$

In the above equation: $s_\theta = sin(\theta)$; $c_\theta = cos(\theta)$ and $v_\theta = 1 - cos(\theta)$.

Combining the individual joint motions, the forward kinematics map of the robot can be found out as:

$${}^0_N\mathrm{T}(\theta) = e^{\hat{\xi_1}\theta_1} e^{\hat{\xi_2}\theta_2} ... e^{\hat{\xi_n}\theta_n} \left[{}^0_N\mathrm{T}(0)\right]. \tag{3.22}$$

The above transformation matrix is of the following form;

$${}^0_N\mathrm{T}(\theta) = \begin{bmatrix} R & P \\ 0 & 1 \end{bmatrix}, \tag{3.23}$$

where R is the rotation matrix and P is the position vector.

The dimensions and types of the symbols are given below;

$$\vec{\omega} \in \Re^3 : 3 \times 1 : vector$$

$$\vec{q} \in \Re^3 : 3 \times 1 : vector$$

$$\vec{v} \in \Re^3 : 3 \times 1 : vector$$

$$\theta : scalar$$

$$\xi \in \Re^6 : 6 \times 1 : vector$$

$$\hat{\xi} \in se(3) : 4 \times 4$$

$$e^{\hat{\xi}\theta} \in SE(3) : 4 \times 4$$

$$R \in SO(3) : 3 \times 3 : rotation\ matrix$$

$$P \in \Re^3 : 3 \times 1 : translation\ vector.$$

3.4.2 Uncertainties in robot parameters

The uncertainty from the combination of $\vec{\omega}$ and $\vec{q}$ constitutes static error where as the uncertainty in the θ builds dynamic error.

In figure 3.3 the effect of these parameters is shown for a simple three link robot. The first two pictures show the isometric view and top view respectively, for the ideal case with no error. The next two pictures show the effect of uncertainty in directional vector and the last two pictures show the combined effect of uncertainty in directional vector and uncertainty in robot link axis points. In addition to these static errors the robot is also subjected to dynamic errors due to path depended motion errors (not shown in figure).

Unlike for macroscale systems, in micro domain these errors are sufficiently significant in comparison to assembly tolerances, thus greatly reducing the yield in manufacturing. We will analyze the effect of this here.

Consider a serial robot with *'n'* links. We will verify the following propositions.

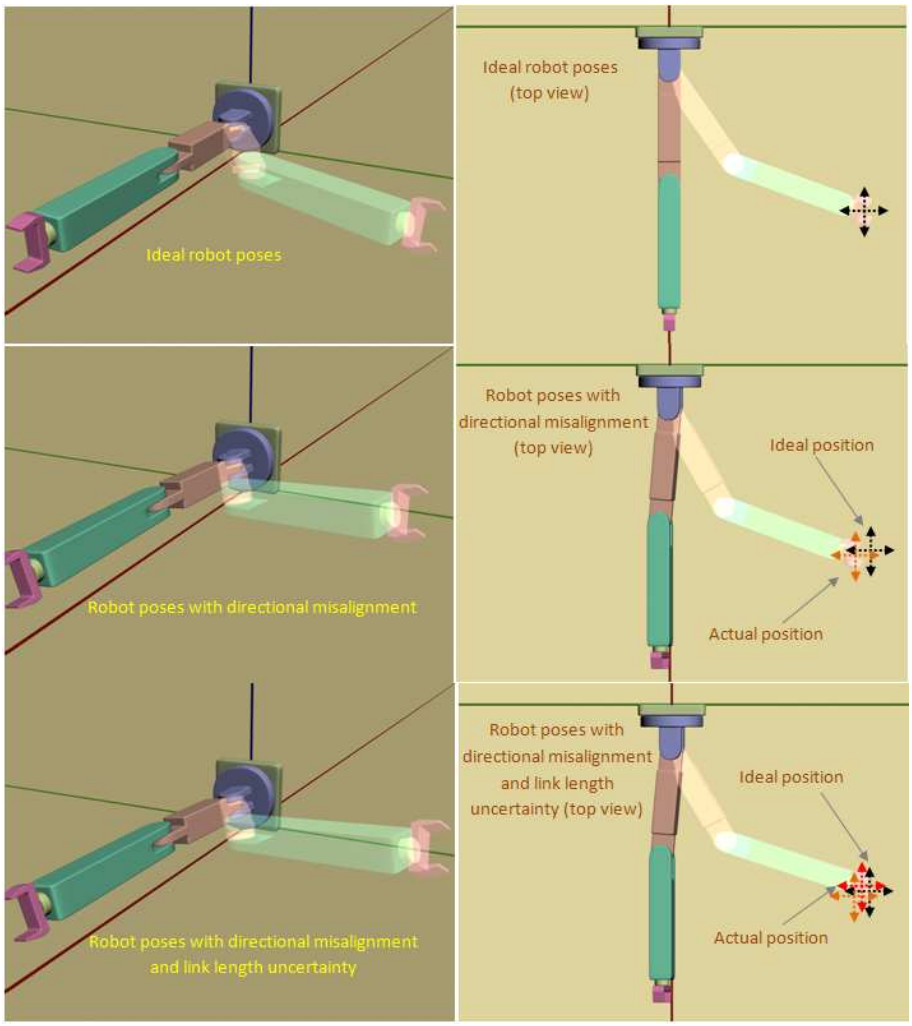

Figure 3.3. Uncertainty in robot precision.

Propositions:

1. Error in endeffector position due to uncertainty in 'θ_i' in link *'i'* is smaller than that for links *'i-1'*, *'i-2'*, *'i-3'* ...
2. Error in endeffector position due to uncertainty in 'ξ_i' in link *'i'* is greater than that for links *'i-1'*, *'i-2'*, *'i-3'* ...; assuming $\|\delta\xi_i\| > \|\delta\xi_{i-1}\| > \|\delta\xi_{i-2}\|$ ....

Figure 3.4 shows the robot links along with uncertainties.

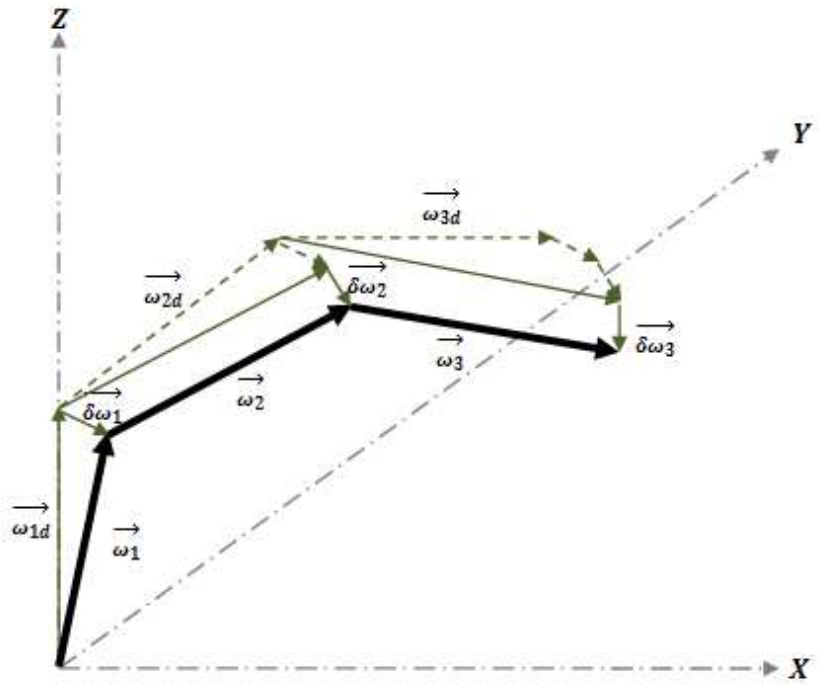

Figure 3.4. Effect of static uncertainty on robot precision.

As shown in the figure, we can consider the misaligned direction vector for a link *'i'* i.e. '$\vec{\omega_i}$' as the resultant of the no-error direction vector '$\vec{\omega_i^{ne}}$' and a error vector '$\vec{\delta\omega_i}$'. Thus;

$$\vec{\omega_i} = \vec{\omega_i^{ne}} + \vec{\delta\omega_i}. \tag{3.24}$$

Next, as the links are connected serially, the start point for the no-error direction vector '$\vec{\omega_i^d}$' is misaligned by a vector which is the resultant of all the error vectors from previous links.

$$\vec{\omega_i^{ne}} = \vec{\omega_i^d} + \vec{\delta\omega_{i-1}} + \vec{\delta\omega_{i-2}} + ... \tag{3.25}$$

In the above equation $\vec{\omega_i^d}$ is the desired direction vector for link *'i'*. Thus we can rewrite the direction vector for a link as;

$$\vec{\omega_i} = \vec{\omega_i^d} + \vec{\delta\omega_i} + \vec{\delta\omega_{i-1}} + \vec{\delta\omega_{i-2}} + ... \tag{3.26}$$

Now introducing uncertainties in equation 3.18 we get;

$$\acute{\xi_i} = \begin{bmatrix} -\left(\omega_i + \delta\omega_i\right) \times \left(q_i + \delta q_i\right) \\ \left(\omega_i + \delta\omega_i\right) \end{bmatrix}. \tag{3.27}$$

Expanding the first term;

$$-\left(\omega_i + \delta\omega_i\right) \times \left(q_i + \delta q_i\right) = -\begin{vmatrix} i & j & k \\ \omega_{xi} + \delta\omega_{xi} & \omega_{yi} + \delta\omega_{yi} & \omega_{zi} + \delta\omega_{zi} \\ q_{xi} + \delta q_{xi} & q_{yi} + \delta q_{yi} & q_{zi} + \delta q_{zi} \end{vmatrix}$$

$$= -\begin{vmatrix} \left(\omega_{yi} + \delta\omega_{yi}\right)\left(q_{zi} + \delta q_{zi}\right) - \left(\omega_{zi} + \delta\omega_{zi}\right)\left(q_{yi} + \delta q_{yi}\right) \\ \left(\omega_{zi} + \delta\omega_{zi}\right)\left(q_{xi} + \delta q_{xi}\right) - \left(\omega_{xi} + \delta\omega_{xi}\right)\left(q_{zi} + \delta q_{zi}\right) \\ \left(\omega_{xi} + \delta\omega_{xi}\right)\left(q_{yi} + \delta q_{yi}\right) - \left(\omega_{yi} + \delta\omega_{yi}\right)\left(q_{xi} + \delta q_{xi}\right) \end{vmatrix}$$

$$= -\begin{vmatrix} \omega_{yi}q_{zi} + \omega_{yi}\delta q_{zi} + \delta\omega_{yi}q_{zi} + \delta\omega_{yi}\delta q_{zi} - \omega_{zi}q_{yi} - \omega_{zi}\delta q_{yi} - \delta\omega_{zi}q_{yi} - \delta\omega_{zi}\delta q_{yi} \\ \omega_{zi}q_{xi} + \omega_{zi}\delta q_{xi} + \delta\omega_{zi}q_{xi} + \delta\omega_{zi}\delta q_{xi} - \omega_{xi}q_{zi} - \omega_{xi}\delta q_{zi} - \delta\omega_{xi}q_{zi} - \delta\omega_{xi}\delta q_{zi} \\ \omega_{xi}q_{yi} + \omega_{xi}\delta q_{yi} + \delta\omega_{xi}q_{yi} + \delta\omega_{xi}\delta q_{yi} - \omega_{yi}q_{xi} - \omega_{yi}\delta q_{xi} - \delta\omega_{yi}q_{xi} - \delta\omega_{yi}\delta q_{xi} \end{vmatrix}.$$

We can neglect product $\delta(.)\delta(.)$ as they are small, and we can rearrange the expression as follows;

$$\left(\omega_i + \delta\omega_i\right) \times \left(q_i + \delta q_i\right) = \begin{vmatrix} \omega_{yi}q_{zi} - \omega_{zi}q_{yi} \\ \omega_{zi}q_{xi} - \omega_{xi}q_{zi} \\ \omega_{xi}q_{yi} - \omega_{yi}q_{xi} \end{vmatrix} + \begin{vmatrix} \omega_{yi}\delta q_{zi} + \delta\omega_{yi}q_{zi} - \omega_{zi}\delta q_{yi} - \delta\omega_{zi}q_{yi} \\ \omega_{zi}\delta q_{xi} + \delta\omega_{zi}q_{xi} - \omega_{xi}\delta q_{zi} - \delta\omega_{xi}q_{zi} \\ \omega_{xi}\delta q_{yi} + \delta\omega_{xi}q_{yi} - \omega_{yi}\delta q_{xi} - \delta\omega_{yi}q_{xi} \end{vmatrix}. \tag{3.28}$$

Thus,

$$\acute{\xi_i} = \xi_i + \delta\xi_i, \tag{3.29}$$

next we will revisit equation 3.22 with uncertainties introduced in ξ_i and θ_i. The mapping for i^{th} link thus given as;

$$e^{\left(\hat{\xi}_i+\delta\hat{\xi}_i\right)(\theta_i+\delta\theta_i)} = e^{\left(\hat{\xi}_i+\delta\hat{\xi}_i\right)\theta_i} \cdot e^{\left(\hat{\xi}_i+\delta\hat{\xi}_i\right)\delta\theta_i} = e^{\left(\hat{\xi}_i\theta_i+\delta\hat{\xi}_i\theta_i\right)} \cdot e^{\left(\hat{\xi}_i\delta\theta_i+\delta\hat{\xi}_i\delta\theta_i\right)} \tag{3.30}$$

Again, We can neglect the term $\delta\hat{\xi}_i\delta\theta_i$ as the individual terms are small. Thus;

$$e^{\left(\hat{\xi}_i+\delta\hat{\xi}_i\right)(\theta_i+\delta\theta_i)} = e^{\left(\hat{\xi}_i\theta_i+\delta\hat{\xi}_i\theta_i\right)} \cdot e^{\hat{\xi}_i\delta\theta_i}. \tag{3.31}$$

Notice that, in general, $\hat{\xi}_i$ and $\delta\hat{\xi}_i$ do not commute. Therefore we use Taylor Series expansion to approximate the exponential. Assuming the two terms in the exponential as A and ΔA we can write;

$$\begin{aligned}
e^{A+\Delta A} &= I + \frac{(A+\Delta A)}{1!} + \frac{(A+\Delta A)^2}{2!} + \frac{(A+\Delta A)^3}{3!} + ... + \frac{(A+\Delta A)^k}{k!} + ... \\
&= I + (A+\Delta A) \\
&+ \frac{1}{2}A^2 + \frac{1}{2}A\Delta A + \frac{1}{2}\Delta AA + \frac{1}{2}\Delta A^2 \\
&+ \frac{1}{6}A^3 + \frac{1}{6}A^2\Delta A + \frac{1}{6}A\Delta AA + \frac{1}{6}A\Delta A^2 + \frac{1}{6}\Delta AA^2 + \frac{1}{6}\Delta AA\Delta A \\
&\qquad + \frac{1}{6}\Delta A^2A + \frac{1}{6}\Delta A^3 + ... + ...,
\end{aligned}$$

or

$$\begin{aligned}
e^{A+\Delta A} &= \left[I + A + \frac{1}{2}A^2 + \frac{1}{6}A^3 + ... + \frac{1}{k!}A^k + ...\right] \\
&+ [\Delta A + \frac{1}{2}A\Delta A + \frac{1}{2}\Delta AA + \frac{1}{2}\Delta A^2 \\
&+ \frac{1}{6}A^2\Delta A + \frac{1}{6}A\Delta AA + \frac{1}{6}A\Delta A^2 + \frac{1}{6}\Delta AA^2 + \frac{1}{6}\Delta AA\Delta A + \frac{1}{6}\Delta A^2A \\
&+ \frac{1}{6}\Delta A^3 + ...],
\end{aligned}$$

or

$$e^{A+\Delta A} = e^{A} + \sum_{k=0}^{\infty}\left[\frac{1}{k!}\sum_{\alpha=0}^{k-1}\left(A^{\alpha}\Delta A A^{(k-1-\alpha)} + \Delta A^{\alpha} A \Delta A^{(k-1-\alpha)}\right)\right]. \tag{3.32}$$

Assuming ΔA to be small we can ignore the second term in the inner summation. Also replacing $A = \hat{\xi}_i\theta_i$ and $\Delta A = \delta\hat{\xi}_i\theta_i$ in the above equation we obtain;

$$e^{\left(\hat{\xi}_i+\delta\hat{\xi}_i\right)(\theta_i+\delta\theta_i)} = \left[e^{\hat{\xi}_i\theta_i} + \sum_{k=0}^{\infty}\left[\frac{1}{k!}\sum_{\alpha=0}^{k-1}\left(\left(\hat{\xi}_i\theta_i\right)^{\alpha}\left(\delta\hat{\xi}_i\theta_i\right)\left(\hat{\xi}_i\theta_i\right)^{(k-1-\alpha)}\right)\right]\right]\cdot e^{\hat{\xi}_i\delta\theta_i}. \tag{3.33}$$

The robot end-effector pose can be written as;

$${}^{0}_{N}T(\theta) = \left[\prod_{i=1}^{n}\left[\left[e^{\hat{\xi}_i\theta_i} + \sum_{k=0}^{\infty}\left[\frac{1}{k!}\sum_{\alpha=0}^{k-1}\left(\left(\hat{\xi}_i\theta_i\right)^{\alpha}\left(\delta\hat{\xi}_i\theta_i\right)\left(\hat{\xi}_i\theta_i\right)^{(k-1-\alpha)}\right)\right]\right]\cdot e^{\hat{\xi}_i\delta\theta_i}\right]\right] \left[{}^{0}_{N}T(0)\right]. \tag{3.34}$$

Furthermore, $\hat{\xi}$ is given as;

$$\hat{\xi} = \begin{bmatrix}\hat{\omega} & -\omega\times q\\ 0 & 0\end{bmatrix} = \begin{bmatrix}\hat{\omega} & -\hat{\omega}q\\ 0 & 0\end{bmatrix}. \tag{3.35}$$

If $\omega = 0$ then;

$$\hat{\xi}^2 = \hat{\xi}^3 = \hat{\xi}^4 = ... = 0. \tag{3.36}$$

And if $\omega \neq 0$ then we can write $\hat{\xi}'$ as;

$$\hat{\xi}' = g^{-1}\hat{\xi}g,$$
$$where,\ g = \begin{bmatrix}I & -\omega\times v\\ 0 & 1\end{bmatrix}, \tag{3.37}$$

This leads to;

$$e^{\hat{\xi}\theta} = g e^{\hat{\xi}'\theta} g^{-1}. \tag{3.38}$$

This simplifies the calculation using $\hat{\omega}\omega = \omega \times \omega = 0$, and thus we get;

$$\hat{\xi'^2} = \begin{bmatrix} \hat{\omega^2} & 0 \\ 0 & 0 \end{bmatrix},\ \hat{\xi'^3} = \begin{bmatrix} \hat{\omega^3} & 0 \\ 0 & 0 \end{bmatrix}, ... \tag{3.39}$$

Also we know that [90];

$$\begin{aligned} Given\, \hat{a}\ \in\ so(3);\ \hat{a^2} &= aa^T - \|a\|^2 I \\ \hat{a^3} &= -\|a\|^2 \hat{a}. \end{aligned} \tag{3.40}$$

Now using this for $a = \omega$ and also from knowing that $\|\omega\| = 1$, we obtain the expressions for higher orders as;

$$\begin{aligned} \hat{\omega^3} = -\hat{\omega}\ \ ;\ \ \hat{\omega^4} &= -\hat{\omega^2} \\ \hat{\omega^5} = \hat{\omega}\ \ ;\ \ \hat{\omega^6} &= \hat{\omega^2} \\ \hat{\omega^7} = -\hat{\omega}\ \ ;\ \ \hat{\omega^8} &= -\hat{\omega^2} \\ and\ so\ on... & \end{aligned} \tag{3.41}$$

Using equation 3.39 and equation 3.41 the homogeneous transformation function in equation 3.34 can be simplified as follows (see Appendix E);

$${}^0_N T(\theta) = \left[\prod_{i=1}^{N} \left[\left\{ e^{\hat{\xi}_i \theta_i} + \left(\delta \hat{\xi}_i \theta_i \right) \left[\frac{sin\theta_i}{\theta_i} + \hat{\xi}_i \frac{(1 - cos\theta_i)}{\theta_i} \right] \right\} \cdot e^{\hat{\xi}_i \delta \theta_i} \right] \right] \left[{}^0_N T(0) \right]. \tag{3.42}$$

If we consider θ_i to be small then $\frac{sin\theta_i}{\theta_i} \rightarrow 1$ and $\frac{(1-cos\theta_i)}{\theta_i} \rightarrow 0$. Hence we can write a simplified form of equation 3.42 for small angles as follows;

$$ {}^{0}_{N}T\left(\theta\right) = \left[\prod_{i=1}^{N}\left[\left(e^{\hat{\xi}_i\theta_i} + \delta\hat{\xi}_i\theta_i\right)\cdot e^{\hat{\xi}_i\delta\theta_i}\right]\right]\left[{}^{0}_{N}T\left(0\right)\right]. \tag{3.43} $$

In equation 3.43 the additive term is called *"static error"* or error due to link misalignment, where as the multiplicative term is called *"dynamic error"* or error due to joint motion.

Comparing the ideal condition (i.e. no error in θ and ξ) as given in equation 3.22, and the misaligned condition (i.e. errors in θ and ξ) as given in equation 3.43 we can draw the following conclusions;

1. Error in endeffector position due to uncertainty in 'θ_i' in link *'i'* is smaller than that for links *'i-1'*, *'i-2'*, *'i-3'* ...
2. Error in endeffector position due to uncertainty in 'ξ_i' in link *'i'* is greater than that for links *'i-1'*, *'i-2'*, *'i-3'* ...; assuming $\|\delta\xi_i\| > \|\delta\xi_{i-1}\| > \|\delta\xi_{i-2}\| ...$ (using 3.26).

Notice that the static errors are the errors which already exist in the robot prior to assembly and dynamic errors are the errors that are incurred gradually during execution of assembly. If these errors are within the tolerable limits then open loop control can be used for assembly. If not then the static error or error in ξ_i can be reduced by *'calibration'* and a calibration based open loop control can be used for assembly. If the error is still high even after calibration then the dynamic error or error in θ_i can be compensated by using *"active servoing"* and a closed loop control needs to be used for assembly.

As it can be observed, uncertainty in position of one link results in localization error in all the following links in the robot kinematic chain. From our previous discussion on the static and dynamic errors, we can see that:

1. The uncertainty in robot end-effector position over a travel path is directly proportional to the number of links used to achieve the motion along the designated path. This uncertainty $e = \sigma^2$ can be accredited to the dynamic errors in each used link.

$$^{Total}e_n \propto m. \tag{3.44}$$

2. The uncertainty in robot end-effector position is also proportional to the order of the used inks. The static errors in a serial linked manipulator kinematic chain combine cumulatively from the root to the end-effector.

$$^{Total}e_n \propto O[link_1 \rightarrow link_n]. \tag{3.45}$$

In the above equations *'n'* is the total number of links, *'m'* is the number of used links for the assembly task and *'O'* is the order of links in the chain from root to end-effector.

To prove the above relationship we proceed as follows;

The error at the end-effector is a combination of all the error incurred by the links. Thus in general;

$$[^{Total}e_{end-effector}] = \sum_{i=1}^{m} [^{Total}e_i]. \tag{3.46}$$

which suggests that the final uncertainty in end-effector position in $\Re^6$ is equal to the combined product of uncertainties from *'m'* used links out of *'n'* total links.

For a link *'i'* the total uncertainty $^{Total}e_i$ can be written as;

$$^{Total}e_i = ^{init}\ e_i + ^{dynamic}\ e_i. \tag{3.47}$$

Further expanding for the initial uncertainty for link *'i'* i.e. ${}^{init}e_i$ we obtain;

$$ {}^{init}e_i = {}^{static}\ e_i + {}^{Total}\ e_{i-1}. \tag{3.48} $$

Thus combining equations 3.47 and 3.48 we obtain;

$$ {}^{Total}e_i = [{}^{static}e_i + {}^{dynamic}\ e_i(P_i)] + {}^{Total}\ e_{i-1}. \tag{3.49} $$

Notice that the dynamic uncertainty ${}^{dynamic}e_i(P_i)$ is dependent of the motion range P_i. Equation 3.46 can be written in a recursive form using equation 3.49 as follows;

$$ [{}^{Total}e_{end-effector}] = \sum_{i=1}^{m} [[{}^{static}e_i + {}^{dynamic}\ e_i(P_i)] + {}^{Total}\ e_{i-1}]. \tag{3.50} $$

From equation 3.50 it can be seen that, in addition to the number of links used to accomplish a specific task, the order of the links used also plays a vital role in deciding the uncertainty in end-effector position. From the third term in equation 3.50 which is a recursive equation, it can be inferred that closer the link to the end-effector of the kinematic chain, lesser the dynamic error (i.e. error due to $\delta\theta_i$) will be. This information is important, especially for redundant serial linked manipulator systems. Thus during path planning for a assembly task, the uncertainty can be minimized by giving priorities to motion by more *precise* links. This may or may not result in a shortest path between the source and the goal, however, it ensures higher precision and consequently higher yield.

3.5 Searching for a precise path in microassembly

A multipart serial microassembly can be seen as a sequence of several grasping, manipulation and releasing steps involving motion through one or more degrees of

freedom of the robotic chain. Hence, in order to ensure high tracking accuracy in a limited sensory feedback environment, the robot kinematic linkage must be analyzed to determine the error accumulated in each of these segments. This information can later be used to carefully choreograph the motion of the links constituting a precise path as opposed to conventional shortest path where no information on localization uncertainty for the robot linkage is taken into account. The definition for the proposed *"precise path search algorithm (PPSA)"* is given as follows:

Definition

A precise path 'P_T' is defined as a collection of ordered motion segments 'P(i)' in a configuration space 'C' such that

$$max\left(\left[\sum_{i=1}^{n}\left(\vec{q}_i\left(P_i\right)\right)\right]-\vec{q}_{goal}\right)\rightarrow 0, \tag{3.51}$$

where $\vec{q}$ is the position in $\Re^6$.

Kinematic identification of a robot is important in order to determine feasibility of a process through the robot. There are two forms of kinematic identification; forward and inverse. Forward kinematics is computation of the position and orientation of robot's end effector as a function of its joint angles. The reverse process is known as inverse kinematics.

3.5.1 Precise path search algorithm (PPSA)

The *"precise path search algorithm (PPSA)"* searches for a non colliding path between two points in the configuration space such that the predicted uncertainty is minimum. Precision is given higher priority over distance between the points. As in microscale assembly the motion distances are generally very small, such approach does not harm the assembly cycle time greatly. The algorithm is given as follows:

PPSA Algorithm:

1. Build a non colliding path from the source to the goal comprising of segments, each one aligned along any of link's direction of motion. Two consecutive path segment join at a *"transit point"*. These transit points are selected in such a manner that, if required, they can be equipped with active sensors for obtaining feedback.
2. Starting with largest one, for each path segment, if more than one possible links are found with same direction of motion then select the link which is more precise. Link precision is estimated based on the effect of dynamic and static errors.
3. Based on the evaluation of different uncertainties, as discussed before, predict the maximum possible uncertainty for each path segment.
4. If the predicted value for uncertainty is greater than the allowable uncertainty at a transit point, then flag the task as complex or *"hard to achieve"*; otherwise flag the task as simple or *"easy to achieve"*. These flags which are called *"Complexity indices"* are used as references while selecting the hybrid control structure (will be discussed in next chapter).
5. For each complex task, a sensor field is suggested for active feedback.
6. The overall path and sensor field distribution plan is thus finalized for a specific assembly task. A hybrid controller designed based on this plan is executed to follow the plan.

Note that, the precision evaluation schemes for resolution, repeatability and accuracy discussed earlier in this chapter are used to determine the uncertainties in end effector positioning due to error in $\vec{\omega}$, $\vec{q}$ and θ.

3.5.2 Example of a simple planning scenario

Consider the scenario in figure 3.5 where there are two PPR robots each carrying a object (as shown by the red and green circles). One robot has the kinematic chain order as $[X \rightarrow Y \rightarrow \theta]$ where as the other robot has the configuration of $[Y \rightarrow X \rightarrow \theta]$.

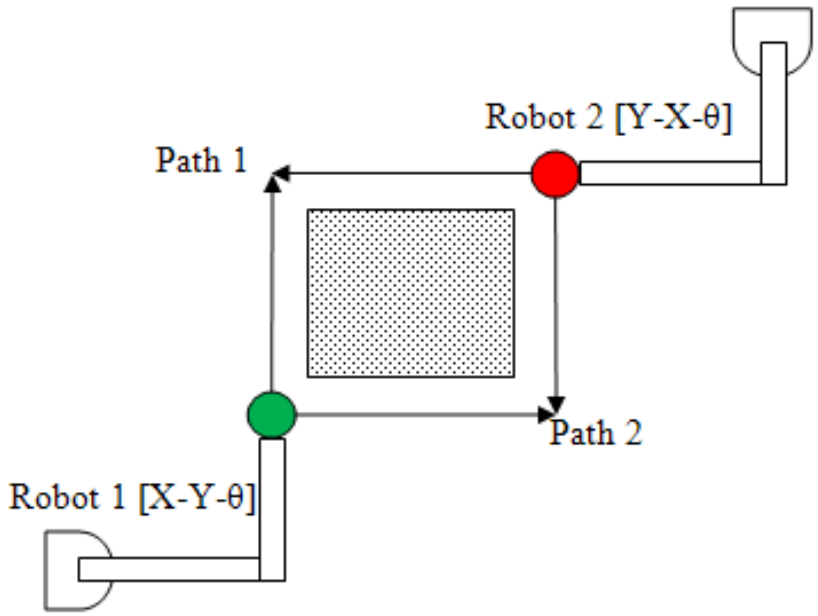

Figure 3.5. Precise path planning example.

In order to assemble these two objects the two robots can be moved in conjunction along either path1 or path2 as both gives shortest distance solution. However, path 2 is more precise than path 1 as it uses more precise links to move the objects.

3.6 Kinematics evaluation and planning with a typical PPR microassembly robotic

manipulator

In this example we will discuss the kinematic identification for one of the robots of the μ^3 microassembly system. The M_3 robot of the μ^3 system (see figure 3.6) and corresponding 3D rendering are shown below (see figure 3.7).

The basic model for the above robot can be represented through the following PPR robot as shown in figure 3.8. It consists of two translational stages and one rotational stage. The translation stages have maximum motion range of 15mm and the rotational stage can be moved to any angle between $[0, 2\pi]$.

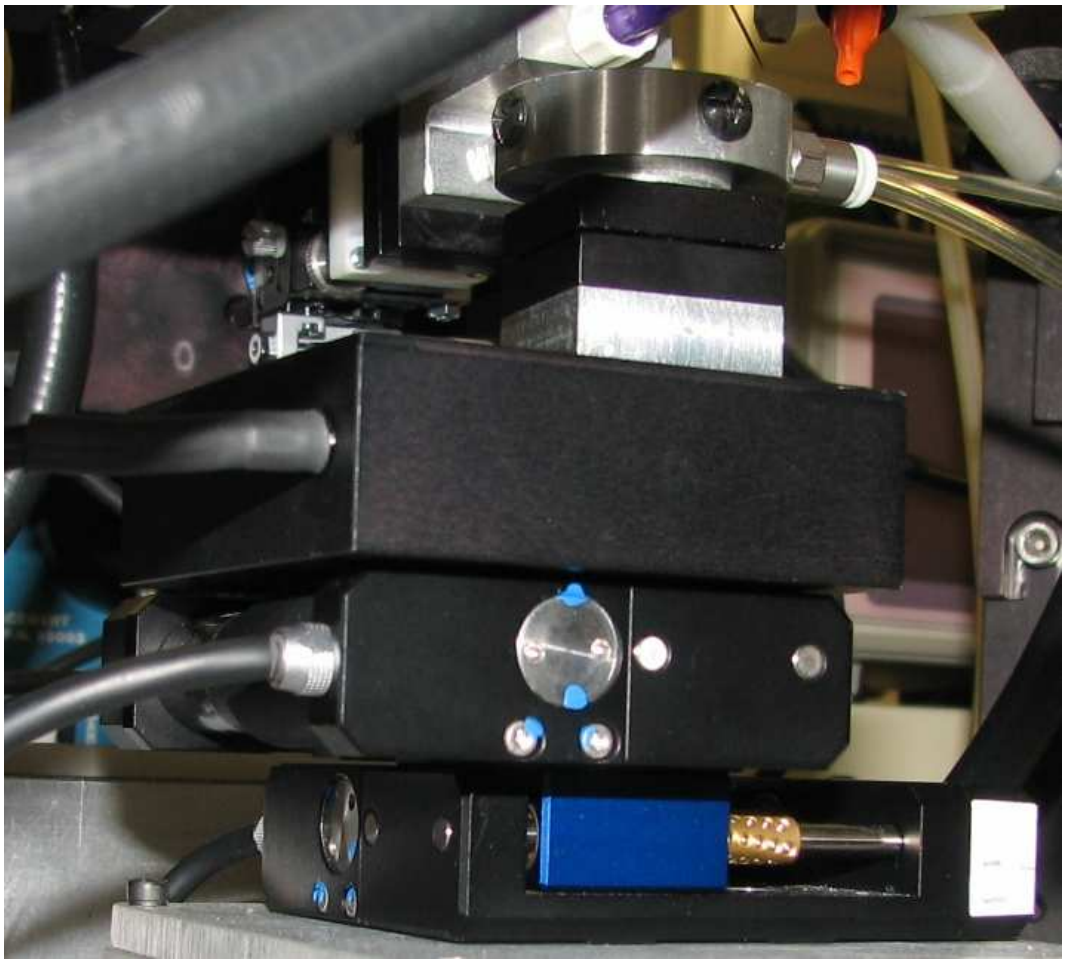

Figure 3.6. Base robot (M_3) of the μ^3 microassembly system.

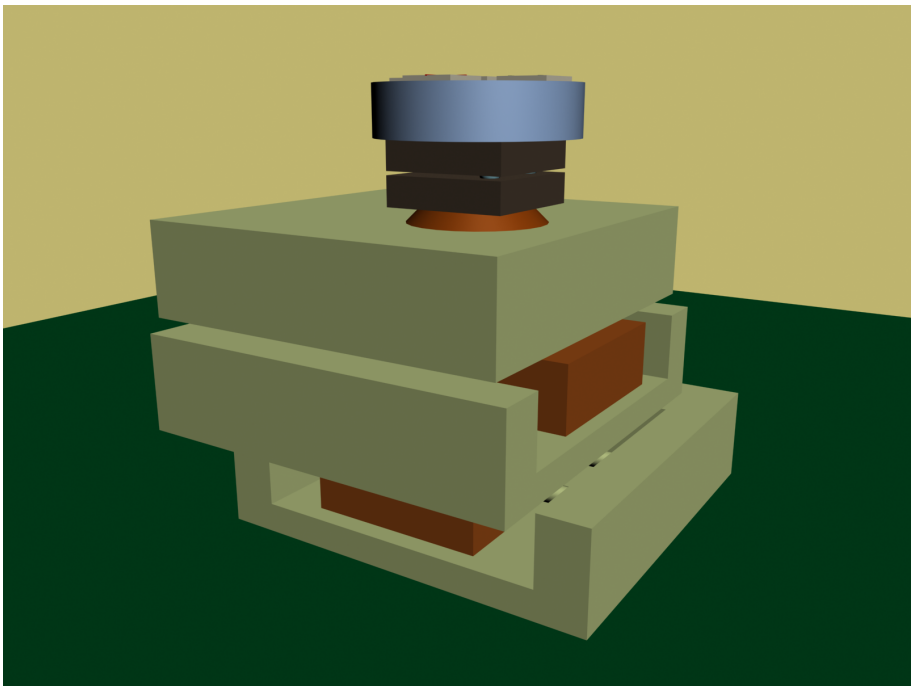

Figure 3.7. 3D rendering of the (M_3) robot of the μ^3 microassembly system.

3.6.1 Forward kinematics and spatial Jacobian for the PPR robot

In ideal case, the axes for the joints are:

$$\omega_1 = \begin{bmatrix} 1 \\ 0 \\ 0 \end{bmatrix}, \omega_2 = \begin{bmatrix} 0 \\ 1 \\ 0 \end{bmatrix}, \omega_3 = \begin{bmatrix} 0 \\ 0 \\ 1 \end{bmatrix}. \tag{3.52}$$

The axis points are selected as;

$$q_1 = \begin{bmatrix} 0 \\ 0 \\ 0 \end{bmatrix}, q_2 = \begin{bmatrix} L_1 \\ 0 \\ 0 \end{bmatrix}, q_3 = \begin{bmatrix} L_1 \\ L_2 \\ 0 \end{bmatrix}. \tag{3.53}$$

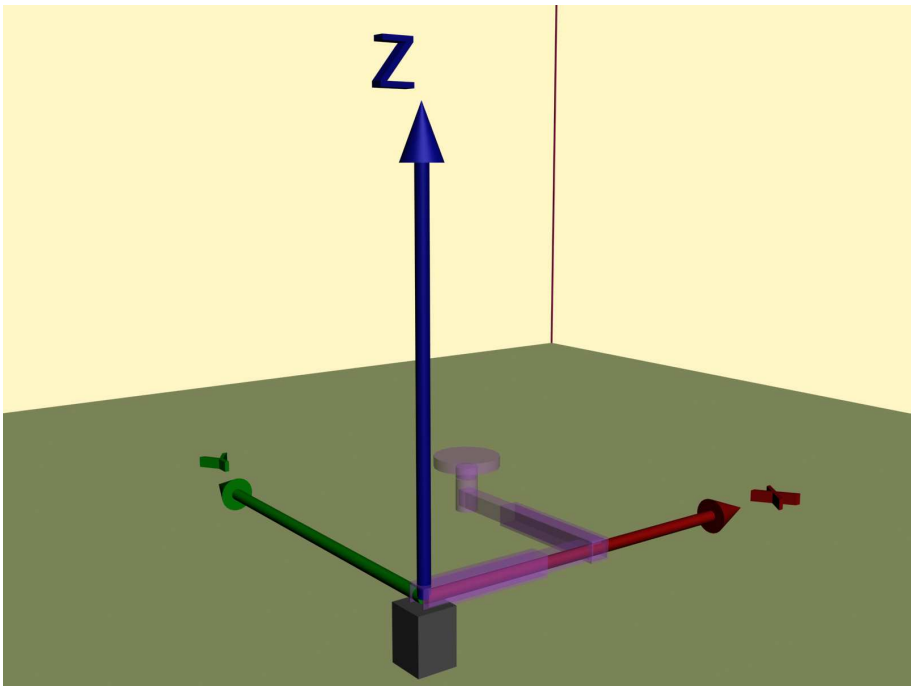

Figure 3.8. A PPR robot equivalent to the M_3 robot of μ^3 system.

If we consider the initial pose as all translational joints fully extended and the rotational angle is zero. Thus, the initial transformation matrix and twists are:

$$ {}^{0}_{N}\mathrm{T}\,(0) = \begin{bmatrix} I & \begin{pmatrix} L_1 \\ L_2 \\ L_3 \end{pmatrix} \\ 0 \quad 0 \quad 0 & 1 \end{bmatrix}, \tag{3.54} $$

$$ \xi_1 = \begin{pmatrix} 1 \\ 0 \\ 0 \\ 0 \\ 0 \\ 0 \end{pmatrix}, \xi_2 = \begin{pmatrix} 0 \\ 1 \\ 0 \\ 0 \\ 0 \\ 0 \end{pmatrix}, \xi_3 = \begin{pmatrix} L_2 \\ -L_1 \\ 0 \\ 0 \\ 0 \\ 1 \end{pmatrix}. \tag{3.55} $$

The forward kinematic of this robot is computed through product of exponential method as to be:

$$ {}^{0}_{3}\mathrm{T}\left(\theta\right) = \begin{pmatrix} \mathrm{Cos}\left[\theta_3\right] & -\mathrm{Sin}\left[\theta_3\right] & 0 & L_1+\theta_1 \\ \mathrm{Sin}\left[\theta_3\right] & \mathrm{Cos}\left[\theta_3\right] & 0 & L_2+\theta_2 \\ 0 & 0 & 1 & L_3 \\ 0 & 0 & 0 & 1 \end{pmatrix}, \tag{3.56} $$

and the spatial jacobian is:

$$ J = \begin{pmatrix} 1 & 0 & L_2+\theta_2 \\ 0 & 1 & -L_1-\theta_1 \\ 0 & 0 & 0 \\ 0 & 0 & 0 \\ 0 & 0 & 0 \\ 0 & 0 & 1 \end{pmatrix}. \tag{3.57} $$

3.6.2 Numerical analysis with static and dynamic errors

Let's reconsider the previous example i.e. the PPR robot with uncertainties (see figure 3.9 and figure 3.10). In the figure the cone around each individual axis represents the possible uncertainty in positioning. This dynamic uncertainty is proportional to distance travelled along the axes. As discussed above the motion range for prismatic links is 15mm and for revolute links it is 0 to 360 degrees. Let's consider for a case in which the links are required to be moved by a offset of [7.5mm, 7.5mm, 90 degrees]. We assume the initial condition in which all the prismatic links are fully retracted and the revolute link is at zero angle. Thus L_1, L_2 are zero in the previous example. L_3 is taken as 2mm. The uncertainties included are as follows:

- In case of directional uncertainties in $\vec{\omega}$, the links are misaligned from their primary axis by a positive angle of 2^o.
- In case of axis point uncertainties in $\vec{q}$, the link lengths are considered to have a positive error of 100microns.
- Finally for the desired range of motions the prismatic joints have a error of 100 microns and the revolute joints have a error on 3 degrees.

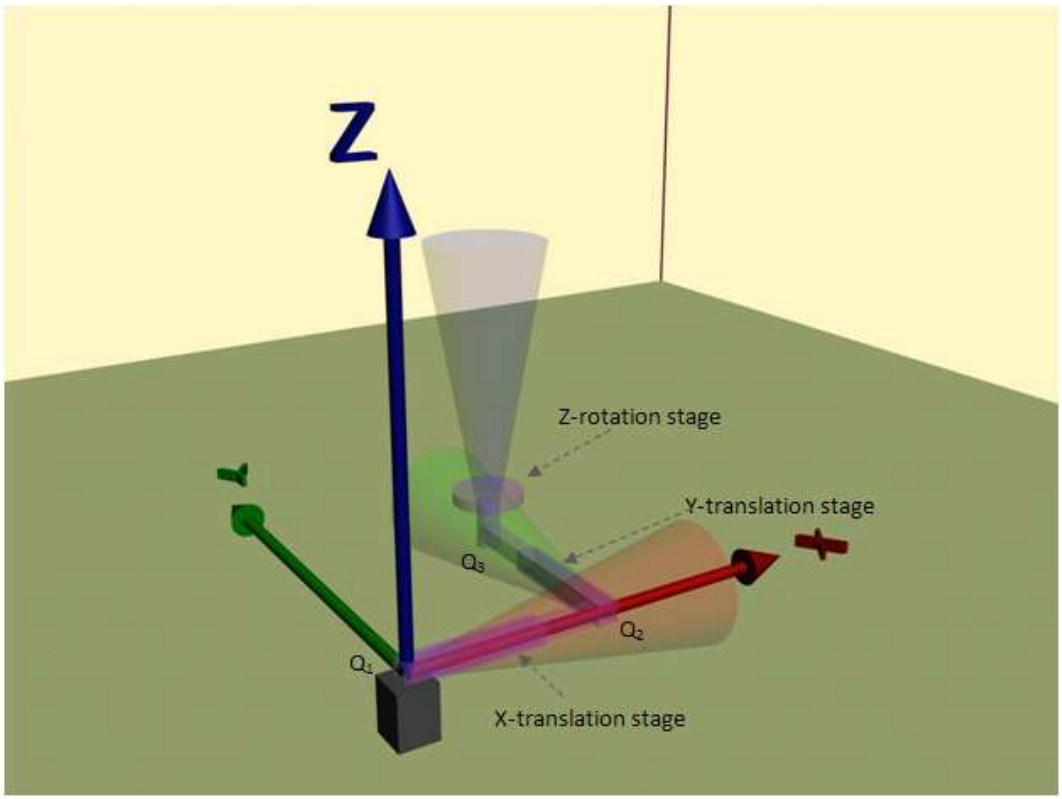

Figure 3.9. A PPR robot with dynamic motion-uncertainties.

The forward kinematics for the above numerical values is computed to be:

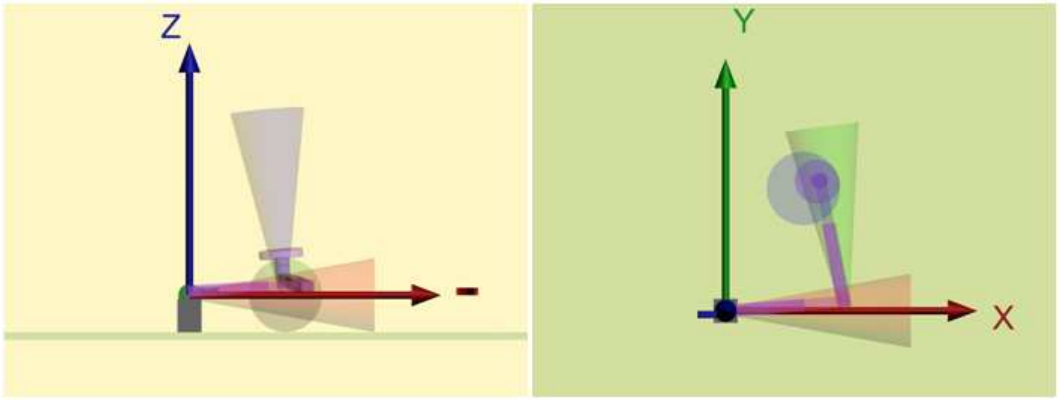

Figure 3.10. A PPR robot with static and dynamic errors.

$$\begin{pmatrix} -0.0479 & -0.998 & -0.002 & 7.676 \\ 0.9966 & -0.0479 & 0.071 & 7.985 \\ -0.072 & 0.002 & 0.997 & 2.016 \\ 0 & 0 & 0 & 1 \end{pmatrix}, \tag{3.58}$$

whereas for ideal case i.e. without any error the forward kinematic expression is:

$$\begin{pmatrix} 0.000796327 & -1 & 0 & 7.5 \\ 1 & 0.000796327 & 0 & 7.5 \\ 0 & 0 & 1 & 2 \\ 0 & 0 & 0 & 1 \end{pmatrix}. \tag{3.59}$$

Similarly for Jacobian matrix we find;

For ideal case without any error:

$$\begin{pmatrix} 1 & 0 & 7.5 \\ 0 & 1 & -7.5 \\ 0 & 0 & 0 \\ 0 & 0 & 0 \\ 0 & 0 & 0 \\ 0 & 0 & 1 \end{pmatrix}, \tag{3.60}$$

and for the actual case with the misalignment errors as discussed above the spatial Jacobian is:

$$\begin{pmatrix} 0.999 & -0.069 & 8.127 \\ 0.035 & 0.997 & -7.366 \\ 0 & 0 & 0.542 \\ 0 & 0 & -0.035 \\ 0 & 0 & 0.035 \\ 0 & 0 & 0.998 \end{pmatrix}. \tag{3.61}$$

From the above example, with the given misalignments the robot end-effector, when commanded to move the desired distance as mentioned above, incurred an error variance:

$$\begin{pmatrix} 0.176 \\ 0.485 \\ 0.016 \\ 0.098 \\ 4.107 \\ 2.755 \end{pmatrix}. \tag{3.62}$$

The last three parameters give the error in angles in degrees along x, y and z direction. From equation 3.62 we notice that although the two prismatic joints were commanded to move equal distance, the link along x-axis incurred less error than the one along y-axis. Also notice that the rotation along y-axis incurred the most error.

The above findings confirm the claim as stated in the previous subsection that the error magnitude grows as the link order increases from the root of the kinematic chain i.e. the farther the used link is situated in the kinematic chain from the root the more the error it can incur.

Thus while planning the path for a specific task, the error in end-effector position can be kept minimum if motion by the links along more precise axes is given higher priority. This information is also useful in arranging the degrees of freedom for a redundant and reconfigurable manipulation system such as the μ^3 microassembly system. Based on the estimated precise path the corresponding links can be arranged in such a manner that the overall error will be minimum.

In figure 3.11 configuration of a redundant robot manipulation system is shown. Two robots have been configured to carry out a typical compliant microassembly operation in which a micropart and a microgripper mounted on two individual robots are brought to each other in order to grasp the micropart by the microgripper. The planning for collision free path for this operations suggests the microgripper be moved only in Y and Z directions and micropart be moved in X and Y directions. Based on this the two manipulation systems are configured as shown in the figure. Notice that the Y axis link on the microgripper manipulation system is placed at the starting of the kinematic chain whereas in case of the micropart manipulation system the starting link is in X direction.

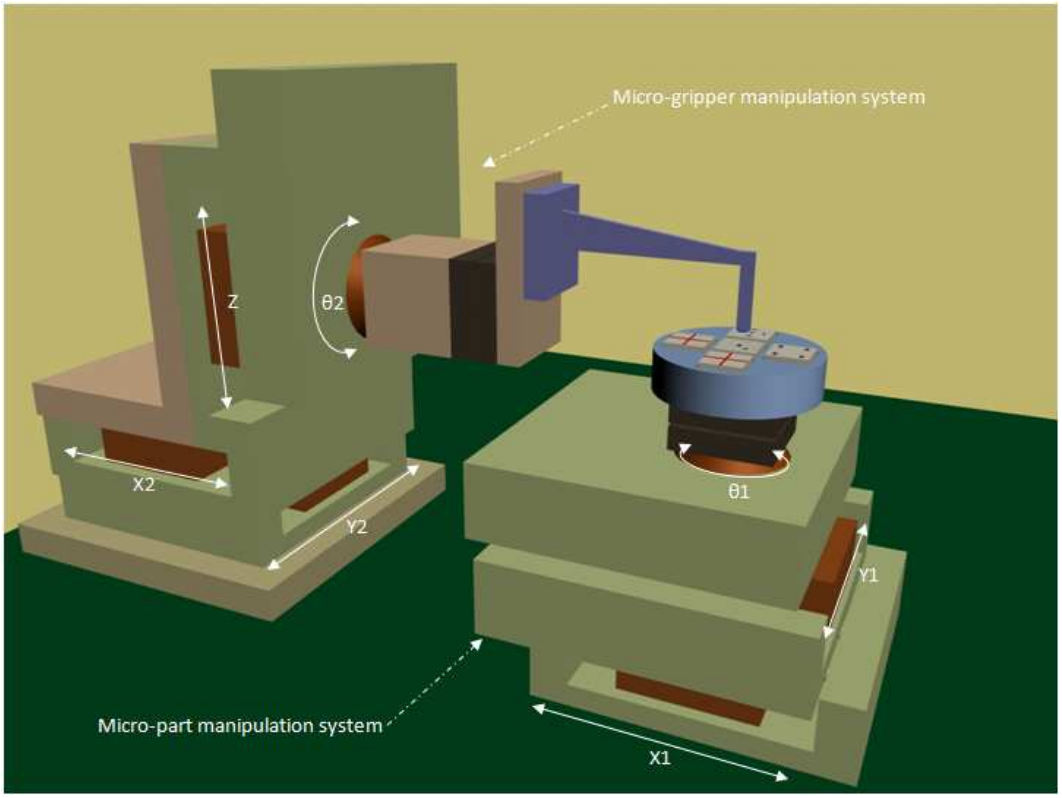

Figure 3.11. Redundant robot configuration based on precision evaluation.

3.7 Discussion on experimental setups for minimizing uncertainty in robot tracking

As discussed, the total error in end-effector position can be categorized into static and dynamic errors. The dynamic errors are dependent on the motion type of stage. On the other hand, the static errors can be reduced using several techniques such mechanical correction, calibration etc.

A commercially available stage position metrology device is shown in figure 3.12. This complex system uses laser and intricate optics to find out the misalignment between robot links.

In microassembly systems where space is greatly restricted and also in reconfigurable systems, incorporation of such complex stage position metrology device is difficult. Alternatively, a simpler and cost-efficient way to identify and eliminate the

Figure 3.12. Stage position metrology device from Zygo Metrology Solutions.

static errors is the use of calibration. Using three or more reference point any location in the workspace can be reached with better precision using calibration. The more the number of calibration points, the more will be the precision. However with more and more points in calibration, the process time also increases. The calibration based feed-forward control will be discussed in the next chapter. The calibration system can be configured in comparatively much simpler manner as shown in figure 3.13. In this figure a single microscope camera is used from top to calibration the robot system.

Figure 3.13. Calibration using single sensor.

CHAPTER 4

PRECISION ADJUSTED HYBRID CONTROLLER

Assembly in micro domain harbor many challenges; one of which is the control of automation process. From previous discussions, it is evident that the ratio between required precision and achievable precision can widely vary among different subtasks. Thus selection of suitable control is a major concern in microscale assembly.

Broadly speaking, control system for a robotic manipulator can be either open loop or closed loop. In case of open loop control the robot end-effecter is moved to reach a desired location by issuing commands for joint increments computed from either a model based or a calibration based transformation matrix. Model based transformation is correct if the robot accuracy is high and calibration based transformation is correct if the robot repeatability is high. On the other hand, in case of closed loop control the robot is moved to the desired location by incremental motion of small steps where is each increment is computed using an active transformation between vision information and instantaneous robot position. The higher the resolution of the robot, the smaller the incremental steps can be and thus smoother will be the approach to the desired location. We can summarize the different control structures for assembly as shown in table 4.1.

As observed from table 4.1, each of the three discussed control schemes has their advantages and disadvantages with respect to the cost functions such as process yield, cycle time and overall cost. If considered from a manufacturing point of view any single control scheme is insufficient to guarantee high yield, less production time and low cost due to their inherent limitations. Therefore, a mixture of the control

Table 4.1. Comparison among different control schemes

Parameters	*open loop (model)*	*open loop (calib)*	*closed loop (servo)*
Precision attained	Low	Moderate	High
Execution time	Low	Moderate	High
Requirement	High accuracy	High repeatability	High resolution
Sensor network	None	Minimal	Extensive
Cost of control	Low	Medium	High

schemes or in other words, a hybrid control is always preferred for better optimization of the cost functions. Note that there can be many more control schemes beyond the mentioned three, however, for serial assembly of microparts, we limited our discussion to the above three schemes. We choose serial microassembly approach over parallel or self assembly approaches because serial assembly is highly controllable, less complex can provide high yield deterministically.

4.1 $2\frac{1}{2}D$ microassembly and compliant micro mechanism

Multi-scale assembly methods can be classified based on throughput (serial or parallel), deliberate intervention (deterministic or stochastic), type of end-effectors (contact, non-contact) or level of human intervention (manual, tele-operated or automated). In addition to these, microassembly can further be categorized based on part dimensions and assembly poses as 2D, 21/2D and 3D.

Inherited from semiconductor industry, fabrication of microparts is typically a micromachining process where the parts are extracted from a substrate such as Silicon using either chemical etching or deposition. The surface micromachining generally yields in thin-film microparts of thickness roughly about a couple of microns. These monolithically fabricated thin-film microparts are essentially inappropriate for out-of-plane assembly due to their structural weakness and hence only used in in-plane

assembly of devices. Such type of assemblies can be treated as 2D microassembly where the thin-film parts are only moved in-plane.

Figure 4.1. 2D assembly.

During late 1990s with the invention of LIGA (Lithographie-Galvanoformung-Abformung; german for Lithography-Electroplating-Molding) and DRIE (Deep-Reaction-Ion-Etching) processes, construction of high aspect ratio microparts were made possible. Although much less in comparison to the length and breadth, the thickness of the microparts now can be made significantly larger i.e. up to a hundred microns. The structural rigidity due to increased thickness opened a new avenue for out-of-plane assembled devices. Such type of assemblies can be treated as $2\frac{1}{2}D$ microassembly where the thick-film parts are assembled by moving them in 3D.

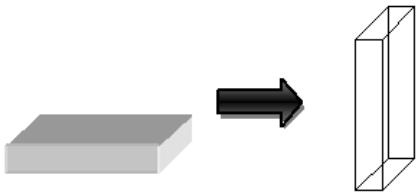

Figure 4.2. $2\frac{1}{2}D$ assembly.

With ever increasing demand for complex designs and added functionalities, the micro devices can no longer remain monolithic; rather they need to incorporate more and more heterogeneous materials. Thus microassembly techniques should also be able to include such materials such as metal fixtures, glass lenses, electronic components and many more. Such type of assemblies can be treated as 3D microassembly

where the microparts are truly three dimensional and require manipulation and assembly in 3D.

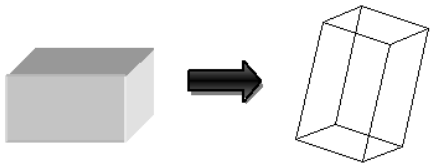

Figure 4.3. 3D assembly.

Furthermore, based on the type joinery, an assembly can be broadly classified as compliant and non-compliant.

In compliant assembly, typically some form of snap-fastening mechanism is used to arrest the assembled parts together through friction. Due to compliance in micro joints, such assemblies can accommodate comparatively higher misalignment and also can self align to certain degree. Major drawbacks of such assembly are complex design for the compliant mechanism and joint weakness due to flexible fixtures.

In non-compliant assembly, the assembled parts are held together by the use of some external agent such as adhesives. As the parts do not have compliance, such type of assemblies requires higher precision in alignment.

4.2 Complexity Index (CI) in microassembly workcell

Success of serial microassembly of a microsystem essentially depends on successful execution of the task list comprising of assemblies of the individual components. While the execution of task list requires conventional assembly planning schemes such as motion planning, obstacle avoidance, control etc, it also requires intermediate alignment and realignment of microparts that are being subjected to ambient errors

and surface forces. High speed mass production of low cost microsystems requires optimized control and planning based on accurate estimation of system and correct prediction of state. To achieve this we introduce a term called *"complexity index (CI)"* that is used to define the complexity of a specific task by assigning a Boolean value *[0, 1]* to it; 1 for complex tasks that are *"hard to assemble"* and 0 for non-complex tasks that are *"easy to assemble"*. The complexity index is then used in selection of the appropriate control scheme for an assembly task. The complexity index Ω is defined as follows:

Definition

The Complexity Index, $\Omega\epsilon[1, 0]$*, is a Boolean flag that defines a specific task in a assembly sequence as complex or noncomplex based on the precision parameters such as resolution, repeatability and accuracy of the part and manipulator end-effectors targeting high yield assembly condition. A value of '1' defines the task as complex and a value of '0' defines the task as non-complex.*

$$\Omega = \frac{1 - sgn\left[\sigma_1^2 - (\sigma_2^2 + \sigma_3^2 + \sigma_4^2)\right]}{2}. \tag{4.1}$$

By rearranging the *'correctable'* and *'uncorrectable'* terms we can rewrite as follows:

$$\Omega = \frac{1 - sgn\left[(\sigma_1^2 - \sigma_2^2 - \sigma_4^2) - \sigma_3^2\right]}{2}. \tag{4.2}$$

The robot uncertainty σ_3^2 can further be interpreted in terms of the RRA (resolution, repeatability and accuracy) metrics. By using the expressions for the RRA from previous chapter, we can obtain the complexity indices with respect to the precision metrics as follows:

Table 4.2. Control schemes based on complexity index

Ω_{res}	Ω_{rep}	Ω_{acc}	*Control scheme*
0	0	0	Open loop, no calibration
0	0	1	Open loop, with calibration
0	1	1	Closed loop, with calibration
1	1	1	Not possible with given hardware

$$\Omega_{acc} = \frac{1 - sgn\left[(\sigma_1^2 - \sigma_2^2 - \sigma_4^2) - \lim_{n\to\infty}\left(\frac{1}{n}\left(\sum_{j=1}^{n}(q_j - q_{ref}) + \sigma_{q_{j0}}^2(P_j)\right)\right) + \sigma_s^2\right]}{2} \tag{4.3}$$

$$\Omega_{rep} = \frac{1 - sgn\left[(\sigma_1^2 - \sigma_2^2 - \sigma_4^2) - \lim_{n\to\infty}\left(\frac{1}{n}\left(\sum_{j=1}^{n}(q_j(P_j) - q_{ref})\right)^2\right) + \sigma_s^2\right]}{2} \tag{4.4}$$

$$\Omega_{res} = \frac{1 - sgn\left[(\sigma_1^2 - \sigma_2^2 - \sigma_4^2) - min\left(\lim_{(q_j - q_{j-1})\to 0}|q_j(P_j) - q_{j-1}(P_j) + \sigma_s^2|\right)\right]}{2}. \tag{4.5}$$

4.3 Hybrid controller for microassembly

A precision-adjusted hybrid controller has been proposed to automate the microassembly process. Based on the RRA metrics the complexity index Ω can be calculated. The three forms for the complexity index i.e. Ω_{acc}, Ω_{rep} and Ω_{res} gives a selective measure to choose the control structure for microassembly. Table 4.2 shows the possible configuration of control scheme based on these complexity indices.

The remaining combinations are inefficient, and hence we omitted from table 4.2.

4.3.1 Design of the hybrid controller

Figure 4.4 shows a standard state-space block diagram for an output feedback controller.

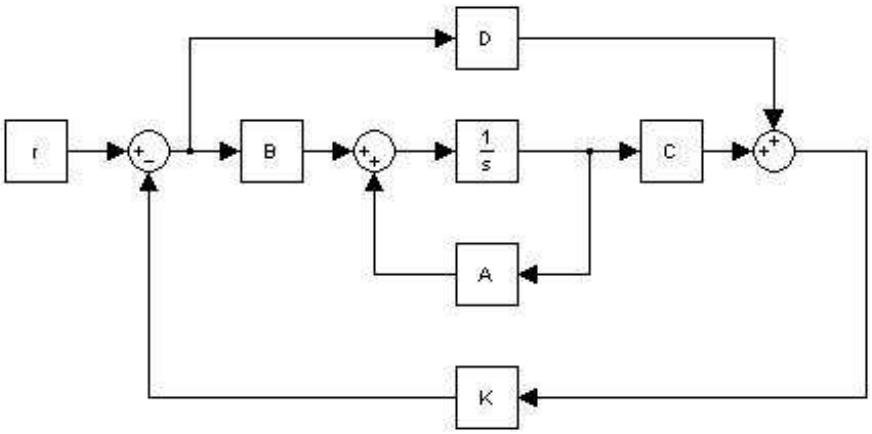

Figure 4.4. Output feedback controller state-space block diagram.

In this case the input to the controller is given as:

$$u[n] = r[n] - Ky[n]. \tag{4.6}$$

In discrete form the above feedback control system can be represented as follow:

$$\begin{aligned} x[n+1] &= (A - BK(I + DK)^{-1}C)x[n] + B(I - K(I + DK)^{-1}D)r[n], \\ y[n] &= (I + DK)^{-1}Cx[n] + (I + DK)^{-1}Dr[n]. \end{aligned} \tag{4.7}$$

Eliminating D from the above equations we can simplify as follows:

$$\begin{aligned} x[n+1] &= (A - BKC)x[n] + Br[n], \\ y[n] &= Cx[n]. \end{aligned} \tag{4.8}$$

In the above equations while $K=0$ the input to the controller $u[n]=r[n]$ and the controller becomes open loop. And when $K=1$ the controller acts as closed loop. The value of K is obtained from one or more sensor readings.

In Figure 4.5 the proposed hybrid controller is shown. This model can be seen as a modified closed loop feedback controller.

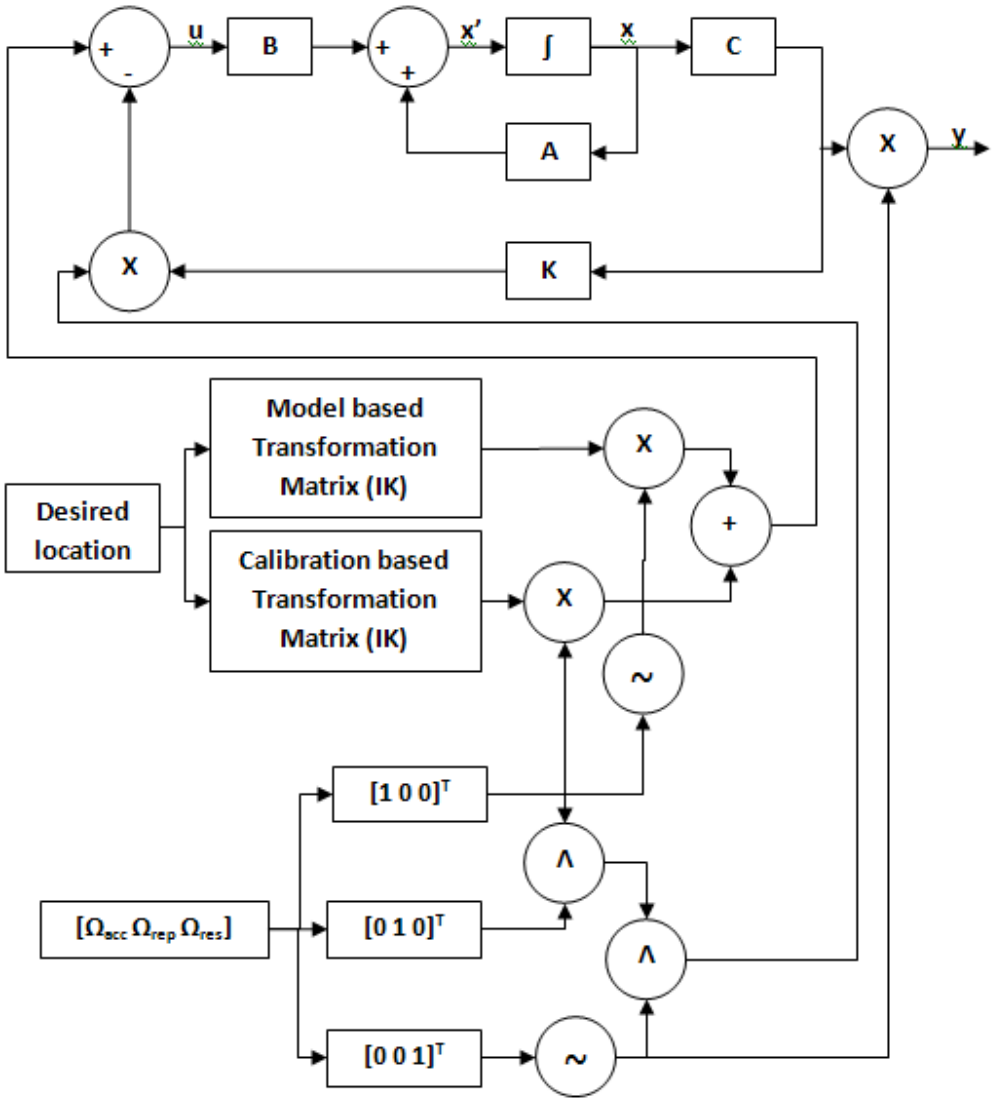

Figure 4.5. Hybrid supervisory controller state-space block diagram.

In addition to the desired location *r[n]*; this hybrid controller has an additional component, which is the *"Complexity Index"*. The input to the hybrid controller is given as:

$$t[n] = \begin{bmatrix} r[n] & S[n] \end{bmatrix}^T. \tag{4.9}$$

In the state space model shown in Figure 4.5 A is the *"state matrix"*, B is the *"input matrix"*, C is the *"output matrix"*, and D is the *"feedthrough (or feedforward) matrix"*. For simplicity, D is often chosen to be the zero matrix, i.e. the system is chosen not to have direct feedthrough.

The simplified discrete state space model is described by:

$$\begin{aligned} x[n+1] &= (A - B\Omega(n)KC)x[n] + Br[n], \\ y[n] &= Cx[n]. \end{aligned} \tag{4.10}$$

Note that in equation 4.10, $\Omega = 0$ reduces the control to open loop and $\Omega = 1$ selects the closed loop control.

4.4 Automation steps in microassembly workcell

The automation framework proposed in this research consists of two parts; *Offline* and *Online*.

4.4.1 Offline estimation of motion path and task complexity

The *"Precise Path Search Algorithm (PPSA)"*, as discussed in previous chapter is used during the offline phase to predict the uncertainties and determine a path for the microassembly task based on *'HYAC'*. For each subtask in a task, complexity indices Ω's are calculated. Based on these indices a preliminary scheme for control

structure is designed and discrete sensor fields are distributed at transit points, if necessary.

In order to determine the task complexities ($\Omega's$) using equations 4.3 to 4.5, we use the measurement procedure as explained in the previous chapter for obtaining the precision metrics. After collecting multiple readings, the probability density function (pdf) is found out. This pdf data distribution is then approximated by a Gaussian curve. From the Gaussian curve we determine precision using 3σ value.

4.4.1.1 Sensor precision σ_s^2

As discussed previously, estimation of sensor precision is essential in determining the precision metrics in the work cell. We determine the sensor precision $sigma_s2$ by fisrt collecting multiple reading at fixed time intervals from a stationary sensor over a fixed feature placed on an unpowered manipulation stage. Figure 4.6 shows a sample raw data collected.

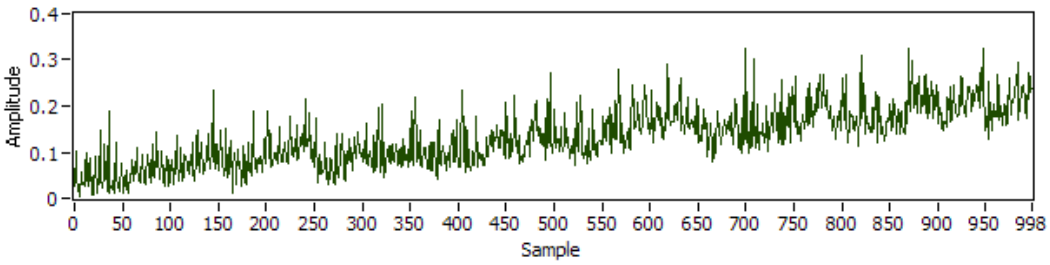

Figure 4.6. Raw data collected from stationary sensor over stationary feature.

This raw data is distributed into bins. A general rule of thumb to find out the number of bins is to use *Sturges' Rule* according to which:

$$number\,of\,bins = 1 + 3.3log(size\,of(X)). \tag{4.11}$$

The discrete histogram of the input data sequence based on the given bin specifications is found out as shown in 4.7. The probability density function is also computed.

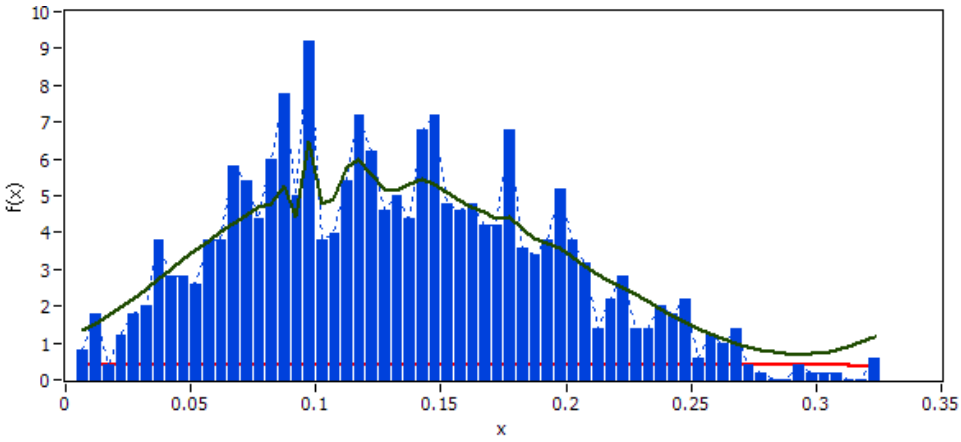

Figure 4.7. Histogram and probability density function.

After normalization we fit a Gaussian curve to the pdf as shown in figure 4.8.

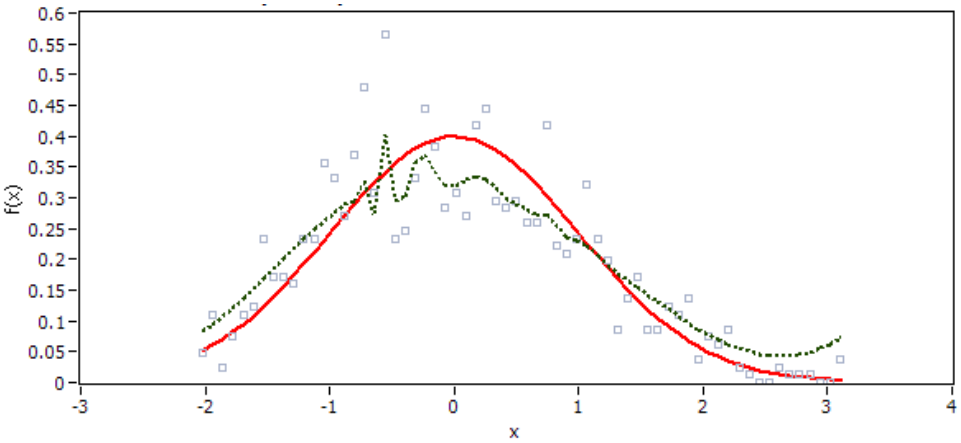

Figure 4.8. Gaussian approximation of sensor precision.

The mean and standard deviation are determined for the distribution. For the above sample case the mean and standard deviation were found to be 0.18 micron and 0.13 micron respectively.

4.4.1.2 Robot precision metrics (σ^2_{acc}, σ^2_{rep} and σ^2_{res})

Using experimental schemes as mentioned in the previous chapter the precision metrics are evaluated.

The sensor readings obtained from the collected data from this experimentation include the sensor uncertainties. So to evaluate the precision metrics for a robot the sensor precision is subtracted from the experimentation data. In figure 4.9 the possible uncertainty in robot positioning 'σ^2_3' is shown.

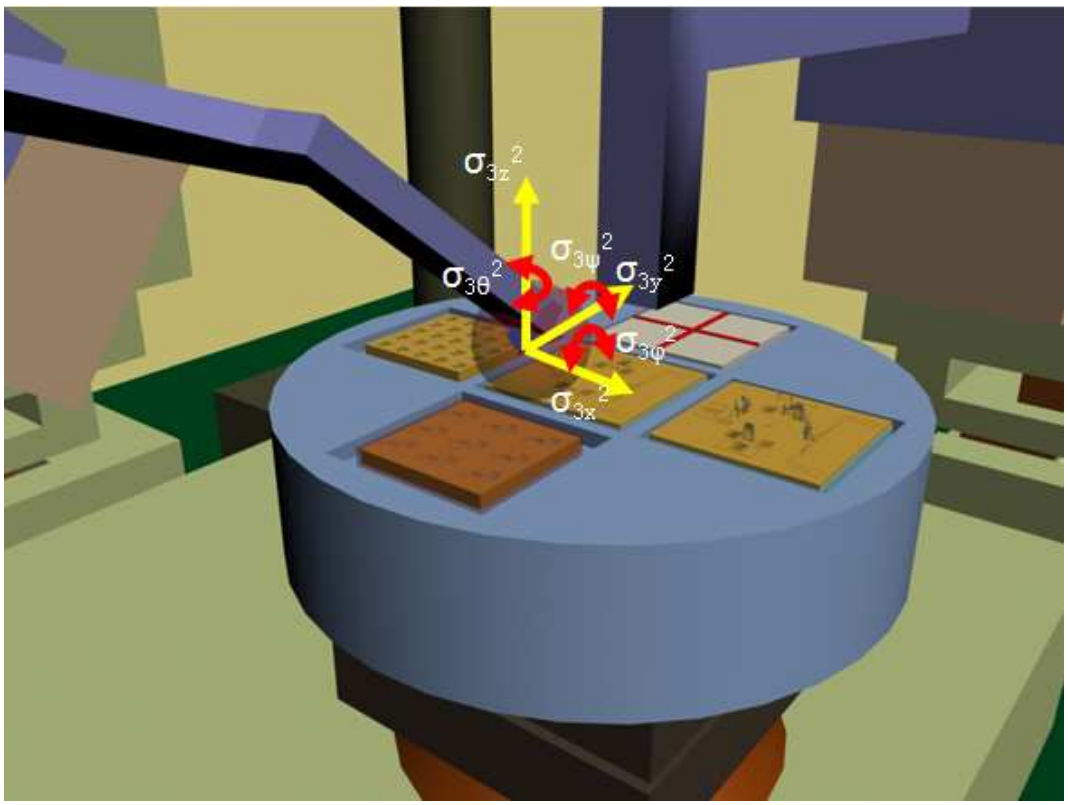

Figure 4.9. Uncertainty in robot positioning.

The robot positioning precision can be represented in terms on accuracy, repeatability or resolution based on the control scheme to be used. Thus we evaluate all of these precision metrics.

A typical experimental data to find out accuracy of a serial robot (PPR) is shown in figure 4.10.

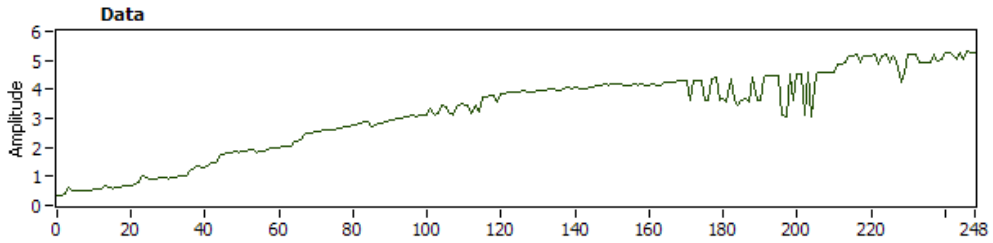

Figure 4.10. Raw data from accuracy test experiment for a PPR robot.

Using similar procedure as discussed above, the Gaussian approximation for this data has been found, as shown in figure 4.11.

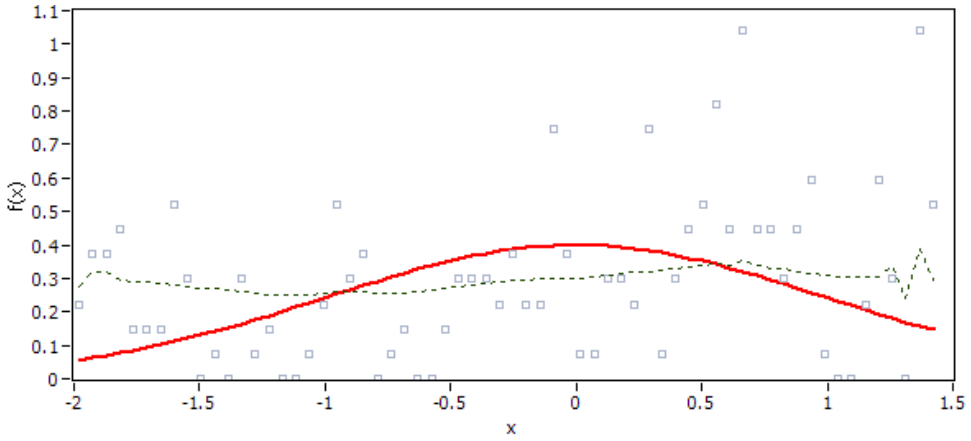

Figure 4.11. Data distribution (with Gaussian fit) for accuracy test experiment for the PPR robot.

From the above data the mean was found to be 0.78microns. Now subtracting the sensor precision as found above, we obtain the accuracy of the robot system for the specific motion along the path was 0.6micron.

Similarly for the repeatability we follow the experimentation process as mentioned in previous chapter. A typical sample data to find the repeatability for the same serial (PPR) robot is shown in figure 4.12.

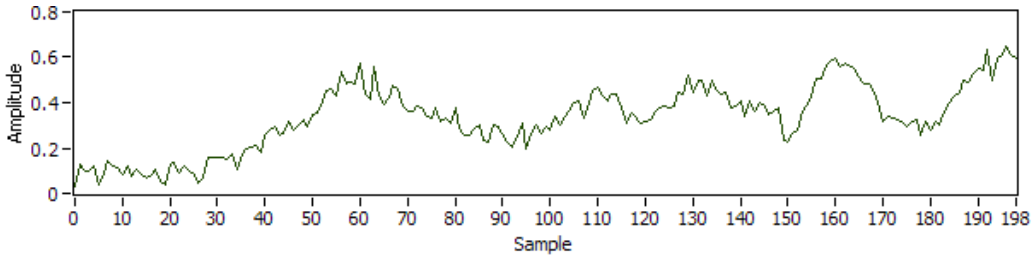

Figure 4.12. Raw data from repeatability test experiment for the PPR robot.

The Gaussian approximation is shown in figure 4.13.

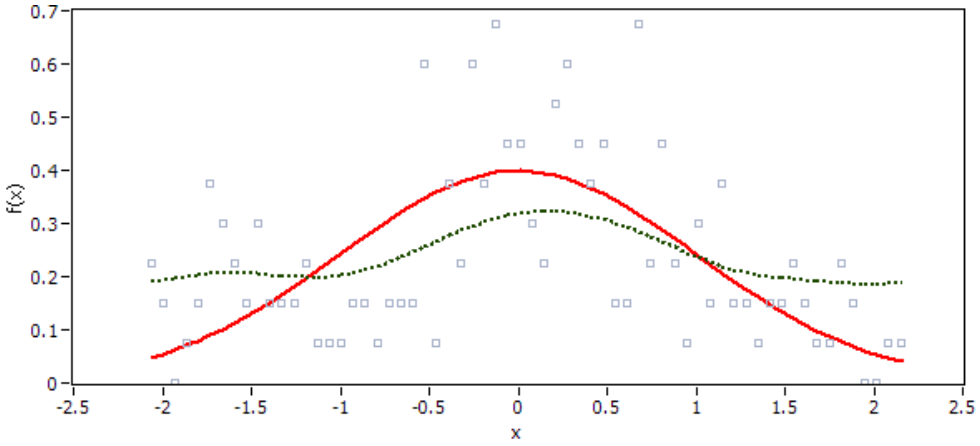

Figure 4.13. Data distribution (with Gaussian fit) for repeatability test experiment for the PPR robot.

From the data and sensor precision information the repeatability was found to be 0.36microns.

Based on the control structure the relevant σ^2 is used to represent σ_3^2.

4.4.1.3 Design tolerance (σ_1^2) and fixturing precision (σ_2^2)

Due to the errors in fabrication, the design tolerance is subjected to a uncertainty. Thus the actual design tolerance σ_1^2 is computed by subtracting the fabrication error from the given design tolerance (see figure 4.14). Typically, DRIE processes have a fabrication error of 1 to 2 micron based on the aspect ratio. Thus a micro-fixture designed with a tolerance of 5microns will exhibit a tolerance range from 3 to 7micron.

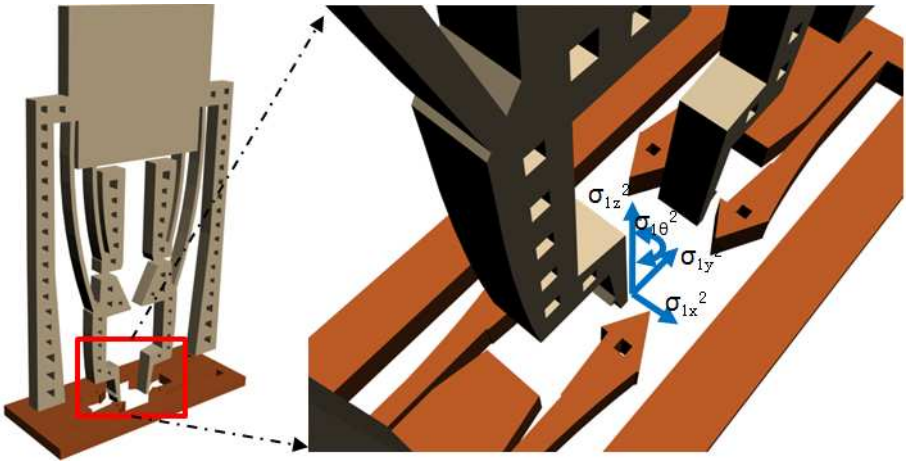

Figure 4.14. Design tolerance given to a MEMS part for assembly.

Similarly to account for uncertainties in fixture i.e. micropart release process i.e. detethering (see figure 4.16), MEMS die placement (see figure 4.15) process we use σ_2^2. To obtain statistical data we simulate detethering of microparts and placement of MEMS dies in to robot workcell using a realistic virtual 3D simulator (see Appendix C).

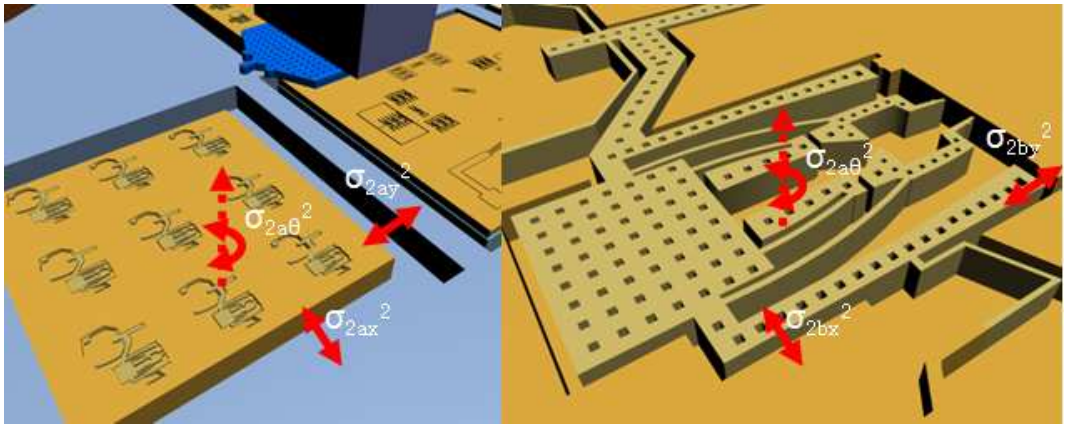

Figure 4.15. Fixturing uncertainty in MEMS parts.

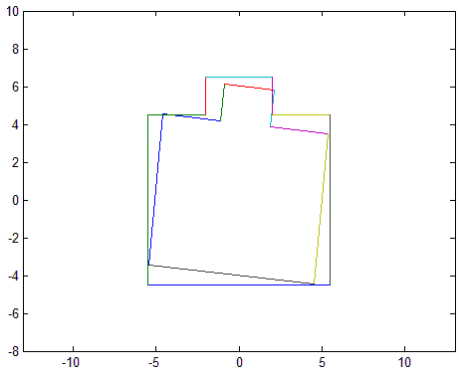

Figure 4.16. Misalignment is MEMS part (inner polygon)inside holder(outer polygon) after detethering.

For this test, we define the ideal shape for the MEMS part and the outer boundary of the holder. Next we find a random offset for x, y, and θ within the max possible offset. The coordinates of the inner shape was multiplied with a transformation matrix to get the points of the offset shape. Then we have tested if all the points were inside the outer polygon; if so then the sample is saved for analysis otherwise it's discarded assuming the pose is not possible. In this simulation we collected 10000 sample poses by varying the x, y, and θ out of which 8500 poses were discarded. The remaining 1500 filtered data were used for obtaining the uncertainty distribution. The

data for a typical micropart detethering simulation for 1500 data samples is shown in figure 4.17.

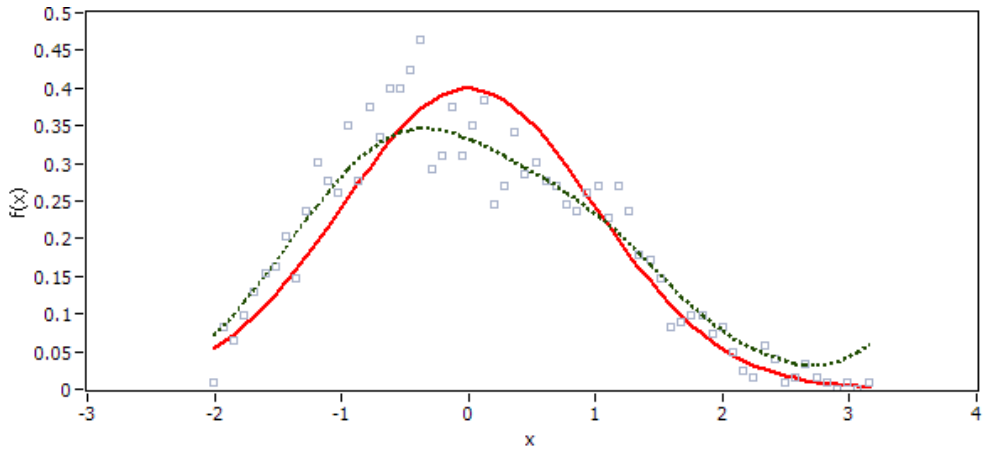

Figure 4.17. Data distribution (with Gaussian fit) for detethering.

The precision in dethering was obtained from the data to be 0.9microns.

Similar simulation for die placement for 1100 data samples, as shown in figure 4.18, yielded an accuracy of 2microns.

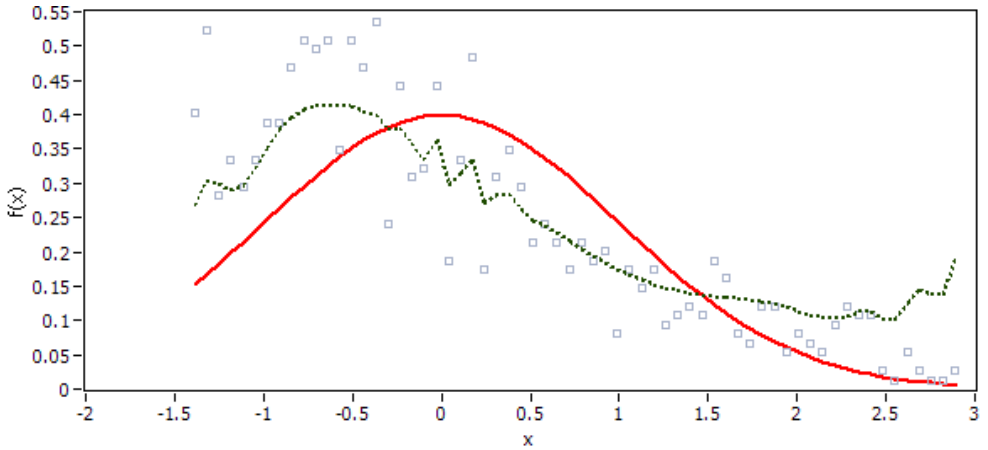

Figure 4.18. Data distribution (with Gaussian fit) for die placement.

4.4.2 Verification of microassembly process in virtual 3D

A virtual reality application called *Microsim 2.0* has been developed (see Appendix C) to realistically verify the microassembly plan proposed by the PPSA. Figure 4.19 shows a typical pick and place operation of virtual micro part.

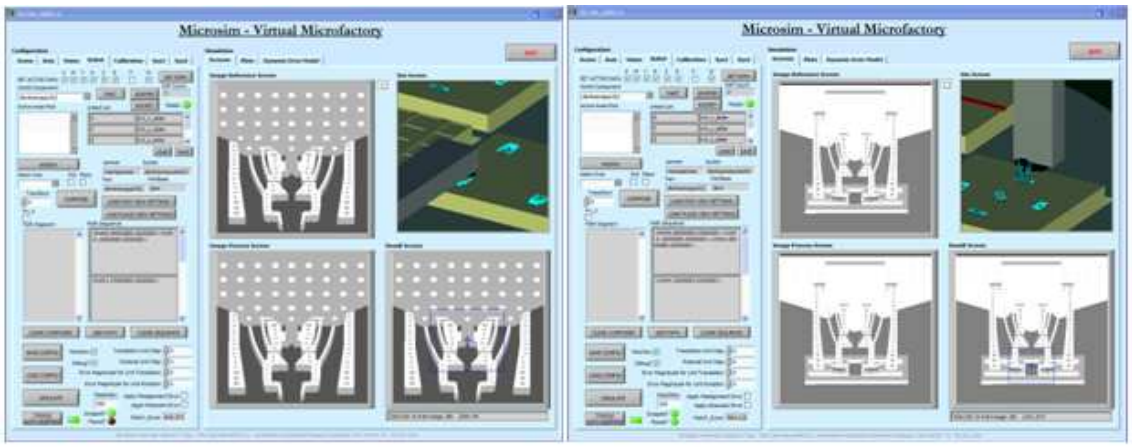

Figure 4.19. Microassembly in virtual reality.

Using this tool, the motion path is tested for multiple iterations to ensure high yield in assembly. Additionally the process time is estimated by including the velocity of the robotic stages and time in closed loop control part.

Figure 4.20 shows a typical result set from repeated execution of a specific microassembly process according to a proposed path given by *'PPSA'*. In figure 4.20 the black line represents the results from execution of the hybrid controller. the green and red lines correspond to pure open loop control and pure closed loop control respectively and are evaluated for a comparative analysis. In the first part of the figure 4.20 the total error unit incurred in the microassembly process is shown for the three cases and in the second part of the figure the time units are shown.

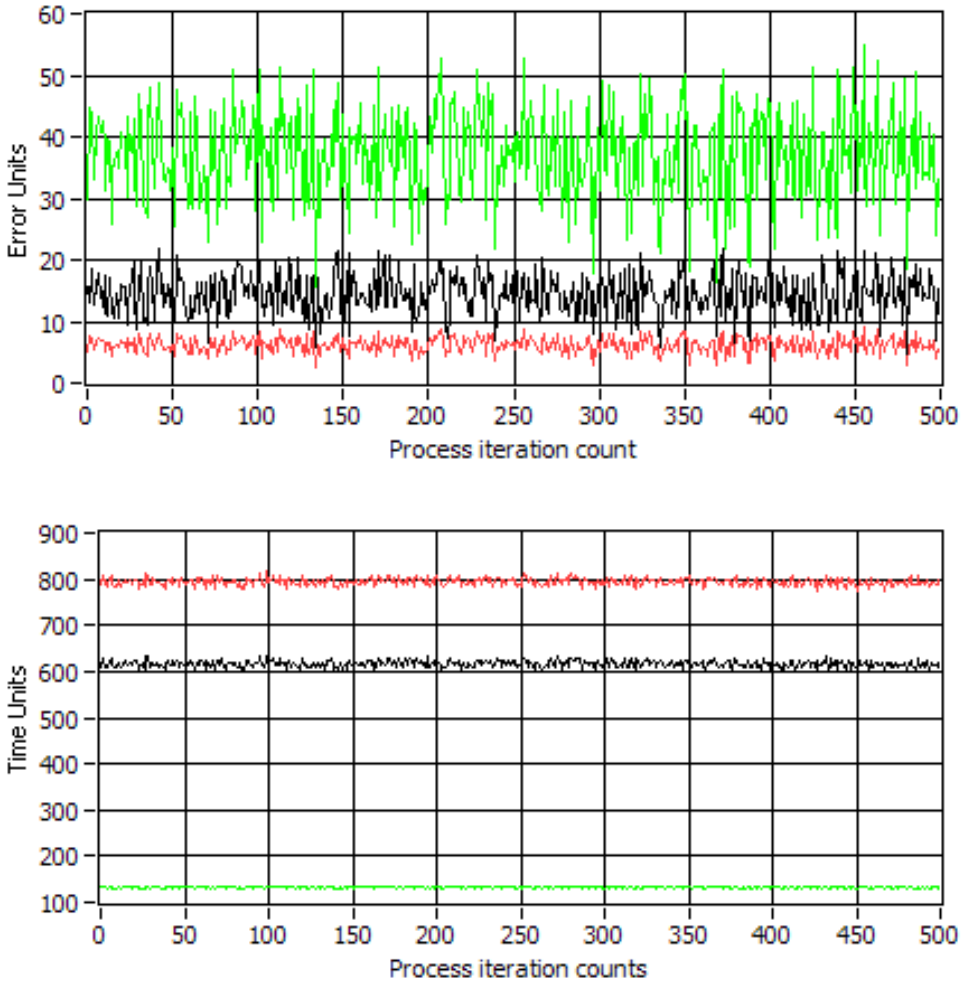

Figure 4.20. Simulation results from repeated microassembly in virtual 3D.

In the above case, if a maximum error unit of 20 or less is assumed to be success then the yield in pure open loop control case is very less i.e. nearly 2% to 3%. The closed loop control of course can provide a yield of 99.9%, however the time units consumed is very high as seen from the second part of the figure 4.20. The hybrid control structure on the other hand is found to provide a yield of 95%. The time units consumed is also less by 25% as compared to the closed loop control. Moreover the hybrid controller used only 2 sensors in contrast to 4 for the closed loop control case.

If the cost functions i.e. the yield, throughput and cost is acceptable by the user then this particular scheme is passed to be executed on the actual microassembly system. However, if the cost functions are found to be too low or unacceptable then the planning stage is repeated to come up with a better solution.

4.4.3 Calibration of workcell

Calibration is required for closed loop servoing of manipulator as well as calibrated open loop control. For this reason, if required for a specific subtask as estimated by the path planning stage, necessary calibrations are carried out to obtain the transformation matrix *'Jacobian'* for the corresponding manipulator. The following scheme is implemented for calibration of the μ^3 robots.

At constant orientation angles relative to the substrate (typically perpendicular), the end-effector of M_1 or M_2 is used to point to reference points and its encoder joint coordinates are recorded. Using this data, the transformation of the encoder coordinate corresponding to any point in the die coordinate is calculated as:

$$
\begin{aligned}
R &= R_1 + (R_2 - R_1)\left(\frac{p - p_1}{p_2 - p_1}\right) + \left(R_3 - \hat{R}\right)\left(\frac{q - q_1}{q_3 - q_1}\right), \\
\hat{R} &= R_1 + (R_2 - R_1)\left(\frac{p_3 - p_1}{p_2 - p_1}\right),
\end{aligned}
\tag{4.12}
$$

where:

- P_1, P_2, and P_3 are fiducials on the MEMS die, with die coordinates (p_1, q_1), (p_2, q_2) and (p_3, q_3) respectively. These values can be expressed in pixels from the CCD, or directly, in die layout coordinates, if fabrication tolerances can be neglected.
- P is an arbitrary point of interest with die coordinates (p, q). This is will later become the target assembly site.

- R_1, R_2, and R_3 are encoder vectors, corresponding to end-effector joints when the gripper tip is at locations P_1, P_2, and P_3. For a 4 DOF M_1 robot, these will be 4 dimensional vectors $[Enc_X, Enc_Y, EncZ, Enc_\theta]$.
- R is the associated M_1 joint coordinate vector when the tip is pointing to P.

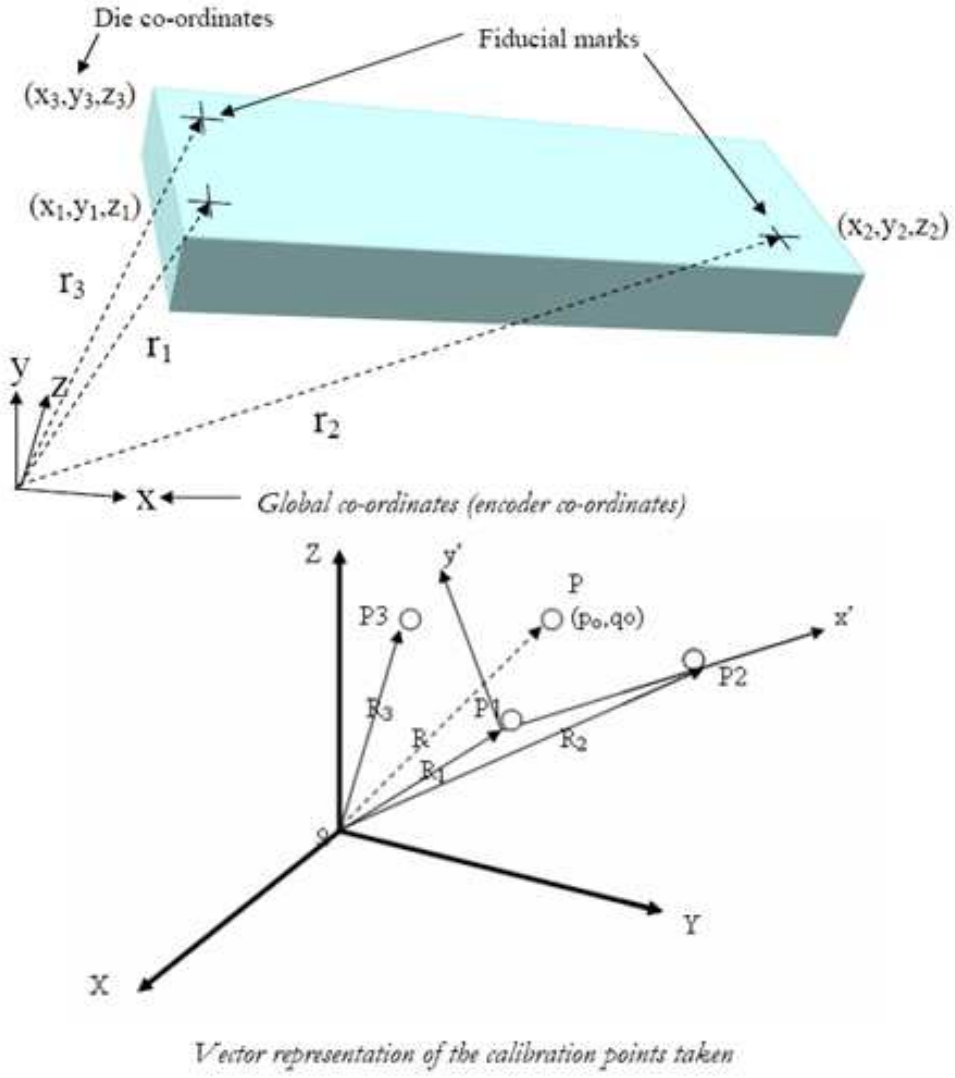

Figure 4.21. Rotated coordinate frames attached to M_1 and M_3 manipulators and calibration of M_1 end-effector using a 3- point teaching method.

In the following experiment, values for P_1, P_2, P_3 and P can be obtained directly from the MEMS design layout of the die, while values of R_1, R_2, and R_3 are read from the M_1 encoders. With knowledge of R, we can simply servo the joint axes of robot M_1 to position the end-effector of M_1 to pick up a part on the MEMS die at position P in die coordinates. Depending on the measurement error during the teaching phase, the inverse kinematics calculations result in a given accuracy for M_1.

4.4.4 Online execution of hybrid controller and event handling

Based on the estimated control scheme the assembly tasks are carried out. During assembly there are several dynamic errors which may occur randomly. These include sticking of microparts to the substrate, vibration in workcell, change in ambient lighting and so on. These may affect the pre-programmed hybrid controller execution plan adversely. For example; stiction may cause a micropart to remain attached to the substrate so rigidly that it may not be picked up by the microgripper. In such a case, it becomes useless to carry out the placement task for a failed pickup. Therefore event handling is very important in microassembly.

In order to incorporate event handling, the hybrid controller uses a discrete reckoning scheme in which at each observable transit points the desired pose of the microparts are accounted for. If, for some reason, the micropart is not located at a transit point then further execution of the assembly subtasks is discarded. The previous step is reversed and the complexity indices are re-computed. The reversal of the previous step is assumed to be possible based on the fact that the robot repeatability is better than its accuracy, (according to the definitions given in the previous chapter). If the previous transit point is not observable then one more back step is taken until an observable transit point is reached.

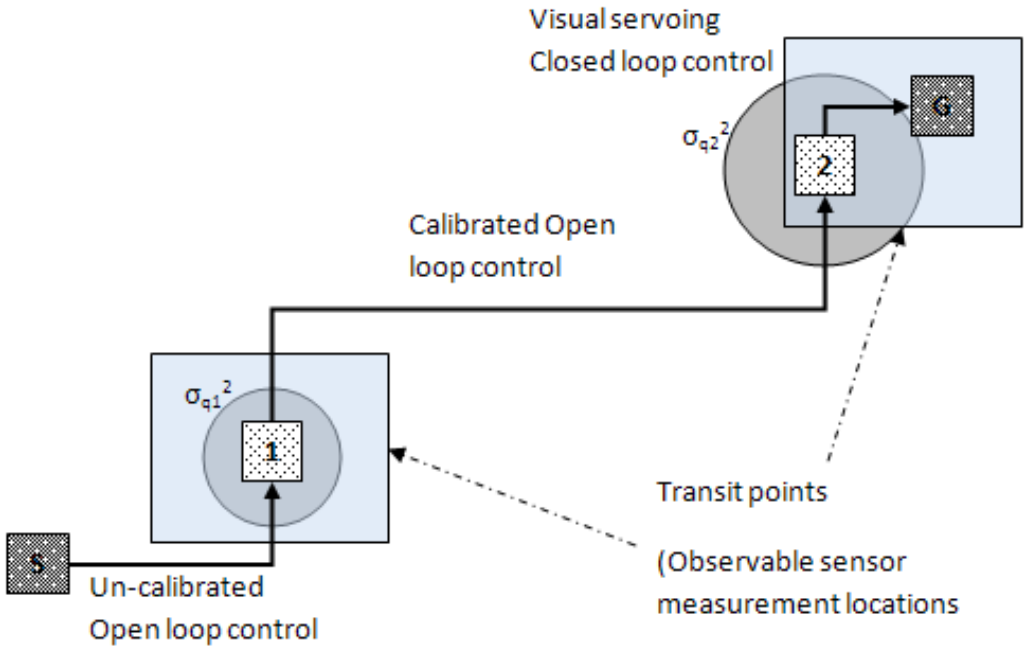

Figure 4.22. Discrete transit point based online event handling.

The process flow, both offline and online, for the precision adjusted hybrid controller implementation is shown in figure 4.23.

4.5 Experimentation in a microassembly workcell

To verify the efficiency of the hybrid controller, in this section, a real time microassembly scenario will be considered.

4.5.1 Scenario description

In this assembly scenario (see figure 4.24), a 1cm x 1cm silicon die holding several compliant micro parts is moved inplane by a robot with three degrees of freedom; two translational and one rotational for x, y and θ respectively. Due to inertia and other parameters, these three degrees of freedom have different accuracies i.e. for unit displacement of 1000μm, the x degree of freedom has accuracy of 0.5μm,

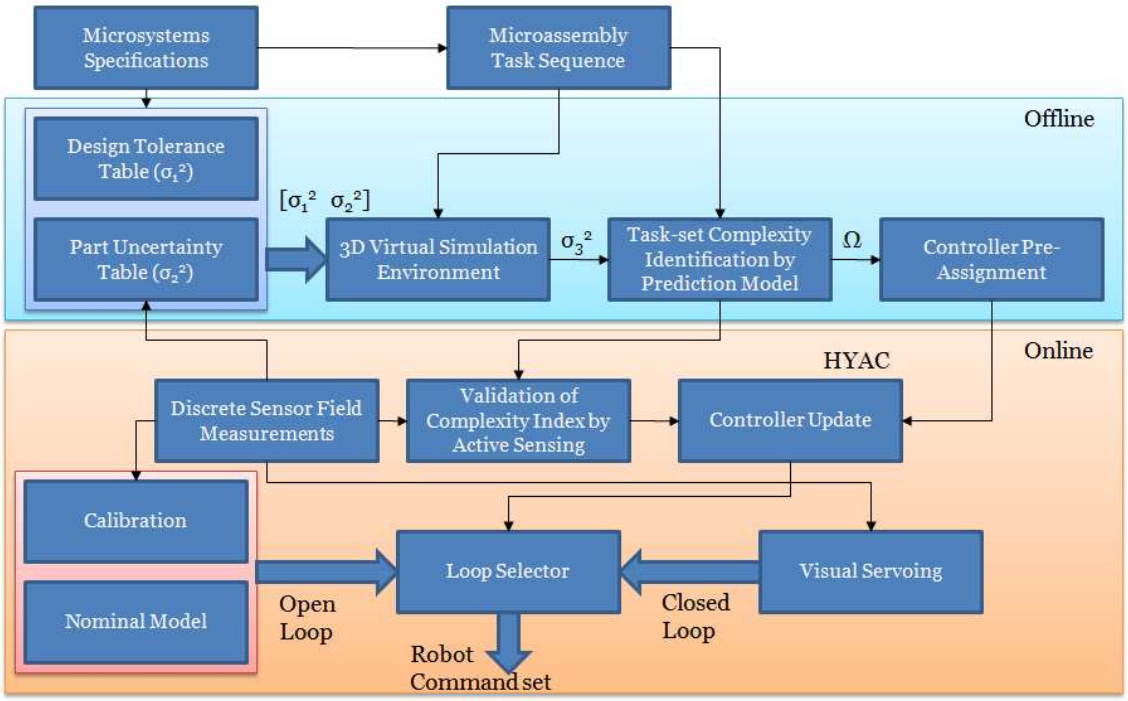

Figure 4.23. Process flow for automated microassembly with precision adjusted hybrid controller.

the y degree of freedom has accuracy of 0.8μm, and the θ degree of freedom has accuracy of 0.02^o. The assembly task is to pick a part from the parts' die using a microjammer and place it on a destination point socket. The sockets designed to be tolerable up to 3μm in x and y and 0.25^o in θ. The microjammer is held by a second robot independent of the first one. Microscopic vision is used as sensor to locate the position of a particular micro object.

In case of microassembly the parts are very small and hence a high magnification vision is required to locate the micro object with higher accuracy. However with higher magnification, generally the field of view (FoV) gets smaller. For example: in this particular case, with a 5X magnification, the field of view (FoV) is 1.536mm x 1.152mm where 1 pixel in the image accounts for 2.4 microns. Therefore servoing with one vision setting is not possible for a assembly motion path larger than the FoV.

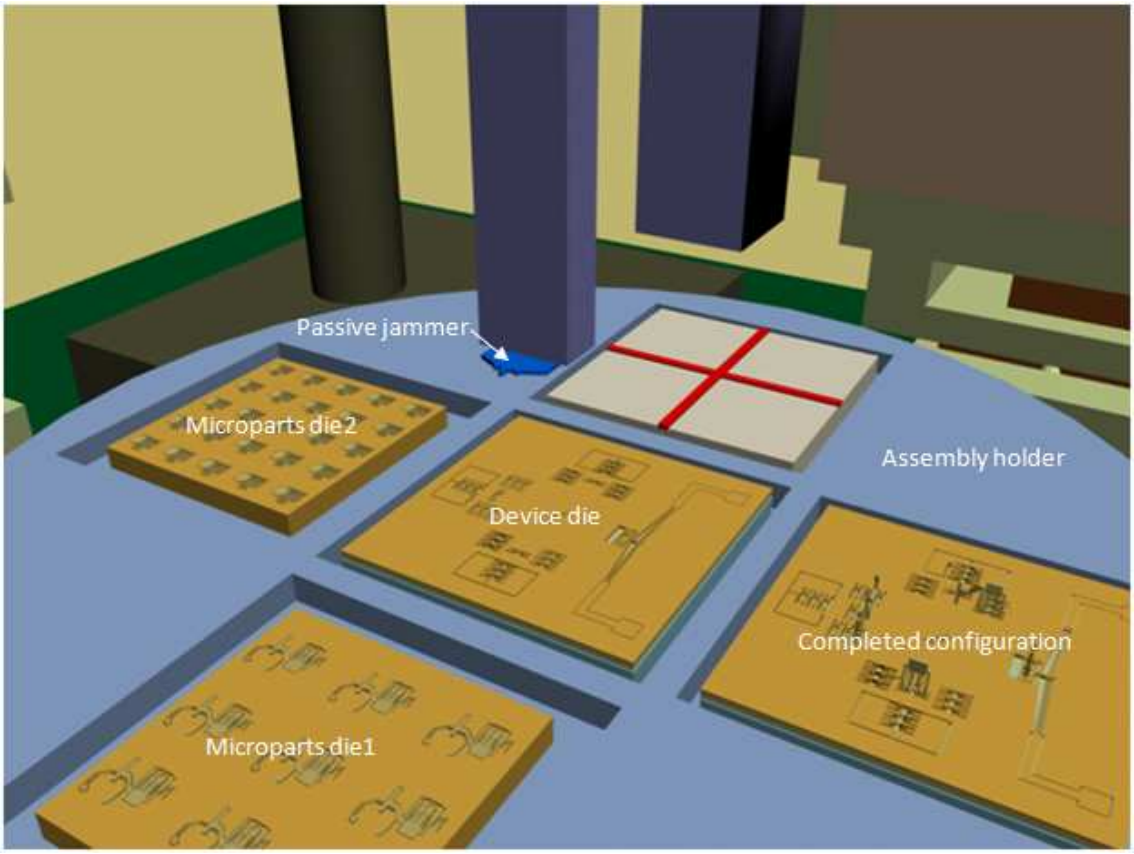

Figure 4.24. A typical assembly scenario for complex microassembly.

Therefore either multiple vision sensors with variable FoV are needed or a combination of coarse and fine positioning schemes required to be employed where the part is roughly positioned closed to the target using robot controls and then it is precisely moved on to the target location using servo control. In either case, however, there are some associated disadvantages. In the first case, i.e. with multiple sensors, a large number of stationary sensors are needed to cover the entire work volume or some mobile sensors are needed, controlling the motion of which further adds to the misalignment overhead. On the other hand, in the second case, where coarse and fine alignment steps are followed, in some cases, depending on the precision (RRA) of the

robot, the coarse positioning might not be good enough to provide a starting location for the fine positioning.

4.5.2 Optimization of servoing based on precision requirement and time consumption

A typical assembly of a micropart can be divided into three sections; (a) pickup 'Ta', (b) mobilization 'Tb', and (c) placement 'Tc'. Ta and Tc are carried out by the robot holding micro jammer which is essentially a displacement vector along one degree of freedom. Whereas, Tb comprises of the robot motion path carrying the parts' die.

If $Tb = 2mm$ along a single degree of translational freedom then with the robot accuracy given in the previous subsection, we can tell that the robot will be able to position the part within 1μm error from the socket. Thus we get, $\sigma_1^2 = (3\mu m, 0.25^o)$, $\sigma_3^2 = (1\mu m, 0^o)$. The value for σ_2^2 was determined using microscope and given as: $\sigma_2^2 = (0.5\mu m, 0.1^o)$. So we find that $\sigma_1^2 > \sigma_2^2 + \sigma_3^2$. So the assembly in this case can be done only with robot control commands without any need of servoing.

However in the case of given assembly task, the assembly socket is located on a second die as shown in the figure 4.24. The relation between the positions of the parts' die and the assembly die is not accurately known.

A comparative analysis regarding different accuracy requirements and corresponding performance of different alignment method has been carried out. These different cases are described as follows:

1. case 1: 3 point calibration
2. case 2: 9 point calibration
3. case 3: 27 point calibration
4. case 4: no calibration, estimated model
5. case 5: no servoing, only calibration data used to move robot

Three types of accuracy requirements are tested for with increasing strictness. The time taken in each case to servo the part successfully to the socket is shown in the figure 4.25.

Time consumption during servoing based on different methods (in seconds)

Alignment Method		Time Taken To Servo For Required Accuracy					Calibration Time
		2μm, 0.5deg	2μm, 0.25deg	1μm, 0.1deg			
				α=10	α=100	α=10,100	
Estimation based servo	No calibration	183.828	257.844	∞	∞	∞	0
Calibration based servo	3 point calibration	130.375	145.562	∞	∞	∞	13.0625
	9 point calibration	84.7344	145.203	∞	1656.25	182.531	48.2187
	27 point calibration	131.766	142.703	200.547	1462.36	173.75	163.234
No servo, Only calibration data used	3 point calibration	0.504	Not reached	Not reached	Not reached	Not reached	13.0625
	9 point calibration	0.508	Not reached	Not reached	Not reached	Not reached	48.2187
	27 point calibration	0.502	0.502	Not reached	Not reached	Not reached	163.234

Figure 4.25. Time consumption in different method of servoing with variation in required accuracy.

The error propagation plots for different cases mentioned in the figure 4.25 are shown in figure 4.26.

Figure 4.27 shows the time consumed in each cases.

And figure 4.28 shows the time consumed in each case including the time for calibration.

From the experiment the following observations are made:

- For low accuracy requirements an estimated model can be used for servoing. Calibration gives better performance in servoing but also takes more time to calibrate.

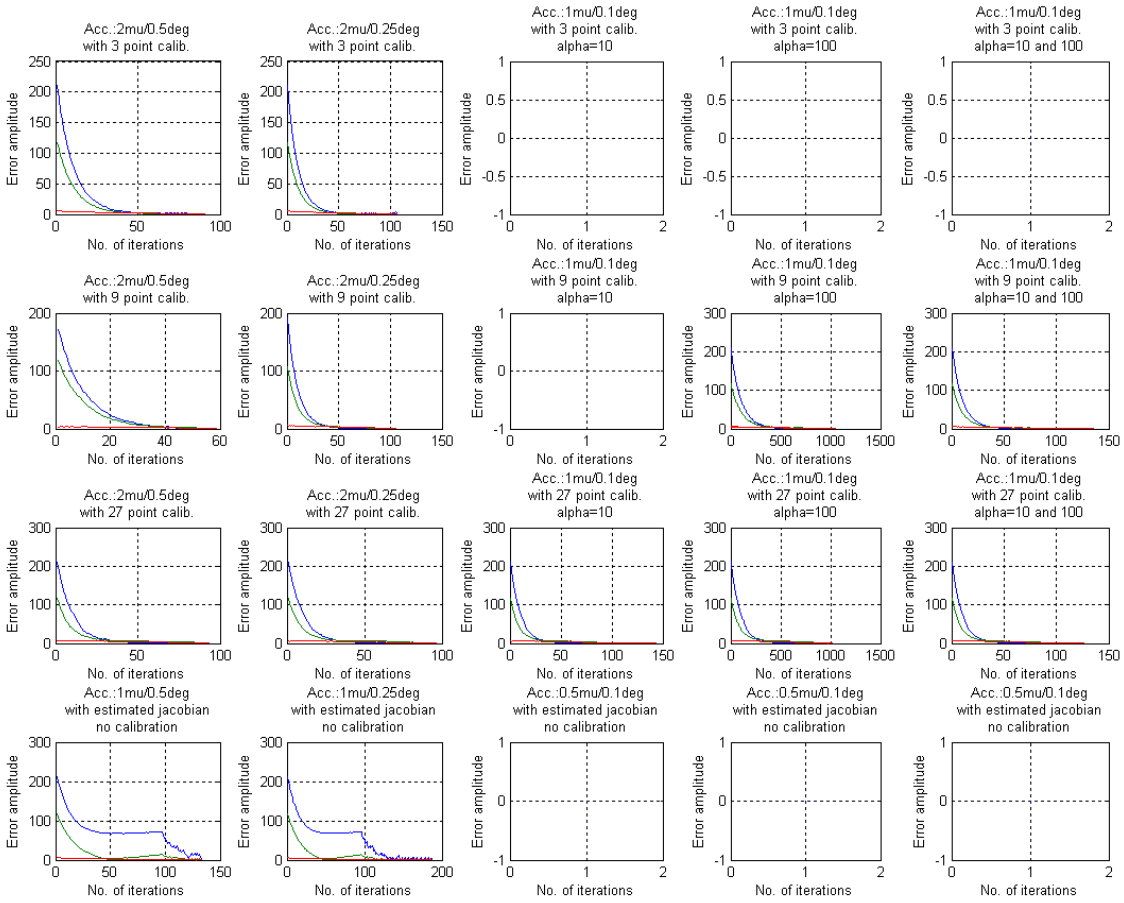

Figure 4.26. Error propagation during servoing for different cases.

- Including more points for calibration add to the time but gives better results for higher accuracy requirements.
- For extremely stringent accuracy requirements, for example 1μm, 0.1^o, it has been observed that the 9-point calibration based servoing could achieve success only when the servoing gain was increased 10 fold i.e. the servoing is done at a much slower velocity. This help in avoiding overshooting.
- For the same accuracy requirement, as above, a 27-point calibration could achieve success with much higher velocity.

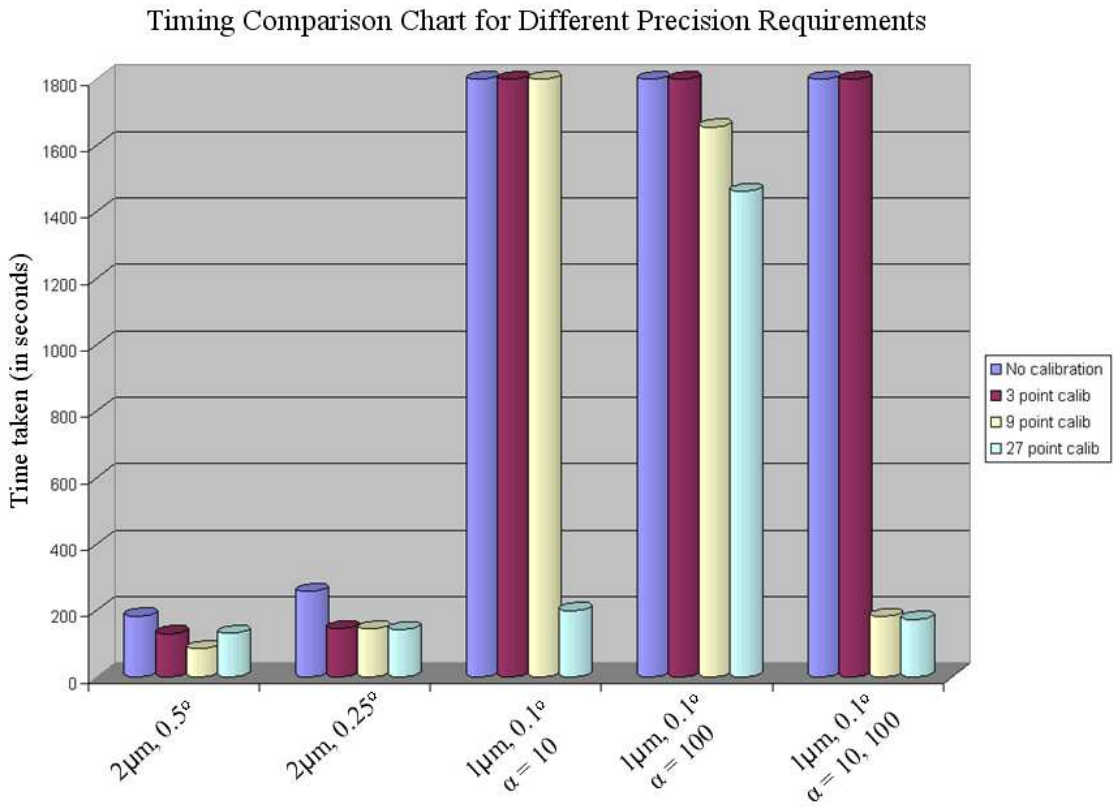

Figure 4.27. Time consumed in servoing for different cases (without including calibration time).

- When a dynamic velocity changing scheme is adopted (i.e. the servoing is done at a higher velocity when the part is far from the socket and done at a lower velocity when the part is close to the socket), it has been observed that both 9-point calibration and 27-point calibration gave similar performance (see figure 4.27). But when we add the calibration time to the cases then the 9-point calibration scheme with dynamic velocity adjustment gave 30 percent better performance on time in comparison to the 27-point calibration (see figure 4.28).

Therefore, it can be inferred that for highly stringent accuracy requirements, an optimized servoing with less number of point based calibration model and dynamic

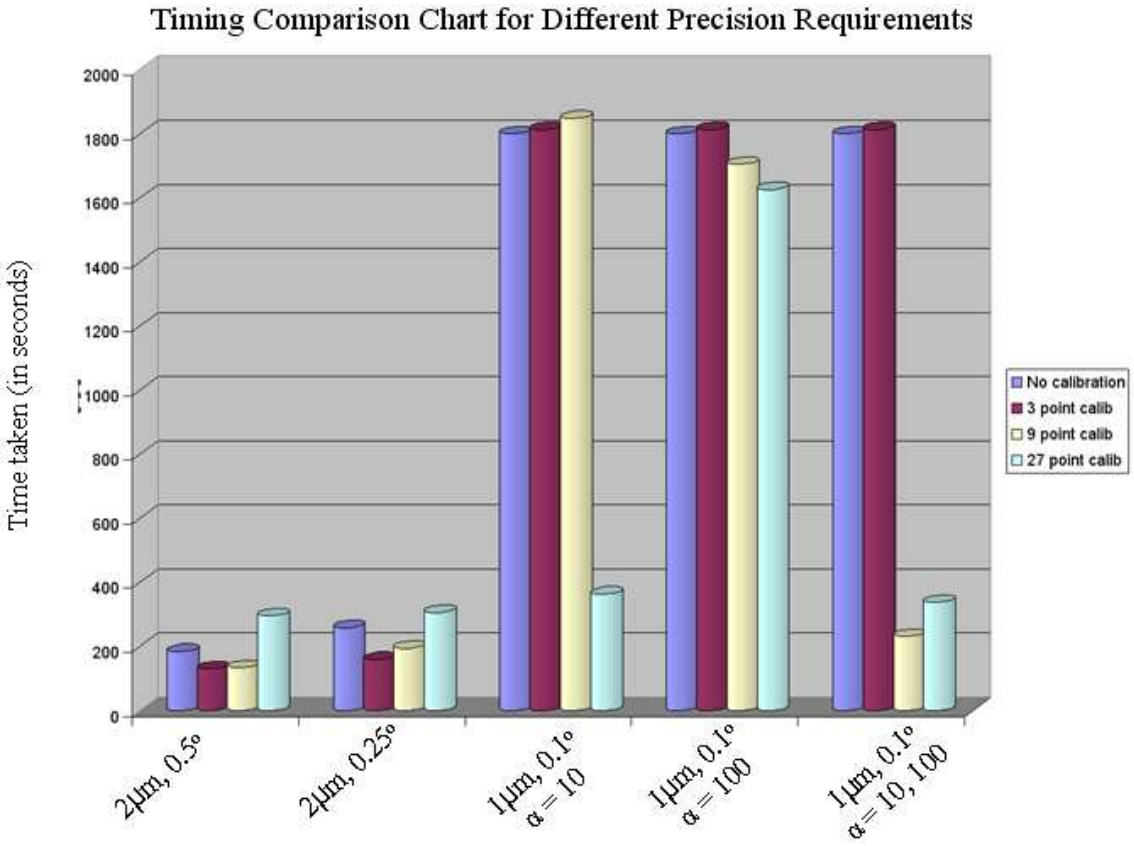

Figure 4.28. Time consumed in servoing and calibration for different cases (including calibration time).

velocity allocation scheme can provide the necessary and sufficient precision to achieve successful alignment.

4.5.3 Optimization of microassembly based on yield, time and cost

In a complex microassembly scenario several micro parts need to be moved over several motion paths to bring out the final microsystem into its final desired configuration. Depending upon the complexity of the motion path a specific subtask of the microassembly process can be carried out through closed loop or open loop.

In a typical case of study an assembly process with 4 sub tasks is considered. 10 repetitions for each of the three control structures i.e. precision hybrid control, closed

loop control and lastly open loop control has been carried out. Figure 4.29 shows a comparison plot for time consumed among different control structures. Figure 4.30 shows the achieved accuracy for each control structure. From the plots it has been observed that the precision adjusted hybrid controller gives a 35 percent improvement over the open loop control. At the same time the precision adjusted hybrid controller saves up to 60 percent of time in comparison to the pure closed loop controller. On an average the hybrid controller has taken 294 seconds for the assembly process and has been able to achieve an accuracy of 2.2 microns which is better than the allowable tolerance of 3 microns in this specific microassembly. Therefore the proposed hybrid controller acts as an good trade-off between the two extreme control structures.

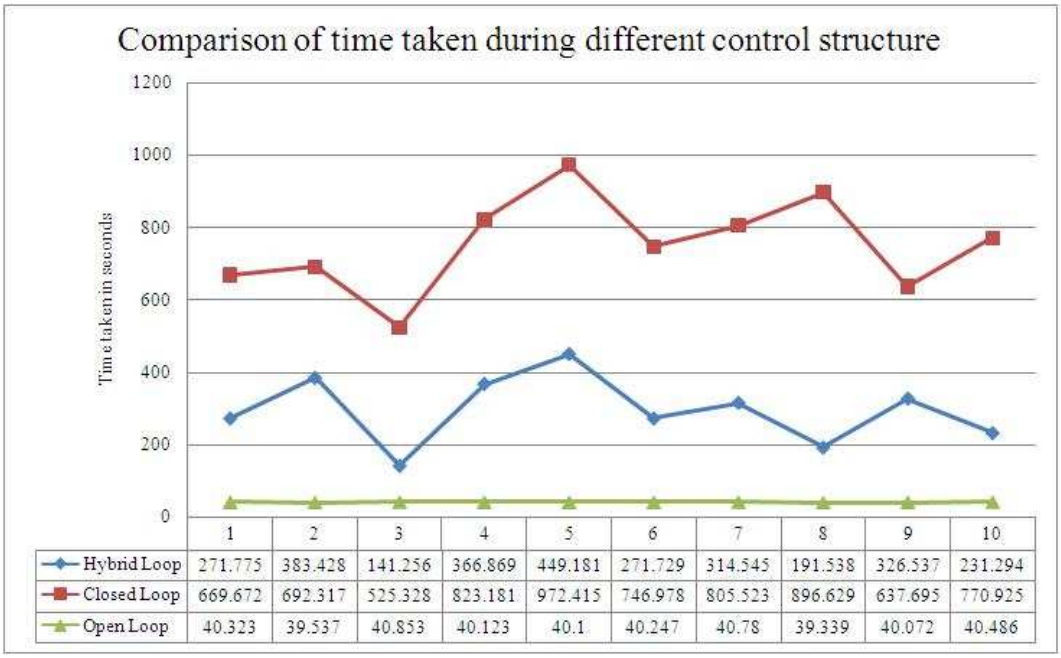

	1	2	3	4	5	6	7	8	9	10
Hybrid Loop	271.775	383.428	141.256	366.869	449.181	271.729	314.545	191.538	326.537	231.294
Closed Loop	669.672	692.317	525.328	823.181	972.415	746.978	805.523	896.629	637.695	770.925
Open Loop	40.323	39.537	40.853	40.123	40.1	40.247	40.78	39.339	40.072	40.486

Figure 4.29. Time taken during hybrid loop, closed loop and open loop control.

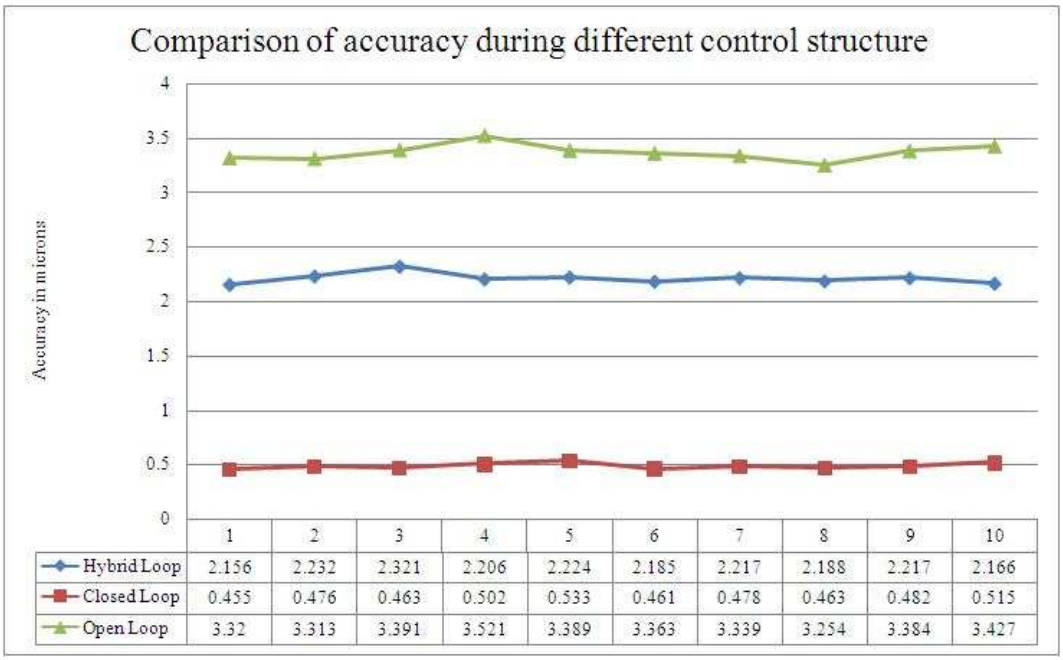

	1	2	3	4	5	6	7	8	9	10
Hybrid Loop	2.156	2.232	2.321	2.206	2.224	2.185	2.217	2.188	2.217	2.166
Closed Loop	0.455	0.476	0.463	0.502	0.533	0.461	0.478	0.463	0.482	0.515
Open Loop	3.32	3.313	3.391	3.521	3.389	3.363	3.339	3.254	3.384	3.427

Figure 4.30. Accuracy achieved during hybrid loop, closed loop and open loop control.

CHAPTER 5

MICROSPECTROMETER: A CASE STUDY FOR MANUFACTURING OF A COMPLEX MOEMS

Integrating optics with MEMS presents numerous challenges in assembly and joining of heterogeneous components, stringent alignment of parts, packaging of the device to protect it, etc. Microspectrometers are examples of micro-opto-electro-mechanical systems (MOEMS) devices where these issues play a significant role to the performance of the device. The motivation behind miniaturization of the spectrometer is strong, because traditional spectrometers are table-top instruments, and they are generally too large, and too costly to be ported outside of lab environments. Micro-Electro-Mechanical-Systems (MEMS) technology combined with microassembly offers promising possibilities to achieve compact and cost-effective miniaturization in such instruments. In this research, a fiber-coupled Fourier-Transform microspectrometer has been studied and prototyped. The microspectrometer is constructed using 3D hybrid microassembly and targeting wavelengths in the visible and NIR spectra. Modular micro scale parts have been used, including minimum energy compliant MEMS fasteners to configure a die-sized microoptical bench. Light coupling, miniature electronics and power are included in a spectrometer package. In order to achieve the required precision on the microoptical bench automated assembly of microcomponents has been employed. In this chapter a systematic two-step assembly and alignment scheme (coarse and fine) using a novel spot Jacobian algorithm has been presented including details related to design, tolerance analysis, calibration, microassembly and visual servoing techniques as well as spectrum data recovery for a completed prototype.

5.1 Related research on MOEMS

Spectrometry has long been used for measuring chemical compositions and purity of materials in industrial, medical and environmental applications by detecting material dependent absorption of wavelength. Traditional spectrometers, however, are table-top instruments, and they are generally too large, and too costly to be ported outside of lab environments. Micro-Electro-Mechanical-Systems (MEMS) technology offers promising possibilities to build compact and cost-effective miniature instruments, including spectrometers. MOEMS are widely used in telecommunication industry, in devices such as optical switches [91, 92], the Texas Instruments (TI) DLP [93], tunable vertical-cavity surface-emitting laser systems (VCSEL) [94, 95], microbolometers used as detector instruments in thermal cameras [96] etc.

5.2 Releated work on miniaturization of spectrometer

Recently, several miniaturized spectrometers using MEMS technology have been proposed, and some of them have become commercially available, such as miniature fiber optics spectrometer from Ocean Optics [97], which uses replaceable slits of different width and as many as 14 gratings to scan over the range from UV to near IR. Another example of on-going work is the miniaturized spectrometer at the University of Freiburg, Institute of Micro System Technology (IMTEK) [98], which has been manufactured using LIGA parts configured as a Michelson interferometer. The optical bench and the actuator have a height of 380μm, with a chip dimension of 11.5x9.4 mm^2. Kung L. et al. have shown a standing wave transform spectrometer [99] which uses an electrostatically actuated MEMS mirror with on-resonance displacement of up to 65μm, a thin-film photo-detector, and an electrical back plane for actuating the mirror. Fraunhofer Institute for Photonic Microsystems is developing Fourier

Transform spectrometers for measurements from near IR to mid IR range [100, 101]. The complete devices are around 10cm x 20cm in size, and use in-plane electrostatic combs which are vacuum-packaged. Work from Lammel et al., is focusing on the development of a microspectrometer based on a tunable interference filter for infrared or visible light which is fabricated by a new porous silicon technology [102]. Two thermal bimorph micro-actuators tilt this plate by up to 90^o. Ataman and Ure have demonstrated a Fourier transform spectrometer implemented with resonant mode out-of-plane comb actuators which are used as movable diffraction gratings [103].

For diffraction grating spectrometers, one major drawback is reduced spectral range and fixed resolution. If a wider range spectrum needs to be analyzed, then a different grating is needed. On the other hand, for scanning mirror microspectrometers, the range and resolution can be adjusted using a longer scanning stroke.

5.3 Design and working principle of ARRI's microspectrometer

5.3.1 Working principle

ARRI's microspectrometer is based on a *Michelson interferometry principle*. This device essentially divides a beam of radiation into two paths and then recombines them to create interference; see fig. 5.1. The variation of intensity emerging from the interferometer is measured as a function of the path difference by a detector [104, 105]. The initial distances of the movable mirror and the fixed mirror from the center of the beamsplitter are d_1 and d_2, which may be different due to fabrication errors and/or offset in beamsplitter positioning. The movable mirror scanning motion has a maximum displacement x. Hence the overall path difference between the two halves of the light beam is $\delta = 2[|d_1 - d_2| + x]$, also known as the retardation.

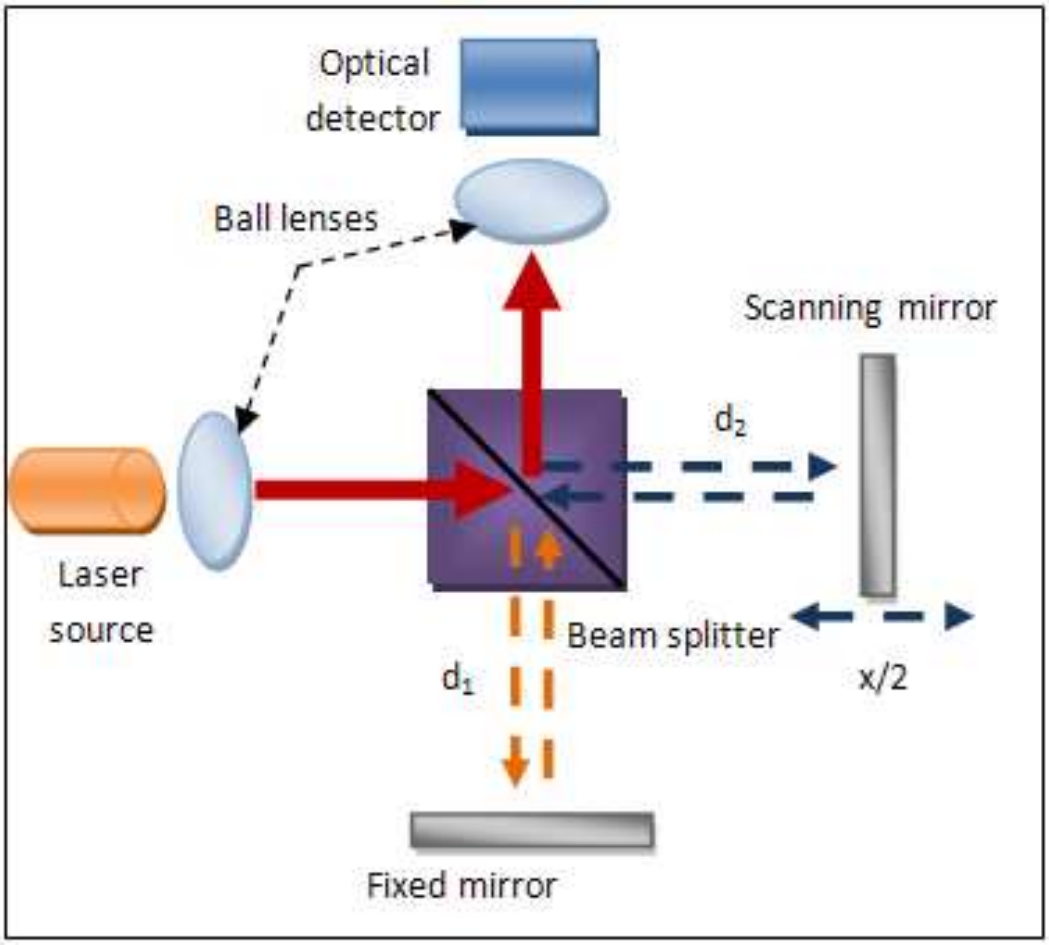

Figure 5.1. Working principle of microspectrometer.

Assuming the intensity or power of the source $I(\lambda)$, is a function of wavelength λ, the intensity of the beam at the detector is given as a function of the retardation as follows:

$$I'(\delta) = \frac{1}{2} I(\lambda) \left(1 + cos 2\pi \frac{\delta}{\lambda}\right). \tag{5.1}$$

The intensity $I(\delta)$ is composed of a constant DC component $\frac{1}{2}I(\lambda)$ and a modulated AC component $\frac{1}{2}I(\lambda)cos2\pi\lambda^{-1}\delta$. This AC component is an interferogram represented as:

$$S(\delta) = B(\lambda) cos 2\pi \lambda^{-1} \delta, \tag{5.2}$$

where $B(\lambda)$ is the intensity of the source at a wavelength λ as modified by the device properties of the components such as beamsplitter, collimator etc. (ideally $B(\lambda) = I(\lambda)$. Equation 5.2 represents a cosine Fourier Transform of $B(\lambda)$, therefore the spectrum can be recovered by computing the cosine Fourier Transform of $S(\delta)$. Assuming $\lambda^{-1} = \nu$ to be the wave number of the source, the spectrum can be represented as:

$$B(\nu) = \int_{-\infty}^{+\infty} S(\delta) \left(cos 2\pi \nu \delta\right) d\delta = 2 \int_{0}^{+\infty} S(\delta) \left(cos 2\pi \nu \delta\right) d\delta. \tag{5.3}$$

Although equation 5.3 suggests that it is theoretically possible to obtain the complete spectrum with infinitely high resolution by scanning the movable mirror over infinitely long distance, in practice the scanning length, i.e. δ, is limited by the physical constraints of the scanning mechanism. Thus the spectral resolution depends on the maximum retardation of the interferometer. By restricting the maximum retardation of the interferometer to ζ nm we effectively multiply the complete interferogram by a truncation boxcar function $D(\zeta)$. Hence the spectrum for a finite resolution microspectrometer is:

$$B(\nu) = \int_{-\infty}^{+\infty} S(\delta) D(\delta) \left(cos 2\pi \nu \delta\right) d\delta. \tag{5.4}$$

The Fourier Transform of $D(\delta)$ is:

$$f\left(\tilde{\nu}\right) = 2\zeta \frac{sin 2\pi \tilde{\nu} \zeta}{2\pi \tilde{\nu} \zeta} = 2\zeta sinc(2\pi \tilde{\nu} \zeta). \tag{5.5}$$

The Fourier Transform of $S(\delta)$ convolved with f is used to obtain the spectrum $B(\lambda)$. Finally, the resulting spectral resolution of the instrument is related to the location of the second lobe of the window function f, $\delta\nu = \frac{1}{2}\zeta$, or $\delta\lambda = \frac{\lambda^2}{2\zeta}$.

5.3.2 Design

The microspectrometer prototype was constructed on a 1 cm $\times$ 1 cm SOI die, and Figure 5.2 shows a 3D rendering of its micro optical bench. The path distance between the first collimator and the MEMS mirror in Figure 5.2 is 5mm.

The scanning and fixed micromirrors, and their corresponding substrate sockets for snap-fastening, are identical. The snap-lock mechanisms provide a little tolerance for minor misalignments in mirror parts by gradually self-aligning the legs as they are inserted into the socket. The socket for the fixed mirror is tied to the SOI handle and device layers, while the socket for the scanning mirror is released and free to move. Thus, assembling the scanning mirror on the movable socket requires a higher degree of alignment precision.. The movable socket provides additional self-alignment as it tends to slip in the direction of misalignment of the mirror part. However, the electro-thermal actuator and moveable socket offers a high degree of in-plane and out-of-plane compliance and does not break easily.

A MEMS thermal Chevron actuator, shown in 5.3, is used to provide the necessary scanning mobility for the mirror.

The MEMS die layout is shown in 5.4.

The mirrors are made of 100 micron thick *Silicon on Insulator (SOI)* wafer by *DRIE (Deep Reaction Ion Etching)*. They use compliant flexure design similar to a *Zyvex* snap-fastener so they can be assembled out of plane. The reflecting surface of the mirror is $1000 \times 800\mu m^2$ in size and is coated with gold to produce the mirror surface. In addition to MEMS mirrors, lens holders have also been designed

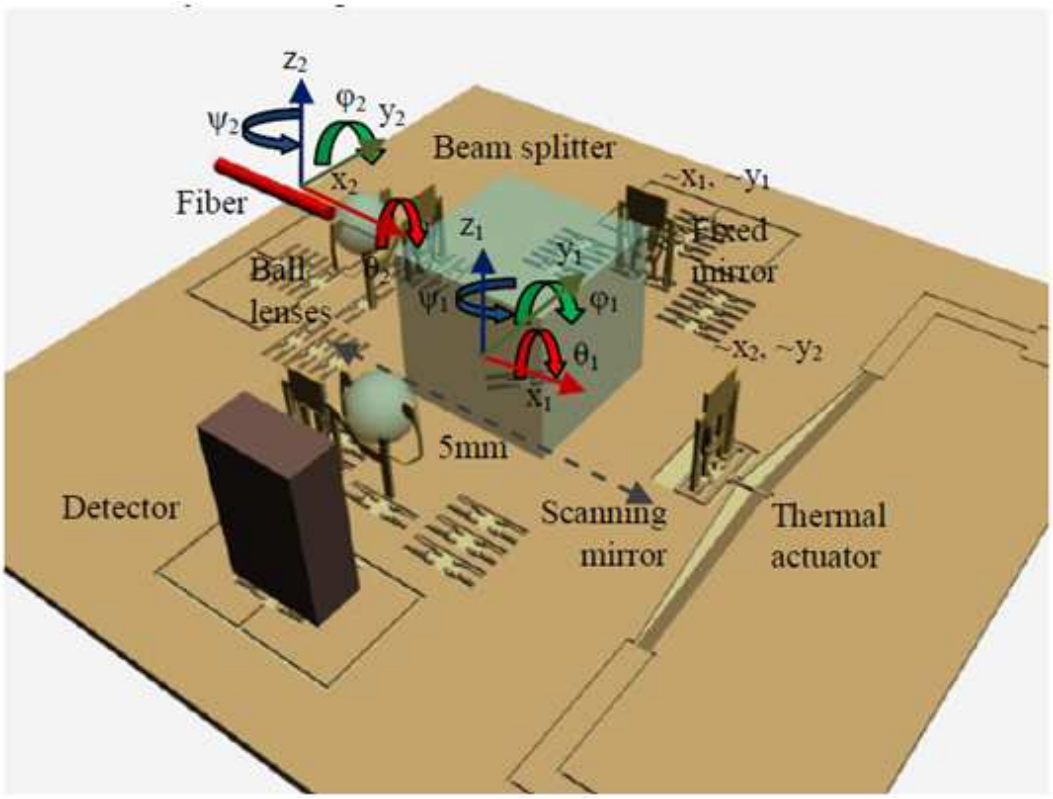

Figure 5.2. 3D rendering of the microspectrometer with the components locations.

to hold the glass spherical lenses that are used to collimate the light coming out of the fiber. Other components include a 1.3mm glass beamsplitter, a die-size detector, and optionally, a VCSEL laser source (see figure 5.5).

5.4 Tolerance analysis

To obtain the desired optical functionality of the microspectrometer it is imperative that the microcomponents be aligned within acceptable tolerance bounds. There are numerous sources of misalignment that have to be corrected during assembly including:

1. Misalignments due to fabrication errors
2. Tilts in mirrors

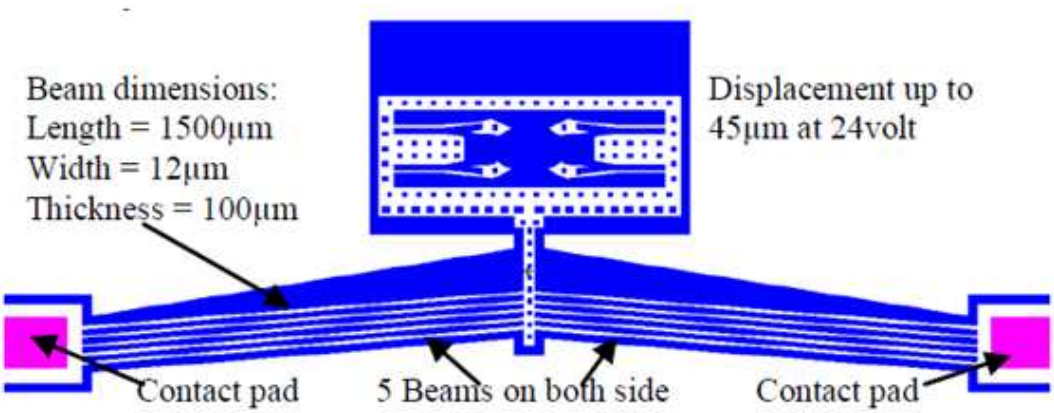

Figure 5.3. Layout of the thermal actuator for scanning mirror mechanism.

3. Misalignments in fiber position and orientation
4. Misalignments in beam splitter 6D pose.

In this section we discuss their impact on the optical performance of the FTIR microspectrometer.

The dimensional errors in a typical DRIE micromachining process are generally less than 2 μm, while sidewall profiles are accurate within 1^o. Translational microbench layout errors within this range will affect the value of the optical path difference δ, however, this value can be lumped together with the scanning mirror displacement and will not affect the recovered spectrum after the instrument is calibrated. The second source of misalignments is due to the optical coupling between the fiber and the spherical ball lens. A glass ball lens of 800μm diameter is used to collimate the laser light emerging from the optical fiber. The effective focal length of a ball lens is given by:

$$F = \frac{nd}{4(n-1)}, \tag{5.6}$$

where n is the index of refraction and d is the diameter of the ball lens. In our case, $d = 800\mu m$, and the index of refraction is $n = 1.517$, resulting in $F =$

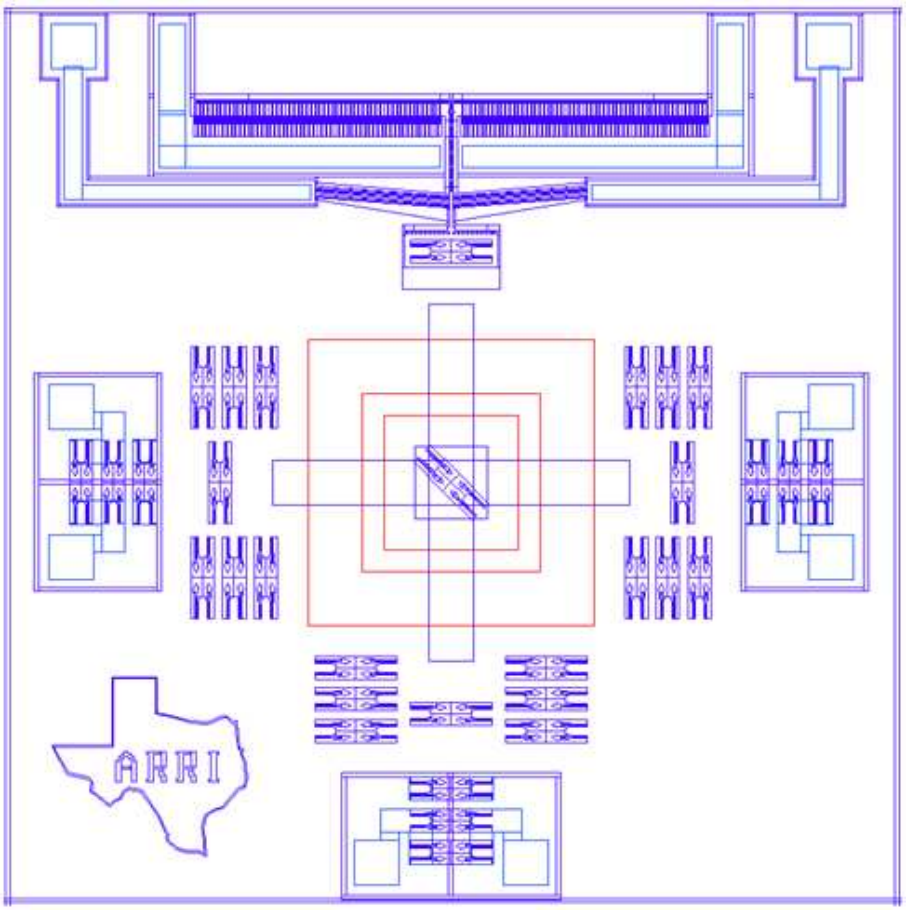

Figure 5.4. Layout of the MEMS die for microspectrometer.

586.85μm. Hence the back focal length (BFL - see Figure 5.6), or the focal distance from the surface of the ball lens where the fiber tip should ideally be to guarantee light collimation is:

$$BFL = f - (d/2) = 186.85\mu m. \tag{5.7}$$

Figure 5.6 shows the typical coupling setups for the fiber optics and the ball lens. In the figure, the fiber positioned at a, b, c, and d has misaligned coupling into the ball lens. Positions a and b show the case where the fiber tip is on the ball lens center axis, but not at the BFL. This configuration affects the spot size on the mirror

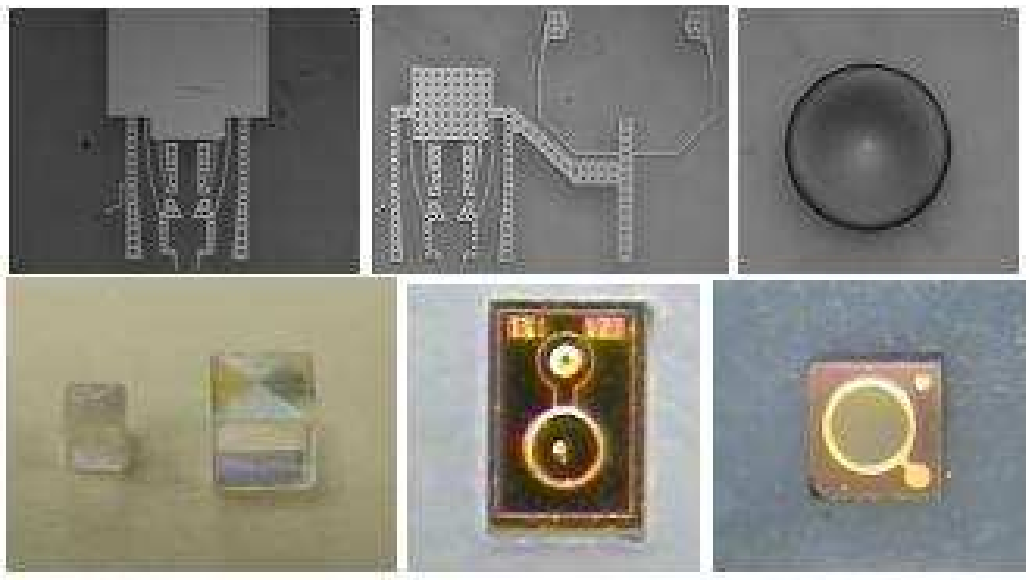

Figure 5.5. Micro-components used in FTIR microoptical bench. The dimensions are: (a) MEMS mirrors 1000μm x 800 μm, (b) Ball lens holder 1000μm x 800 μm (c) ball lenses 800 μm, (d) beamsplitter cube 1300 μm, (e) laser source 180 μm x 300 μm, and (f) detector 450 μm x 450 μm..

and the intensity of the light. Position c shows the case where the fiber is translated in a direction perpendicular to the focal axis. Position d shows the case of the more general 5 DOF fiber pig-tailing situation.

The tilt angle in mirror(s) (see figure 5.7) with respect to the device substrate is another source of misalignment which can be quantified by estimating the corresponding loss in fringe pattern due to the tilt. Assuming the tilt angle between a mirror and the substrate to be β, the increase in optical path difference Δd can be written as:

$$\Delta d = 2Dtan\beta. \tag{5.8}$$

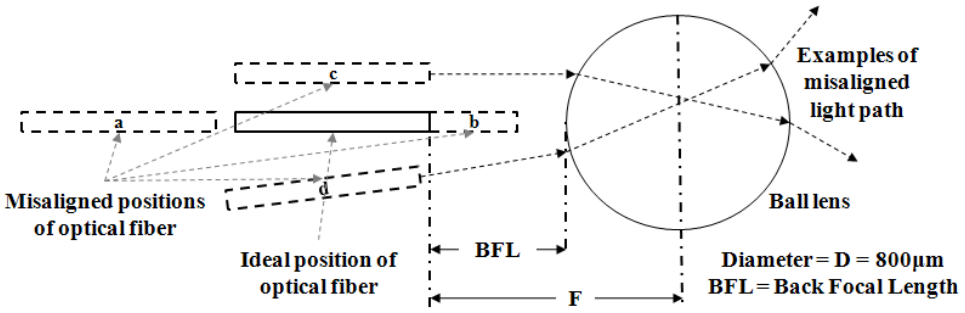

Figure 5.6. Misalignment in fiber coupling with ball lens.

Path differences above $\Delta D = 0.1\lambda$, will result in a visible deterioration of interference fringes. Hence in order to avoid any degradation of resolution we should have:

$$\beta < \frac{\lambda}{20D}, \tag{5.9}$$

where D is the diameter of the laser light spot.

For typical values of $D = 10\mu m$ (collimated light out of a fiber), and $\lambda = 650nm$ (for visible wavelength) we calculate the value of β to be less than 4 mrad or 0.2 degrees.

The last source of misalignment comes from the pose of the beamsplitter. In the assembly sequence discussed in next section, the beamsplitter is manipulated using 6 DOFs and it is the last component to be assembled onto the microbench. Three types of misalignment can occur: (i) tilts along roll, pitch or yaw angles, (ii) rotation along the vertical Z-axis, and (iii) offset in X and Y direction. Figure 5.8 shows these misalignments and their effect on the two resulting laser spots at the detector plane. In order to obtain interference fringes, the spots should be overlapping.

The X and Y translations of the beamsplitter move the semi-transparent mirror linearly and thus the two spots just shift in corresponding direction as a group as

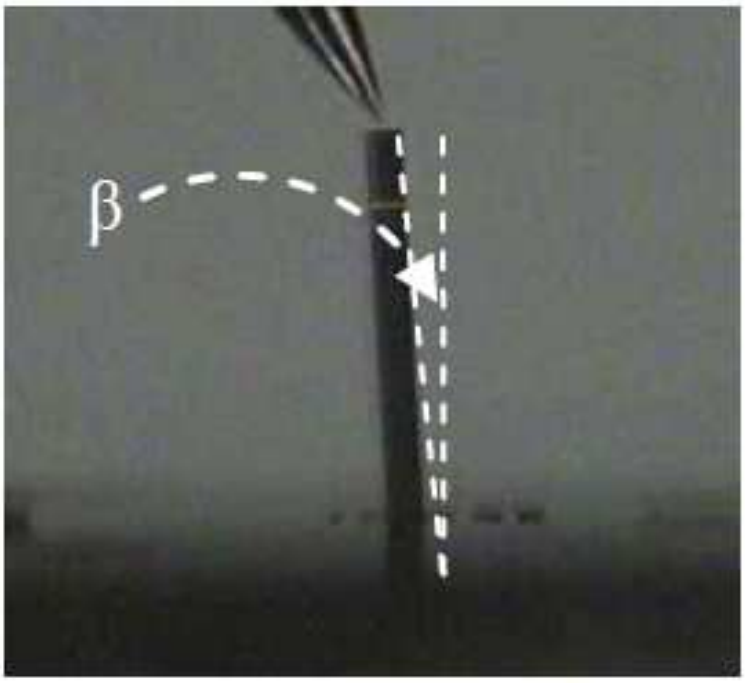

Figure 5.7. Effect of mirror tilt angle in microspectrometer.

shown in the figure. In addition to changing the spot positions, the beamsplitter misalignments also contribute to the path difference or retardation δ in the same manner as $|d_2 - d_1|$ in figure 5.1. This modifies the intensity of beam on detector as shown in equation 5.1 and the spectrum is thus changed according to equation 5.4.

As light travels twice through the beamsplitter, the overall path length is approximately L=3cm. Following a similar calculation as previous, with *'D'* replaced by *'L'*, we can see that a slight angular misalignment of the beamsplitter can cause a spot misalignment $\Delta d = 0.1\lambda$ on the detector plane, e.g. a loss of fringe contrast. Thus to avoid any degradation of resolution we should have:

$$\beta = arctan\left(\frac{\lambda}{20L}\right) = 11\mu rad. \tag{5.10}$$

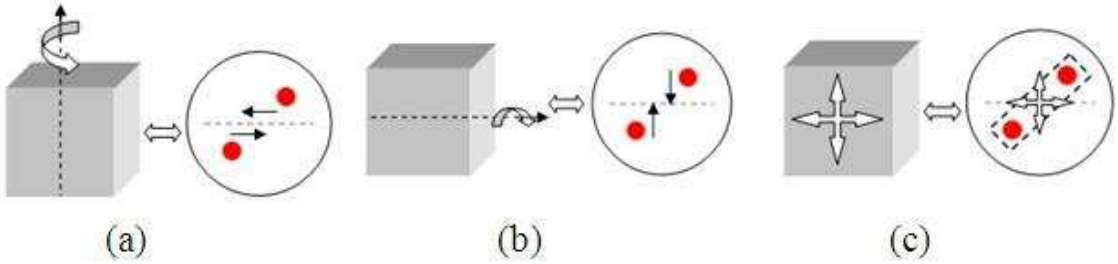

Figure 5.8. Effect of misalignment in beam splitter, (a) Effect of rotation of the beamsplitter around the Z-axis, (b) Effect of pitching of the beamsplitter around X-axis, (c) Effect of translation of beamsplitter in X and Y angles..

Therefore, the beamsplitter needs to be aligned at a much higher precision than the rest of the optical bench. Thus the following alignment strategy for the microspectrometer has been adopted:

1. Assemble the micromirrors, and coarsely adjust their verticality.
2. Align the optical fiber to the ball lens to collimate the light, again, coarsely.
3. Correct any resulting misalignments by fine adjustments in the beamsplitter pose.

Apart from these sources of misalignment there are several other sources of misalignment such as: (i) misalignment due to shrinkage in bonding materials used to secure the location of microcomponents after alignment (ii) misalignment due to external vibration and mirror scanning straightness, and (iii) misalignment in detector positioning. For (i), with the exception of the beamsplitter position, these misalignments will not have a major impact on the performance of the instrument. (ii) and (iii) can be compensated after assembly.

5.5 Evaluation of precision budget

As discussed in Chapter 3, to ensure high yield in micro manufacturing it is essential that a good estimation be obtained regarding the precision of the sensor

system and along individual degrees of freedom of the robot system. Therefore to check for the *HYAC* inequality we first determine the uncertainties i.e. σ_1^2, σ_2^2 , σ_3^2 and σ_4^2.

5.5.1 Fabrication uncertainty (σ_1^2)

The chemical processes incorporated for surface micromachining of microparts is subjected to several factors such as gas flow, exposure area, etch time and so on. For example: deep reactive ion etching (DRIE) process generally yields an aspect ratio of 20 to 60. Thus dimensional errors in a typical DRIE micromachining process are generally less than 2 to 5 μm, while sidewall profiles are accurate within 1^o. Figure 5.9 shows a typical fabrication error distribution in DRIE process.

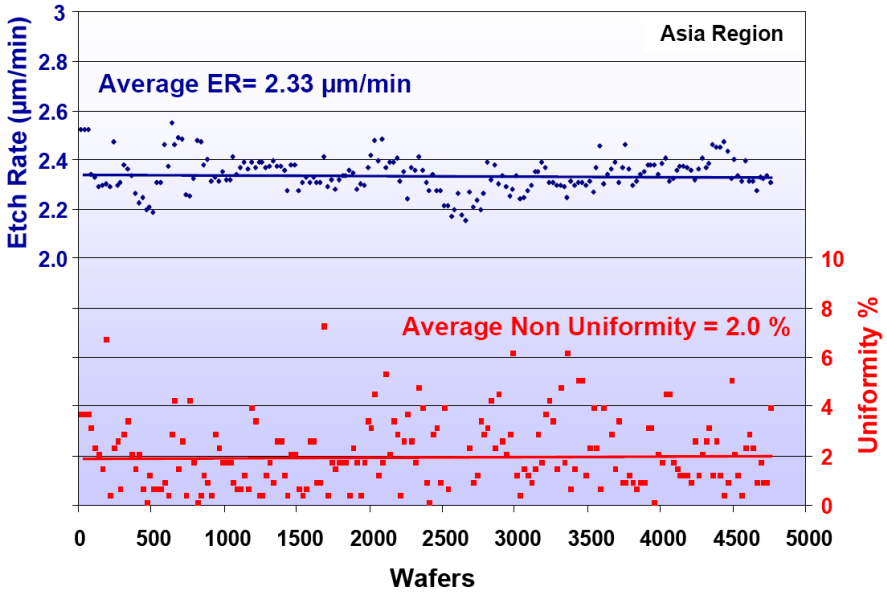

Figure 5.9. Frabrication error distribution in DRIE process (source: tegal corporations [106].

5.5.2 Vision system uncertainty (σ_s^2)

A stationary microscope with 10 frames per second has been used for this test. The field of view of the image captured is 1280×960 pixels at 5X magnification. For these parameters 1pixel corresponds to 1?m on the feature. For better resolution, sub-pixel accuracy has been used in measurements. 1000 measurements were taken at 100ms intervals for a stationary target under the camera as shown in figure 5.10.

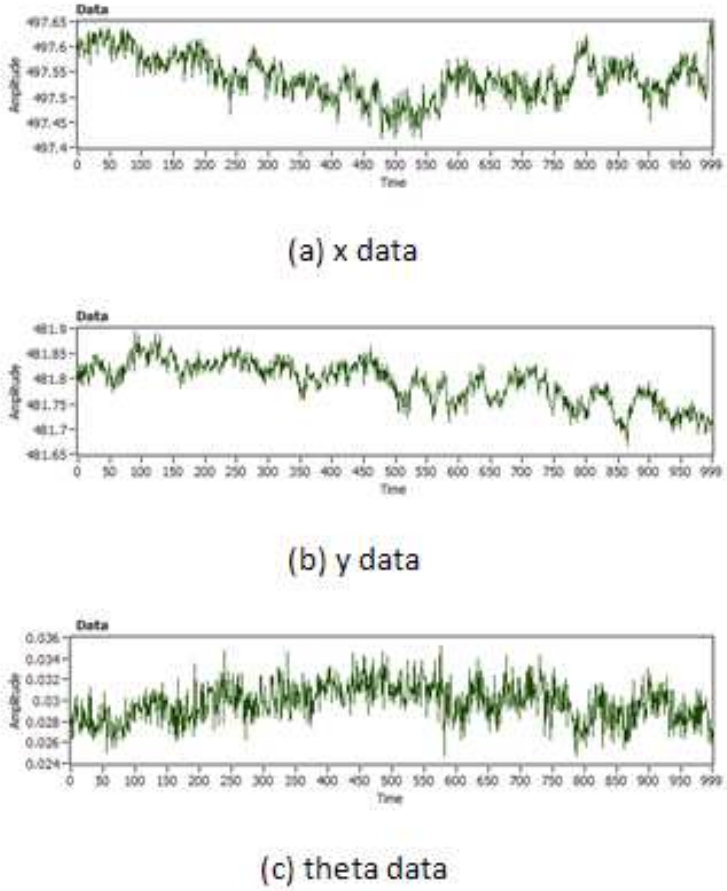

Figure 5.10. Measurement data for repeated readings from vision system.

The probability density function for each DoF has been calculated, as shown in figure 5.11.

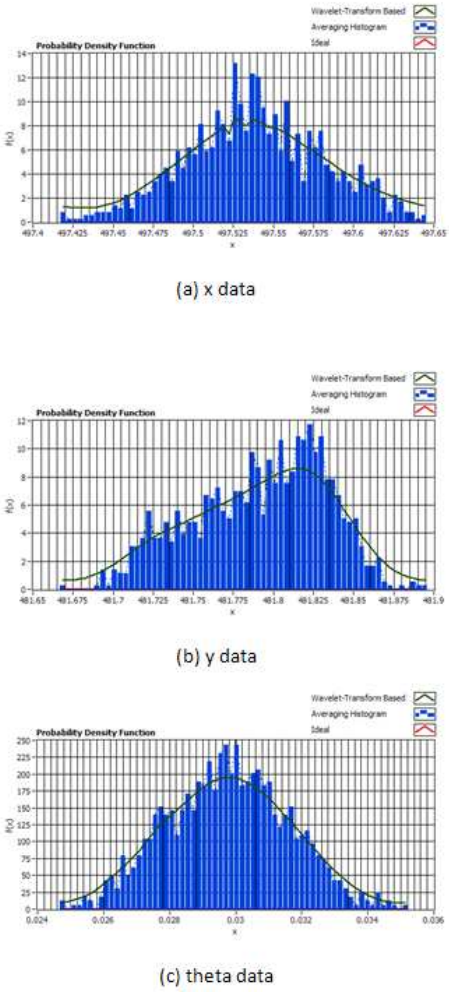

Figure 5.11. Probability density function calculation for sensor precision.

The data has been normalized and a Gaussian curve has been fitted to find out the 3σ variance range. Figure 5.12 shows the experimentation results.

From the above experiment, we can determine that the precision of the vision system in idle condition is 129nm along x axis, 124nm along y axis and 20 arcsecs in θ rotation axis.

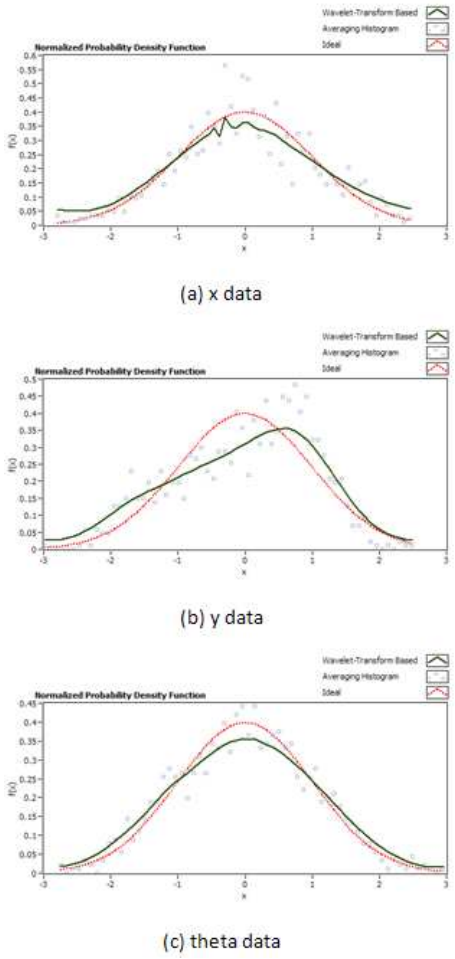

Figure 5.12. Uncertainty distribution in sensor precision.

5.5.3 Fixturing uncertainty (σ_2^2)

To estimate σ_2^2, we conducted simulation of 1100 die placement and 1100 de-tethering tasks in the Microsim 2.0 (see Appendix-B) virtual 3D environment. Using the method discussed in (i) we find that the die placement has an accuracy of 2.4μm and a repeatability of 0.6μm. Precision in locating the feature with part misalignment turned out to have an accuracy of 0.9μm and a repeatability of 0.3μm. Figure 5.13 shows the simulation results for fixturing uncertainty.

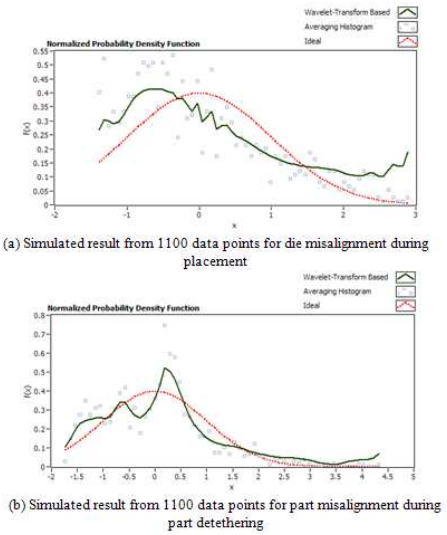

(a) Simulated result from 1100 data points for die misalignment during placement

(b) Simulated result from 1100 data points for part misalignment during part detethering

Figure 5.13. Fixturing uncertainty distribution.

5.5.4 Robot uncertainty (σ_3^2)

After determining the precision of the vision system, we continue to estimate the precision of the robot system along individual degrees of freedom based on the path travelled by the robot. The robot used for this test case is a Cartesian robot with kinematic links configured in the order of x-translation $\rightarrow$ y-translation $\rightarrow$ θ rotation. In this experiment, the robot is moved to several distances such as 1mm, 2mm, 5mm and 10mm etc along x, y, θ and xy directions. 250 measurement data points were collected for each case and the precision is estimated (see table 5.1).

From the data, it can be seen that the robot precision worsens as the distance travelled by the robot increases. Also, the precision attained along different degrees of freedom is different, even if the robot has been moved equal distances along the degrees of freedoms.

Table 5.1. Robot system precision test σ_3^2

Move case	*X Precision in* μ *m*	*Y Precision in* μ *m*	θ *Precision in arcsec*
idle x	0.129	0.124	19.645
1mm x	0.444	0.166	15.637
2mm x	0.519	0.940	26.389
5mm x	0.632	1.203	33.083
1mm y	0.150	0.325	19.765
2mm y	0.280	0.455	35.709
5mm y	2.687	3.721	72.410
1mm xy	0.468	0.269	31.335
2mm xy	0.521	0.324	30.478
5mm xy	0.494	1.481	32.882

5.6 Assembly of microspectrometer

The assembly of the microspectrometer is done using the μ^3 microassembly system. This workbench is used for assembly, active alignment and prototype testing of the optical components of the microspectrometer.

5.6.1 Description of assembly operations and process flow

The assembly of the microspectrometer involves multiple pick and place operations with heterogeneous parts of varied dimension. The micro components requiring assembly are as follows:

1. 2 MEMS mirror
2. 2 MEMS holder for ball lens
3. 2 Spherical glass lenses
4. 1 Glass beamsplitter cube

Out of these seven components the MEMS parts use a compliant socket mechanism. To assemble these components a MEMS jammer made out of silicon and a

vacuum micro nozzle have been used. The two end effectors have been mounted on two robotics manipulators of μ^3.

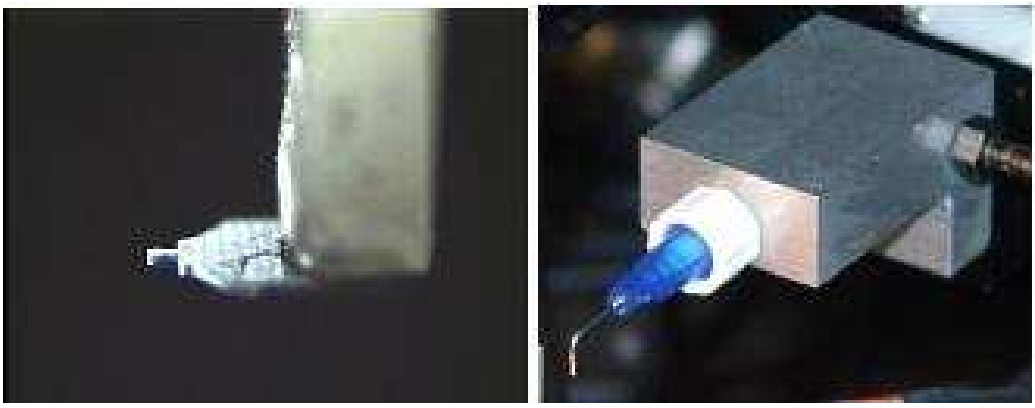

Figure 5.14. Micro jammer and micro needle.

The packaged die was mounted on the base robot M3. The assembly steps for the MEMS parts with the jammer are as follows:

1. Rotation centering of the MEMS jammer this ensures that there is no offset generated while the jammer went through a rotation between part pick up and alignment.
2. Calibration of robots the goal of the calibration step is to map the two-dimensional die coordinate system into the three-dimensional robot coordinate system. This helps with path planning and pre-computing the final pose of the robot for assembly.
3. Detethering of MEMS part tethered MEMS parts were fabricated on SOI (silicon on insulator) wafer using DRIE. During assembly, tethers are broken using the jammer microgripper, as shown in figure 5.15(a).
4. Part pick up and alignment the released parts are picked up with the jammer and held off the parts die. The jammer is then rotated by 90o, in order to align

the part over the socket. The calibration steps ensure that the part is directly above the socket and the tilt with respect to the device die has been corrected as depicted in figure 5.15(b).

5. Part placing and jammer release after the part is aligned, the jammer assembles it into the compliant socket on the die. The progressive downward motion also releases the jammer from the assembled part. This step is shown in figure 5.15(c), (d).

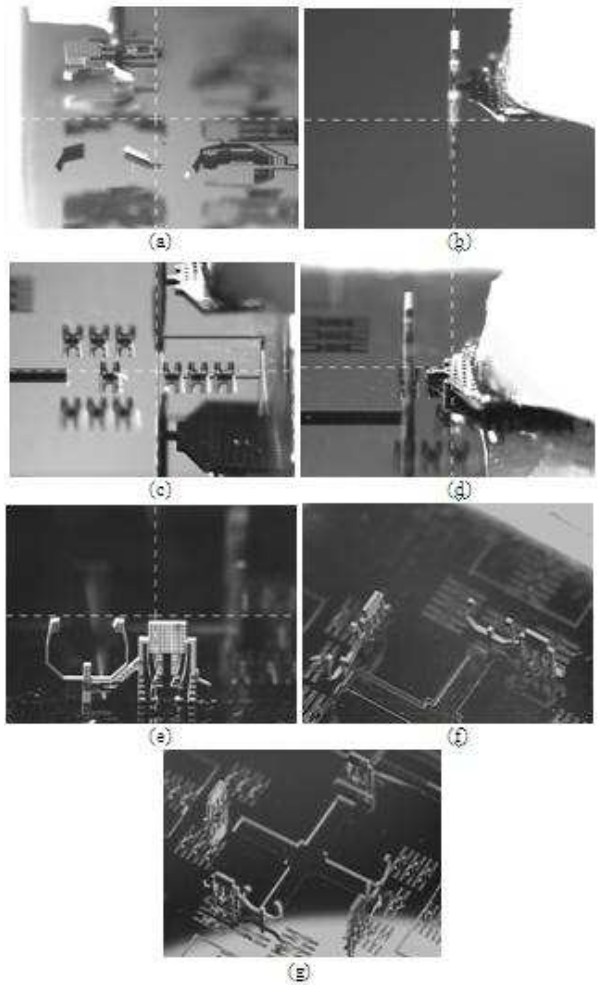

Figure 5.15. Assembly of MEMS parts by micro jammer, (a) Detethering, (b) 90^o Rotation, (c) Approach, (d) Release, (e) One assembly, (f) Two assemblies, (g) Completed assembly of silicon MEMS parts..

The assembly of these four MEMS components has been automated using custom developed software module to implement the calibration algorithm. The software module is written in Labview®and Matlab®.

Next, the glass parts are manipulated using a vacuum needle and the steps involved are:

1. The spherical glass ball lens is picked up by vacuum using a needle and placed into the socket of the previously assembled MEMS holder. The process of ball lens assembly is shown in the figure 5.16.
2. The assembly of the beam-splitter cube requires active alignment for detectable optical fringe pattern and thus is assembled last.

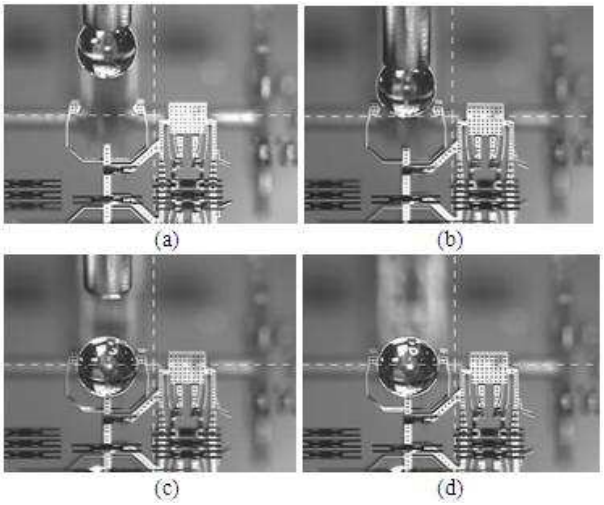

Figure 5.16. Assembly of ball lens with vacuum nozzle, (a) approach, (b) contact, (c) release (d) assembly.

Although the compliant snap fasteners are used to hold the assemblies in place, it is necessary to increase the bonding strength because the devices optical performance deteriorates when subjected to vibration, shock or scanning motion. Therefore curable UV epoxy is used to strengthen the assemblies. Probing tests conducted after

curing confirm proper bonding strength between the parts. The test involved pushing the assembled MEMS part by a fiber from both front and side to as shown in figure 5.17.

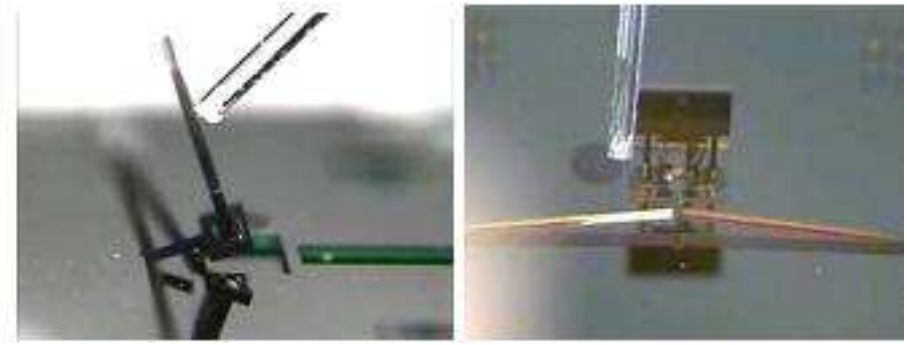

Figure 5.17. Epoxy bond strength test experiment indicating the mirror assembly is strong and allows scanning motion.

The selection of package is another important factor in the performance of the microspectrometer. The MEMS thermal actuator requires electrical interconnects accomplished via wire-bonds to the package. The wire bonding process requires preheating of the substrate to 150^o, and therefore it needs to be done prior to the microassembly. In addition, the introduction of a package results in less clearance for manipulation, therefore a collision-free sequence needs to be adjusted accordingly.

Figure 5.18 shows the assembly of two MEMS ball lens holders, two MEMS mirrors, ball lenses, MEMS parts for holding the on chip laser source and the detector. Finally the beam splitter cube has been aligned and attached at the center of the microspectrometer. In addition to the steps above, there are a few other processes that might be necessary, including:

1. In case of a fiber-coupled microspectrometer, an optical fiber needs to be attached to the package. A side groove is cut in the package prior to assembly to

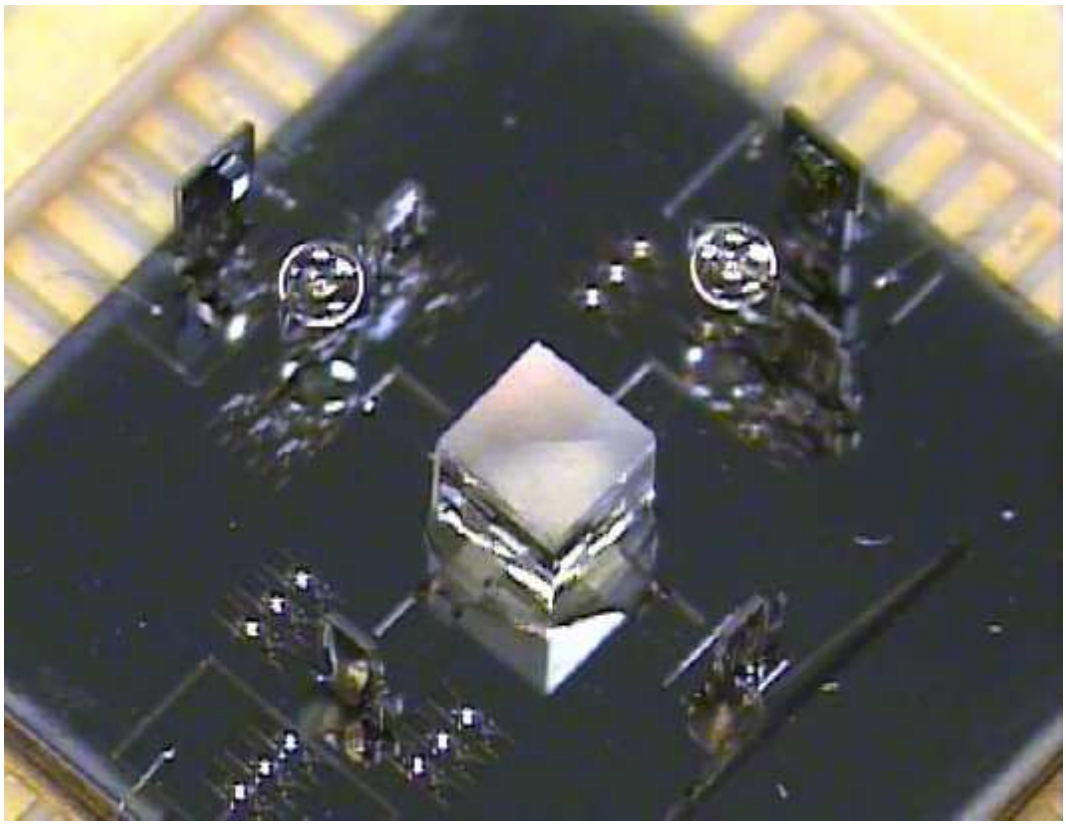

Figure 5.18. Completely assembled of microspectrometer.

provide passage for the optical fiber. The fiber is bonded to the package using low-shrinkage UV epoxy. Details related to fiber pig-tailing and characterizations of optical coupling are discussed in the next section.

2. Similar to the case above, if an external optical detector is used, then a corresponding groove must be cut in the package to provide a light path.
3. If an on-chip micro laser source and detector (figure 3(e) and 3(f)) are used, then these assemblies have to be completed prior to all the rest. In this case, electrical interconnects need to be provided.
4. Finally the package is sealed by attaching a top cover over the package.

5.6.2 Microspectrometer assembly tasklist and hybrid controller implementation

5.6.2.1 Part 1: Offline planning based on HYAC

According to the *HYAC* condition, a nominal plan for microspectrometer parts assembly is derived as follows:

1. Move the robots M_1, M_2 and M_3 to assembly ready positions i.e. robot M_3 carrying the parts and device die is moved to present the part feature into the sensor field 1 (top microscope looking vertically down) and robot M_2 carrying the microjammer to pickup ready position. These moves are carried out using ***calibrated open loop control***.
2. Using active visual servoing move robot M_3 to bring the part feature to the center of the image frame (or any other location that has been assigned as the pickup point). This operation is carried out using ***calibrated closed loop control***.
3. Bring the needle on M_1 to break the tether to release the micro part. This operation is carried out using ***calibrated open loop control***.
4. Break the tether by ramming the needle to it. This operation is carried out using ***un-calibrated open loop control***.
5. Retract the needle on M_1 back to its home position. This operation is carried out using ***un-calibrated open loop control***.
6. Using active visual servoing move robot M_3 to realign the part feature to the center of the image frame (or any other location that has been assigned as the pickup point). This operation is carried out using ***calibrated closed loop control***.
7. Pick up the part using the micro jammer on M_2 robot. This operation is carried out using ***un-calibrated open loop control***.

8. Correct the error (if any) in pick up, if any, by active servoing through sensor 2 (side microscope looking horizontally). This operation is carried out using ***calibrated closed loop control***.
9. Move the M_3 robot to bring the socket feature into sensor field 1. This operation is carried out using ***calibrated open loop control***.
10. Using active visual servoing move robot M_3 to bring the socket feature to the center of the image frame (or any other location that has been assigned as the placement point). This operation is carried out using ***calibrated closed loop control***.
11. Place the part into the socket by moving the jammer on robot M_2. This operation is carried out using ***un-calibrated open loop control***.
12. Bring back the robots to ready position as in step (1).

5.6.2.2 Part 2: Online control execution

If $HYAC$ is not satisfied prior to steps (7) and (11) respectively then discard the subsequent steps and restart from step (1). Moreover, if the feature patterns cannot be detected due to unavailability of parts, or ambient lighting variation during steps (2), (6), (8) or (10) in the previous case then:

1. Go back to the previous step by reversing position.
2. Update the uncertainty information in estimator.
3. Re-evaluate the new path and/or control structure.
4. Execute new plan.

The above steps are repeated four times to complete the microspectrometer assembly.

Table 5.2. Cost function comparison for 1200 simulated microspectrometer assemblies in virtual 3D

Parameters	*Open loop*	*Closed loop*	*Hybrid control*
Overall yield	20%	99.9%	92.5%
Estimated time	6 to 10 minutes	50 to 80 minutes	20 to 35 minutes
Sensor count	0	4	2

5.6.3 Manufacturability metrics analysis

We examined the efficiency of the hybrid controller through simulation in virtual 3D as well as with the actual assembly setup. In case of simulation, we carried out 1200 simulated microassemblies using pure open loop control, closed loop control and proposed hybrid controller. The comparison results are given in table 5.2.

Actual experimental implementation was carried out for 10 assemblies of microspectrometer on the μ^3 setup. As seen in figure 5.19, for the 10 actual assembly attempts using each of the three control structures, the hybrid controller gives 35% better accuracy than the open loop controller, while its throughput is 60% faster than a closed-loop controller. Typical value for the assembly tolerance σ_1^2 was 3.3μm. 7 out of 10 assembly attempts failed in the open loop case, where as the hybrid control managed to achieve a higher accuracy and thus succeeded in assembling all 10 microspectrometers. Closed loop control also succeeded in assembling all 10 microsystems however it took a long time (90 minutes per system), whereas the hybrid controller managed to do the same with an average time of 20 minutes per system.

5.7 Optical coupling analysis

5.7.1 Steps involving coarse alignment

The coarse alignment of the microoptics includes several steps such as aligning the fiber to the device die, placing the fiber axis on the expected light path, the laser

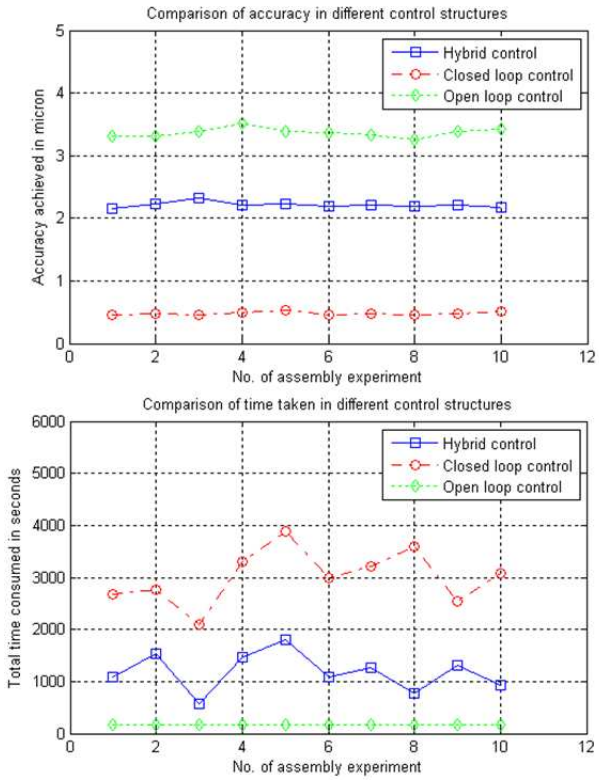

Figure 5.19. Comparative analysis of precision adjusted hybrid controller with pure open loop and pure closed loop control (results from 10 experimental microassembly attempts in each case are shown).

spot at the center of the first mirror and correcting its tilt. These steps are performed prior to active beamsplitter alignment, in order to bring the optical components close enough to their ideal positions and obtain two laser spots onto the detector plane. Note that all coarse alignment steps are performed using motorized stages in *teleoperated mode*, with the aid of image processing edge detection tools. Any residual misalignments will be actively compensated (e.g. with feedback) via the beamsplitter pose correction discussed in the next section. During the experiments, a fiber-coupled Fabry-Perot diode laser source of 635nm wavelength was used. The three major factors affecting optical fiber coupling losses into the FTIR are:

1. Power loss in the fiber channel

2. Fiber tip offset from the center of the ball lens
3. Fiber tilt with respect to the device die

Experiments conducted provide information about the last two factors. In the first experiment the fiber tip is placed directly in front of the optical detector. The detector is then moved backward and the corresponding drop in the amplitude of the detected signal is noted which is shown in figure 5.20. The measurement parameters are as follows: ambient voltage reading (P-P) of 4 mV, max = 12 mV, min = 8 mV, ambient power reading of 1 μW, initial distance between the fiber tip and the ball lens of 0 (detectable contact with the lens), initial distance of fiber tip from detector of 25mm, fiber length of 685 mm, and a diode laser power of 2.5 mW.

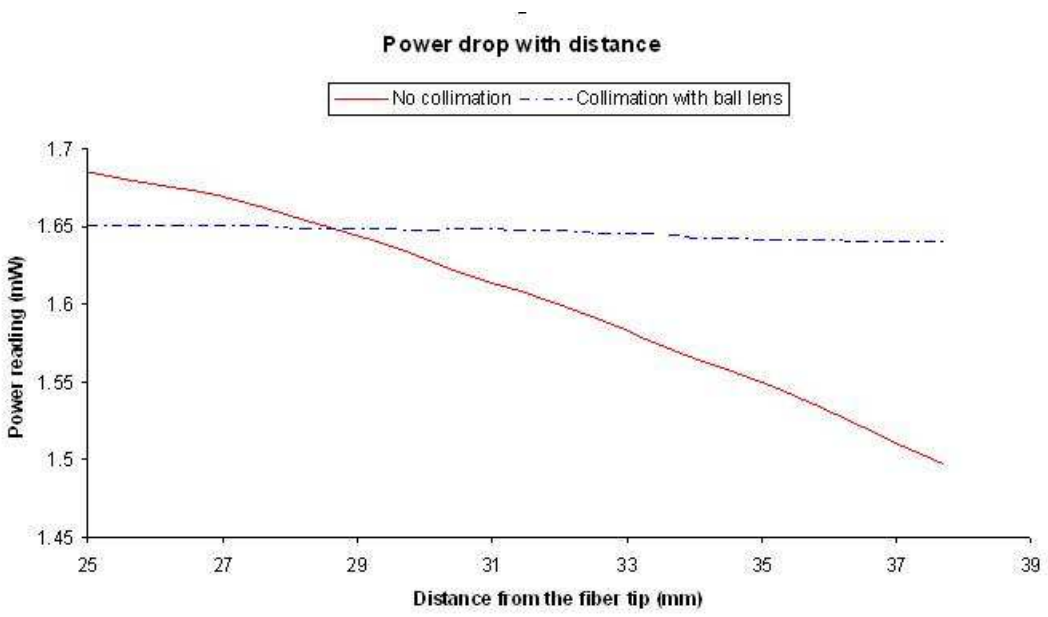

Figure 5.20. Power transmission with and without collimation.

The second experiment shows the effect of fiber tip offset from the center of the ball lens. The Y-offset of the fiber tip from the ball lens is the to and fro movement and thus is the same as focal displacement. For the specific microspectrometer design

with a known distance between the ball lens and the MEMS mirror in front of it, the back focal length of the lens has been experimentally determined to be approximately 188 μm. The X and Z offsets in the fiber tip with respect to the ball lens, however, are directly proportional to the spot location on the MEMS mirror. Due to the nature of the ball lens the offsets in fiber tip behind the ball lens appears as magnified offsets in the spot location on the mirror with respect to its center. In this experiment this magnification factor was determined, and provides valuable information regarding the tolerance budget of bonding the fiber to the package. The fiber has been mounted on a precision calibrated XYZ stage and thus can be moved to a known offset position. By the measuring the offset in spot size on the MEMS mirror from design data, the two parameters can be correlated to give the magnification factor of 10, as shown in Figure 5.21. From the experiment, a 3 μm displacement of the fiber tip results in a 30 μm offset in the spot size on the first mirror.

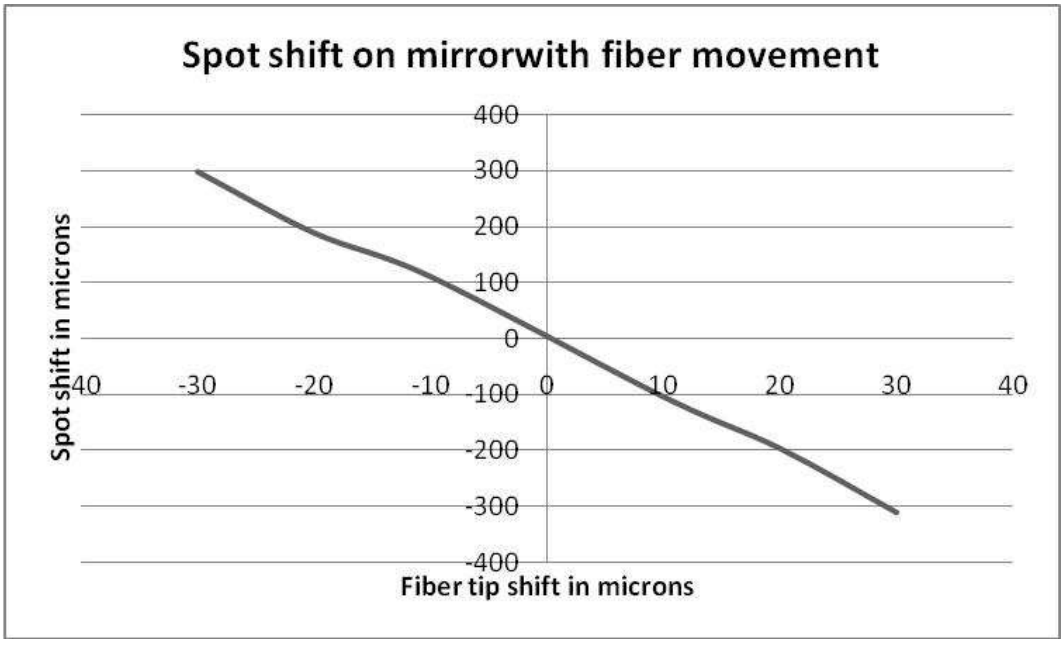

Figure 5.21. Test of fiber offset - the fiber is moved in X and Z direction and the corresponding movement in spot on mirror is plotted.

The third power-loss factor is the tilt angle in fiber with respect to the device die. Angular misalignment causes a loss of fringe contrast due to overlapping of different ray paths. Machine vision edge detection is used to determine the angle of the device die and the fiber separately with respect to a die coordinate system. The difference in these two angles gives the measure for tilt angle, which is then corrected by adjusting the tilt stage that mounts the fiber. In the case shown in Figure 5.22, an angle between fiber and device die of 0.44 degrees has been measured.

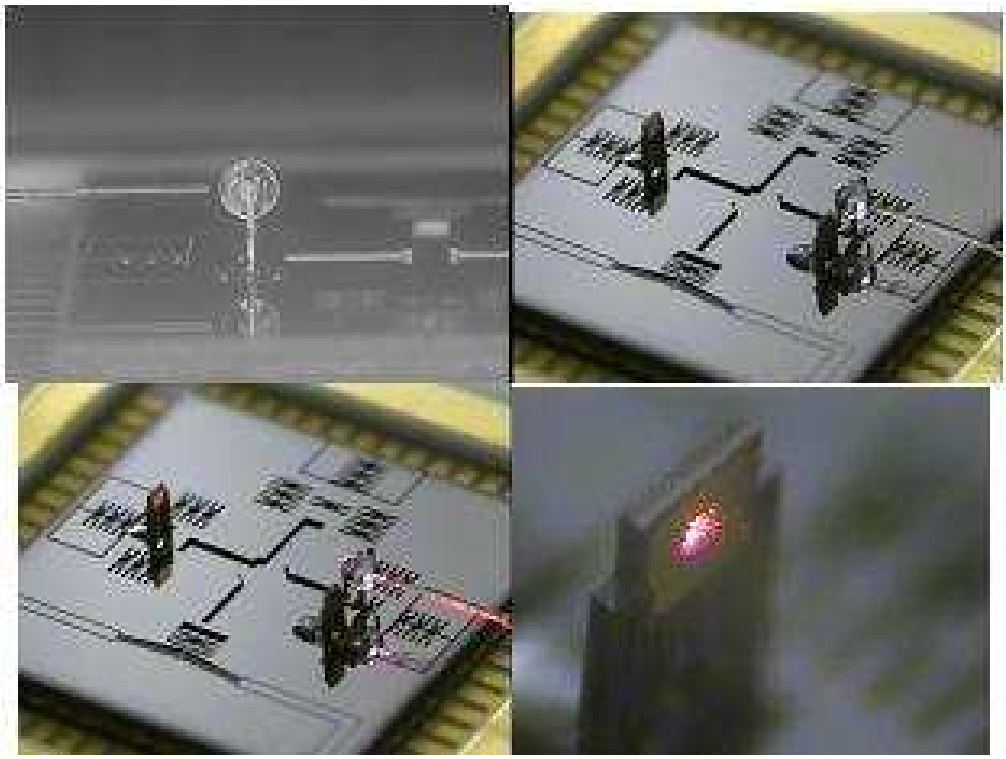

Figure 5.22. Experimental setup and implementation of machine vision edge detection technique for tilt correction.

The next step of the coarse alignment is the correction of tilt in the mirror. Machine vision edge detection is again used to determine the slope of the mirror as well as the die, as shown in figure 5.23. In this particular case, we found that the

micromirror tilt was 0.8^o, and using an optical fiber tip, the tilt is corrected to below 0.5^o by pushing onto the mirror.

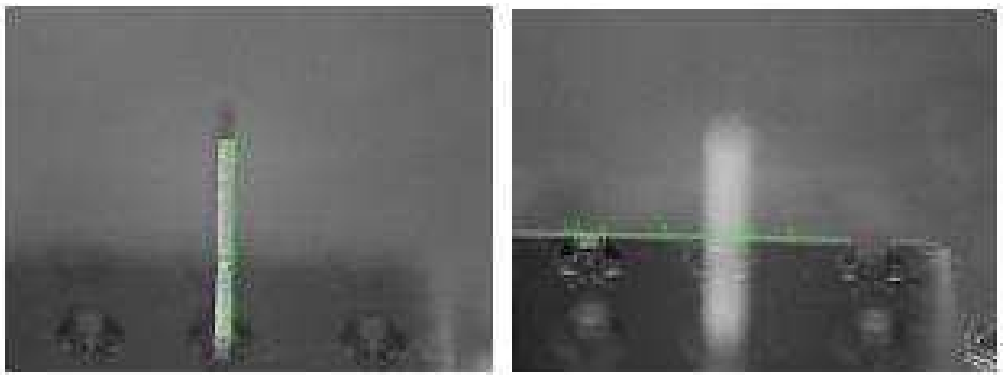

Figure 5.23. Machine vision edge detection for mirror tilt measurement and adjustment.

In order to adjust the optical fiber relative to the ball lens, we observed the reflected spot position from the mirror. If the reflected spot coming from the mirror is close to the fiber origin then the fiber is approximately along the light path (figure 5.24).

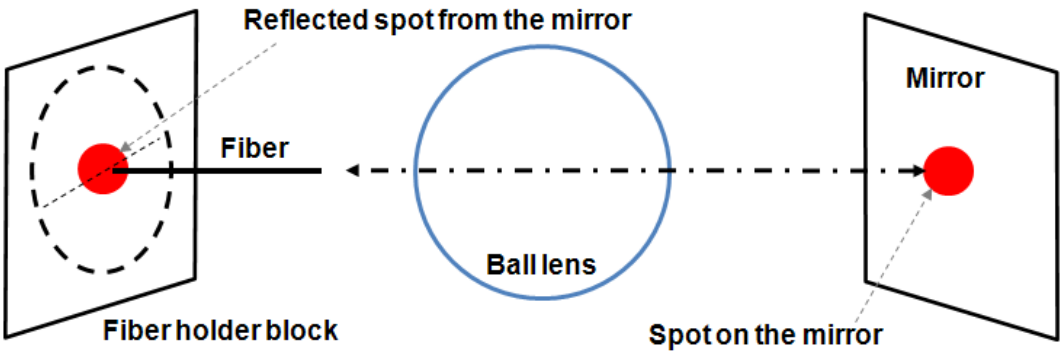

Figure 5.24. Coarse alignment of the fiber.

The third coarse alignment step includes adjusting the fiber tip position at the back focal length (BFL) of the ball lens, as discussed previously. This can be achieved indirectly by observing the spot size of the mirror. The fiber tip is close to the BFL of the ball lens when the size of the spot on the mirror is minimum.

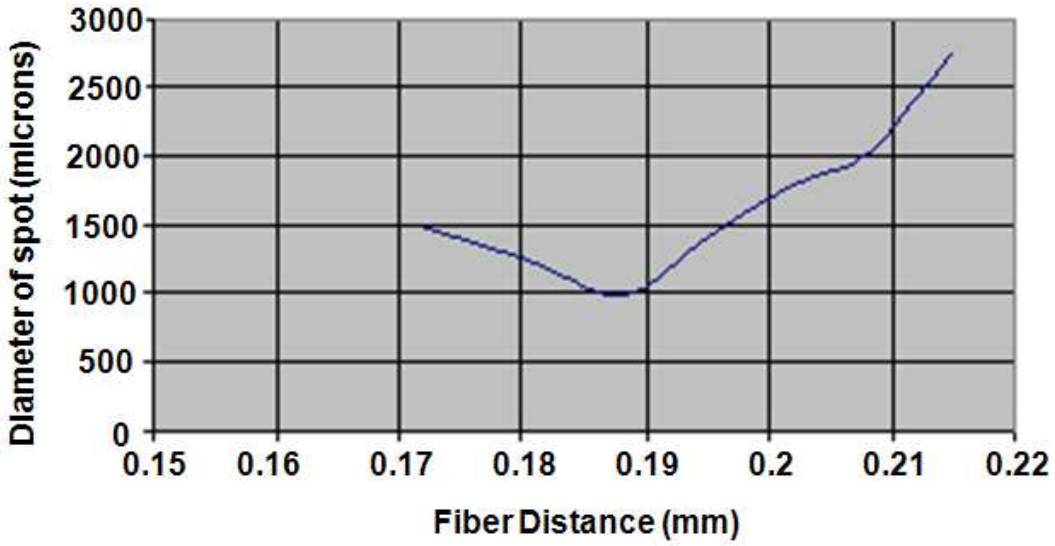

Figure 5.25. Diameter of the spot on the mirror vs. the corresponding fiber distance from the ball lens surface.

A simple experiment was carried out, in which the fiber was gradually retracted back from a position where it just touches the ball lens surface. Figure 5.25 shows the diameter of the spot on the mirror vs. the corresponding fiber distance from the ball lens surface. From the plot we found that the back focal length (BFL) is 188 m, close to the predicted value from equation 5.7.

Finally, we adjust the position of the focused spot to be at the center of the MEMS mirror. Due to the magnification factor of 10 from the ball lens the spot moves 10 times faster as the fiber tip is moved behind the ball lens (figure 5.22).

5.7.2 Steps involving fine alignment

The role of the coarse alignment performed in the previous section is to ensure that two spots are obtained on the detector plane when the beamsplitter is inserted into the light path. Once this is achieved, the beamsplitter cube is manipulated in multiple DOFs by directly monitoring the effect on the optical output. Active alignment is often necessary in microoptics, because the alignment tolerances are below 1 m, below robotic accuracy in most cases. In our case, the feedback output consists of the two laser spot positions projected on onto a microscope CCD camera. We make use of a spot Jacobian mapping that connects small changes in beamsplitter position to small changes in the relative distance between the projected laser spot positions, as shown in figure 5.26.

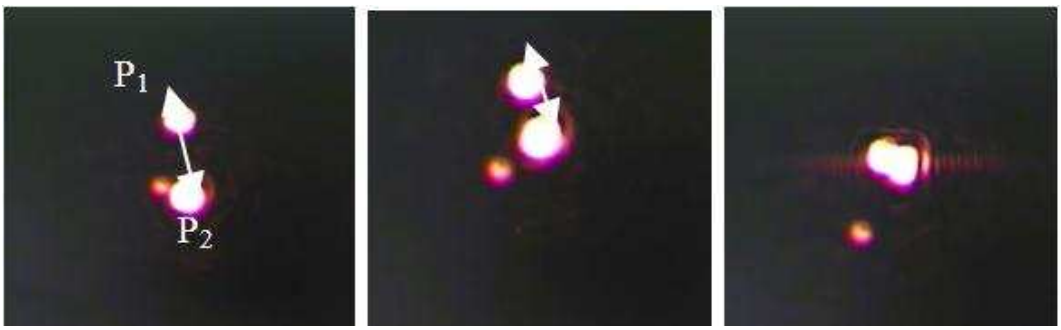

Figure 5.26. Image consisting of two laser spots projected onto a microscope CCD camera with a 5x zoom lens. Fine rotations of the beamsplitter cause the distance d between the spots to converge to zero.

The degrees of freedom for the beamsplitter cube manipulation are given as $q_1 = [x_1, y_1, z_1, \theta_1, \varphi_1, \psi_1]$ (measured in axis encoder counts), and the corresponding position of the two spots on to the detector plane are $[P_{x1}, P_{y1}]$, and $[P_{x2}, P_{y2}]$ (measured in pixels). The separation vector $[\tilde{x}, \tilde{y}]$ is equal to $[P_{x1} - P_{x2}, P_{y1} - P_{y2}]$, and has a midpoint at $[\tilde{x_c}, \tilde{y_c}] = \frac{1}{2}[P_{x1} + P_{x2}, P_{y1} + P_{y2}]$.

We noted previously that translations of the beamsplitter along the die plane (X, Y, Z) cause a shift in $[\tilde{x_c}, \tilde{y_c}]$, but no change in $[\tilde{x}, \tilde{y}]$. On the other hand, rotations cause a change in both vectors. Since translations and rotations are decoupled, we can relate changes in spot positions to joint robot velocities through *spot Jacobian* maps:

$$\begin{bmatrix} \dot{\tilde{x}_c} & \dot{\tilde{y}_c} \end{bmatrix}^T = J_1(q_1)\,\dot{q_1} \begin{bmatrix} \dot{\tilde{x}} & \dot{\tilde{y}} \end{bmatrix}^T = J_2(q_1) \begin{bmatrix} \dot{\theta_1} & \dot{\varphi_1} & \dot{\psi_1} \end{bmatrix}^T, \tag{5.11}$$

where J_1 and J_2 are pose-dependent 2×6 and 2×3 Jacobian matrices, respectively. The goal of fine adjustment of the beamsplitter pose is to make the spots overlap, e.g. to stabilize the separation vector $[\tilde{x}, \tilde{y}]$ to zero. Next, we identify the Jacobian J_2 by approximating it with a constant evaluated at the nominal aligned position. In practice, this was done by collecting incremental beamsplitter pose data according to:

$$\begin{bmatrix} \Delta\tilde{x_1} & \Delta\tilde{y_1} \end{bmatrix}^T \cong J_2 \begin{bmatrix} \Delta\theta_1 & \Delta\varphi_1 & \Delta\psi_1 \end{bmatrix}^T. \tag{5.12}$$

For the fine alignment with the beam splitter cube, as discussed above, we implement an automated visual servoing scheme to cause the spots to overlap. In the first step, the spot Jacobian is identified by scanning on a grid. The beam-splitter is rotated in 3D space and the corresponding image containing the two spot locations on the CCD is recorded. 216 individual points were used in 3D space. The pose increments of the beamsplitter are measured using axis encoders of the corresponding rotational DOFs, while the spot positions are measured via image processing.

The spot Jacobian matrix J_2 provides a way to automate servoing on the beamsplitter poses in order to perform the alignment. Fine alignment is now accomplished with exponential convergence by moving the beamsplitter according to:

$$\begin{bmatrix} \dot{\theta}_1 & \dot{\varphi}_1 & \dot{\psi}_1 \end{bmatrix}^T = -cJ_2{}^+ \begin{bmatrix} \tilde{x} & \tilde{y} \end{bmatrix}^T, \tag{5.13}$$

where c is a positive constant, and $J_2{}^+$ is the Moore-Penrose inverse.

This Jacobian is then used for servoing the robotic manipulator holding the beam splitter from a position where the two spots are misaligned (as achieved by coarse alignment) to a position where the two spots overlap.

Using $c = 100$, in equation 5.13, and joint angle increments instead of time-derivatives, we servoed to overlap the laser spots. After servoing for 25 joint axis increments the two laser spots are separated by less than 10 μm, as shown in Figure 5.27. In the future, additional alignment accuracy can be obtained by servoing on the directly on the fringe pattern instead of the spot image, however, this alignment accuracy is sufficient to establish a spectrum measurement with the FTIR.

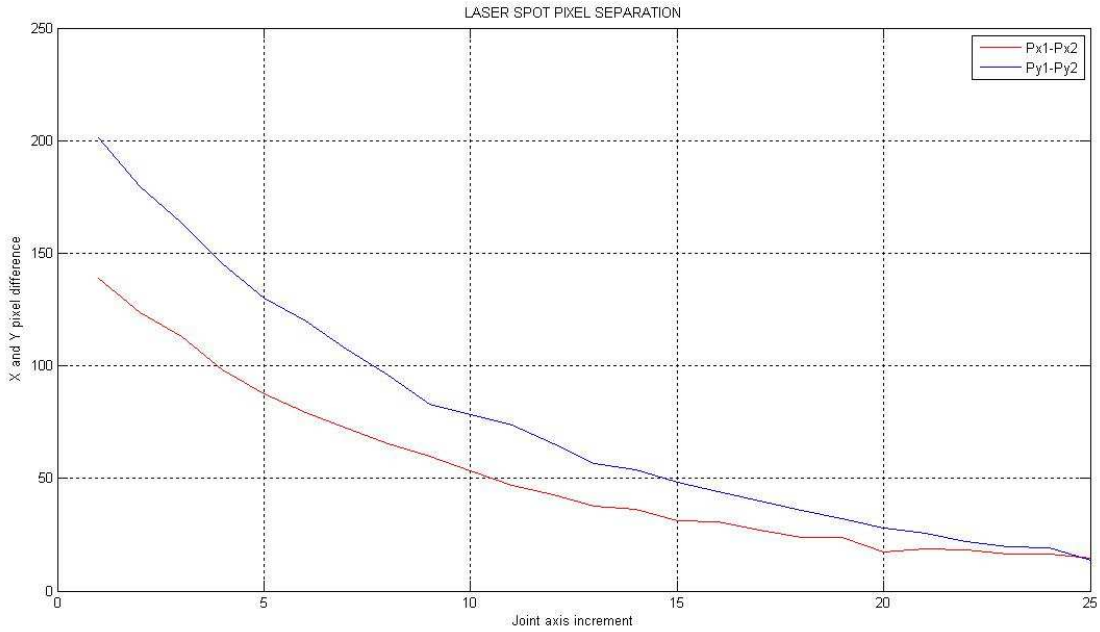

Figure 5.27. Decrease in laser spot separation in μm using spot Jacobian servoing.

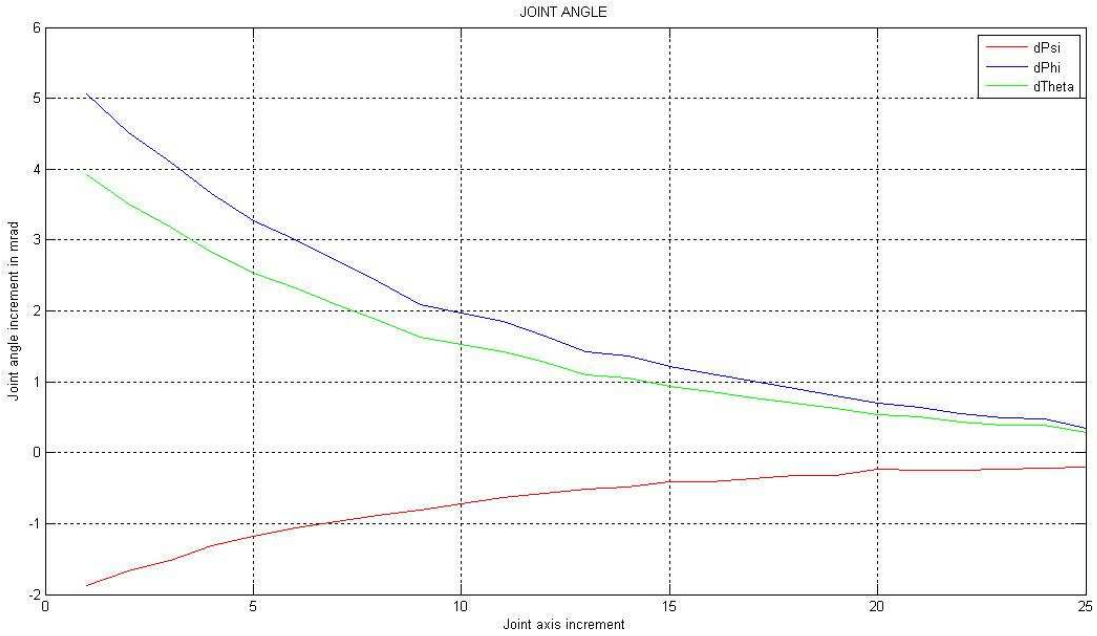

Figure 5.28. Joint angle increments in mrad during servoing.

5.8 Spectrum results

The microoptical bench was assembled and aligned using the methods described in previous section. At the pose when the spots overlap on the detector, the fiber and beamsplitter positions are set in place using low-shrinkage epoxy. The CCD camera is replaced by an intensity detector, and the interference signal is recorded. We tested the recovered signal obtained from a 635nm fiber-coupled laser source. Figure 5.29(a) shows a sample subset of the acquired signal with actuation frequency of 1Hz. This signal was sampled at 1KHz and then filtered by an 4th order band-pass elliptical filter with ripple factor 12, stop band attenuation of 40dB, and bandwidth of 20 Hz to 220Hz. This filter is necessary to remove optical noise in the laser source, and electrical noise on the detector. Finally, using equation 5.4, the input spectrum has

been recovered. The plot in figure 5.29(c) shows a detected peak at 0.63m which is 5nm away from the wavelength of input source.

The success of prototyping the microspectrometer shows that automating the assembly process is possible in three stages: assembly of the mirrors and ball lenses, coarse adjustments in the fiber, mirror tilt, and beamsplitter position, and finally fine adjustments of the beamsplitter. The first two parts are performed using visual information from microscopes and the appropriate design of MEMS snap-fasteners, while the third part is performed using optical feedback, by active alignment. A laser *spot Jacobian* mapping is used in the beamsplitter alignment step. A similar scheme could also be used for fiber alignment and, therefore, the assembly operations can be automated. After assembly and bonding, the spectrum of the input diode laser source has been recovered to demonstrate basic functionality of the instrument. This can be accredited to the accuracy in active alignment along with precision 3D assembly of the microparts.

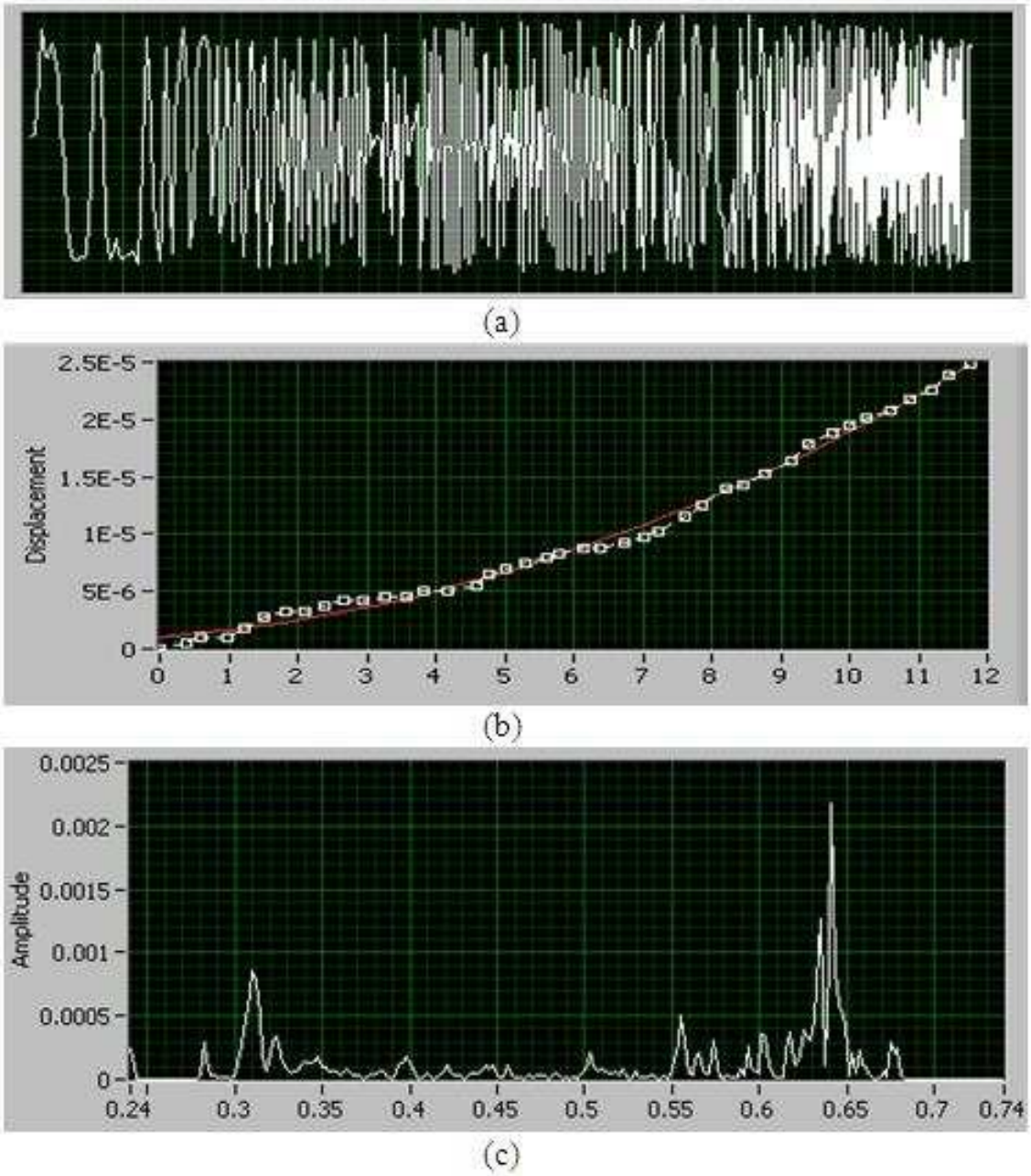

Figure 5.29. (a) Spectrogram data (intensity vs. samples), (b) Actuation profile of the MEMS mirror (voltage vs. displacement) and (c) Spectrum of calculated laser source (635nm) from our MEMS FTIR spectrometer.

CHAPTER 6

CONCURRENT MICROMANUFACTURING FOR MICROSYSTEMS

Concurrent Engineering is a work methodology based on the parallelization of tasks (i.e. concurrently). It refers to an approach used in product development in which functions of design engineering, manufacturing engineering and other functions are integrated to reduce the elapsed time required to bring a new product to existence. Concurrent engineering replaces the traditional product development process with one in which tasks are done in parallel and there is an early consideration for every aspect of a product's development process. This strategy focuses on the optimization and distribution of resources in the design and development process to ensure effective and efficient product development process.

6.1 Need of concurrent engineering in MEMS development

Concurrent engineering is effective, especially in the case of micro- and nanosystem technology. Generally, the design process for the microsystem's functional units, such as electronic design, sensor design, actuator design, microassembly, package selection etc., is decoupled, mainly due to the lack of appropriate design and simulation tools and know-how. Most of the time decisions are made intuitively. With the exception of a few sparingly used *"finite element analysis (FEA)"*, the norm has mostly been to employ *'experience'*. A similar situation exists in the context of test, which is mostly perceived as a post design task. This design and manufacture cycle often results in major difficulties in guaranteeing specifications across full operating conditions and, in most cases, pushes tests cost to above 50% of total manufacturing

costs. As a result of all these problems, several design iterations are required for post prototype manufacturing. It is clear that in order to reduce the number of redesign cycles, *"design for manufacture"* activities have to be moved from the back-end into the front-end design cycle. An effective network of reliability, test and packaging engineering integrated through modeling and simulation research and tied closely into the design environment appears to be a sensible route to increasing the applications of micro and nano system technology in near future. Figure 6.1 shows a basic framework for concurrent micromanufacturing involving major steps.

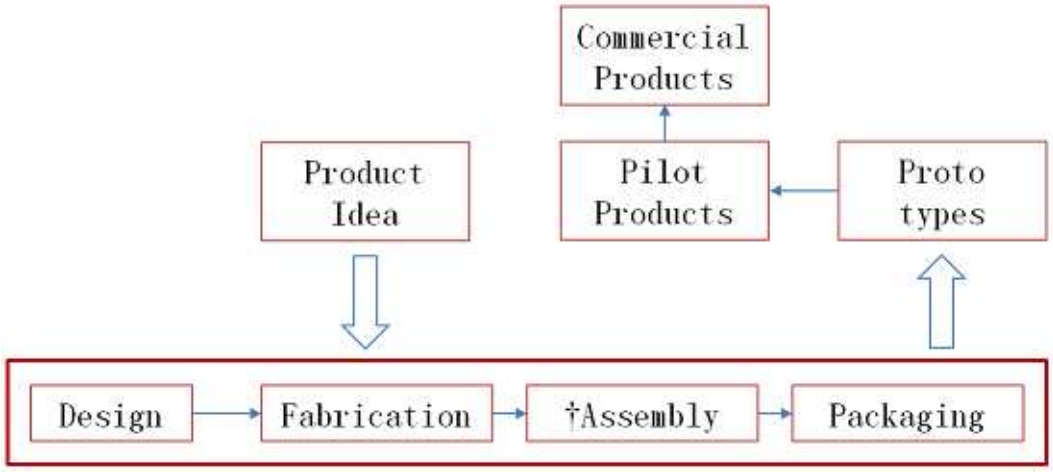

Figure 6.1. Concurrent micromanufacturing framework.

6.2 Characteristics and requirements for concurrent micromanufacturing

Before employing concurrent engineering for microsystem development, it is imperative that extended knowledge must be acquired about:

- appropriate design environments and design methodologies;
- packaging and testing;
- reliability;

- cost functions for production.

The core elements for concurrent micromanufacturing are best described by the phrase *"design for manufacture"*. These elements are:

- Design for manufacturability
- Design for testability
- Design of reliability
- Design for maintainability
- Design for environment

Design for manufacturability deals with setting the guidelines for part counts, ability to verify the design, specifying the tolerances while maintaining the robustness.

Design for testability involves finding design choices, specifying test points and providing access to them through standard connections and interfaces, physical and electrical partitioning to facilitate test and isolation of faults.

Design for reliability deals with designing based on the expected range of operating environment, reducing sensitivity to stress and thermal loads and so on.

Design for maintainability primarily revolves around providing basic design rules for easier replacement of faulty parts and using built-in self-test modules to quickly identify and isolate problems.

Design for environment specify design guidelines for environment-friendly manufacturing through non-toxic process and optimum utilization of energy. Recycling, safe-disposal, contamination avoidance are some of the measures that are taken into consideration.

It is evident from the above discussion that a large amount of prior information must be acquired, processed, analyzed, stored and updated in order to effectively employ concurrency in manufacturing. Obtaining such versatile information in mi-

croscale can be very difficult considering the fact that every process is highly system specific and unrelated.

6.2.1 Areas for concurrency in micromanufacturing via microassembly

As discussed in the previous section, concurrent manufacturing can be a very effective standard, if not the only standard, for microsystem development. There are several major phases in a complex heterogeneous microsystem development process via microassembly. These phases are:

- Concept design and selection of microparts
- Structural design for parts and devices
- Batch fabrication
- Automated microassembly
- Integration of electronics and packaging of system
- Testing and deployment

Unfortunately, these phases are unrelated and thus the overall cost, time and yield of production cannot be predicted nor optimized easily without a lot of production cycles. One way to look at deploying concurrency in such diversified steps is to have a centralized database of individual information from these steps which are collected over the time through different testing and evaluations; not necessarily related. An analytic organizer may then be used to query the database based upon a new development process and extract information specifically related to current development. By establishing a correlation among these data, prior knowledge from unrelated steps can be used to quantitatively predict the cost functions associated with a specific microsystem development process.

6.3 Discussion on the range of choices for different parameters

There are several parameters which require optimization in selection for effective implementation of concurrent micromanufacturing such as material, mechanics, sensors, actuators, electronics, packages, assembly methods and so on. A few are discussed below.

6.3.1 Family of actuators and sensors

Sensors and actuators are commonly the interface between microsystems and the physical world. A key contribution of MEMS technology is that it has enabled the integration of sensors, actuators and signal processing on a single chip, and their integration has positive effects upon performance, reliability and cost. Based on the required functionality and available real-estate, actuators and sensors for a specific microsystem must be selected accordingly. Numerous research in recent times have resulted in a wide range of MEMS actuators which can be broadly classified into four groups; (i) electrostatic, (ii) thermal, (iii) piezoelectric and (iv) magnetic.

Electrostatic actuators include comb drive, inch worm, parallel plate, relay, scratch drive, curved electrode etc. Piezoelectric actuators are generally used in the form of bimorphs and expansion types. Thermal actuators are also very popular type of MEMS actuators that include bimorphs, shape memory alloy (SMA), expansion types, relays, and state change types. Lastly, magnetic actuators are generally of electromagnetic, magnetostrictive, external field and magnetic relay types.

Major categories of MEMS sensors involve displacement sensors and force sensors; sometimes optical sensors. The displacement sensors can be of capacitive, optical, electron tunneling. Similarly force sensors can be of piezoresistive, piezoelectric and compliant based. In case of optical sensors, the primary types can be electron microscopy, probe microscopy or confocal optical microscopy.

Table 6.1. Typical characteristics for different MEMS actuators

Actuator	*Force*	*Range*	*Resolution*	*Size*	*Heterogeneity*
Comb drive	High	High	High	Large	No
Parallel plate	Low	Low	High	Large	No
Inch worm	Low	High	Low	Moderate	No
Thermal bimorph	Moderate	High	Low	Low	No
Piezoelectric	High	High	High	Low	Yes
Shape memory alloy	High	High	Low	Low	Yes
Electromagnetic	Low	High	High	Low	Yes
Fluid expansion	High	High	Low	High	Sometimes
External field	Low	High	Low	Low	Yes

Table 6.2. Typical characteristics for different MEMS sensors

Sensor (type)	*Force needed*	*Displacement*	*Resolution*
Capacitive (displacement)	None	High	Moderate
Piezoresistive (displacement)	None	High	High
Piezoelectric (displacement)	None	High	High
Electron tunnelling (displacement)	None	Low	High
Optical (displacement)	None	High	High
Piezoresistive (force)	High	None	High
Piezoelectric (force)	High	None	High
Visual/compliant (force)	None	Low	Moderate

Table 6.1 shows a comparative chart of different MEMS actuators.

As seen from table 6.1 selection of actuator for a microsystem is basically a trade-off among available device area, force and displacement requirements. Some of the actuators involve mixture of different materials and thus require assembly of components.

Similarly the comparisons among different MEMS sensors are given in table 6.2.

6.3.2 Materials for microsystems

Similar to sensors and actuators, microsystems also have a range of choices for materials. Although Silicon is most widely used for MEMS there are other potential materials. These include metals such as gold, silver, aluminium, TiNi, TiW, ITO, W, Ir, Pt; polymers such as SU8, polyimide; and silicon compounds such as silicon dioxide, silicon nitride and so on. The material selection is generally based on the following properties:

- Electrical conductivity
- Thermal conductivity
- Chemical
- Bio-compatibility
- Optical
- Processing complexity
- Cost

Sometimes for better and cost effective performance of microsystems, it becomes necessary to combine several different materials. This requires active assembly of components as they cannot be fabricated monolithically.

6.3.3 Trade-offs among design, fabrication and assembly

The complexity of a microsystem dictates the balance between microassembly versus monolithic micro fabrication and that in turn, decides the component design. For example; a simpler microsystem such as a pressure sensor can be achieved by a single-layer in-plane canti-lever, thus can be easily fabricated monolithically. On the other hand a micro robot have multiple degrees of freedom requires much greater complexity in performance. Monolithic fabrication for such system would require a large number of layers and intricate in-plane joining mechanisms in multiple layers.

Design of such system can be very complex and difficult unless microassembly is used. Microassembly can simplify the design and reduce the device foot-print. Additionally it can provide greater strength and robustness to the system. On similar note, an optical microsystem or MOEMS can be manufactured in a easier way by a blend of batch fabrication and assembly of heterogeneous micro components.

6.3.4 Packaging of MEMS

Due to the proximity to semiconductor industry which is predominantly Silicon processing, most of the MEMS packaging technologies most likely use off-the-shelf packaging borrowed from the semiconductor microelectronics field. In case of MEMS, however, packaging has to deal with establishing interconnections and an appropriate operating environment for electromechanical structures to process and/or store information. MEMS packages can contain many electrical and mechanical components which need interconnections to be useful to the outside world. Microsystems are extremely fragile and must be protected from mechanical damage and hostile environments. To function, electrical circuits need to be supplied with electrical energy, which is consumed and transformed into mechanical and thermal energy. Because the system operates best within a limited temperature range, packaging must offer an adequate means for removal of heat. The main objectives of MEMS packaging are:

- Mechanical support
- Protection from environment
  - Mechanical sealing
  - Hermetic packaging
  - Non-hermetic packaging
- Electrical connectivity to other systems

- Thermal dissipation

Unlike macro scale systems, microsystems are, in general, highly un-related i.e. independent of each others in terms of component design, mechanical configuration and so on. This leads to a new package design problem for each new microsystem. Thus almost 75% of the cost of manufacturing goes into packaging. Although the range of packages is vast, they can be loosely grouped into several categories such as: (i) metal package, (ii) ceramic package, (iii) plastic package, (iv) thin-film multilayer package.

Metal packages are often used for RF MEMS because of their excellent thermal dissipation and electromagnetic shielding ability. Also these packages can offer high mechanical reliability.

On the other hand, ceramic packages provide low mass, low cost and they can be easily mass produced. They can be made hermetic and can be integrated in signal lines.

Plastic packages are widely used because of their low manufacturing cost. But they are not hermetic and thus may have reliability issues. The packages are also susceptible to cracking in humid environments during temperature cycling of the surface mount assembly of the package.

Thin-film multilayer packages use sheets of polymide in a laminated fashion. They have low permittivity and thus provide low capacitance.

Typical packaging types are:

- Package to MEMS attachment
  - Die attach
- Chip scale packaging
  - Flip chip
  - Ball Grid Array (BGA)

        * Ceramic Ball Grid Array (CBGA)
        * Plastic Ball Grid Array (PBGA)
        * Micro Ball Grid Array (μBGA)
- Multichip packaging
    - Multichip module High density integration (MCM/HDI)
        * Chip on flex (COF/HDI) technology
        * MEMS test chip
    - System on a chip (SOAC)
- Plastic encapsulated microelectronics (PEM)

6.3.5 Compliant vs. non-compliant mechanism for microassembly

In case of microassembly, the micropart joinery can be established through compliant or non compliant mechanisms. Snap-fastener based compliant mechanisms can offer easier assembly steps as the parts snap lock to each other. They also provide tolerance to minor misalignment. Non-compliant joints require application of some form of adhesive to secure the joinery. They also require greater degree of precision in alignment. However, non-compliant joineries can be achieved within lesser area. Compliant joints require larger area to accomodate additional mechanisms. Figure 6.2 shows a rendering of typical compliant and non-compliant 3D microassemblies.

Figure 6.3 shows compliant MEMS part held by a passive jammer next to a non-compliant assembly. As seen, the non-compliant part is much smaller than the compliant part.

6.4 Centralized database and query-based evaluator for micromanufacturing process

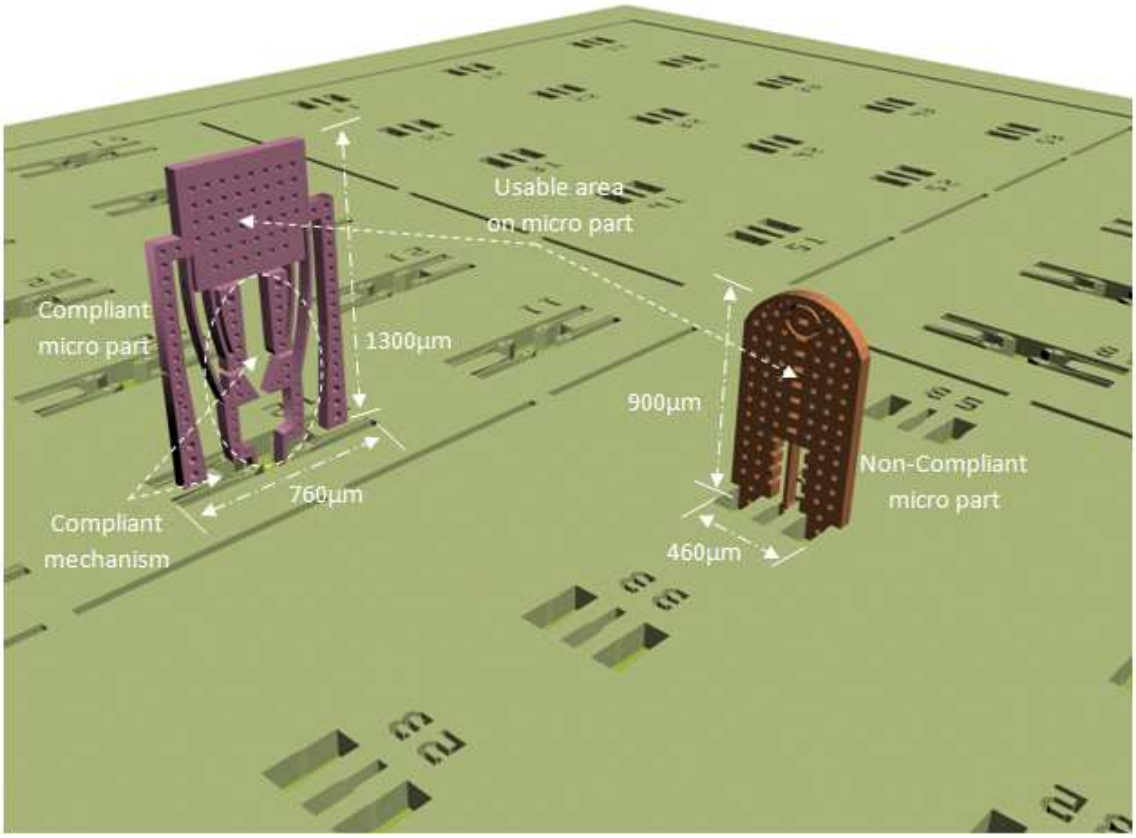

Figure 6.2. Compliant microassembly vs noncompliant microassembly.

analysis

In our research, we employ a simple and modular approach to concurrent micro-manufacturing. The framework consists of two main parts; the first one is a modular centralized database and the second one is a query-based evaluator. The database has been built and updated from time to time based on available information from known data and experimental results. The structure of this database is shown in figure 6.4.

The more the data available and the more they are updated to-date, the more will be the assurance of success in concurrent evaluation.

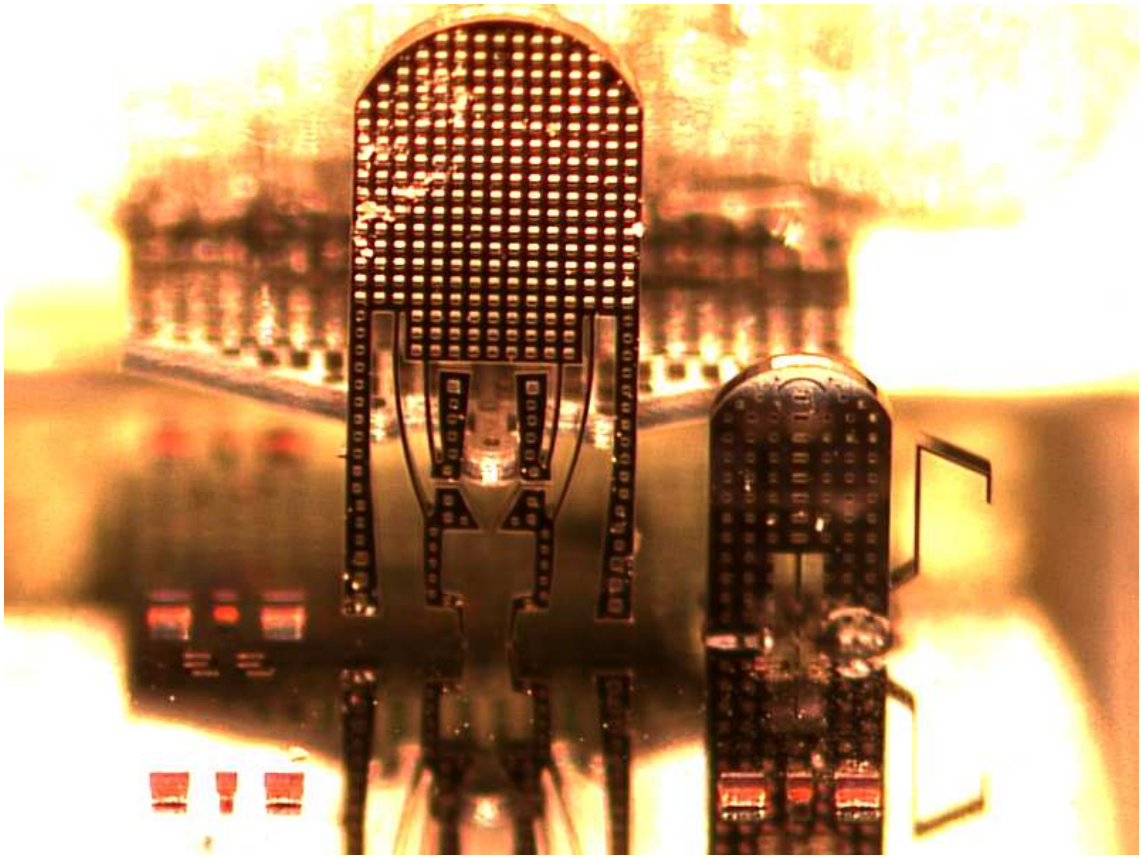

Figure 6.3. Compliant and noncompliant microparts.

The second part to the proposed framework is a front-end query-based evaluator which seeks relevant information for a specific system, task or design. All related information are collected from the database and a set of possible solutions for processes are presented to the user for a specific set of cost functions such as yield, throughput, cost etc. Figure 6.5 shows a snapshot of the query-based evaluator.

Alternatively, a neural network framework can be used for such concurrency. However, for highly un-correlated data from widely diverse processes, as in case of microsystem development, neural net approach does not prove to be beneficent. Hence we use the dicussed two-fold framework (i.e. the modular database and the query-based evaluator) which much simpler and faster in execution.

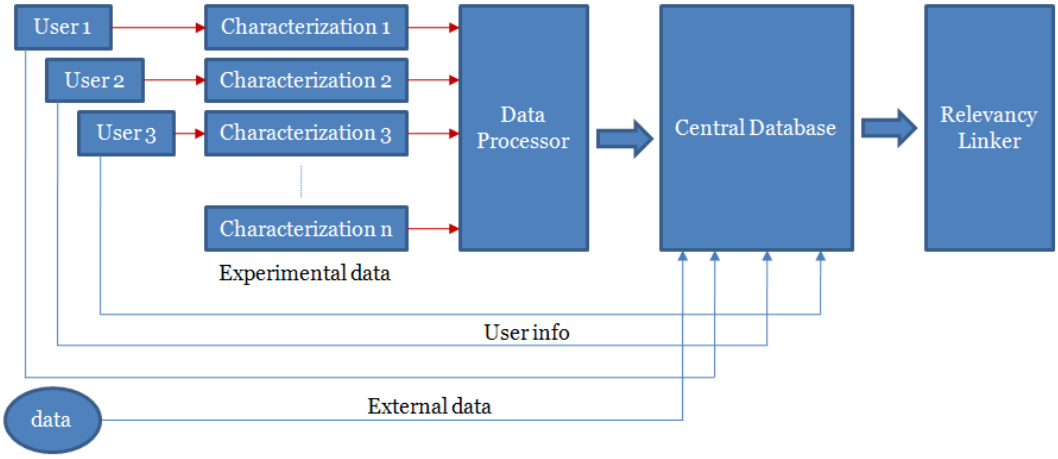

Figure 6.4. Centralized database structure for concurrent micromanufacturing.

6.5 Example: automated microassembly of ARRIpede microrobot

In this example we will be discussing how concurrent micromanufacturing can be used to successfully build a microrobot.

6.5.1 Microrobot description

The ARRIpede microrobot consists of an array of prismatic joints fabricated on a 1cm × 1cm area Silicon on Insulator (SOI) die using deep-reactive-ion-etching (DRIE). The prismatic joints consist of chevron electro-thermal actuators with a micro snap fastener. Silicon legs assembled to these micro snap fasteners move back and forth to create a stick and slip crawling motion. The prototypes were designed to consist of 4, 6 and 8 actuated legs.

6.5.2 Setting the requirements

To begin with, we build a set of functionality requirements as listed below.

1. The overall device area must be 1cm × 1cm or less.

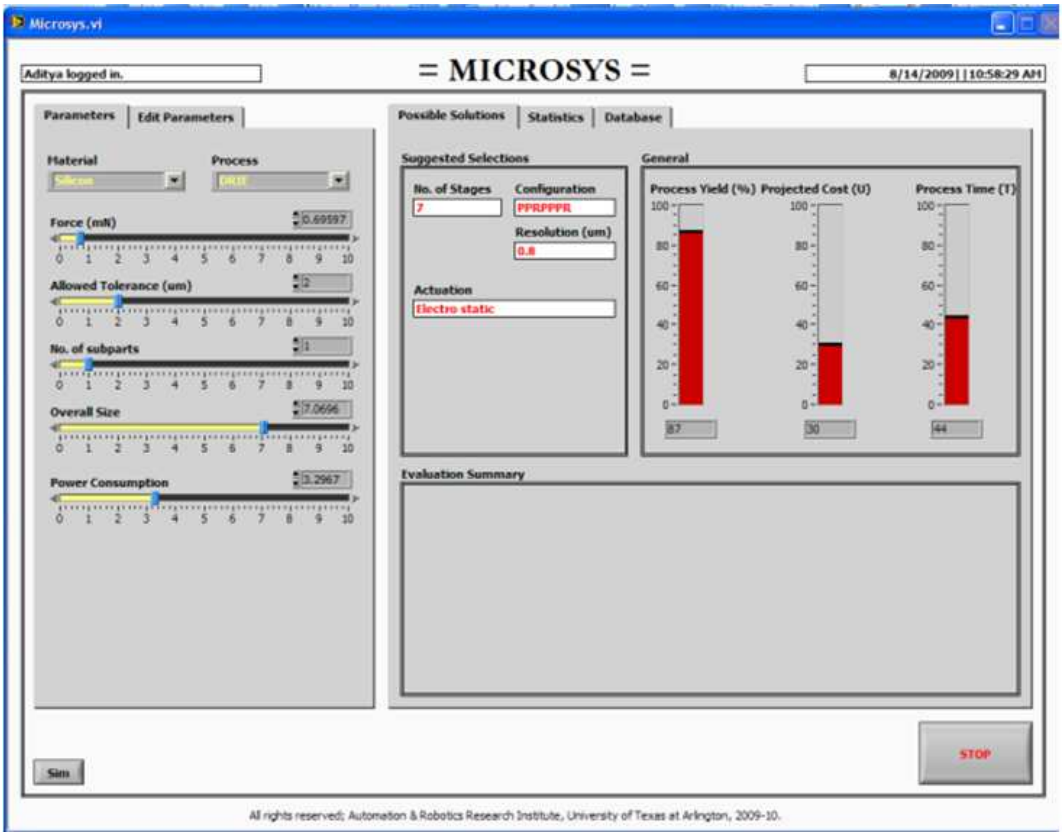

Figure 6.5. Query-based evaluator for concurrent micromanufacturing.

2. The robot leg count and design must be selected such that it should be able to overcome the static friction from completely rest position to reach a velocity of 15mm/s as well as steer.
3. The mechanical structure should be able to carry its own weight and payload of accessories such as electronics backpack, sensors etc.
4. The robot should be able to run in untethered mode for at least 10 to 15 minutes without having to recharge the onboard power source.

6.5.3 Finding the solutions

According to these basic requirements, we query the database for possible solutions which suggested the following:

1. Considering the space constraint for the device, 3D microassembly should be used to simplify the micropart and joinery designs. We avoid in-plane hinge joint mechanisms as they can consume a lot of space for the specified number of legs as well as monolithic fabrication will require a lot of layers, thus making the device a lot expensive.
2. Considering the possible materials, SOI MEMS through DRIE process is a good choice for making the microparts as it can provide the necessary mechanical rigidity through thicker parts.
3. Considering the complexity of assembly automation and workspace limitations to include additional end effectors such as adhesive dispenser, compliant snap fastening joints are selected.
4. Considering the type of actuator, we require higher force and displacement with low foot-print on the device. The evaluator suggested the use of either piezoelectric or thermal actuators. In case of piezoelectric actuators additional assembly steps are required to attach the piezo element and provide interconnects. Thus we select thermal actuators. The disadvantage of thermal actuators, however, is large power consumption and heat dissipation issues.
5. A novel power cycling technique is incorporated to optimize the power consumption, speed and run-time. A microcontroller based gait profile generation circuit is used along with power electronics module.

6.5.4 Assembly scheme, packaging with electronic backpack

The device die for the ARRIpede microrobot is shown in figure 6.6.

Compliant SOI microparts, which are to be used as robot legs, are batch fabricated. These compliant parts are picked up using a micro jammer, rotated by 90^o

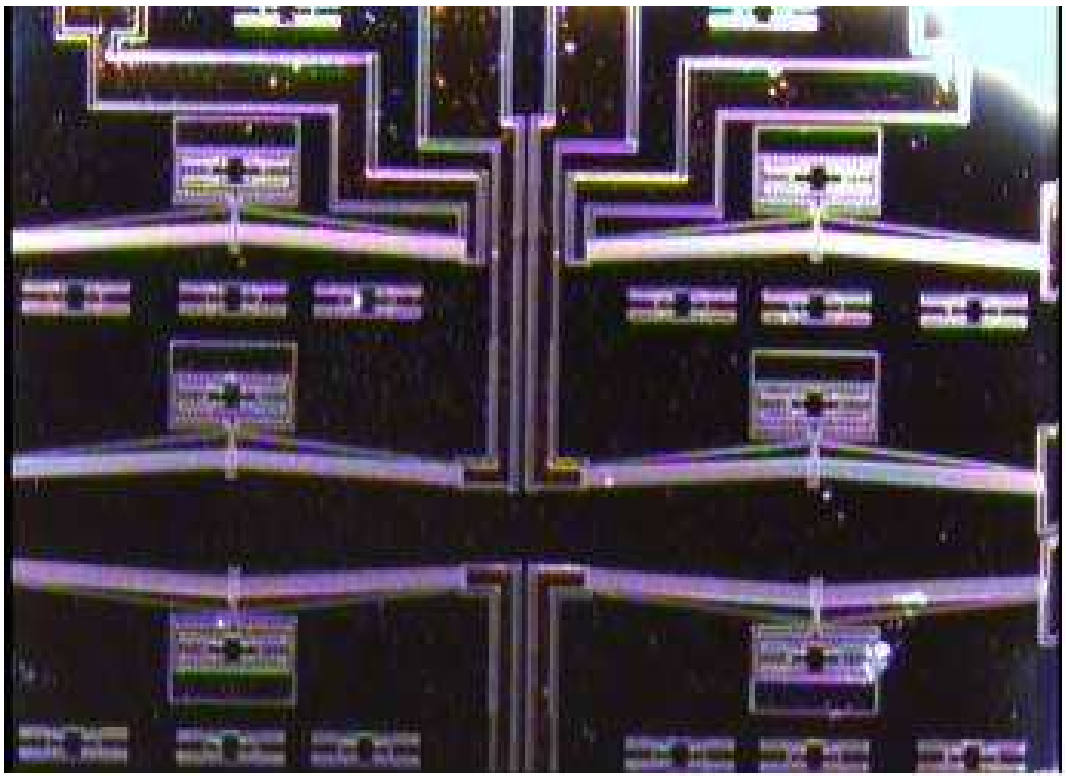

Figure 6.6. Arripede microrobot device die.

and placed in compliant sockets. The automated assembly scheme to assemble eight legs is as follows:

1. Move the robots M_1, M_2 and M_3 to assembly ready positions i.e. robot M_3 carrying the parts and device die is moved to present the part feature into the sensor field 1 (top microscope looking vertically down) and robot M_2 carrying the microjammer to pickup ready position. These moves are carried out using ***calibrated open loop control***.
2. Using active visual servoing move robot M_3 to bring the part feature to the center of the image frame (or any other location that has been assigned as the pickup point). This operation is carried out using ***calibrated closed loop control***.

3. Bring the needle on M_1 to break the tether to release the micro part. This operation is carried out using ***calibrated open loop control***.
4. Break the tether by ramming the needle to it. This operation is carried out using ***un-calibrated open loop control***.
5. Retract the needle on M_1 back to its home position. This operation is carried out using ***un-calibrated open loop control***.
6. Using active visual servoing move robot M_3 to realign the part feature to the center of the image frame (or any other location that has been assigned as the pickup point). This operation is carried out using ***calibrated closed loop control***.
7. Pick up the part using the micro jammer on M_2 robot. This operation is carried out using ***un-calibrated open loop control***.
8. Correct the error (if any) in pick up, if any, by active servoing through sensor 2 (side microscope looking horizontally). This operation is carried out using ***calibrated closed loop control***.
9. Move the M_3 robot to bring the socket feature into sensor field 1. This operation is carried out using ***calibrated open loop control***.
10. Using active visual servoing move robot M_3 to bring the socket feature to the center of the image frame (or any other location that has been assigned as the placement point). This operation is carried out using ***calibrated closed loop control***.
11. Place the part into the socket by moving the jammer on robot M_2. This operation is carried out using ***un-calibrated open loop control***.
12. Bring back the robots to ready position as in step (1).

The above process is repeated eight times for eight legs. The assembled micro-robot with eight legs is shown in figure 6.7.

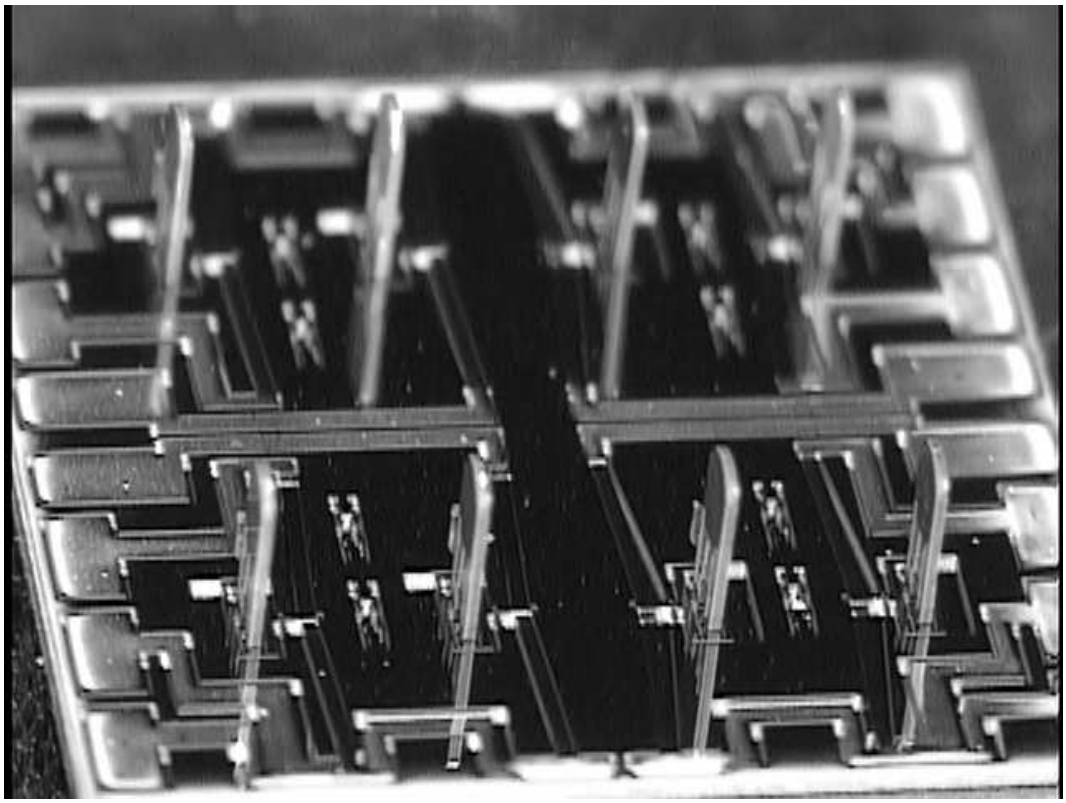

Figure 6.7. Arripede microrobot device die.

Next the electronics backpack is put together and combined to the assembled device die. The completed robot with electronics backpack is shown in figure 6.9. The gait profile generated by the microcontroller electronics for four of the robot legs is shown in figure 6.8.

6.6 A few other examples: Compliant, noncompliant and heterogeneous microsystems

Chapter 5 discusses the microspectrometer with great detail. The microspectrometer is a heterogeneous microsystem which consists of several different microparts of different material, size and shape. Both compliant and noncompliant microparts are used to build this complex system. Compliant mechanism is used for $2\frac{1}{2}D$ MEMS

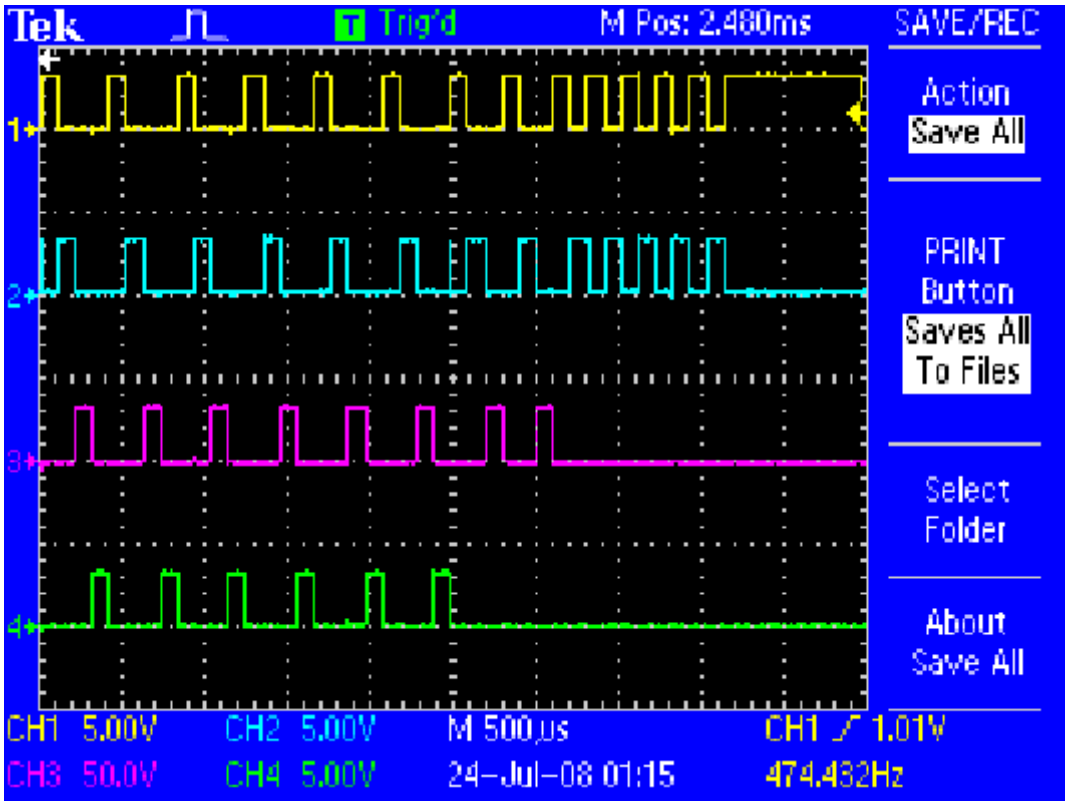

Figure 6.8. Arripede gait signal as observed by a CRO (for four channels).

parts where as noncompliant bonding is used for bigger 3D parts. The electronics backpack for completed microspectrometer is discussed in Appendix-D.

In addition to these microsystems, it has also been demonstrated that through careful selection of design and processes manufacturing of complex MEMS structures can be automated with high yield. Figure 6.10 shows steps of a multilayer microassembled MEMS structure.

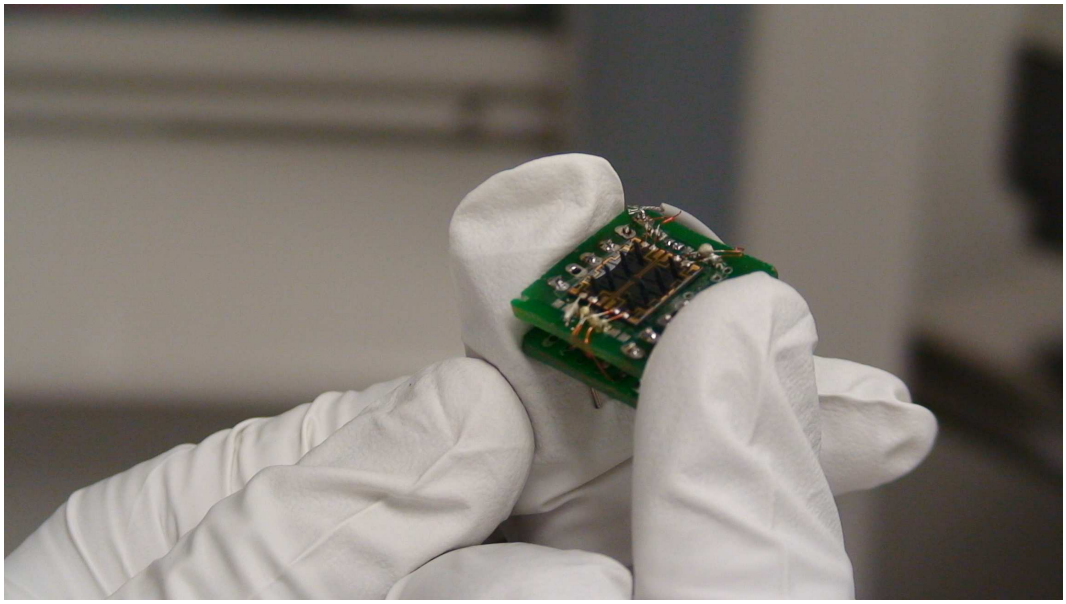

Figure 6.9. Arripede microrobot packaged with electronics backpack.

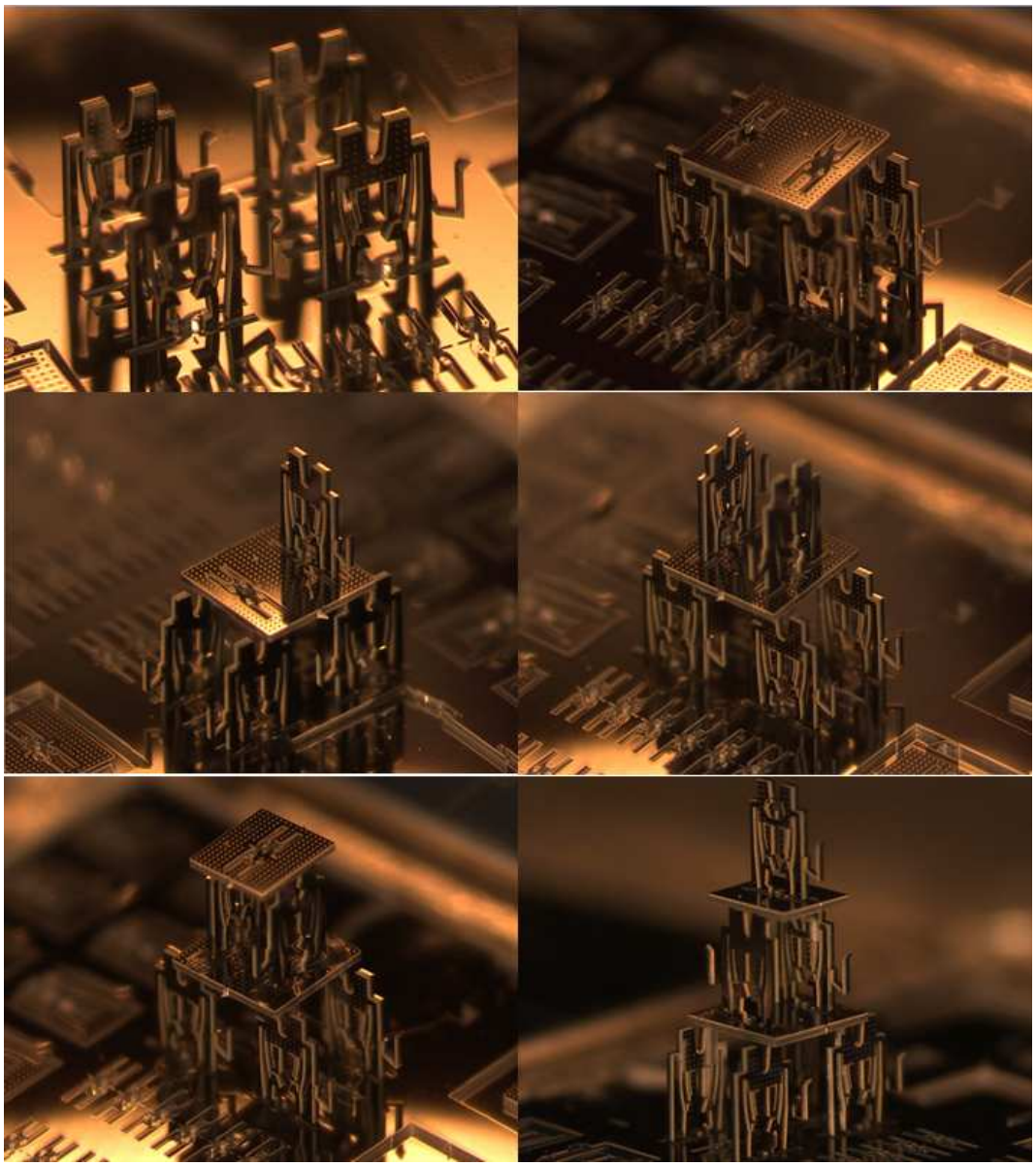

Figure 6.10. Construction of a multilayer MEMS structure.

CHAPTER 7

CONCLUSION

7.1 Conclusion

Microassembly is an enabling technology for micro manufacturing that offers well-known pathways to building heterogeneous microsystems with a higher degree of robustness and more complex designs than monolithic fabrication. The success of assembly in micro domain, however, is directly related to the level of precision automation employed. Control and planning are two defining factors for the microassembly yield and its cycle time. Assembly at the microscale harbors many difficult challenges due to scaling of physics, stringent tolerance budget, high precision requirements, limited work volumes, and so on. These difficulties warrant new control and planning algorithms, different than their macro-scale counterparts.

In this research, we have investigated different aspects of automated microassembly. From the survey and analysis it has been found that microassembly can emerge as a viable alternative to conventional surface micro machining techniques for building complex microsystems of future. Some features such as heterogeneousness, robustness with less foot-prints, simple part design etc. can only be addressed through microassembly.

We examined different approaches to microassembly and concluded that, when used with proper planning and control scheme, deterministic serial top-down assembly approach can guarantee high yield. The limitations of such approach, i.e. complex setup and longer process time with closed loop control structure, can be minimized by using a hybrid controller based on reliable estimation of precision during execution of

intermediate tasks. To ensure high reliability in precision estimation, we re-defined the classical exegesis for metrics, such as *"resolution, repeatability and accuracy (RRA)"*, to include sensor precision in the evaluation process. Further we defined a criterion called *"High Yield Assembly Condition (HYAC)"* which gives quantitative measure of assemblability in a microassembly workcell.

Using this *HYAC* quantitative tool, we formalize a precision-adjusted hybrid controller switching between open, closed, and calibrated operation in the microassembly cell. The precision adjusted hybrid supervisory controller has been proposed to reduce the assembly time keeping the precision and consequently the yield at maximum. A binary logical operator defined as "complexity index" has been defined and used to flag a subtask as complex or non-complex based on the HYAC after computing the precision metrics through (resolution-repeatability-accuracy) RRA rules. Based on the complexity index, the hybrid supervisory controller determines the necessary and sufficient control structure for the particular assembly subtask. Preliminary experimentations with the proposed hybrid controller demonstrates that the precision adjusted hybrid supervisory controller can improve the time expense by up to 60% in comparison to pure feedback open loop control and also improving the accuracy by up to 35% in comparison to pure open loop control structure.

Planning is another aspect of automation which in the end determines the feasibility and cost overhead of the process. We formulate a *"Precise path search algorithm (PPSA)"* for motion planning in microassembly. In contrast to conventional shortest path planning techniques, the proposed *"PPSA"* searches for a precise path. The precise path may or may not be equal to the shortest path, therefore does not ensure minimum travel time. However it ensures minimum uncertainty at the end point of the path. Robot kinematics and precision along individual degrees of freedom has been incorporated to determine the precise path.

A complex micro-opto-electro-mechanical-systems (MOEMS) in the form of a microspectrometer has been studied. The microspectrometer is a complex microsystem consisting of multiple heterogeneous parts configured in a tightly tolerable optical alignment. The microspectrometer works on the principle of Michelson interferometry and uses Fourier transformation of the acquired signal to reconstruct the spectrum of a medium ranging from visible to near infra red. The assembly of microspectrometer requires precise optical as well as mechanical alignment and minimum error securing mechanics. Compliant snap fasteners have been used to join the micropart. Using a twofold alignment procedure namely a coarse alignment for more tolerable micro components and a fine alignment based on a novel spot Jacobian servoing the microspectrometer has been prototyped and tested for its functionality. Using a moving mirror scanning in contrast to fixed gratings, the operational range of the microspectrometer has been increased by a large factor. It has been demonstrated that the microspectrometer can identify the wavelength of light with 5nm resolution in visible range and 25nm resolution in NIR range.

Concurrency in manufacturing is useful and almost essential in micro domain considering the diverse process specifications. Through pre-fabrication evaluation of manufacturing cost functions such as yield, throughput and cost; these parameters can be greatly improved. In this research we use realistic simulation in a custom build virtual reality application to reliably predict the manufacturability of a specific micro assembly/packaging task. Based on this information and result from extensive experimentation with actual MEMS parts, we have developed a tool that can be used to provide solutions to a micromanufacturing process for a specific set of cost functions i.e. yield, throughput and process cost. A centralized modular database as the backend and a user friendly software interface application as the frontend have been designed to implement concurrent aspects of micromanufacturing.

Miniature electronics modules for power systems as well as logic control have been built for untethered microsystems. Custom built reconfigurable software applications helps in automation of modular multiscale assembly, testing and characterization.

7.2 Future work

Future works include further characterization and refinement of the planner and controller, including formal performance guarantees, and a study of tradeoffs between real-time change in tolerances, cycle time and yield, and dynamic reconfiguration of the system for wide range of microassembly tasks.

Concurrenncy is not only beneficial but also essential in micro manufacturing. Future works will also focus on building manufacturable MEMS through automated microassembly by further analysis of process parameters and their effect on manufacturing cost functions.

APPENDIX A

HARDWARE CONFIGURATION - μ^3 MICROASSEMBLY SYSTEM

The μ^3 microassembly setup is a reconfigurable robotic manipulation system comprising of three primary robots named as M_1, M_2 and M_3. These robots are configured using a collection of high precision linear, rotational and tilt stages in a certain way to provide the required degrees of freedom for microassembly task at hand. There robots are fully reconfigurable and interchangeable. In addition to these robots, there are two XYZ nano positioners with 1nm resolution.

A.1 Robot stages

- ***Translation stages***

  The μ^3 robots use single axis translation stages from *physikinstrumente: model no. M-112-1DG*. The technical specifications are given in table A.1. Figure A.1 shows a picture of the translation stages.

Figure A.1. Translation Stages.

- ***Rotational stages***

  Each of the three robots of μ^3 systems is equipped with a rotational stage. The stages are from *physikinstrumente: model no. M-116-1DGH*. The technical

Table A.1. Technical specifications of linear stages

Parameter	*Specification*	*Unit*
Travel range	25	mm
Sensor	Rotary encoder	-
Sensor resolution	2048	counts/rev.
Motion resolution	0.05	μm
Repeatability (unidirection)	0.1	μm
Maximum velocity	1.5	mm/s
Maximum load	20	N
Operating volatge	12	V
Power consumption	1.75	W
Mass	0.5	kg

specifications are given in table A.2. Figure A.2 shows a picture of the rotation stages.

Figure A.2. Rotational Stages.

- ***Tilt stages***

  The M_3 robot of the μ^3 system is equipped with a two-axis tilt stage that can tilt the die holder upto 7 degrees. The technical specifications for this

Table A.2. Technical specifications of rotational stages

Parameter	*Specification*	*Unit*
Rotation range	360	degrees
Sensor	Rotary encoder	-
Sensor resolution	2048	counts/rev.
Motion resolution	3.16	μrad
Repeatability (unidirection)	10	μrad
Maximum velocity	20	degrees/s
Operating volatge	12	V
Power consumption	1.75	W
Mass	0.4	kg

physikinstrumente: model no. M-044 stage are given in table A.3. Figure A.3 shows a picture of the tilt stage.

Figure A.3. Tilt Stages.

- ***Nano Positioners***

  The M_1 M_2 robots of the μ^3 system are equipped with one three-axis nano positioning stage, each. The technical specifications for this *physikinstrumente*

Table A.3. Technical specifications of tilt stage

Parameter	*Specification*	*Unit*
Tilt range	7	degrees
Motion resolution	65	μrad
Mass	1.2	kg

piezo stages are given in table A.4. Figure A.4 shows a picture of the nano cube.

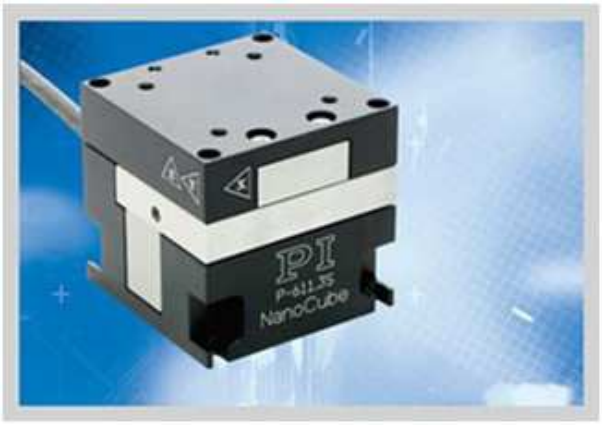

Figure A.4. Nanocube Stages.

A.2 Stage Controllers

- ***Motorized stage controller***

  The linear, rotational and tilt stages are controlled by common stage controllers from *physikinstrumente: model no. C-862 or C-863.* For each servo stage there is a controller. These controllers are connected in a daisy chain fashion and finally the chain is connected to the host computer through a standard serial

Table A.4. Technical specifications of Nanocube

Parameter	*Specification*	*Unit*
Active axes	X, Y, Z	-
Travel range	100	μm
Motion resolution	1	nm
Repeatability	10	nm
Pitch in X, Y	5	μrad
Load capacity	15	N
Mass	0.32	kg

port. The technical specifications are given in table A.5. Figure A.5 shows a picture of the controller.

Figure A.5. Servo Stage Controller.

- ***NanoCube piezo stage controller***

  The two nanocube stages on M_1 and M_2 are controlled by special piezo controllers from *physikinstrumente: model no. E-664*. The technical specifications are given in table A.6. Figure A.6 shows a picture of the controller.

Table A.5. Technical specifications of servo stage controller

Parameter	*Specification*
Function	Stand alone DC-servo-motor controller
Servo characteristic	31-bit registers, 16-bit PID
Output Power	15-watt PWM
Limit switches	2 TTL
Origin switch	1 TTL
Motor brake output	5V TTL
Additional I/O lines	5V TTL
Interface	RS-232, 9-pin D-Sub
Operating voltage	12 - 15 volts, 1 - 2 A
Weight	0.3 kg

Figure A.6. Nanocube Controller.

A.3 Robot Configuration

As dicussed above, the μ^3 system consists of three reconfigurable robots M_1, M_2, and M_3. Among them, they provide 19 degrees of freedom in total. Figure A.7 shows the three robots and their degrees of freedom. In figure A.8 the actual μ^3 hardware setup in ARRI's *"Texas Micro Factory"* is shown. Figure A.9 shows a simplified 3D rending of the microassembly system.

Figure A.10 shows the servo controller for the stages.

Table A.6. Technical specifications of nano cube controller

Parameter	*Specification*
Function	Power amplifier
Axes	3
Servo characteristic	P-I (analog), notch filter
Input voltage	-2 to +12 V
Output voltage	-20 to +120 V
Peak Output Power	14-watt per channel
Average Output Power	6-watt per channel
Peak Output Current	140mA per channel
Average Output Current	60mA per channel
Voltage gain	10
Operating voltage	90-120/220-240VAC
Weight	3 kg
Max power consumption	60 W

A.4 Vision system

The μ^3 microassembly system consists of four high magnification microscopes. Two of these microscopic cameras are used for active closed loop control during automated microassembly. All of these four cameras can be used for tele-operated (visually guided) manual microassembly as well. One microscope, looking vertically down, is fixed on a dedicated motorized z-stage which can move the camera up or down to automatically adjust focus on feature. Another camera, looking horizontally from side, is placed on a manually adjustable xyz stage which can be used to move the camera in X, Y, and Z direction upto a maximum travel range of 1 inch. The rest two microscopes are strategically placed at an angle of 60^o looking from the front and the back. The magnificaiton of the vertical camera can be selected among fixed values of 2X, 5X, 10X and 20X by changing the *"mitutoyo"* objective lens (see figure A.11). The magnification for the rest three cameras can be adjusted between 0.7X to 4.5X (*"Manufacturer: Edmund Optics, model no.:VZM-450"*) as shown in figure

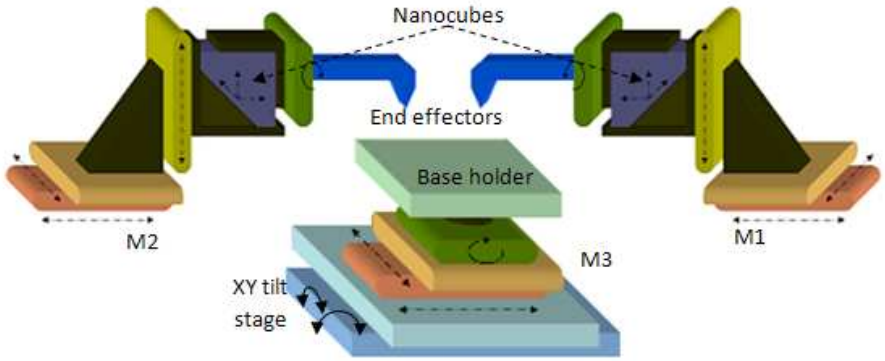

Figure A.7. Schematic of μ^3.

A.12. Finally high resolution color digital cameras from *"Hitachi", model no.:KP-FD140F* are used for image acqusition. These maximum resolution of these cameras are 1390 pixels x 1024 pixels. They connect to the host computer through high speed IEEE-1394-b (800Mbps) bus.

A.5 Signal communication hardware

Various signal communications such as image acquisition, data acqusition, motion control etc. are achieved using *National Instrument's* hardware (PCI-6229, PCI-6733, PCI-7350, PCI-1410, BNC-2110). These interfaces connects the external hardware to the host computer. Figure A.13 shows the interface cards.

A.6 Other peripherals

To accomplish multiple tasks the μ^3 system also consists of several peripherals. A vacuum generator from *Virtual Industries (model no.:SMD-VAC-HP)* (see figure A.14) and an autocollimator from *Micro radian (model no.:TL 40)* (A.15) are couple of such peripherals.

Figure A.8. μ^3 Microassembly system at *ARRI*.

To bond micro structures for better strength and robustness we use an epoxy glue curable by ultra violet light. The three different types of epoxy glues used are from *Dymax* and the viscousity of them are 750centiPoise, 3500centiPoise and 11000centiPoise. A ultraviolet light curing system (see figure A.16) is used to cure these adhesives.

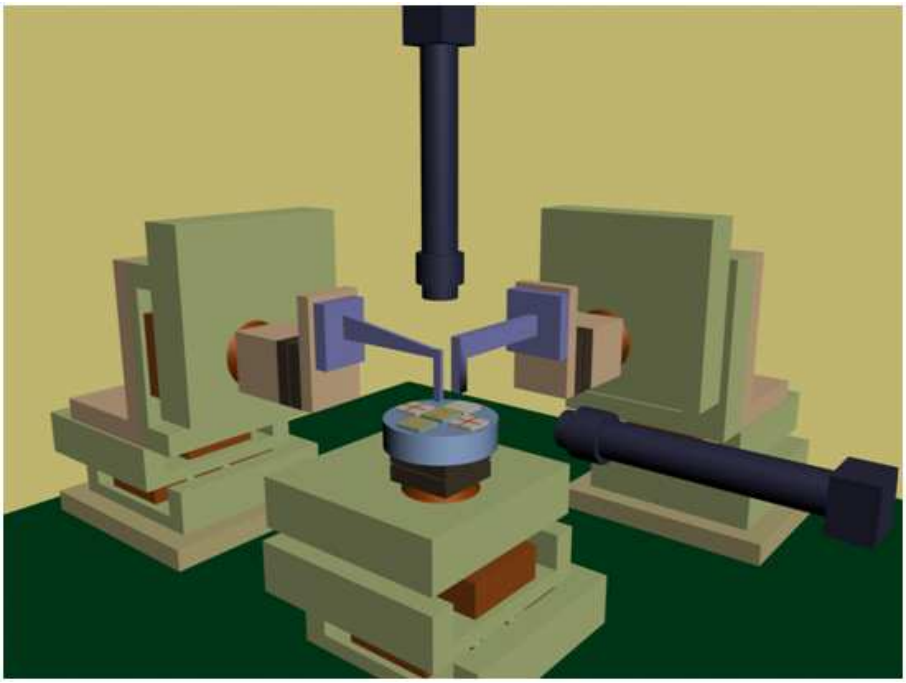

Figure A.9. Simplified 3D rendering of μ^3 microassembly system.

Figure A.10. Controller Box of μ^3 microassembly system.

Figure A.11. High magnification objective lenses.

Figure A.12. Adjustable zoom lenses.

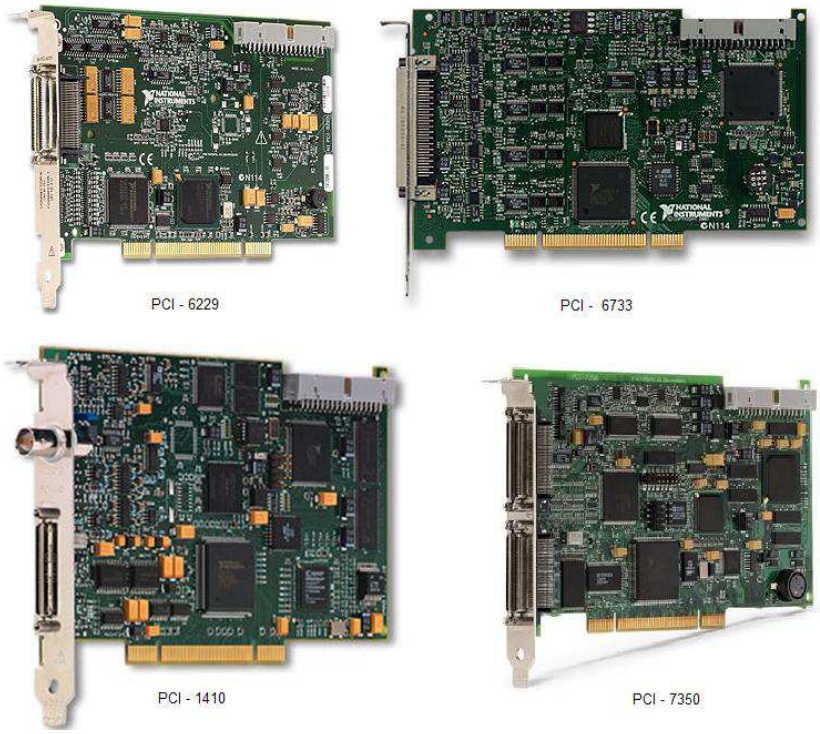

Figure A.13. Signal communication interface cards from *National Instruments*.

Figure A.14. Vacuum generator system.

Figure A.15. Autocollimator.

Figure A.16. Ultra violet curing system.

APPENDIX B

SOFTWARE APPLICATION - NEPTUNE 3.0

As we discussed in the previous section, the μ^3 microassembly system comprises of multiple robotic manipulation stages having different type of controllers. In addition, the system also integrated with multiple high resolution microscopes, measurement units, dispensing units, curing module, power supplies and so on. To integrate all these diverse systems and provide the user an easier and interactive way to handle the system for general microassembly tasks, it is necessary that an easy-to-use, readily reconfigurable and interactive software application be made available. *"Neptune version 3.0"* is an indigenously developed software application that serves this purpose. This complex application program has been written using *National Instrument's LabVIEW* development tool, *Microsoft's visual studio .NET* and *Mathwork's Matlab*. Along with basic features such as robot configuration, machine vision, robot controls, the *Neptune 3.0* is also capable of performing manual microassembly, semi-automated as well as fully automated microassembly through advanced machine vision algorithms for system calibration and visual servoing. Moreover, the *Neptune 3.0* is equipped with testing modules to analyze the precision of the robot and vision system through statistical analysis. Figure B.1 shows a snapshot of the *Neptune 3.0* interface. In the following sections we will briefly discuss some of the algorithms used in this application.

B.1 Image acquisition

The image acquisition module of *Neptune 3.0* can simultaneously capture four high resolution cameras connected to the PC through Firewire 1394.b interface. To use this module follow these steps (see figure B.2).

1. To change default settings toggle the [Unlock VideoMode] switch to ON position.

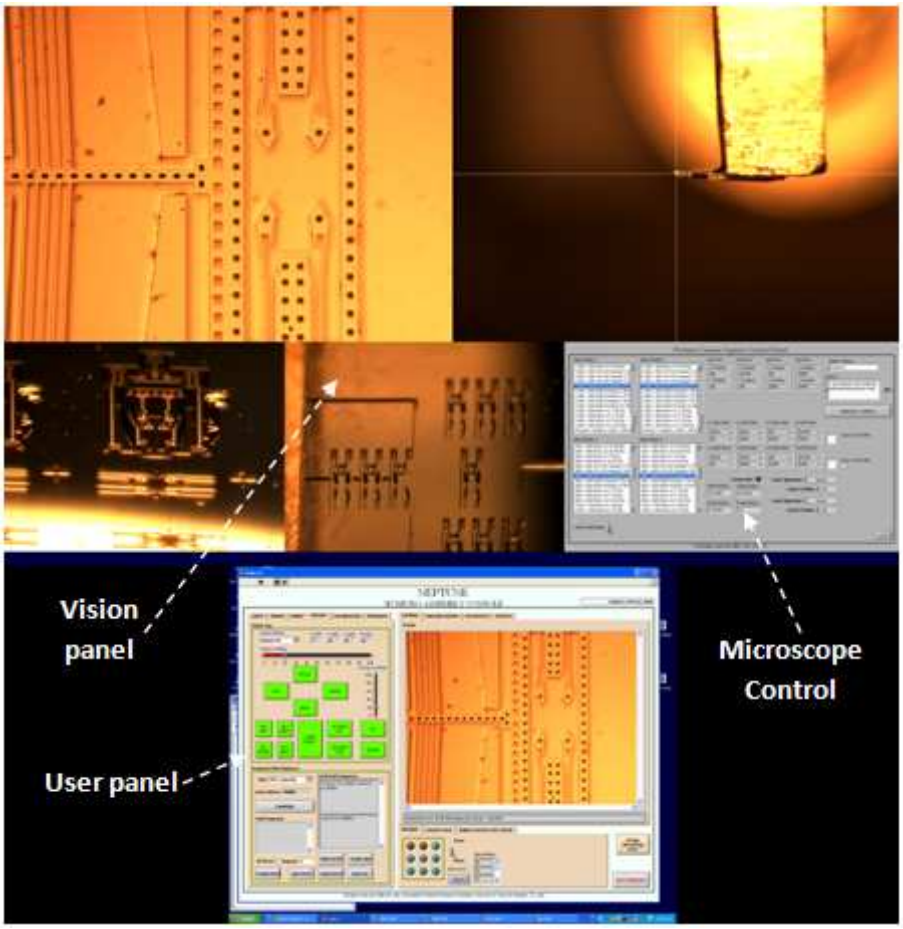

Figure B.1. Automation software *Neptune 3.0*.

2. The video mode for each camera can be selected from the available list for corresponding camera.
3. The location for camera view window on the monitor can be altered by changing the corresponding XY position.
4. Camera 1 and camera 2 images can be overlaid with customizable cross hairs by clicking on the [Cam 1 Cross Hair] and [Cam 2 Cross Hair] check boxes. The lines for the cross hair and color can also be configured.
5. In grayscale mode (selectable in the main user interface) the captured images from camera 1 and camera 2 can be optionally processed by a set of pixel

operators such as square, square root, log, power X and so on. Note that these setting only work in grayscale mode.

6. This module also allows the user to save snapshots. To grab a frame select the camera, select a file name to save and click on [SNAPSHOT CAMERA].
7. The frame rate for each camera capture is displayed on the interface. High resolution video mode on more cameras reduces the frame rate.

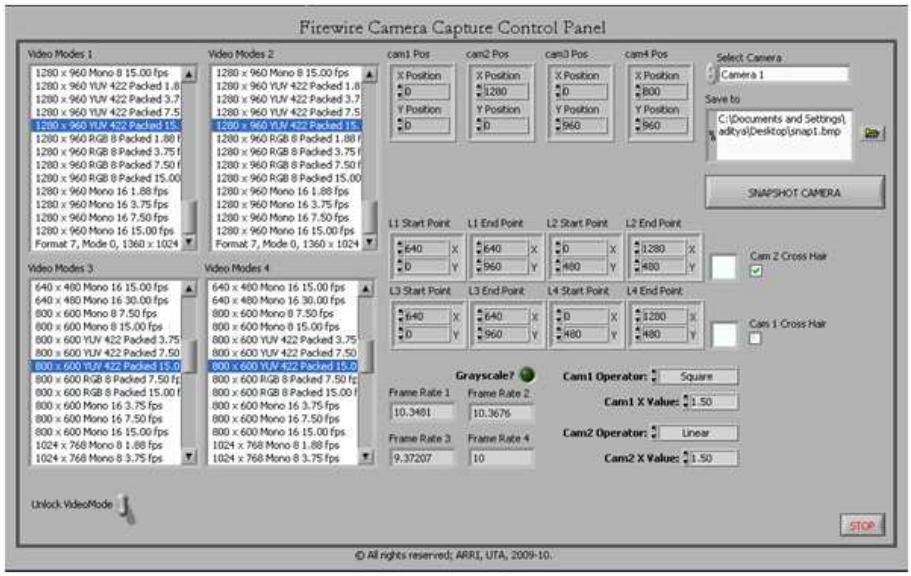

Figure B.2. Image acquisition with *Neptune 3.0*.

B.2 Machine vision

The machine vision module of *Neptune 3.0* takes care of pattern selection and matching applications for calibration and active servoing. The following steps describe how to use this module (see figure B.3).

1. Make sure camera is streaming image and proper camera is selected on the main user interface. You can optionally select to process as grayscale image by selecting the [Process as grayscale] check box.
2. There are two slots [Template Image A] and [Template Image B] for templates. Select the slot by checking the appropriate radio button.
3. To select a feature as pattern go to the [VISION] tab on the user interface. Click on the [CREATE TEMPLATE] button. A new window will open with the most recent image and a set of selection tools.
4. To create a template select a tool, drag and/or resize around the feature you wish to select and then click OK to save. Select the filename in the file dialog box and save the template image.
5. To load a previously saved template you can click on [LOAD TEMPLATE] button.
6. After loading the template click on the [LEARN TEMPLATE] to learn the template information for machine vision.
7. Once learnt the template can be searched on any image frame by clicking on the [SEARCH PATTERN] button. The search parameters can be altered for specific tasks. Note that in grayscale mode color options will not be processed.
8. The pattern, if found, will be identified by a small circle with crosshair at the center of mass and a bounding box around it for the template. The color of this bounding box and center of mass can be user-selected.
9. The match data is displayed in the [Pattern Matches] box.

B.3 Autofocus

Camera 1 is mounted on a motorized Z-stage to adjust the focus for different zoom settings and view planes. To use the focusing module follow these steps.

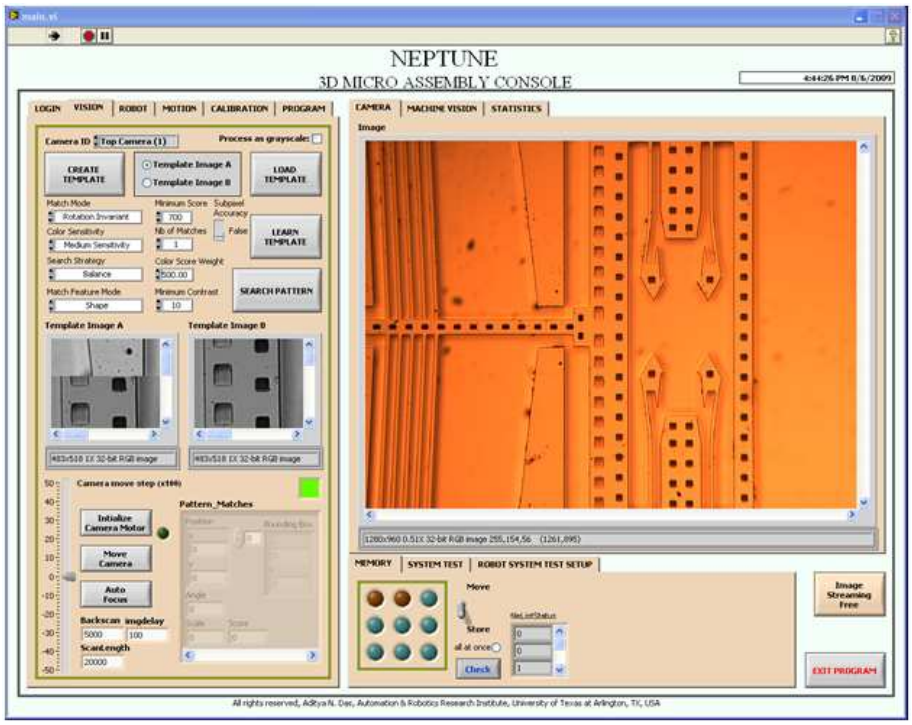

Figure B.3. Machine vision with *Neptune 3.0*.

1. Initialize the camera motor by clicking on the [Initialize Camera Motor] button, if it is not already initialized.
2. The vertical scale near the motor control buttons selects the up/down displacement in terms of positive/negative motor encoder readings. Note that each number is internally multiplied by 100.
3. An auto focusing algorithm can be initiated by clicking on the [Auto Focus] button. This algorithm first retracts the motor by the amount specified by the [Backscan], and then stepwise moves the camera motor by the amount specified by [ScanLength].
4. At each step a camera image frame is captured. The contrast level for each image is calculated from pixel data.

5. At the end of scanning the contrast data is plotted and a curve is fitted to the data. The maximum is found out from the curve and the corresponding motor encoder is interpolated.
6. Finally the motor is moved to the computed location.

A typical contrast interpolation data is shown in figure B.4.

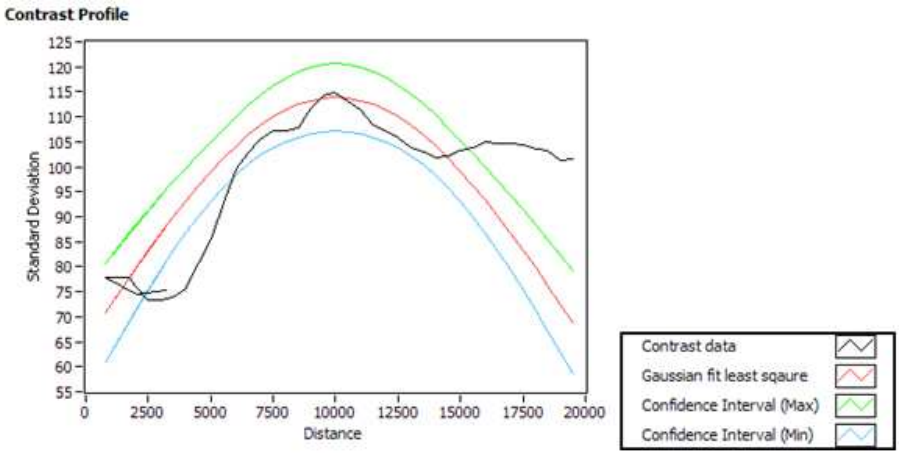

Figure B.4. Contrast interpolation for auto focusing.

B.4 Robot manipulation

The next tab on i.e. [ROBOT] tab (see figure B.5) on the main interface is used to configure and control the robots. To move the robot using this application following these steps.

1. To start with select the communication port and click on [CONNECT] button on the [ROBOT] tab. Upon successful connection the light next to Connect Error box will glow.
2. Click on [INITIALIZE CONTROLLERS] button to initialize all the controllers. Upon successful initialization the light next to Initialization Error box will glow.

3. The software can handle up to 16 controllers. Each controller is assigned with a checkbox. Select some of all of them as per requirement.
4. Clicking on [GET CURRENT VALUES] button gives the speed and acceleration of the selected stage.
5. The operator can set the speed and acceleration values for one or more controllers by clicking on [SET PARAMETERS] button.
6. Click on the [RETRACT AND HOME ALL SELECTED AXES] to retract the linear stages to their hard stop limit and set home as home position. For rotation and tilt stage the current position will be set as home position.
7. The next set of buttons serve for basic stage controls such as retraction [RETRACT], setting the home position [SET HOME], moving to home position [GO HOME], basic relative move command [MOVE] and extracting current position [POSITION]. To use these buttons for a specific axis select the axes from the [Motor ID] drop down menu. For [MOVE] button enter the desired displacement in [Offset:] box. Clicking on the [POSITION] button gives the current position and positional error in encoder reading for the selected axes.

B.5 Manual assembly in jog mode

The [MOTION] tab (see figure B.6) offers the user to perform manual microassembly in jog mode. The default manipulation system is configured into three robots M_1, M_2 and M_3. By selecting robot from the [Select Robot] drop down menu the manipulation for that configuration can be activated. The following steps explain how to use this module.

1. Select the robot to move.
2. The horizontal slider is used for linear XY, rotation and tilt displacements. The value in this slider is internally multiplied by 1000.

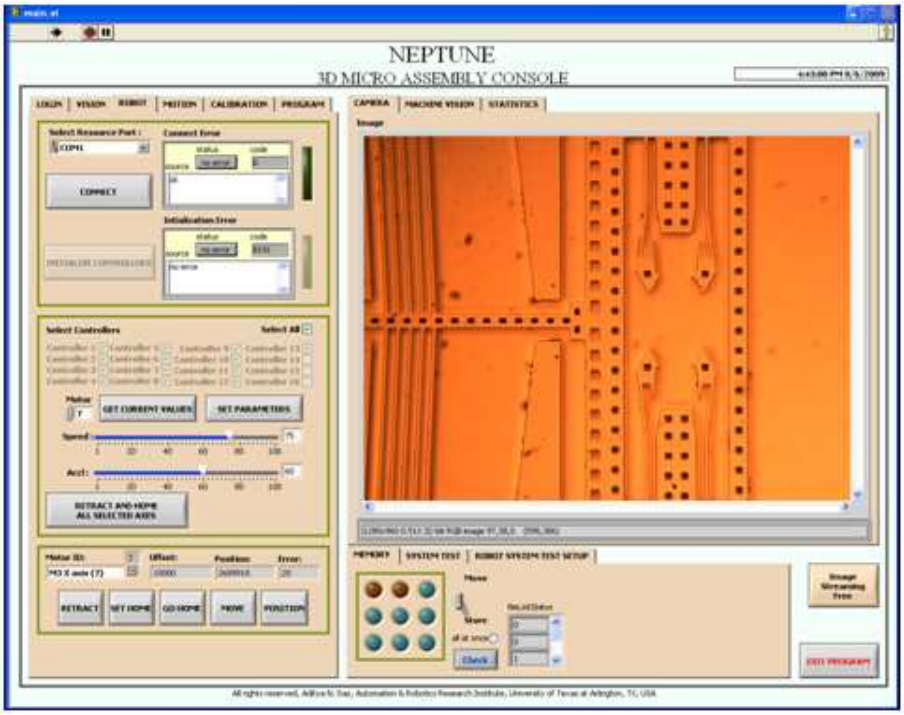

Figure B.5. Robot stage control using *Neptune 3.0*.

3. The vertical slider is used for specifying Z displacements. The value in this slider is internally multiplied by 1000.
4. The jog buttons are set from a perspective of a user sitting in front of the system. These buttons can be used for tele-operated manual micro assembly.

B.6 Semi-automated assembly module

In semi-automated microassembly mode, the operator can design, load, save and execute a path sequence for the robots to accomplish specific tasks. The steps are explained below.

1. To create a path, go to [Program Path Sequence] section on the [MOTION] tab on the main user interface.

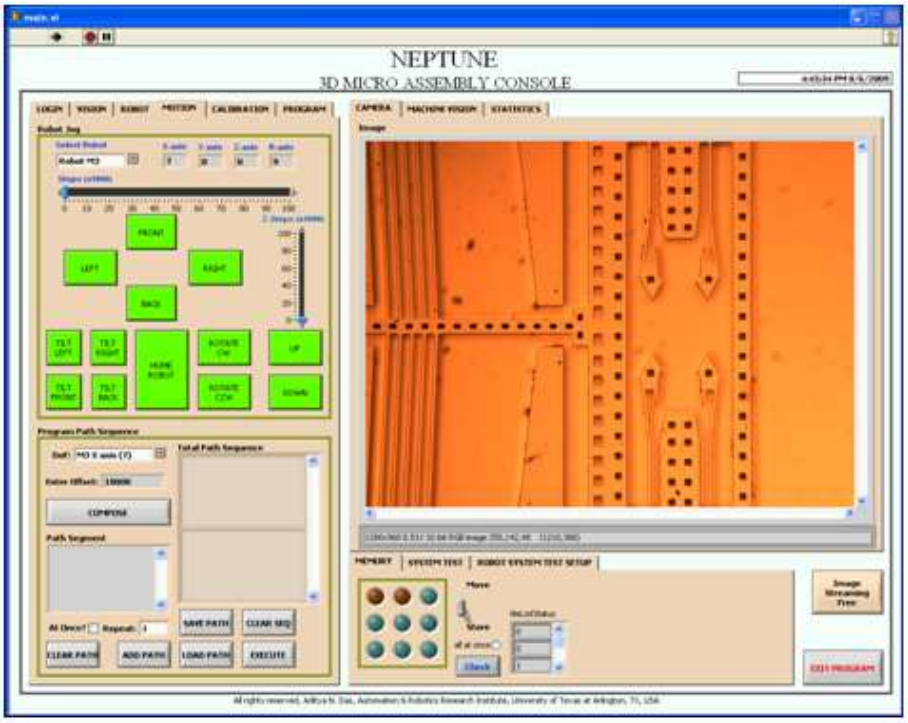

Figure B.6. Manual assembly using jog mode of *Neptune 3.0*.

2. Select the axes to include in the path and enter displacement value in encoder readings in the [Robot Offset] field.
3. Click on [COMPOSE] button to add to the path.
4. Repeat step ii and iii to add more paths to the path segment.
5. Once a path segment is composed, click on [ADD PATH] button to add the composed path to the [Total Path Sequence]. If more than one axes are selected in the path segment, the operator can choose to move all of them at the same time by checking the [At Once?] checkbox prior to adding the path segment to [Total Path Sequence]. Also enter a non-zero value in the [Repeat:] field to specify the number of repetitions required in the [Total Path Sequence].
6. The operator can save and load designed paths by clicking on the [SAVE PATH] and [LOAD PATH] buttons.

7. By clicking on the [EXECUTE] button the designed path in [Total Path Sequence] can be executed.

Another way to save and run motion segments is by the use of memory dots in the [MEMORY] tab on the lower right tab control.

1. There are 9 memory dots in total. Each can hold a pose configuration of the entire system. Cyan dots represent available memory locations whereas dark red dots are occupied.
2. To store a location throw the toggle switch to [Store] position and click on any memory dot. This action will write the current pose if the dot is free or it will overwrite the previous pose if the dot is occupied.
3. To move to any of the stored pose throw the toggle switch to [Move] location and click on the memory dot. This will move the robots to assume the stored pose. By checking the [all at once] radio button, all of the stages can be simultaneously moved.
4. Click on the [Check] button to check the memory dot status.

B.7 Fully automated assembly module

Fully automated microassembly required additional features such as system calibration, visual servoing, path planning and control and multiple event handling. For calibration and visual servoing use the [CALIBRATION] tab on the main UI (see figure B.7). The following steps gives an idea on how to use the module.

1. Follow the steps in sub-section (b) to create or load a template and learn it using the [VISION] tab.
2. On the [CALIBRATION] tab you can find checkboxes for each connected axis. Select the axes that you wish to include in calibration. Then click on the

[SET] button. This will fill the [Axes auto] array with the select axes and their corresponding positions.

3. Next, enter values for [translation offset], [rotation offset], [tilt offset] and [No. of points]. The offset values decide the maximum displacement that the type of axis is allowed to move. A random number is generated between the positive and negative values for this offset and the selected axes of the robot are moved to assume a random pose. The number of calibration points is specified in [No. of points] field.
4. If you wish to exclude rotation information then check the [Disregard Angle:] check box.
5. For small angles check the [Small Angle Correction:] checkbox. This will rectify the ambiguity in tracking due to symmetry in template image.
6. The delay between completion of robot move and acquisition of image can be specified in the [wait milliseconds to process:] field.
7. Finally, click on the [CALIBRATE] button to start calibration. The robot will move to the specified number of calibration points and image processing will be done. At the end of calibration the image Jacobian matrix will be computed which can be located on the [MACHINE VISION] tab on the top right tab control panel.
8. The pseudo inverse of this Jacobian matrix will also be displayed there. The user can save this calibration data or load a previously saved data by using the [SAVE CAL] or [LOAD CAL] buttons.
9. At the end of calibration process, the program automatically filters out bad data points and the number of good data points can be located in the [good data count:] field along with the time taken for calibration in the [Calibration (sec):] field on the [MACHINE VISION] tab.

10. The image Jacobian is computed using a least square solution method.

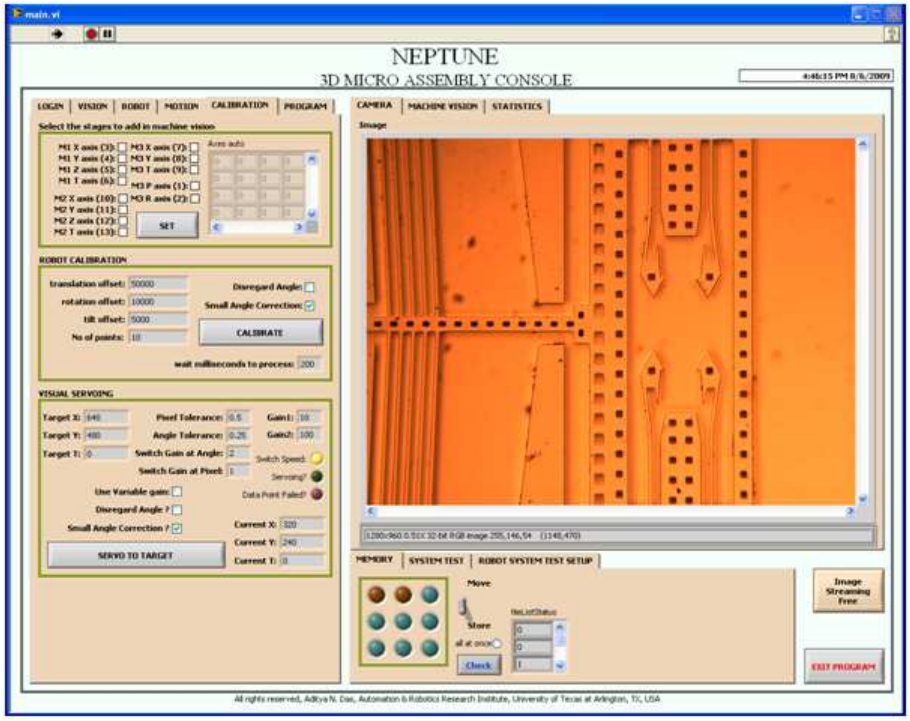

Figure B.7. Calibration and visual servoing using *Neptune 3.0*.

The next main part in automation is visual servoing. Use the visual servoing section on the [CALIBRATION] tab of the main UI.

1. Enter values for [Target X:], [Target Y:] in pixels and [Target T:] in angles to set the desired location to servo to.
2. Enter the tolerance values in the [Pixel Tolerance] and [Angle Tolerance] fields. Servo will stop once the feature being tracked comes within this tolerance limit at the target location.
3. Select the value for Gain in [Gain 1] field. The higher this number is the slower the servo will be.

4. If a variable gain is used use [Gain 2] field to set the second gain value. Also set the values at which to switch the gain by using the [Switch Gain at Angle:] and [Switch Gain at Pixel:] fields. Also check the [Use Variable gain?] check box.
5. If you wish to exclude rotation information then check the [Disregard Angle:] check box.
6. For small angles check the [Small Angle Correction:] checkbox. This will rectify the ambiguity in tracking due to symmetry in template image.
7. Finally click on the [SERVO TO TARGET] button to start servoing. You can manually stop servoing at any time by clicking on the same button.
8. At each servo step the current position can be observed in [Current X:], [Current Y:] and [Current T:] fields.
9. The [Error Propagation during servoing] chart on the [MACHINE VISION] tab updates the error between target and current location in pixels for X and Y and in degrees for orientation. This data can be saved for further analysis by clicking on the [SAVE ERR] button.
10. The servoing time, no. of servo points and no. of failed data points are displayed in the [Servo (sec):], [Servoing points:] and [Failed data points:] fields respectively.

Another important aspect of automated assembly is un-assisted execution of process. An assembly can consist of many different tasks. In the [PROGRAM] tab on the main UI (see figure B.8) the automation process can be configured.

1. There are nine general purpose reconfigurable buttons on the [PROGRAM] tab. This buttons can be assigned and reassigned to any specific task.
2. Using the steps mention in previous sub-section (f) for semi-automated assembly, build the process paths and save them in the [MOTION] tab of the UI.

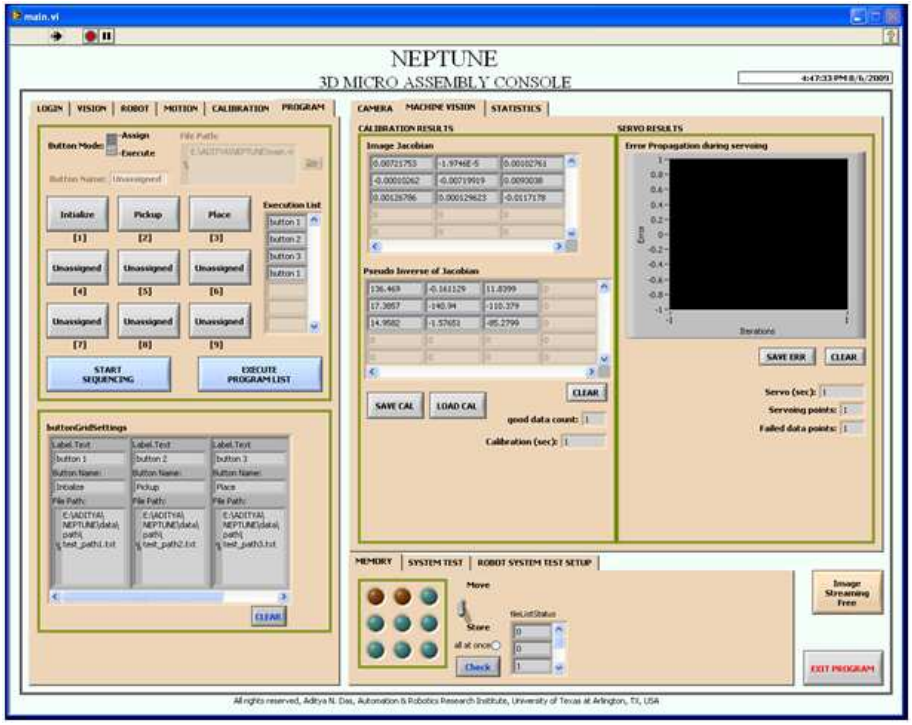

Figure B.8. Assembly programmer module in *Neptune 3.0*.

3. To assign a task to a button, move the [Button Mode:] slider on the [PROGRAM] tab to Assign. The programmable buttons will start blinking. Then navigate to a saved path file location and load it using the [File Path:] control.
4. Give a name for the button in the [Button Name:] field.
5. Then click on any of the nine buttons to configure the button. If the button has a task already assigned to it then this action will overwrite the task with the new one.
6. Similarly you can assign different tasks to the button. To use the buttons, move the [Button Mode:] slider back to Execute mode. Then click on any of the task-assigned buttons to execute the designated task.

7. These reconfigurable buttons can further be used to fully integrate a complete process. To use this click on the [START SEQUENCING] button. The task-assigned buttons will start blinking.
8. Click on these buttons in the order the process need to be executed. This will populate the [Execution List] with the button ids in the order of selection.
9. Once done click on the [STOP SEQUENCING] button with is the same as [START SEQUENCING] button. The [Execution List] will be finalized and compiled.
10. Now click on the [EXECUTE PROGRAM LIST] button to automatically execute the entire process.

B.8 System testing and statistical analysis

The *Neptune 3.0* software application is also equipped with multiple evaluation modules to test the performance of the vision and robot system. The testing scheme has been kept modular which allows the user to add new tests in future without much hassle. A statistical analyzer has been augmented with the application to analyze the test data and derive conclusions regarding precision. To use the tests we will be using the controls in the [SYSTEM TEST], [ROBOT SYSTEM TEST SETUP] and [STATISTICS] tabs on the main user interface (see figure B.9).

Some of the test case scenarios are discussed below.

Test 1: Sensor precision

In this test, we measure the precision of the sensor i.e. the microscope. Multiple sensor measurements of a stationary feature on the robot are taken at fixed time intervals. From the collected data the sensor measurement error distribution is estimated.

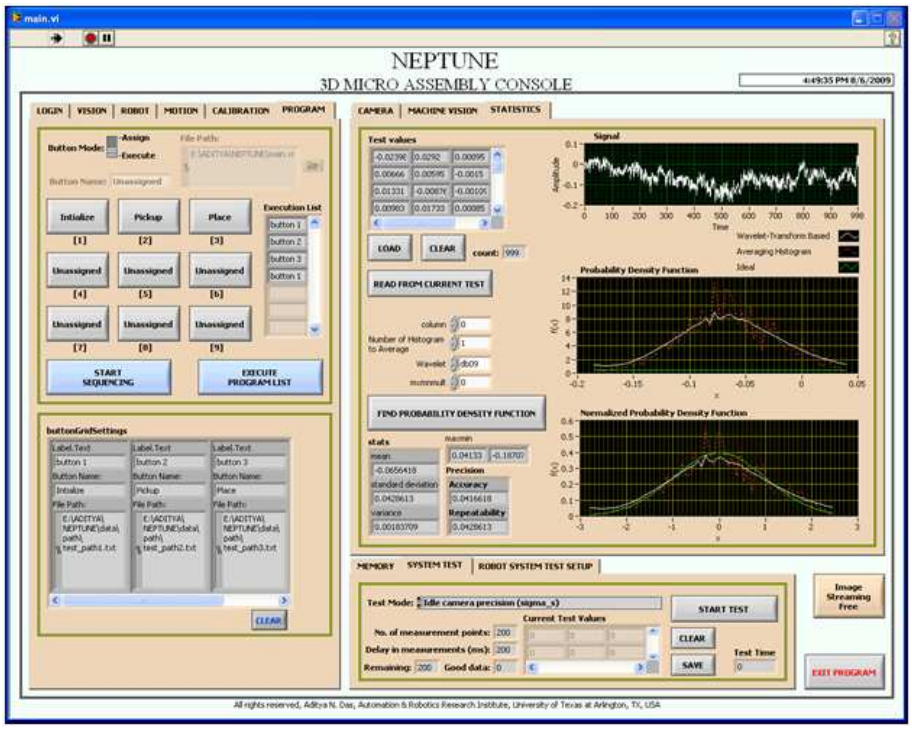

Figure B.9. System analyzer module in *Neptune 3.0*.

1. Select the test mode as [Idle camera precision ($sigma_s$)] from the [Test Model:] drop down menu in the [SYSTEM TEST] tab.
2. Enter the value for [No. of measurement points:] and [Delay in measurements (ms):].
3. Click on the [START TEST] button.
4. The measurements will populate the [Current Test Values] array. The test time is displayed in the [Test Time] field at the end of testing. The test can be saved using the [SAVE] button.
5. On the [STATISTICS] populate the [Test Values] array either clicking on the [LOAD] button or [READ FROM CURRENT TEST] button. The [LOAD] button will load a previously saved test data whereas the [READ FROM CURRENT TEST] will copy the test data from [Current Test Values] to [Test Values].

6. Choose the column of the data to process in [column] field. Also enter values for [Number of Histogram to Average] and [Wavelet] for statistical analysis. The value in [maxminmult] field will expand the view area of the plot.
7. Click on the [FIND PROBABILITY DENSITY FUNCTION] button to determine the pdf. The raw data, as shown in [Signal] chart is processed to find of the probability density function. Then a Gaussian curve is fitted to approximate the computed pdf.
8. The statistical data is shown in the [stats] field and 3-σ precision data is shown in the [Precision] field.

Test 2: Robot repeatability

In this test the robot is moved between two points, one of which is monitored by a sensor. The repeatability of the manipulation system is estimated using the formula given in the previous chapter.

1. In the [ROBOT SYSTEM TEST SETUP] tab select the robot axis from the [Select axis] drop down menu.
2. Enter a value for [Axis offset].
3. Click [ADD] button to add the axis move data to the [Selected Axes] array.
4. Repeat steps (i) through (iii) to add more axes.
5. Once set, go the [SYSTEM TEST] tab. Select the test mode as [Robot Repeatability (σ_3)] from the [Test Model:] drop down menu.
6. Follow steps (ii) through (vii) as mentioned in Test 1 case to perform the repeatability test.

Test 3: Robot accuracy

In this test a feature is selected with the sensor. Then the robot is moved to a random location. At the end of move the positional error at that location is recorded from the encoder reading. Then this position is set as a pseudo home position. The

robot is moved back from this pseudo home position to the starting position by reversing the initial move command. The feature is again detected to determine the error. By repeating this experiment for multiple random pseudo home location, the accuracy of the robot system can be found out.

1. Follow the steps (i) through (iv) as mentioned in Test 2 case to configure the move command for the manipulator.
2. Once set, go the [SYSTEM TEST] tab. Select the test mode as [Robot Accuracy (σ_3)] from the [Test Model:] drop down menu.
3. Follow steps (ii) through (vii) as mentioned in Test 1 case to perform the repeatability test.

APPENDIX C

SIMULATION IN VIRTUAL REALITY - MICROSIM 2.0

Fabrication of microparts can be a time consuming and expensive process. Also off-the-shelf micro components (such as nuts and bolts in macro-scale) are not readily available. These reasons act as impeding factors in having a large number of test case scenario iterations to reliably project the optimized yield and cycle time variables. Simulation can provide the necessary statistical data however these are often far from realistic value, especially in micro domain due to scaling laws. Therefore, in order to achieve realism in simulation and better prediction model, we have developed a virtual 3D simulation environment called *"Microsim 2.0"* which allows the user to realistically evaluate the system and task scenario. Coupled with approximated model for ambient variation such as luminosity, vibration, dynamic noises the Microsim 1.0 application can test for success of any specific assembly task for multiple cases such as robot kinematic linkage, link misalignment, tolerance variation and so on. Figure C.1 shows a snapshot of the *"Microsim 2.0"* application along with some of the virtual world and virtual parts.

The simulation application has been written in such as a way that the algorithms for major functionalities can remain same in the actual and virtual assembly automation applications. (Please contact the author for further details on *"Microsim 2.0"*).

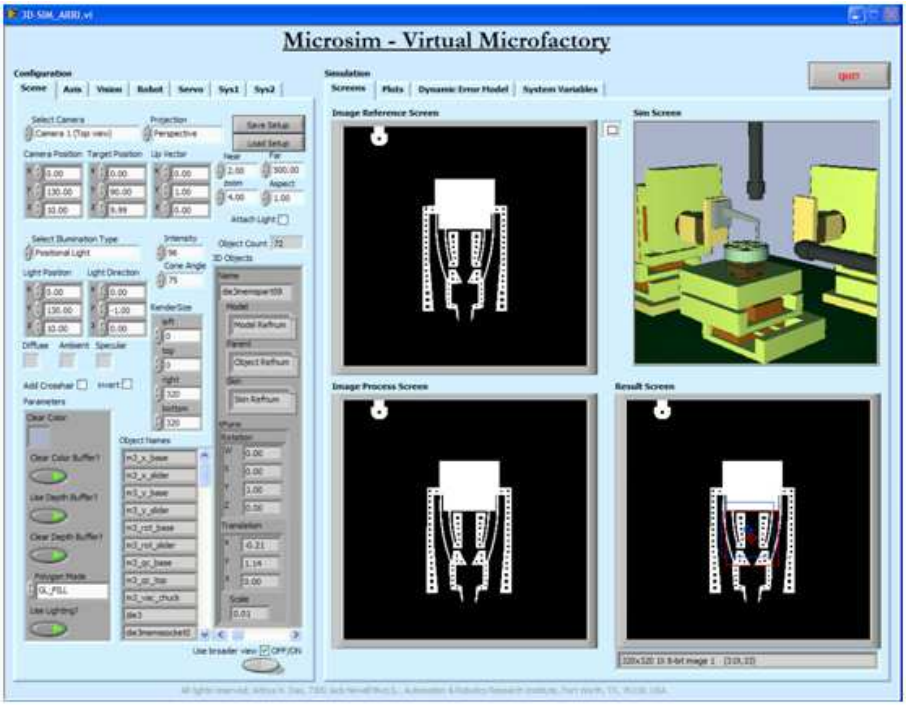

Figure C.1. Process simulation in virtual 3D using *Microsim 2.0*.

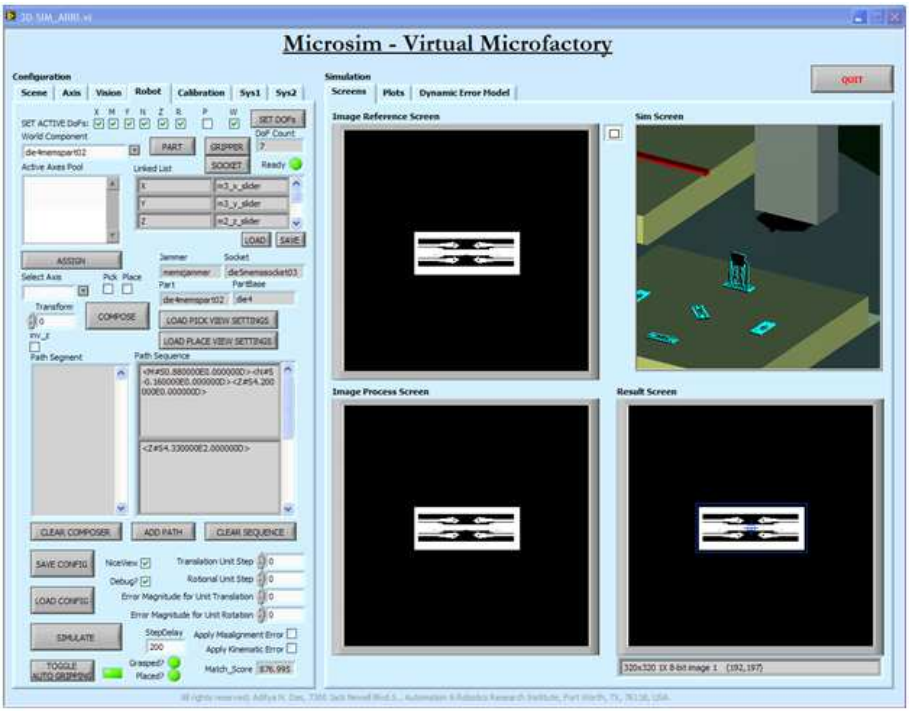

Figure C.2. Virtual assembly in *Microsim 2.0*.

APPENDIX D

MINIATURE ELECTRONIC BACKPACK FOR MICROSYSTEMS

Miniature electronics modules can be merged with die-scale MEMS devices to provide untethered power supply and control logic for desired functionality of the microsystems.

D.1 Configuration factors

1. *Form factor:* The electronics modules must be of similar size as the MEMS die.
2. *Light weight:* The electronics must be light weight so that it can be carried by the MEMS device without hindering its performance i.e. mobility in case of micro robots and compound inertia in case of micro sensors.
3. *Optimum current:* Thermal actuators are essentially current driven devices. They work on the principle of Joule heating i.e. when current is passed through a silicon beam it produces heat due to the resistivity of the beam. This heat bends the beam. Thus more the current, more will be the deflection in the beam which is also known as actuation.
4. *Small power source:* Generally, bulkier and heavier power sources are used when higher current is required. However in case of microsystems the power source must be small and light weight which consequently reduces its current output. Therefore a charge pump is required to extract more current from a small power supply.
5. *Actuation profile:* Circuitry must be added to generate programmable actuation signal profiles such as sinusoidal, saw-tooth, pulse width modulated etc for testing and functioning of the Microsystems.
6. *Data acquisition:* Sensor data acquisition and processing is a crucial factor in microsystems. On-board signal processing and information display capability can make microsystems more portable and self-sufficient.

7. *Interconnection:* Finally, interconnections between MEMS device and miniature electronics must be optimized to increase the robustness and performance of the completed microsystem package.

The on-board electronics for the microsystems thus should consist of the following modules:

1. A power supply unit comprising of a voltage booster and a current amplifier
2. A logic control unit to profile the input signal to the thermal actuator
3. A data acquisition unit to collect the intensity profile of the fringe pattern
4. A signal conditioning unit to prepare and normalize the interferogram data
5. A final output unit to perform the Fourier transform and display the results

D.2 Electronic modules

The building blocks of the electronics module for the above discussed microsystems is shown in figure D.1.

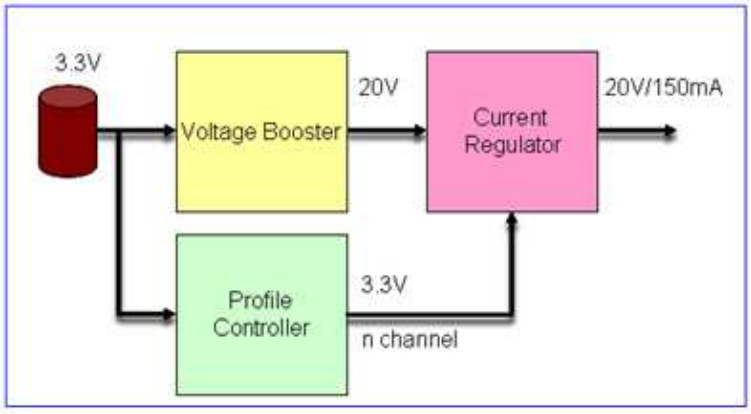

Figure D.1. Block digram for miniature electronics backpack.

The system consists of three main units:

1. Voltage booster

2. Current Regulator
3. Logic Controller

A lithium polymer battery was used as the power source which produces 3.7volts at 600mAh current discharge rating. The battery weighs 1.16grams and has dimensions of 11mm x 17mm x 3.6mm.

D.2.1 Voltage booster

Thermal actuators work based on Joule heating. Thus higher heat *'Q'* is required for longer actuation stroke *'d'*.

$$d \propto Q \tag{D.1}$$

Joule's law gives the amount of heat *'Q'* liberated by current *'I'* flowing through a resistor with resistance *'R'* for a time *'t'*.

$$Q = I^2 Rt \tag{D.2}$$

The resistance *'R'* of the thermal actuator is in the range of $100\Omega - 200\Omega$ and is given by the following relationship, where 'ρ' is the resistivity, *'L'* is the beam length and *'A'* is the cross-sectional area of the beams.

$$R = \frac{\rho L}{A} \tag{D.3}$$

From experimentation it has been found that for 45μm to 50μm of microsystems deflection, the thermal actuator designed for the two microsystems (microspectrometer and ARRIpede), typically 2.5watts to 3watts of power is required. From this a necessary power rating has been established as 20V/150mA. Generally a small lithium ion battery is used as the power source for these microsystems which can provide up

to 3.6volts. Thus a boost converter from *Texas Instruments (part no. TPS61081 HV)* was used to boost the voltage up to 20volts. The circuit diagram for the voltage booster is shown in figure D.2. The output voltage *'VRAIL'* is set by the potential divider *RF1* and *RF2* according to the equation **??**.

$$RF1 = RF2 \times \left[\left(\frac{V_{RAIL}}{1.229V}\right) - 1\right] \tag{D.4}$$

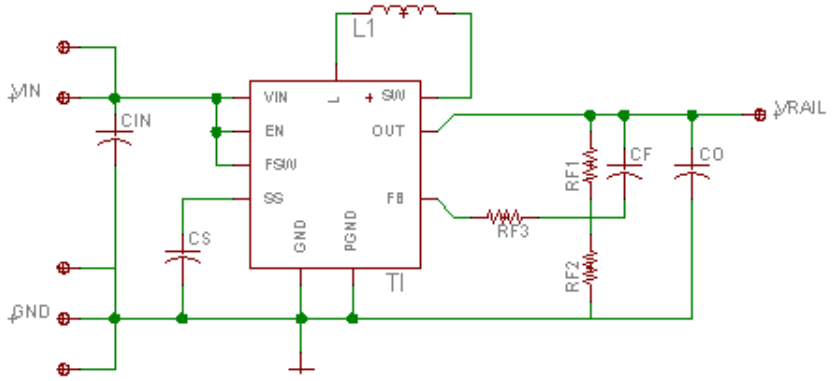

Figure D.2. Circuit diagram for voltage booster.

A typical set of values for components to obtain 20V output is given as follows: $C_{IN} = 4.7\mu F$, $C_S = 47nF$, $L_1 = 4.7\mu H$, $RF3 = 100\Omega$, $RF1 = 768K\Omega$, $RF2 = 49.9K\Omega$, $C_F = 33pF$, $C_O = 4.7\mu F$.

D.2.2 Current regulator

The output of the voltage booster circuit provides 20V which is directly fed across the load resistance of the MEMS thermal actuator which typically draws a current in the range from 150mA to 200mA. A microcontroller produces the actuation profile for the thermal actuator. To drive the larger thermal actuator current biasing

according to the low current actuation profile, a NPN transistor was used. To keep the circuitry of minimal footprint, a simple common emitter configuration was used where the larger collector current I_C is proportional to the base current I_B according to the relationship:

$$I_C = \beta * I_B \tag{D.5}$$

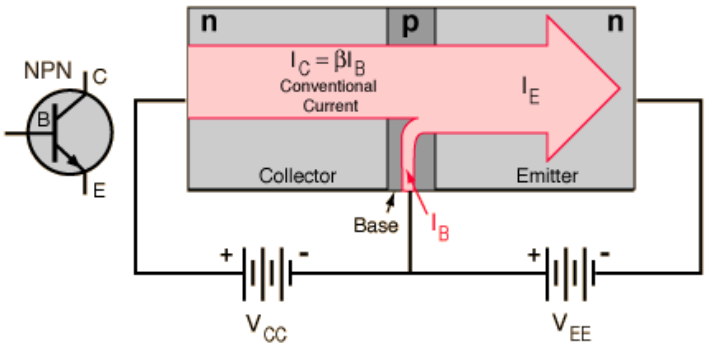

Figure D.3. Basic transistor function.

The smaller current in the base acts as a *"valve"*, controlling the larger current from collector to emitter. A "signal" in the form of a variation in the base current is reproduced as a larger variation in the collector-to-emitter current, achieving an amplification of that signal. The current regulator circuit is shown in figure D.4.

Typical values for components are as follows: $R_b = 1K\Omega$, $R_e = 10K\Omega$, $Q = 20V7.0ANPNTransistor(OnSemiconductorsPartnoNSS20501UW3TG)$.

D.2.3 Logic Controller

The voltage booster and the current regulator jointly constitute the power supply unit for the electronics system for the microsystems. The third element of the

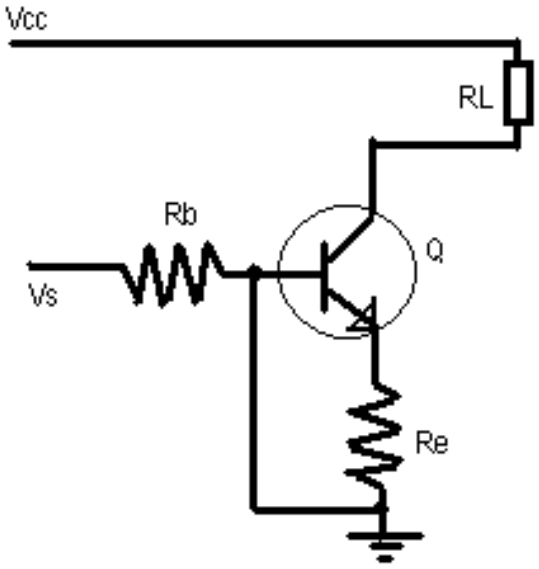

Figure D.4. Circuit diagram for current regulator.

system is a control unit which generates the desired actuation profile and handles acquired data processing. A microcontroller from *Microchip (part no. dsPIC33FJ32GP202)* was used for the logic control. The microcontroller specifications are given in table D.1

The circuit as shown in figure D.5 contains an optional set of circuitry to allow the user to program the microcontroller on-the-fly to generate multiple signal profiles. A dedicated power regulator maintains the operating voltage at 3.3volts for the microcontroller.

D.3 Miniature PCB design

Eagle Layout Editor, a PCB layout editor software, has been used to design the PCB. For micro robots such as arripede, individual circuit boards are prepared and then stacked to reduce the projection area in order to be mounted on the micro-robot. For other microsystem applications, such as microspectrometer, the three blocks are

Table D.1. Specifications of the microcontroller

Parameter	*Specification*
Package	6mm 6mm (QFN)
No. of I/O	21
Output Power	15-watt PWM
Program memory	32KB
Architecture	16 bit
Digital peripherals	1 UART, 1 SPI, 1 IIC
PWM resolution	16 bit
No. of pins	28
Operating voltage	3 to 3.6 volts
CPU speed	40 MIPS
Internal oscillator	7.37 MHz
Capture/Compare/PWM	4/2
Timers	3 (16-bit)

merged in a single PCB which is then integrated to the microsystem in the package. The schematic is shown in figure D.6 and the board is shown in figure D.7.

The circuits are built on a footprint of 15mm by 15mm. To save space the three circuit modules were stacked on top of each other using stand-off interconnects that also provide electrical inter-connectivity. The overall weight of the electronic backpack is around 4 to 5 grams.

Circuit boards are designed using Eagle layout editor software. Machine drilling job used by *Gerber Computer-Aided Manufacturing (CAM) processing software*; contains a compiled set of Gerber files, are used for fabrication layers of printed circuit boards. In order to keep the fabrication cost low and better organization, multiple CAM files are merged together using a software application called GerbeMerge. A typical gerb-merged cam file is shown in figure D.8.

The final miniature backpacks are shown in figures D.9 and D.10.

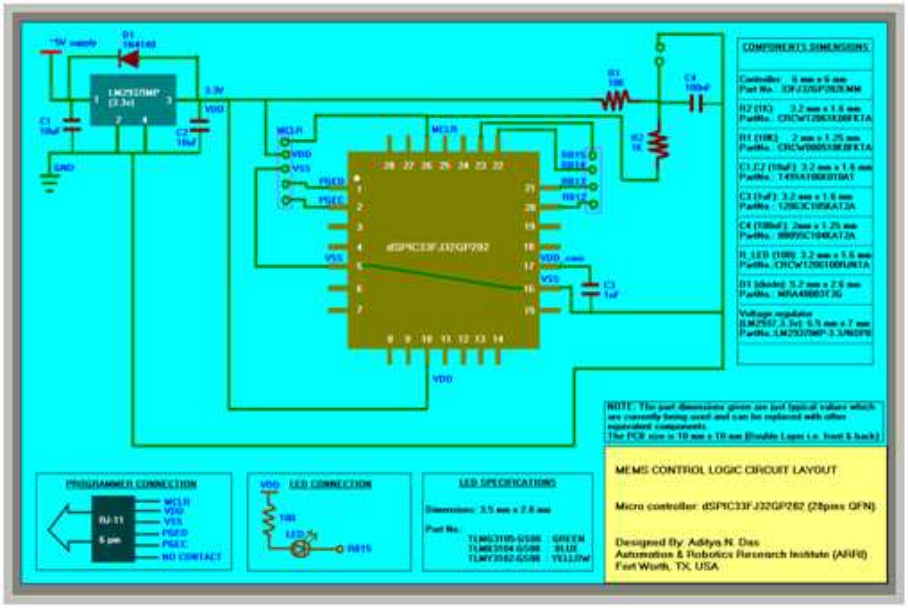

Figure D.5. Circuit diagram for micro controller.

These miniature electronic backpack module help to construct untethered microsystems.

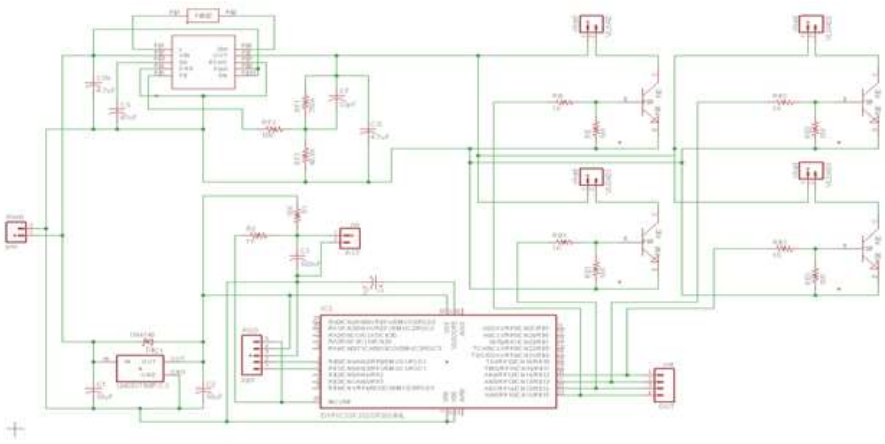

Figure D.6. Circuit layout schematic.

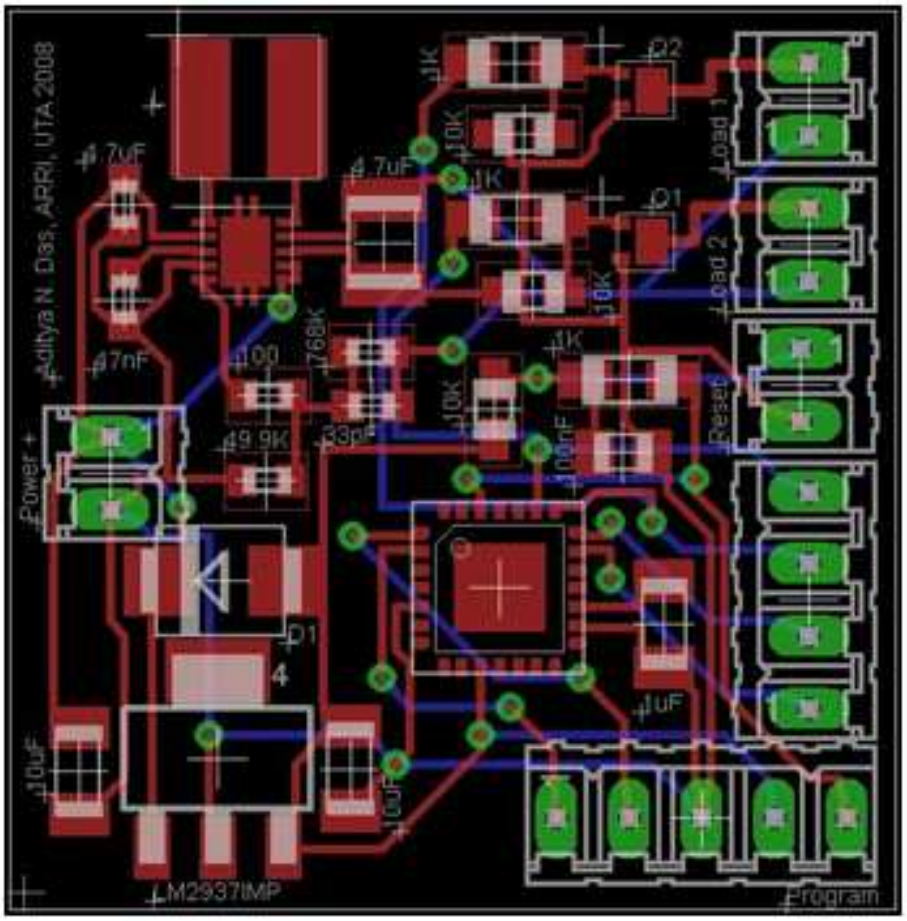

Figure D.7. Circuit layout board.

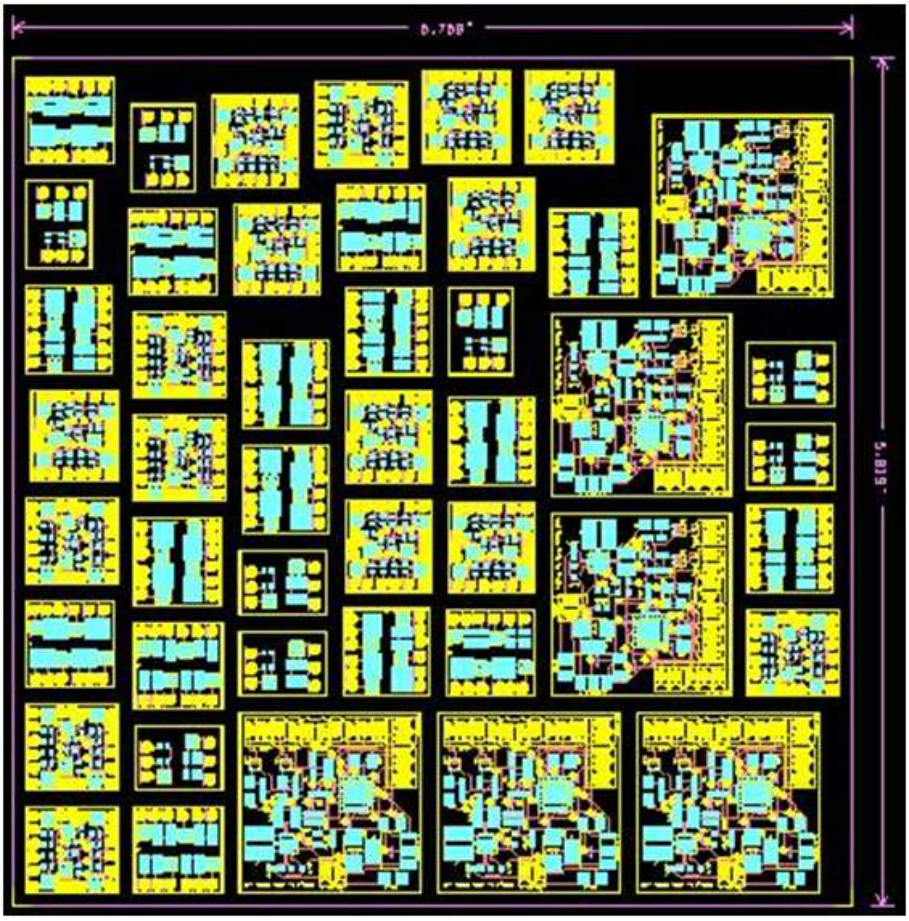

Figure D.8. Gerber merged circuit CAM file.

Figure D.9. Microspectrometer with electronic backpack.

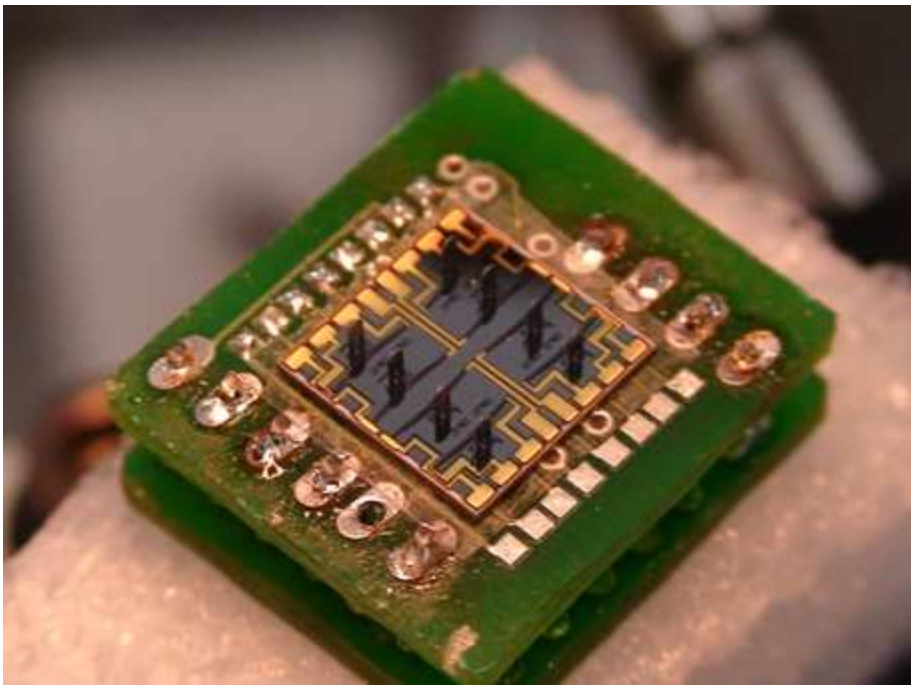

Figure D.10. ARRIpede with electronic backpack.

APPENDIX E

DERIVATION OF EFFECT OF UNCERTAINTIES

$$\sum_{k=0}^{\infty}\left[\frac{1}{k!}\sum_{\alpha=0}^{k-1}\left[\left(\hat{\xi}_i\theta_i\right)^{\alpha}\left(\delta\hat{\xi}_i\theta_i\right)\left(\hat{\xi}_i\theta_i\right)^{(k-1-\alpha)}\right]\right]=\frac{1}{1!}\left(\delta\hat{\xi}_i\theta_i\right)$$
$$+\frac{1}{2!}\left[\left(\delta\hat{\xi}_i\theta_i\right)\left(\hat{\xi}_i\theta_i\right)+\left(\hat{\xi}_i\theta_i\right)\left(\delta\hat{\xi}_i\theta_i\right)\right]$$
$$+\frac{1}{3!}\left[\left(\delta\hat{\xi}_i\theta_i\right)\left(\hat{\xi}_i\theta_i\right)^2+\left(\hat{\xi}_i\theta_i\right)\left(\delta\hat{\xi}_i\theta_i\right)\left(\hat{\xi}_i\theta_i\right)+\left(\hat{\xi}_i\theta_i\right)^2\left(\delta\hat{\xi}_i\theta_i\right)\right]$$
$$+\frac{1}{4!}[\left(\delta\hat{\xi}_i\theta_i\right)\left(\hat{\xi}_i\theta_i\right)^3+\left(\hat{\xi}_i\theta_i\right)\left(\delta\hat{\xi}_i\theta_i\right)\left(\hat{\xi}_i\theta_i\right)^2+\left(\hat{\xi}_i\theta_i\right)^2\left(\delta\hat{\xi}_i\theta_i\right)\left(\hat{\xi}_i\theta_i\right)$$
$$+\left(\hat{\xi}_i\theta_i\right)^3\left(\delta\hat{\xi}_i\theta_i\right)]$$
$$+\frac{1}{5!}[\left(\delta\hat{\xi}_i\theta_i\right)\left(\hat{\xi}_i\theta_i\right)^4+\left(\hat{\xi}_i\theta_i\right)\left(\delta\hat{\xi}_i\theta_i\right)\left(\hat{\xi}_i\theta_i\right)^3+\left(\hat{\xi}_i\theta_i\right)^2\left(\delta\hat{\xi}_i\theta_i\right)\left(\hat{\xi}_i\theta_i\right)^2$$
$$+\left(\hat{\xi}_i\theta_i\right)^3\left(\delta\hat{\xi}_i\theta_i\right)\left(\hat{\xi}_i\theta_i\right)+\left(\hat{\xi}_i\theta_i\right)^4\left(\delta\hat{\xi}_i\theta_i\right)]$$
$$+...+... \tag{E.1}$$

=

$$\left(\delta\hat{\xi}_i\theta_i\right)\left[I+\frac{1}{2!}\left(\hat{\xi}_i\theta_i\right)+\frac{1}{3!}\left(\hat{\xi}_i\theta_i\right)^2+\frac{1}{4!}\left(\hat{\xi}_i\theta_i\right)^3+...\right]$$
$$+\left(\hat{\xi}_i\theta_i\right)\left(\delta\hat{\xi}_i\theta_i\right)\left[\frac{1}{2!}+\frac{1}{3!}\left(\hat{\xi}_i\theta_i\right)+\frac{1}{4!}\left(\hat{\xi}_i\theta_i\right)^2+\frac{1}{5!}\left(\hat{\xi}_i\theta_i\right)^3+...\right]$$
$$+\left(\hat{\xi}_i\theta_i\right)^2\left(\delta\hat{\xi}_i\theta_i\right)\left[\frac{1}{3!}+\frac{1}{4!}\left(\hat{\xi}_i\theta_i\right)+\frac{1}{5!}\left(\hat{\xi}_i\theta_i\right)^2+\frac{1}{6!}\left(\hat{\xi}_i\theta_i\right)^3+...\right]$$
$$+\left(\hat{\xi}_i\theta_i\right)^3\left(\delta\hat{\xi}_i\theta_i\right)\left[\frac{1}{4!}+\frac{1}{5!}\left(\hat{\xi}_i\theta_i\right)+\frac{1}{6!}\left(\hat{\xi}_i\theta_i\right)^2+\frac{1}{7!}\left(\hat{\xi}_i\theta_i\right)^3+...\right]$$
$$+...$$
$$+... \tag{E.2}$$

≈

$$\left(\delta\hat{\xi}_i\theta_i\right)\left[I+\frac{1}{2!}\left(\hat{\xi}_i\theta_i\right)+\frac{1}{3!}\left(\hat{\xi}_i\theta_i\right)^2+\frac{1}{4!}\left(\hat{\xi}_i\theta_i\right)^3+...\right] \tag{E.3}$$

=

$$\left(\delta\hat{\xi}_i\theta_i\right)\left[I+\frac{1}{2!}\left(\hat{\xi}_i\theta_i\right)+\frac{1}{3!}\left(\hat{\xi}_i\theta_i\right)^2+\frac{1}{4!}\left(\hat{\xi}_i\theta_i\right)^3+...\right]\left(\hat{\xi}_i\theta_i\right)\left(\hat{\xi}_i\theta_i\right)^{-1} \tag{E.4}$$

$$=$$

$$\left(\delta\hat{\xi}_i\theta_i\right)\frac{\left[\hat{\xi}_i\theta_i+\frac{1}{2!}\left(\hat{\xi}_i\theta_i\right)^2+\frac{1}{3!}\left(\hat{\xi}_i\theta_i\right)^3+\frac{1}{4!}\left(\hat{\xi}_i\theta_i\right)^4+...\right]}{\theta_i}\left(\hat{\xi}_i{}^{-1}\right) \tag{E.5}$$

$$=$$

$$\left(\delta\hat{\xi}_i\theta_i\right)\frac{\left[\left(\theta_i-\frac{\theta_i^3}{3!}+\frac{\theta_i^5}{5!}-...\right)\hat{\xi}_i+\left(\frac{\theta_i^2}{2!}-\frac{\theta_i^4}{4!}+\frac{\theta_i^6}{6!}-...\right)\hat{\xi_i^2}\right]}{\theta_i}\left(\hat{\xi}_i{}^{-1}\right) \tag{E.6}$$

$$=$$

$$\left(\delta\hat{\xi}_i\theta_i\right)\frac{\left[\left(\theta_i-\frac{\theta_i^3}{3!}+\frac{\theta_i^5}{5!}-...\right)+\left(\frac{\theta_i^2}{2!}-\frac{\theta_i^4}{4!}+\frac{\theta_i^6}{6!}-...\right)\hat{\xi}_i\right]}{\theta_i} \tag{E.7}$$

$$=$$

$$\left(\delta\hat{\xi}_i\theta_i\right)\left[\frac{sin\theta_i}{\theta_i}+\hat{\xi}_i\frac{(1-cos\theta_i)}{\theta_i}\right] \tag{E.8}$$

REFERENCES

[1] A. Ayon, R. Bayt, and K. Breuer, "Deep reactive ion etching: a promising technology for micro- and nanosatellites," *IOP journal of Smart Materials and Structures*, vol. 6, 2001.

[2] V. Saile, U. Wallrabe, O. Tabata, and G. K. Fedder, *LIGA and Its Applications.* Weinheim, Germany: Wiley-VCH, 2009.

[3] NEXUS, "Nexus market analysis for mems and microsystems," 2006. [Online]. Available: http://www.enablingmnt.com/html/nexus_market_report.html

[4] A. Requicha, *Nanomanipulation with the atomic force microscope in R. Waser, Ed. Nanotechnology, Volume 3: Information Technology.* Weinheim, Germany: Wiley-VCH, 2008.

[5] W. Wang and S. Soper, *Bio-MEMS Technologies and Applications.* USA: CRC Press, 2007.

[6] T. Hsu, *MEMS Packaging.* London, United Kingdom: INSPEC, The Institute of Electrical Engineers, 2004.

[7] F. Arai, D. Ando, T. Fukuda, Y.Nododa, and T. Oota, "Micro manipulation based on micro physics-strategy based on attractive force reduction and stress measurement," in *Proceedings of the 1995 IEEE/RSJ International Conference on Intelligent Robots and Systems (IROS 95)*, vol. 2, 1995, pp. 263–266.

[8] R. Fearing, "Survey of sticking effects for micro part handling," in *Proceedings of the 1995 IEEE/RSJ International Conference on Intelligent Robots and Systems (IROS 95)*, vol. 2, 1995, pp. 212–217.

[9] H. Saito, H.Miyazaki, and T. Sato, "Pick and place operation of micro object with high reliability and precision based on micro physics under sem," in *Proceedings of the 1999 IEEE International Conference on Robotics and Automation, (ICRA 99)*, 1999, pp. 2736–2743.

[10] M. Sitti and H. Hashimoto, "Tele-nanorobotics using atomic force microscope," in *Proceedings of the 1998 IEEE/RSJ International Conference on Intelligent Robots and Systems, (IROS 98)*, 1998, pp. 1739–1746.

[11] Y. Zhou and B. Nelson, "Adhesion force modeling and measurement for micromanipulation," in *Proceedings of SPIE in Microrobotics and Micromanipulation (SPIE 98)*, 1998, pp. 169–180.

[12] J. Feddema, P. Xavier, and R. Brown, "Assembly planning in micro scale," in *Proceedings 1998 IEEE International Conference on Robotics and Automation (ICRA 98)*, Leuven, Belgium, 1998.

[13] ——, "Microassembly planning with van der waals force," in *Proceedings of the 1999 IEEE International Symposium on Assembly and Task Planning,(ISATP 99)*, 1999, pp. 32–38.

[14] Y. Zhou and B. Nelson, "Simulation of micro-manipulations: Adhesion forces and specific dynamic models," *International Journal of Adhesion and Adhesive*, vol. 19, pp. 35–48, 1999.

[15] Q. Zhou, P. Kallio, F. Arai, T. Fukuda, and H. Koivo, "A model for operating spherical micro objects," in *Proceedings of the 1999 International Symposium on Micromechatronics and Human Science, (MHS 99)*, 1999, pp. 79–85.

[16] K. Johnson, *Contact Mechanics*. Cambridge University Press, 1985.

[17] K. Rabenorosoa, C. Clevy, P. Lutz, M. Gauthier, and P. Rougeot, "Measurement of pull-off force for planar contact at the microscale," in *IET Micro Nano Letters*, vol. 4, 2009, pp. 148–154.

[18] M. J. Madou, *Fundamentals of Microfabrication.* USA: CRC Press, 2002.

[19] J. Bryzek, E. Abbott, A. Flannery, D. Cagle, and J. Maitan, "Control issues for mems," in *Proceedings of IEEE International Conference on Decision and Control (CDC 03)*, 2003.

[20] D. O. Popa, B. H. Kang, J. T. Wen, H. E. Stephanou, G. Skidmore, and A. Geisberger, "Dynamic modeling and input shaping of thermal bimorph actuators," in *Proceedings of IEEE International Conference on Robotics and Automation (ICRA 03)*, vol. 1, 2003, pp. 1470–1475.

[21] A. Q. Liu, X. M. Zhang, C. Lu, F. Wang, C. Lu, and Z. S. Liu, "Optical and mechanical models for a variable optical attenuator using a micromirror drawbridge," *Journal of Micromechanics and Microengineering (JMM 03)*, vol. 13, 2003.

[22] B. Borovic, C. Hong, A. Q. Liu, L. Xie, and F. L. Lewis, "Control of a mems optical switch," in *Proceedings of IEEE International Conference on Decision and Control (CDC 04)*, 2004.

[23] B. Ebrahimi and M. Bahrami, "Robust sliding-mode control of a mems optical switch," *Journal of Physics: Conference Series 34*, pp. 728–733, 2006.

[24] L. Y. Pao, J. A. Butterworth, and D. Y. Abramovitch, "Combined feedforward/feedback control of atomic force microscopes," in *Proceedings of American Control Conference(ACC 07)*, New York, USA, 2004.

[25] S. Jagannathan and M. Hameed, "Adaptive force-balancing control of mems gyroscope with actuator limits," in *Proceedings of American Control Conference(ACC 04)*, vol. 2, no. 30, July 2004, pp. 1862–1867.

[26] L. Wang, J. Dawson, J. Chen, P. Famouri, and A. Hornak, "Stroke-length control of a mems device," in *Proceedings of the 2000 IEEE International Symposium on Industrial Electronics (ISIE 00)*, vol. 2, 2000, pp. 535–539.

[27] A. A. Geisberger, N. Sarkar, M. Ellis, and G. D. Skidmore, "Electrothermal properties and modeling of polysilicon microthermal actuators," *Journal of MicroElectroMechanical Systems (JMEMS 03)*, vol. 12, no. 4, pp. 513–523, August 2003.

[28] Y. Yang and K. Shen, "Nonlinear heattransfer macromodeling for mems thermal devices," *Journal of Micromechanics and Microengineering (JMM 03)*, vol. 15, no. 2, pp. 408–418, 2005.

[29] S. Wolf and R. N. Tauber, *Silicon Processing for the VLSI Era, Volume 1: Process Technology.* Sunset Beach, CA, USA: Lattice Press, 1986.

[30] J. Darnell, H. Lodish, and D. Baltimore, *Molecular cell biology.* New York, USA: W.H. Freeman, 1986.

[31] C. Cantor, *The behavior of biological macromolecules.* San Fransisco, USA: W.H. Freeman, 1980.

[32] M. Cohn, C. J. Kim, and A. Pisano, "Self-assembling electrical networks: An application of micromachining technology," in *Proceedings of International Conference on Solid- State Sensors and Actuators*, San Fransisco, USA, 1991, p. 493.

[33] M. Hakamada and M. Mabuchi, "Nanoporousgold prism microassembly through a self- organizing route," in *American Chemical Society NanoLetters*, vol. 6, no. 4, 2006, pp. 882–885.

[34] B. Vikramaditya and B. J. Nelson, "Visually guided microassembly using optical microscopes and active vision techniques," in *Proceedings of IEEE Intemational Conference on Robotics and Automation (ICRA 97)*, Albuquerque, New Mexico, USA, April 1997.

[35] J. Thompson and R. Fearing, "Automating microassembly with ortho-tweezers and force sensing," in *Proceedings of IEEE/RSJ International Conference on Intelligent Robots and Systems*, vol. 3, Maui, USA, 2001, pp. 1327–1334.

[36] M. A. Greminger and B. J. Nelson, "Vision-based force sensing at nanonewton scales," in *Proceedings of SPIE*, 2001.

[37] C. Liguo, S. Lining, R. Weibin, and B. Xinqian, "Hybrid control of vision and force for mems assembly system," in *Proceedings of IEEE International Conference on Robotics and Biomimetics*, Shenyang, China, August 2004.

[38] K. Santa, S. Fatikow, and G. Felso, "Control of microassembly-robots by using fuzzy-logic and neural networks," *Journal on Computers in Industry*, vol. 39, pp. 219–227, 1999.

[39] M. Cohn, Y.-C. Liang, R. Howe, and A. Pisano, "Wafer-to-wafer transfer of microstructures for vacuum packaging," in *Proceedings of Solid-State Sensor and Actuator Workshop*, Hilton Head Island, SC, USA, June 1996.

[40] A. Singh, D. Horsley, M. Cohn, A. Pisano, and R. Howe, "Batch transfer of microstructures using flip-chip solder bonding," *Journal of Microelectromechanical Systems (JMEMS 99)*, vol. 8, no. 1, pp. 27–33, 1999.

[41] J. Wang, X. Tao, H. Deokhwa, and C. Hyungsuck, "A fuzzy adaptive pd controller based microassembly system," in *Proceedings of the conference on international society for optical engineering (SPIE)*, 2006.

[42] B. Kim, J. Park, C. Moon, G. Jeong, and H. Ahn, "A precision robot system with modular actuators and mems micro gripper for micro system assembly," *Journal of mechanical science and technology*, vol. 22, no. 1, pp. 70–76, 2008.

[43] G. Yang, J. Gaines, and B. Nelson, "A supervisory wafer-level 3d microassembly system for hybrid mems fabrication," *Journal of Intelligent and Robotic Systems*, vol. 37, no. 1, pp. 43–68, 2003.

[44] R. Schmitt, S. Driessen, and B. Engelmann, "Controlling the assembly of micro systems by image processing," *Journal of Microsystem Technologies*, vol. 12, no. 7, pp. 640–645, 2006.

[45] G. Chung, K. Choi, and J. Kyung, "Development of precision robot manipulator using flexture hinge mechanism," in *Proceedings of the IEEE conference on robotics, automation and mechatronics*, 2006.

[46] K. Saitou, D. Wang, and S. Wou, "Externally resonated linear microvibromotor for microassembly," *Journal of Microelectromechanical systems*, vol. 9, no. 3, pp. 336–346, 2000.

[47] B. Kim, H. Kang, D. Kim, G. Park, and J. Park, "Flexible microassembly system based on hybrid manipulation scheme," in *Proceedings of the IEEE/RSJ international conference on robots and systems (IROS)*, vol. 2, Las Vegas, USA, 2006, pp. 2061–2066.

[48] Q. Zhou, A. Aurelian, B. Chang, C. delCorral, and H. N. Koivo, "Microassembly system with controlled environment," *Journal of micromechatronics*, vol. 2, pp. 227–248, 2002.

[49] B. E. Kratochvil, K. B. Yesin, V. Hess, and B. J. Nelson, "Design of a visually guided 6 dof micromanipulator system for 3d assembly of hybrid mems," in *Proceedings of the 4th International Workshop on Microfactories*, 2004.

[50] B. Nelson, Y. Zhou, and B. Vikramaditya, "Sensor-based microassembly of hybrid mems devices," *IEEE Control Systems Magazine*, vol. 18, pp. 35–45, 1998.

[51] S. Fatikow, J. Seyfried, S. Fahlbusch, A. Buerkle, and F. Schmoeckel, "A flexible microrobot-based microassembly station," *Journal of Intelligent and Robotic Systems (JIRS 00)*, vol. 27, pp. 135–169, 2000.

[52] S. Fatikow and J. Seyfried, "Control architecture of a flexible microrobot based microassembly station," in *Proceedings of the 7th Mediterranean Conference on trol and Automation (MED99)*, 1999, pp. 1974–1981.

[53] K. Rabenorosoa, C. Clevy, P. Lutz, A. N. Das, R. Murthy, and D. O. Popa, "Precise motion control of a piezoelectric microgripper for microspectrometer assembly," in *Proceedings of the ASME International Design Engineering Technical Conferences and Computers and Information in Engineering Conference (IDETC/CIE)*, 2009.

[54] A. Mardanov, J. Seyfried, and S. Fatikow, "An automated assembly system for a microassembly station," *Computers in industry*, vol. 38, no. 2, pp. 93–102, 1999.

[55] K. Tsui, A. Geisberger, M. Ellis, and G. Skidmore, "Micromachined end-effector and techniques for directed mems assembly," *Journal of Micromechanics and Microengineering*, pp. 542–549, 2004.

[56] A. Fernandez, B. Staker, W. Owens, L. Muray, J. Spallas, and W. C. Banyai, "Modular mems design and fabrication for an 80 x 80 transparent optical cross-connect switch," in *Proceedings of SPIE Micro-optomechatronic systems*, vol. 5604, 2004.

[57] M. Stubenrauch, U. Frober, D. Voges, C. Schilling, M. Hoffmann, and H. Witte, "A modular biomems platform for new procedures and experiments in tissue engineering," *Journal of Micromechanics and Microengineering*, 2009.

[58] M. Berg, M. Kreveld, M. Overmars, and O. Schwarzkopf, *Computational Geometry 2nd revised edition.* Springer-Verlag, 2000.

[59] J. Latombe, *Robot motion planning.* Kluwer Academic Publishers, 1991.

[60] L. He, C. Han, and W. Wee, "Object recognition and recovery by skeleton graph matching," in *IEEE International Conference on Multimedia and Expo*, Los Alamitos, CA, USA, 2006, pp. 993–996.

[61] A. Okabe, B. Boots, K. Sugihara, and S. N. Chiu, *Spatial Tessellations - Concepts and Applications of Voronoi Diagrams, 2nd edition.* John Wiley, 2000.

[62] A. Watt, *3D Computer Graphics, 3rd edition.* Addison Wesley, 1999.

[63] T. Cormen, C. Leiserson, R. Rivest, and C. Stein, *Introduction to Algorithms, 2nd edition.* MIT press and McGraw-Hill, 2001.

[64] J. Barraquand, B. Langlois, and J. Latombe, "Numerical potential field techniques for robot path planning," *Transactions on systems and man and cybernetics*, vol. 22, no. 2, pp. 224–241, 1992.

[65] J. Fan, M. Fei, and S. Ma, "Rl-art2 neural network based mobile robot path planning," in *Proceedings of International Conference on Intelligent Systems Design and Applications*, vol. 2, Los Alamitos, CA, USA, 2006, pp. 581–585.

[66] D. Xin, C.Hua-hua, and G. Wei-kang, "Neural network and genetic algorithm based global path planning in a static environment," *Journal of Zhejiang University - Science A*, vol. 6, no. 6, pp. 549–554, 2008.

[67] M. Wang and J. Liu, "Fuzzy logic based robot path planning in unknown environment," in *Proceedings of International Conference on Machine Learning and Cybernatics*, vol. 2, Guangzhou, China, 2005, pp. 813–818.

[68] D. Knuth, *The Art of Computer Programming. Volume 3: Sorting and Searching.* Addison-Wesley, 1998.

[69] M. Sniedovich, "Dijkstra's algorithm revisited: the dynamic programming connexion," *Journal of Control and Cyberntics*, vol. 35, no. 3, pp. 599–620, 2006.

[70] J. Kruskal, "On the shortest spanning subtree of a graph and the traveling salesman problem," in *Proceedings of the American Mathematical Society*, vol. 7, no. 1, 1956, pp. 48–50.

[71] V. Garcia, E. Debreuve, and M. Barlaud, "Fast k nearest neighbor search using gpu," in *Proceedings of the CVPR Workshop on Computer Vision on GPU*, Anchorage, Alaska, USA, 2008.

[72] R. Prim, "Shortest connection networks and some generalizations," *Bell System Technical Journal*, vol. 36, pp. 1389–1401, 1957.

[73] R. Dechter and J. Pearl, "Generalized best-first search strategies and the optimality of a*," *Journal of the ACM*, vol. 32, pp. 505–536, 1985.

[74] H. Berliner, "The b* tree search algorithm. a best-first proof procedure," *Journal of Artificial Intelligence*, vol. 12, pp. 23–40, 1979.

[75] A. Stentz, "Optimal and efficient path planning for partially- known environments," in *Proceedings of the International Conference on Robotics and Automation (ICRA)*, 1994, pp. 3310–3317.

[76] D. of Defense, *Computer-aided acquisition and logistic support (CALS) program implementation guide*. DoD, 1990.

[77] D. Hoffman, "An overview of concurrent engineering," in *Proceedings of the Annual Reliability and Maintainability Symposium*, Philadelphia, Pennsylvania (USA), 1997, pp. 1–6.

[78] J.V.Michaels and D. Younker, "Value engineering in the tqm environment," in *Proceedings of the Society of American Value Engineers*, New Orleans, USA, 1994.

[79] M. Museau, C. Masclet, and S. Tichkiewitch, "Integrated design of mems: aiming at manufacturability," *Journal on Interactive Design and Manufacturing*, vol. 1, no. 3, pp. 127–134, 2007.

[80] M. da Silva, R. Giasolli, S. Cunningham, and D. DeRoo, "Mems design for manufacturability (dfm)," in *Proceedings of the sensor expo and conference*, 2002.

[81] M. Orshansky, S. R. Nassif, and D. Boning, *Design for maufacturability and statistical design - A constructive approach*. Springer US, 2007.

[82] D. Popa, R. Murthy, and A. N. Das, "m^3: Deterministic, multiscale, multi-robot platform for microsystems packaging: Design and quasi-static precision evaluation," *Transactions on Automation Science and Engineering*, 2008.

[83] A.N.Das, P.Zhang, W.H.Lee, D.O.Popa, and H.E.Stephanou, "μ^3: Multiscale, deterministic micro-nano assembly system for construction of on-wafer micro-robots," in *Proceedings of IEEE International Conference on Robotics and Automation (ICRA 07)*, vol. 10, no. 14, Roma, Italy, April 2007, pp. 461–466.

[84] J. R. Taylor, *An Introduction to Error Analysis: The Study of Uncertainties in Physical Measurements*. University Science Books, 1999.

[85] S. A. Hutchinson, G. D. Hager, and P. I. Corke, "A tutorial on visual servo control," *IEEE Transactions on Robotics and Automation*, vol. 12, pp. 651–670, 1996.

[86] J. J. Craig, *Introduction to Robotics: Mechanics and Control (3rd Edition)*. Prentice Hall, 2004.

[87] W. Lee, M. Dafflon, H. Stephanou, S. Young, J. Hochberg, and G. Skidmore, "Tolerance analysis of placement distributions in tethered micro-electro-mechanical systems components," in *Proceedings of the International Conference on Robotics and Automation (ICRA)*, vol. 1, 2004, pp. 884–889.

[88] H. Tijms, *Understanding Probability: Chance Rules in Everyday Life*. Cambridge: Cambridge University Press, 2004.

[89] R. Hartenberg and J. Denavit, *Kinematic Synthesis of Linkages*. McGraw-HIll Book Company, 1964.

[90] R. Murray, Z. Li, and S. Sastry, *A Mathematical Introduction of Robotic Manipulation*. CRC Press, 1994.

[91] J. Barthel and T. Chuh, "Optical switches enable dynamic optical add or drop modules," in *WDM solutions*, vol. 3, no. 8, 2001, pp. 93–96.

[92] R. Bates, *Optical Switching and Networking Handbook*. New York, USA: McGraw-Hill, 2001.

[93] TI, "Texas instruments dlp tech," 2006. [Online]. Available: http://www.dlp.com/tech/what.aspx

[94] K. Iga, "Surface-emitting laser - its birth and generation of new optoelectronics field," *IEEE Journal of Selected Topics in Quantum Electronics*, vol. 6, pp. 1201–1215, 2000.

[95] N. Kanbara, S. Tezuka, and T. Watanabe, "Mems tunable vcsel with concave mirror using the selective polishing method," in *IEEE/LEOS International Conference on Optical MEMS and Their Applications*, vol. 9, 2006.

[96] H. Wang, Y. Xinjian, J. Lai, and Y. Li, "Fabricating microbolometer array on unplanar readout integrated circuit," *International Journal of Infrared and Millimeter Waves*, vol. 26, pp. 715–762, January 2005.

[97] O. Optics, "Spectrometers," 2008. [Online]. Available: www.oceanoptics.com/ products/ spectrometers.asp

[98] C. Solf, J. Mohr, and U. Wallrabe, "Miniaturized liga fourier transformation spectrometer," in *Proceedings of IEEE Sensors*, vol. 2, October 2003, pp. 773–776.

[99] H. Kung, S. Bhalotra, J. Mansell, D. Miller, and J. Harris, "Standing-wave fourier transform spectrometer based on integrated mems mirror and thin-

film photodetector," *IEEE Journal of Selected Topics in Quantum Electronics*, vol. 8, pp. 98–105, January 2002.

[100] T. Sandner, A. Kendra, C. Drabe, W. Scherf, and H. Schenk, "Miniaturized ftir-spectrometer based on optical mems translatory actuator," in *Proceedings of SPIE, MOEMS and Miniaturized Systems VI*, vol. 6466, 2007.

[101] A. Kendra, C. Drabe, H. Schenk, A. Frank, M. Lenzhofer, and W. Scherf, "Application of a micromachined translatory actuator to an optical ftir spectrometer," in *Proceedings of SPIE, MEMS, MOEMS, and Micromachining II*, vol. 6186, 2006.

[102] G. L. an S. Schweizer, S. Schiesser, and P. Renaud, "Tunable optical filter of porous silicon as key component for a mems spectrometer," *Journal of Microelectromechanical Systems (JMEMS 02)*, vol. 11, pp. 815–828, December 2002.

[103] C. Ataman and H. Ure, "Vertical resonant comb actuators for fourier transform spectroscopy," in *IEEE/LEOS International Conference on Optical MEMS and Their Applications*, 2006, pp. 44–45.

[104] P. Griffiths and J. Haseth, *Fourier Transform Infrared Spectrometry, 2nd Edition.* John Wiley and Sons Inc., 2001.

[105] D. Burns and E. Ciurczak, *Handbook of Near-Infrared Analysis , 2nd Edition.* Practical Spectroscopy series, Volume 27, Marcel Dekker Inc, 2001.

[106] S. Selbrede and Y. Pilloux, "Drie technology for mems," 2009. [Online]. Available: www.tegal.com

BIOGRAPHICAL STATEMENT

Aditya N. Das was born in Cuttack, India, in 1981. He received his B.S. degree from Utkal University, India, in 2002, his M.S. and Ph.D. degrees from The University of Texas at Arlington in December 2005 and December 2009, respectively, all in Electrical Engineering. From 2005 to 2009, he was with the Automation and Robotics Research Institute, University of Texas at Arlington as a Graduate Research Asst.His current research interest is in the area of Multiscale Robotics, Microsystems and MEMS Control. He is a member of several IEEE societies.